UNIVERSITY OF OKLAHOMA

GRADUATE COLLEGE

A 20-YEAR SURVEY OF SHORT-DURATION EXTREME RAINFALL EVENTS FROM SUMMERTIME CONVECTION OVER THE CENTRAL AND EASTERN UNITED STATES: CLIMATOLOGY, TRENDS, AND METEOROLOGICAL PATTERNS

A THESIS

SUBMITTED TO THE GRADUATE FACULTY

in partial fulfillment of the requirements for the

Degree of

MASTER OF SCIENCE

By

JASON CHIAPPA
Norman, Oklahoma
2023

A 20-YEAR SURVEY OF SHORT-DURATION EXTREME RAINFALL EVENTS FROM SUMMERTIME CONVECTION OVER THE CENTRAL AND EASTERN UNITED STATES: CLIMATOLOGY, TRENDS, AND METEOROLOGICAL PATTERNS

A THESIS APPROVED FOR THE
SCHOOL OF METEOROLOGY

BY THE COMMITTEE CONSISTING OF

Dr. David B. Parsons, Chair

Dr. Alan Shapiro, Co-Chair

Dr. Jason C. Furtado

Dr. James H. Ruppert

Acknowledgments

First off, I would like to express my deepest appreciation to my advisor, Dr. David Parsons, for his endless kind support and encouragement throughout my time at OU, even after undergoing several medical surgeries. Dave always gave me the freedom to explore topics I was most passionate about and provided invaluable feedback and advice that would help me grow as a scientist. Also, I would like to thank Dave, as well as my co-advisor, Dr. Alan Shapiro, for giving me the opportunity to be a coauthor of their works currently in the process of being published. Many thanks to my entire defense committee for reviewing this lengthy thesis and providing important questions and helpful suggestions. A special thanks goes out to Dr. Jason Furtado for not only meeting with me to provide helpful advice on improving the statistical methods, but also for providing a basis for the analysis through his outstanding Advanced Statistical Meteorology course in Spring 2022. In fact, this thesis stemmed from the class project for that course, which yielded impactful results that surpassed those of my previously proposed thesis topic. I am also deeply grateful to the National Science Foundation for providing continuous funding for this research and supporting the MAD (Multiscale Atmospheric Dynamics) research group through grant NSF-AGS 1921587.

The precipitation dataset used for this work was provided by NCAR's Earth Observing Laboratory under the sponsorship of the National Science Foundation. I would like to thank the representatives from the River Forecast Centers that responded to our questions regarding the data.

I would also like to acknowledge my undergraduate advisor from Florida Tech, Dr. Steven Lazarus, for getting me involved in research and data analysis and giving me the opportunity to coauthor on his paper. I would not have ended up where I am without his mentoring and support.

Last, but not least, I would like to thank my friends and family. To my friends that I've made during my time at OU after being secluded during the pandemic: Thank you Jonah, Emily, Laura, Alec, Brandon, and Angela. Our fun Friday night dinners and game nights always provided me with much-needed relief during tough semesters and weeks of work. Also, my deepest gratitude goes to my mom and stepdad for always supporting me, including helping me move halfway across the country in 2020, and to my older sister, Rachel, for being my best friend.

Table of Contents

Abstract

Short-duration extreme rainfall events (EREs) caused by convection are often associated with flash flooding, which can have devastating impacts on society. An increase in the frequency and intensity of EREs has been documented over multiple continents with evidence of a direct link to anthropogenic climate change. Over the central and eastern Continental United States (CONUS), EREs peak in frequency during June, July, and August (JJA) due to the summertime maximum in convective activity, with the most significant EREs resulting from mesoscale convective systems (MCSs). These MCSs and their associated rainfall have a nocturnal maximum over the central CONUS.

This study utilizes gridded hourly Stage IV precipitation analyses to detect short-duration EREs and record their properties over the central and eastern CONUS over a 20-year period (2003–2022). The Stage IV dataset consists of gauge-corrected radar-derived quantitative precipitation estimates on a 4-km grid, which has the advantage of capturing localized extreme rainfall that can occur between rain gauge sites. Extreme rainfall is defined in this study when the 12-hour accumulation exceeded the 10-year average recurrence interval threshold at that location based on the NOAA Atlas 14 dataset. All nearby grid points simultaneously exceeding the threshold were grouped into event objects. Several spurious events that were detected due to errors in the Stage IV dataset were filtered out using consistent quality control procedures.

Results of the 20-year climatology mainly solidify previous studies, but this study provides additional quantitative evidence that nocturnal MCSs are the most prolific producers of extreme rainfall over the domain during JJA. Unfortunately, the accurate prediction of nocturnal convective rainfall has been shown to be a challenge in numerical weather prediction models. In addition, the highly localized and chaotic nature of the extreme rainfall is revealed, motivating the need for high resolutions in precipitation data and numerical models.

The few previous studies that utilized Stage IV analyses for the purposes of studying EREs did not examine interannual or long-term changes in ERE frequency or characteristics. With acknowledgments of the potential caveats of using the Stage IV dataset, this study discovered statistically significant increasing trends in ERE frequencies through the 20-year period that are dominated by MCSs during JJA, as opposed to more localized convection. Despite the short period of record, this finding aligns with previous studies suggesting an increase in heavy rainfall from MCSs in a warming climate.

This thesis also discusses the discovery of a wide range of interannual variability in the frequency and severity of the JJA convective EREs. Composite and correlation analyses using reanalysis fields reveal statistically significant large-scale meteorological patterns that may help explain this variability, which can potentially aid in medium and long-term forecasting. These patterns include higher low–mid-level moisture over the Southern and Central Great Plains, enhanced southerly moisture transport from the western Gulf Coast to the Midwest, and enhanced mid-level ridging over the southeastern CONUS. Bolstered by composite analysis of five intense nocturnal EREs over the central CONUS, there is a strong argument that the enhanced moisture transport is driven by a westward expansion of the climatological North Atlantic Subtropical High into the eastern CONUS. Higher geopotential heights over the eastern CONUS relative to the Rockies results in an enhanced pressure gradient and southerly flow over the central CONUS, leading to a stronger and/or more frequent low-level jet. The low-level jet is a key ingredient in the development of nocturnal extreme-rain-producing MCSs. However, the low-level jet observed in this study extended well to the east of the climatological low-level jet driven by the sloping terrain of the Great Plains. With studies suggesting a westward expansion of the North Atlantic Subtropical High in a future climate, the increase in intense MCS-related EREs over the central CONUS during the summer is likely to continue.

Chapter 1

Introduction & Background

Numerous studies have documented an increase in the frequency and intensity of extreme rainfall events (EREs) over many locations on multiple continents (e.g., Easterling et al., 2000; Fischer and Knutti, 2016; Westra et al., 2013). These increases in the intensity and frequency of EREs have been linked to anthropogenic climate change (e.g., Coumou and Rahmstorf, 2012; Min et al., 2011). Understanding how the location and magnitude of these EREs have and will vary in our changing climate is of critical importance due to the impacts of EREs on public safety, the environment, and the economy (e.g., Knapp et al., 2008; Khajehei et al., 2020). EREs often result in significant flooding, which is among the world's most deadly and destructive natural hazards with about 19% of the world's population (nearly 1.5 billion people) facing a substantial risk of a 100-year (yr) flooding event (Rentschler and Salhab, 2020).

Knowledge of the trends in and the characteristics of EREs within the Continental United States (CONUS) and predicting their occurrence is particularly critical as flooding has been ranked as the deadliest storm-related phenomenon in the nation over the last 10–30 years (NWS/NOAA, 2021). Flash flooding resulting from convective EREs is most common east of the Rockies during the summer months (June, July, and August; JJA) due to the climatological peak in convective activity (e.g., Brooks and Stensrud, 2000; Maddox et al., 1979). The majority of warm season precipitation over the central and eastern CONUS is associated with mesoscale convective systems (MCSs) (e.g., Fritsch et al., 1986). MCSs are large, long-lived collections of thunderstorms, the largest of which also referred to as mesoscale convective complexes (Maddox et al., 1986). MCSs are among the largest types of thunderstorms on Earth, ranging from one to several hundred

kilometers in size (Houze, 2004), and have been shown to be the most prolific producers of extreme rainfall and flash flooding in the CONUS (e.g., Maddox et al., 1979; Schumacher and Johnson, 2006; Stevenson and Schumacher, 2014). Research has shown that MCSs will become more frequent and produce significantly heavier rainfall in a future climate (e.g., Feng, 2017).

Forecasting of the magnitude and location of convective EREs is difficult (e.g., Herman and Schumacher, 2016, 2018; Nielsen and Schumacher, 2016). Hence, understanding and predicting these convective EREs is currently a major focus in the atmospheric sciences. Predicting EREs on weather timescales and modeling how EREs will likely increase with climate change requires an accurate representation of the diurnal cycle of convection since MCSs over a large portion of the central CONUS have been long known to have a nocturnal maximum during the warm season (e.g., Wallace, 1975; Easterling and Robinson, 1985). Unfortunately, the accurate representation of elevated nocturnal convection and propagating MCSs that occur over land masses remains a major challenge for weather and climate (Bechtold et al., 2014, 2020; Geerts et al., 2017; Tang et al., 2021). With nocturnal MCSs being common culprits for EREs, it is imperative that we understand the environmental factors that correspond to changes in the frequency and intensity of those EREs, which may have implications on future trends.

1.1 Climatology of EREs in the CONUS

Studies such as Brooks and Stensrud (2000), Schumacher and Johnson (2006), Hitchens et al. (2012, 2013), Stevenson and Schumacher (2014), Moore et al. (2015), and Dougherty and Rasmussen (2019) have surveyed the nature and characteristics of EREs over the CONUS over multiyear periods and documented the seasonal and diurnal cycle of heavy rainfall events over different regions of the CONUS. These studies have unanimously found a peak in the frequency

of these events during the summer (JJA) associated with the annual maximum in convective activity over the central and eastern CONUS.

Short-duration convective EREs that are associated with the JJA maximum often result in severe flash flooding. Flash flooding can be defined as a rapid rise of water in normally dry areas that occurs within minutes or up to 6 hours of excessive rainfall (or other causes) over a relatively localized area (NWS/NOAA, 2023). The first flash flood climatology was published by Maddox et al. (1979), who grouped 151 intense flood events (1973–1977) into the following types: synoptic, frontal, mesohigh, and western. Mesohigh events were not associated with synoptic scale features, but instead, quasi-stationary outflow boundaries generated by prior convection. These events, likely associated with MCSs, produced the most severe cases, and were found to peak during the nighttime hours in JJA. Stevenson and Schumacher (2014), surveying EREs from 2002–2011, used a high-resolution gridded precipitation dataset (the same dataset used in this study) and found that over half of all 100-yr EREs were associated with MCSs. Over most of the central CONUS, MCSs produce the majority of warm season precipitation (Haberlie and Ashley, 2019; Fig. 1.1) and have a nocturnal maximum in their associated rainfall (Haberlie and Ashley, 2019; Fig. 1.2).

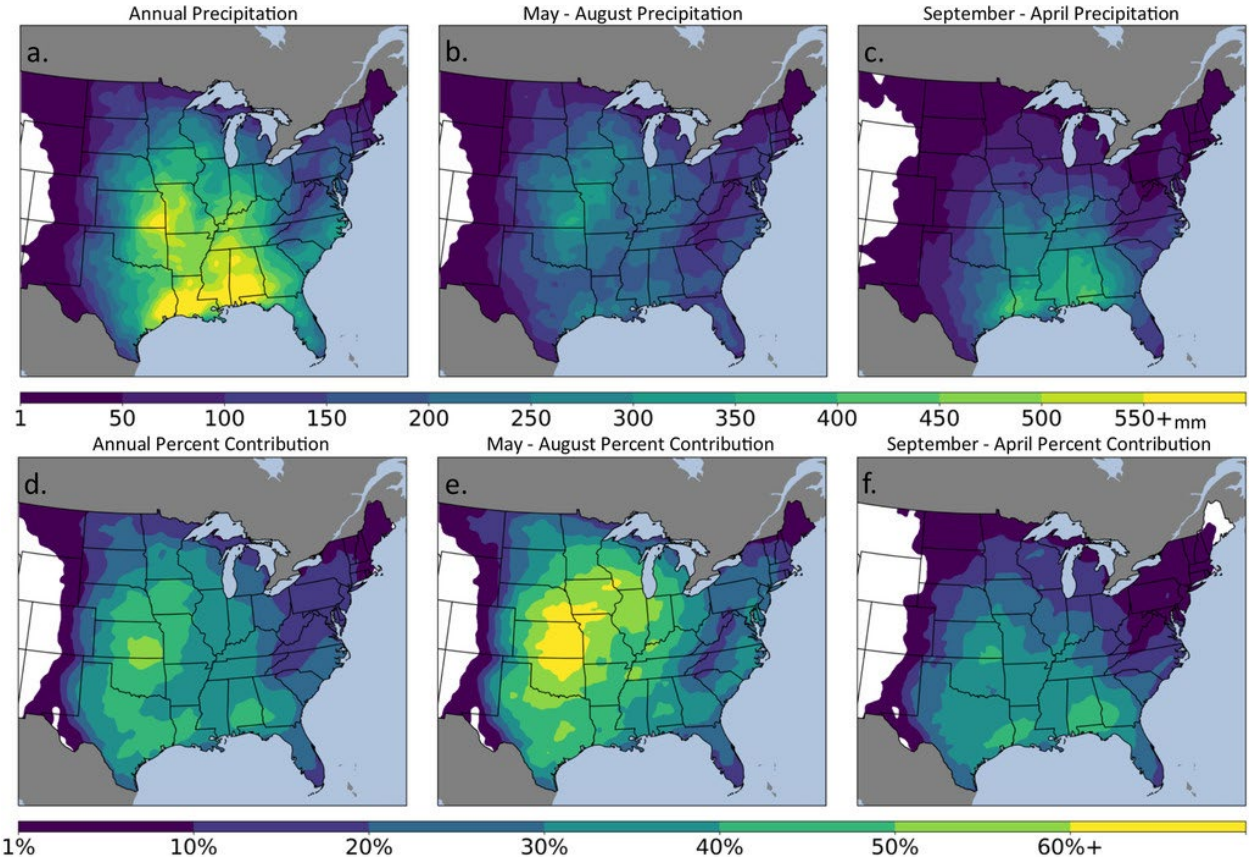

Figure 1.1: From a 1997–2017 climatology, (a–c) mean MCS total precipitation (mm) and (d–f) percent contribution of MCS precipitation to the total precipitation, valid for (a,d) the full year, (b,e) May–August, and (c,f) September–April. (Fig. 6 of Haberlie and Ashley (2019))

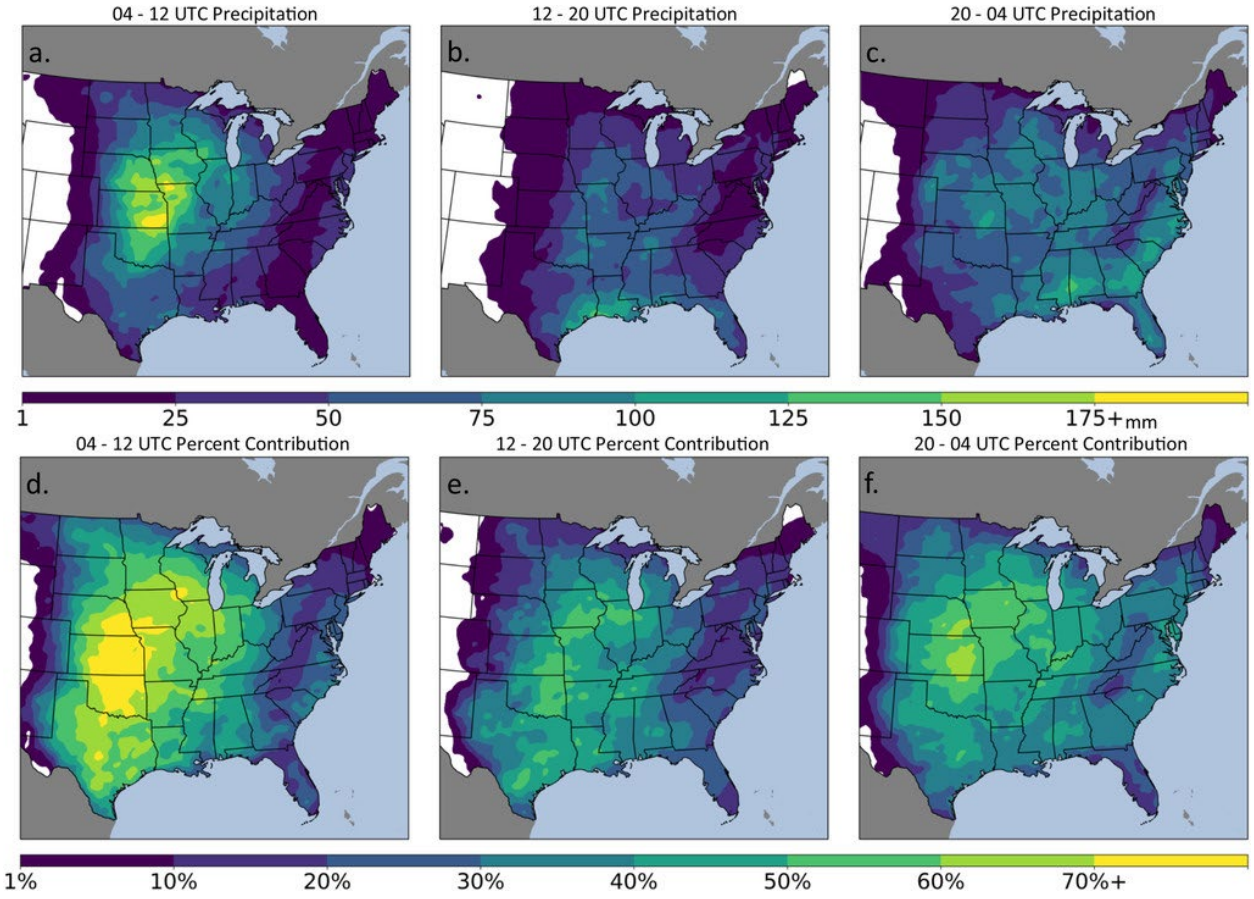

Figure 1.2: As in Fig. 1.1, but valid May–August for the following periods of the diurnal cycle: (a,d) 0400–1200, (b,e) 1200–2000, and (c,f) 2000–0400 UTC. (Fig. 7 of Haberlie and Ashley (2019))

Studies that further examined the diurnal cycle using hourly rainfall data found that diurnal variations in heavy rain were much more apparent during the summer (Hitchens et al., 2013; Winkler et al., 1988) and that most JJA EREs in the central and eastern CONUS are nocturnal (Schumacher and Johnson, 2006; Stevenson and Schumacher, 2014). Stevenson and Schumacher (2014) found that the peak in 1-hour (hr) extreme rainfall varied by region, but a general peak was found during the late evening hours, around 2300 local time (Fig. 1.3). This nocturnal peak in extreme rainfall was most distinct over the climatological area with a nocturnal maximum in JJA

heavy rainfall (Haberlie and Ashley, 2019; Fig. 1.2a), which runs along an axis from Northern Texas to the Upper Midwest (Easterling and Robinson, 1985; Wallace, 1975).

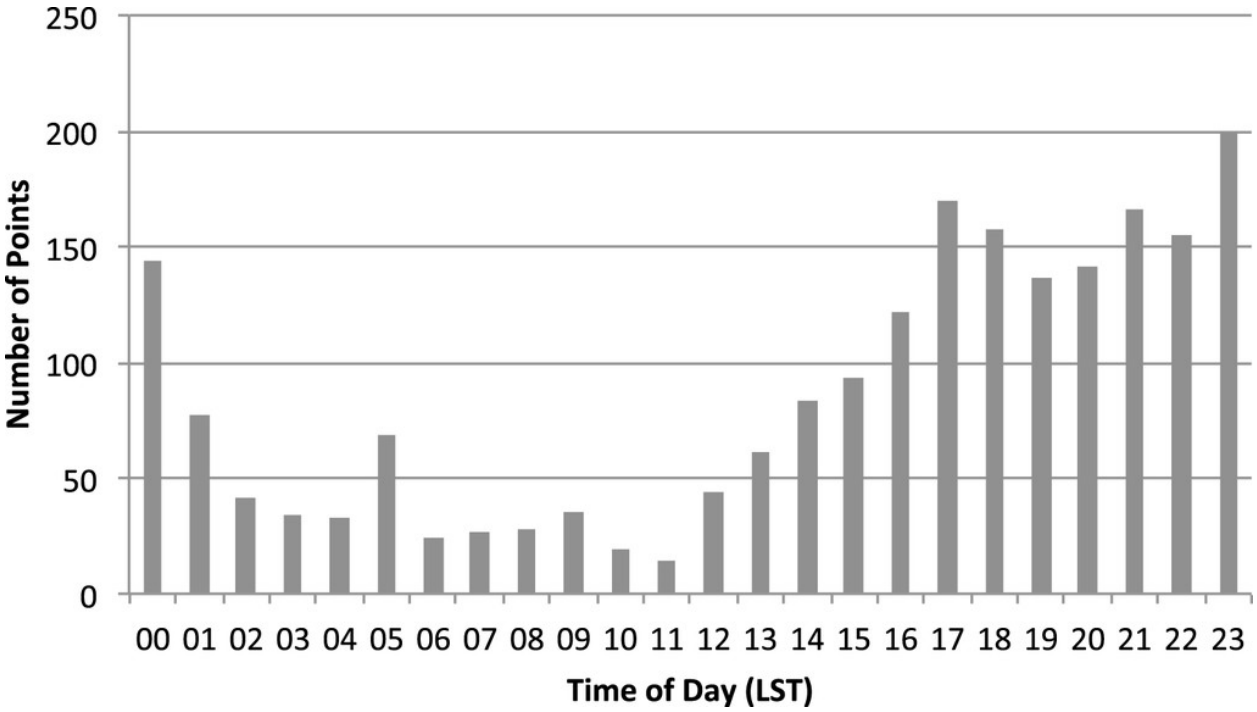

Figure 1.3: From a 2002–2011 climatology of 1-hr precipitation exceeding the 50-yr average recurrence interval threshold over the central and eastern CONUS using the Stage IV 4-km gridded precipitation dataset, the distribution of time of day (local standard time) for all points of exceedance. (Fig. 6 of Stevenson and Schumacher (2014))

In addition to MCSs, extreme precipitation and flooding can result from a variety of meteorological phenomena (e.g., Kunkel et al., 2012), including tropical cyclones, atmospheric rivers, extratropical cyclones, frontal boundaries, monsoons, air mass convection, and even supercells and mesovortices (e.g., Nielsen and Schumacher, 2020). Several heavy rainfall climatology studies have documented the seasonality and most common locations for some of these storm types in the CONUS. For example, the most intense EREs along the east coast are associated with tropical cyclones, with a peak during the early fall (e.g., Villarini et al., 2014).

Atmospheric river events are commonly observed along the West Coast with a peak during the cold season associated with extratropical cyclones (e.g., Villarini, 2016). EREs associated with extratropical cyclones in general show less seasonal variation overall and do not favor any particular region, though they are less common during the summer due to weaker jet stream dynamics.

A portion of this thesis aims to conduct a climatology of EREs that is similar to those conducted by Hitchens et al. (2013), Stevenson and Schumacher (2014), and Moore et al. (2015). However, our study employs slightly different methods to define EREs (see section 2.1) and examines additional characteristics of convective EREs such as the size and duration of associated precipitation features and additional attributes of extreme rainfall swaths. In this study, we utilized the same high resolution gridded precipitation dataset as some previous climatology studies, but over a period of 20 years, longer than all previous studies that used high resolution gridded rainfall data to date.

1.2 Convective ERE Properties & Environmental Conditions

Convection produces extreme rainfall when it is "*quasi-stationary*" in nature (Chappell, 1986), meaning it is either very slow-moving or consists of multiple cells moving repeatedly over the same area, sometimes referred to as "*echo training*". Various types of convection can be quasi-stationary, including the localized variety—air mass thunderstorms (i.e., ordinary cell convection) and high precipitation supercells—and the nonlocalized variety, including multicell convective clusters, frontal squall lines, and MCSs. This study focuses on EREs associated with convection of the nonlocalized variety, with an emphasis on summertime MCSs, which, again, are the most

prolific producers of extreme rainfall during the warm season in the CONUS (e.g., Schumacher and Johnson, 2006; Stevenson and Schumacher, 2014).

As first described by Maddox et al. (1979), Schumacher and Johnson (2005) distinguished two common organizational structures of extreme-rain-producing MCSs: (1) training line/adjoining stratiform, typically an east–west oriented line with training convective elements and an adjoining region of stratiform precipitation to the north of the convective line (Fig. 1.4a); and (2) back building convection with a stratiform region downstream (Fig. 1.4b).

Training line/adjoining stratiform type MCSs typically form on the cool side of a preexisting slow-moving surface boundary with an elevated moist and unstable airmass (Schumacher and Johnson, 2005). These MCSs, also described as upwind-propagating MCSs, may also be preceded by a forward-propagating convective line, leaving behind an elongating cold pool with a quasi-stationary gust front that acts as the aforementioned surface boundary (Corfidi, 2003), illustrated in Fig. 1.5. When the midlevel steering flow is largely parallel to the boundary, convective cells will then organize into a training line, producing excessive rainfall.

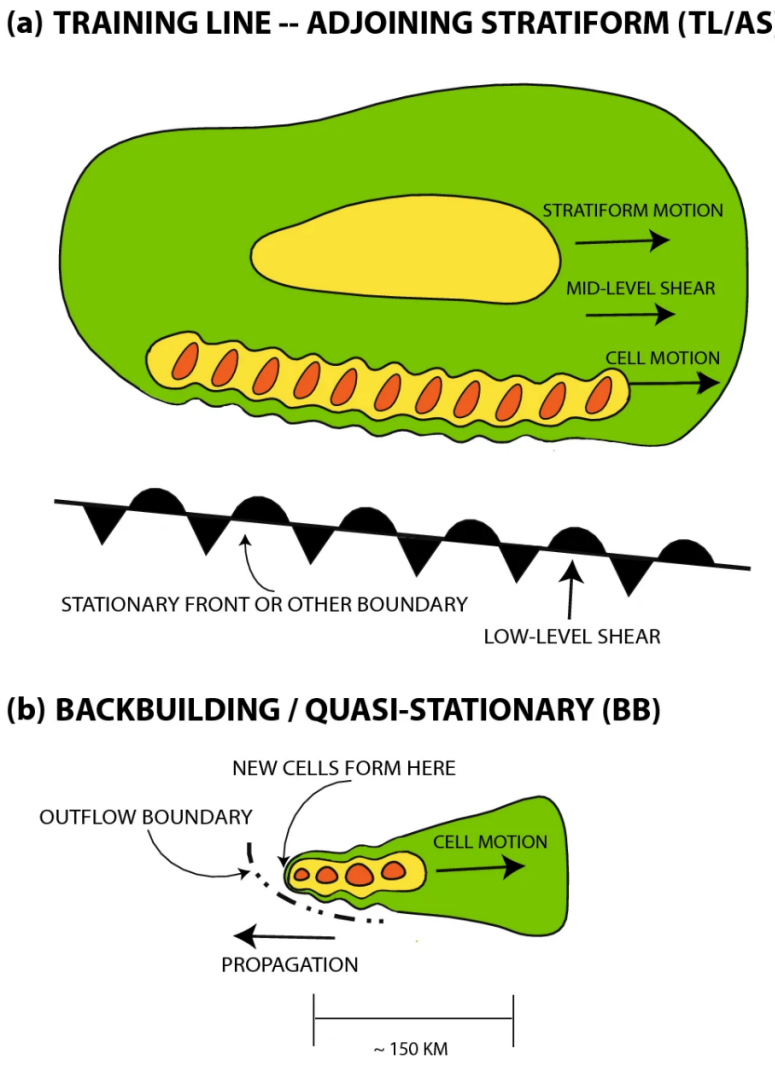

Figure 1.4: Schematic of typical radar-observed features and environmental characteristics associated with (a) training line/adjoining stratiform and (b) back building extreme-rain-producing MCSs. Color filled contours represent approximate radar reflectivity at the 20-, 40-, and 50-dBZ levels. In (a), the low-level shear vector refers to the surface–925-hPa layer and the mid-level shear vector refers to the 925–500-hPa level. No shear vectors are shown in (b) due to lack of a consistent relationship between environmental shear and the orientation of back building MCSs. The length scale in (b) can vary substantially in real cases. (Barlow et al. (2019) adaptation of Fig. 3 from Schumacher and Johnson (2005))

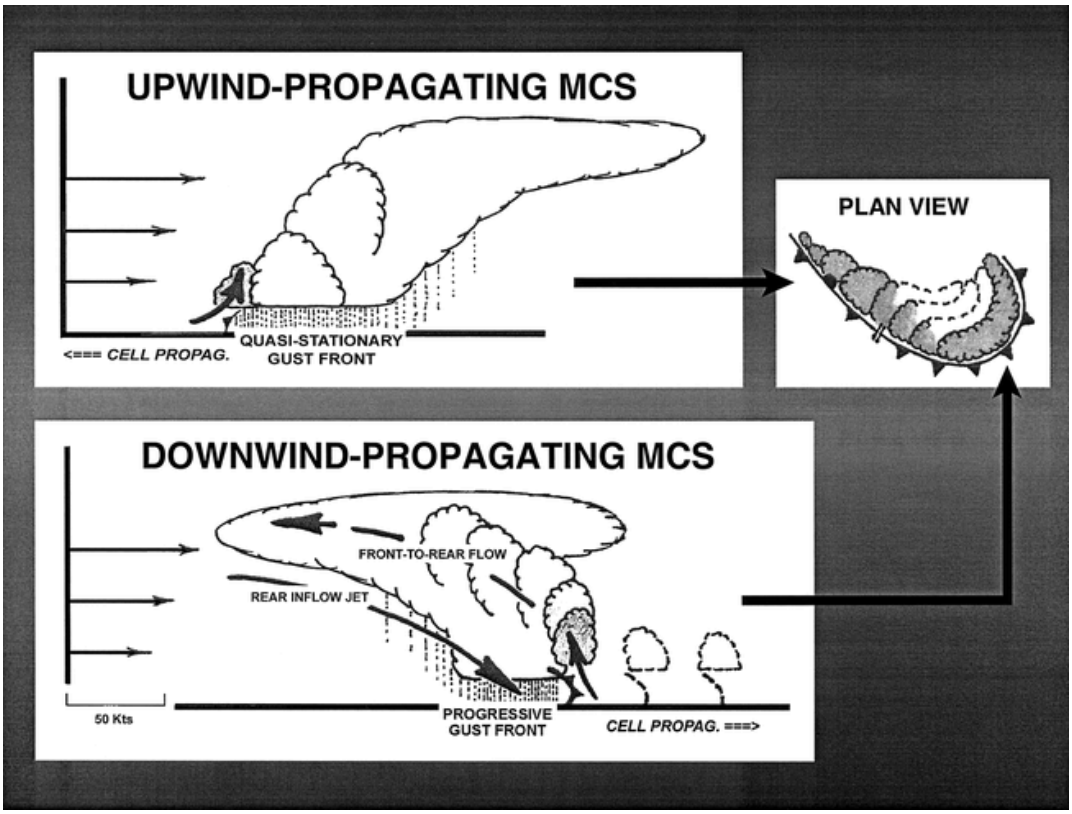

Figure 1.5: Schematic representation of a training line/adjoining stratiform MCS that has a forward-propagating and upwind-propagating training convective line. Diagrams include a plan view of the horizontal convective structure and associated boundaries (right) and vertical cross sections perpendicular to the gust front along the trailing quasi-stationary line (top) and the progressive line (bottom), with representations of cell propagation and dynamical mechanisms involved in convective maintenance. The environmental vertical wind profiles are hypothetical. (Fig. 3 of Corfidi (2003))

Convective initiation typically occurs in this environment when a low-level jet (LLJ) has a sufficiently perpendicular component to the boundary that lifts higher-θ_e air over the sloping frontal surface (i.e., isentropic lift) to the level of free convection, and hence, the resulting convection is elevated. This lifting mechanism is a common trigger for nocturnal convective initiation and the formation of nocturnal MCSs (e.g., Trier and Parsons, 1993) as the LLJ often forms or is enhanced during the nighttime hours (e.g., Pitchford and London, 1962). LLJs often occur over the Great Plains as a result of diurnal variations over sloping terrain, occurring

exclusively at night and during the warm season (e.g., Shapiro et al., 2016), or they can occur elsewhere as a result of synoptic scale processes such as upper-level jet streaks (e.g., Uccellini and Johnson, 1979) and extratropical cyclones (e.g., Browning and Pardoe, 1973).

Back building MCSs are typically smaller in area but can produce more intense EREs (Schumacher and Johnson, 2005). While the convective initiation mechanisms in these back building MCSs are similar to training line/adjoining stratiform cases (i.e., isentropic lifting of moist air to the level of free convection), back building type MCSs are more dependent on storm-scale processes. For back building MCSs, lifting is often provided by storm-generated, upstream propagating cold pools and/or quasi-stationary gravity waves, as opposed to preexisting boundaries. In this paradigm, the upstream propagation of the cold pool often nearly cancels with the mean steering flow, leading to quasi-stationary convection (Peters and Schumacher, 2014). The location of this repeated convective initiation depends on where an optimal balance exists between the low-level shear (often enhanced by the LLJ) relative to the orientation of the cold pool (Rotunno et al., 1988). However, recent high-resolution simulations of back building MCSs suggest that more complex mechanisms may be at play with different inflow layers supporting different regions of the MCS, including parcels originating from within the stable boundary layer after modification by storm downdrafts (Hitchcock and Schumacher, 2020).

The preexisting environment in which back building MCSs occur often consists of an LLJ interacting with a mesoscale convective vortex (Bartels and Maddox, 1991)—a midlevel cyclonic circulation generated by prior MCSs—within a very moist and weakly-sheared air mass (Schumacher and Johnson, 2009; Schumacher et al., 2013), as documented by numerous case studies (e.g., Schumacher and Johnson, 2008; Trier and Davis, 2002). The moisture convergence and shear generated by this interaction favors sustained isentropic upglide on the downshear side

of the midlevel circulation (Trier et al., 2000), and hence the development of quasi-stationary convection (Schumacher and Johnson, 2009; Fig. 1.6). Albeit rarer, back building MCSs can also occur behind a bow echo, manifesting as the “arrow region” of a “bow and arrow” type MCS structure (Keene and Schumacher, 2013; Zhang et al., 2023), formed by the interaction of the LLJ and the mesoscale convective vortex generated by the bowing MCS.

The fact that many of these extreme-rain-producing MCSs are nocturnal has implications for numerical weather prediction. Operational models, particularly those using convective parameterization schemes, often fail to capture EREs associated with elevated nocturnal convection (e.g., Schumacher and Johnson, 2008), consistent with the difficulties in representing nocturnal convection in the earlier cited studies (e.g., Bechtold et al., 2014). Higher resolution models that are able to directly resolve convective scale processes and localized high rainfall rates may be a potential solution (e.g., Fritsch and Carbone, 2004; Gao et al., 2017; Judt, 2018, 2020; Kendon et al., 2012). However, ongoing issues suggest that the challenge of representing elevated deep convection in numerical weather prediction models will persist. Some of these issues include the high computational demand of employing multiple high resolution ensembles on larger scales and the sparseness of upper-air observations that are necessary for accurate simulations of the conditions that lead to elevated convection.

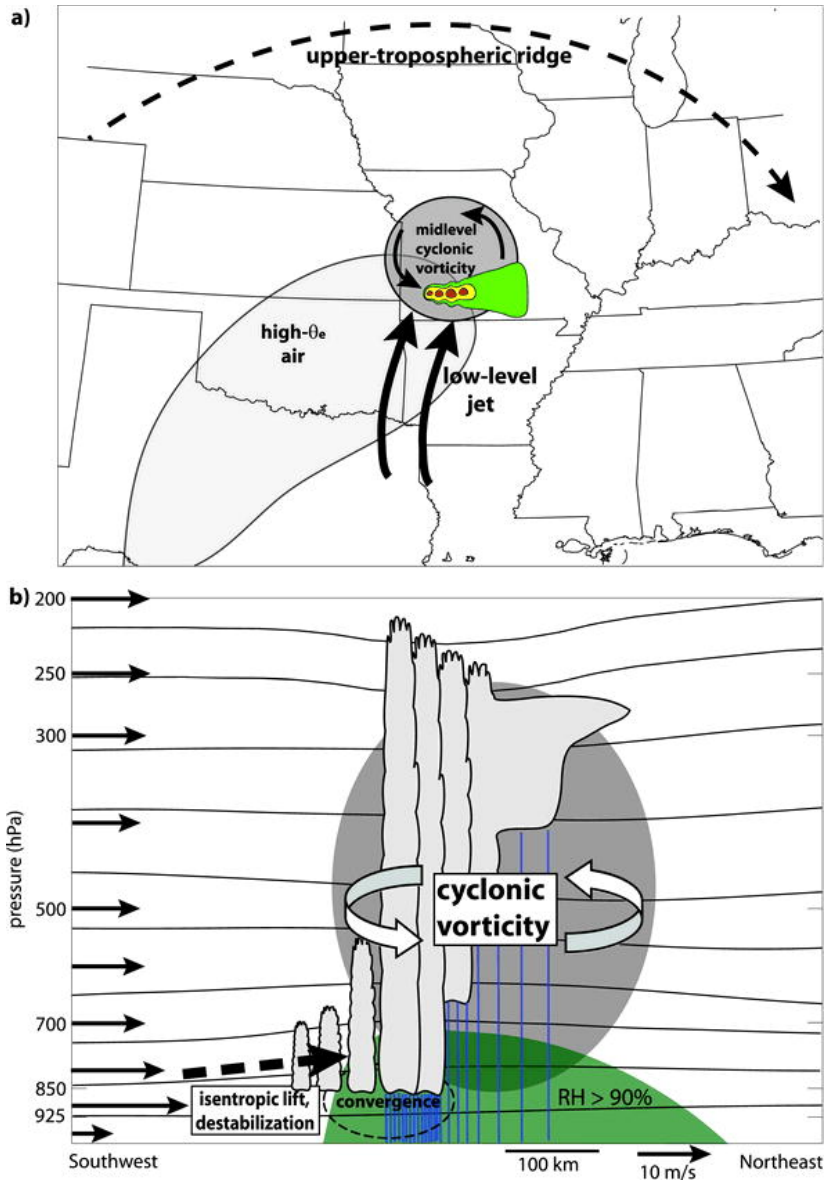

Figure 1.6: Schematic representation of the important processes involved in the development and maintenance of back-building MCSs associated with midlevel circulations. (a) Plan view showing the radar reflectivity structure of the MCS (color fill) and its position relative to the midlevel circulation and larger scale features (labeled). The high-θ_e air refers to the low levels (e.g., 925–800 hPa). (b) Southwest–northeast cross section through the MCS. Thin black lines are representative isentropes (every 5 K) and the wind profile is shown by the vectors on the left. Green shading indicates relative humidity >90% and grey shading indicates high values of cyclonic vorticity. The thick dashed arrow represents air undergoing isentropic upglide. (Fig. 13 of Schumacher and Johnson (2009))

1.3 Large Scale Meteorological Patterns Associated with EREs

Large scale meteorological patterns (LSMPs) play an important role in the occurrence of extreme precipitation. Barlow et al. (2019) surveyed the current state of knowledge regarding the relationship between LSMPs and short duration (<1 week) extreme precipitation events over North America. LSMPs are defined as synoptic scale patterns influencing individual events that are well-resolved in weather and climate models and have medium-range predictability. The authors expressed concerns regarding the differences in methodology and definitions of extreme precipitation between studies, often leading to different results. Results are also seasonally and regionally dependent and are highly sensitive to the type of event (e.g., atmospheric rivers, extratropical cyclones, or MCSs). Nevertheless, there are some common important characteristics of LSMPs that are associated with extreme precipitation. Generally, the key physical factors that control EREs on a mesoscale level include sustained moisture transport, lift, and instability, which are strongly dependent on LSMPs. For example, as described in the previous section, the mesoscale environments associated with "frontal" and "mesohigh" type events (Maddox et al., 1979) are typically characterized by an LLJ transporting anomalous moisture poleward and intersecting with a quasi-stationary baroclinic boundary, such as a front or outflow boundary. On the synoptic scale, while midlatitude precipitation is commonly associated with mid-level troughs, "mesohigh" type EREs often occur near the axis of a mid–upper-tropospheric ridge (Maddox et al., 1979), as shown in Fig. 1.6 (Schumacher and Johnson, 2009).

On seasonal and annual timescales, most studies that identified LSMPs associated with rainfall over the central and northern CONUS found a strong connection with northward moisture transport from the western Gulf of Mexico (e.g., Abel et al., 2022; Flanagan et al., 2018; Mo et al., 1997). For example, a composite of flood events versus drought events over the central CONUS by Mo

et al. (1997) revealed a pattern of strong moisture flux from the Caribbean to the Great Lakes during the wet periods (Fig. 1.7). This moisture transport is often associated with enhanced moisture flux convergence near its northern terminus, which is where EREs are likely to occur (e.g., Holman and Vavrus, 2012). Analogous to the "Pineapple Express" for atmospheric river events on the Pacific west coast, this pattern of moisture transport was dubbed the "Maya Express" by Dirmeyer and Kinter (2009) because the fetch of tropical moisture originates from the Western Caribbean, Central America, and Mexico, including the Yucatan Peninsula. The "Maya Express" is apparently linked to an enhanced east–west pressure gradient throughout the low–mid troposphere due to positive height anomalies over the southeastern CONUS and/or negative height anomalies over the western CONUS.

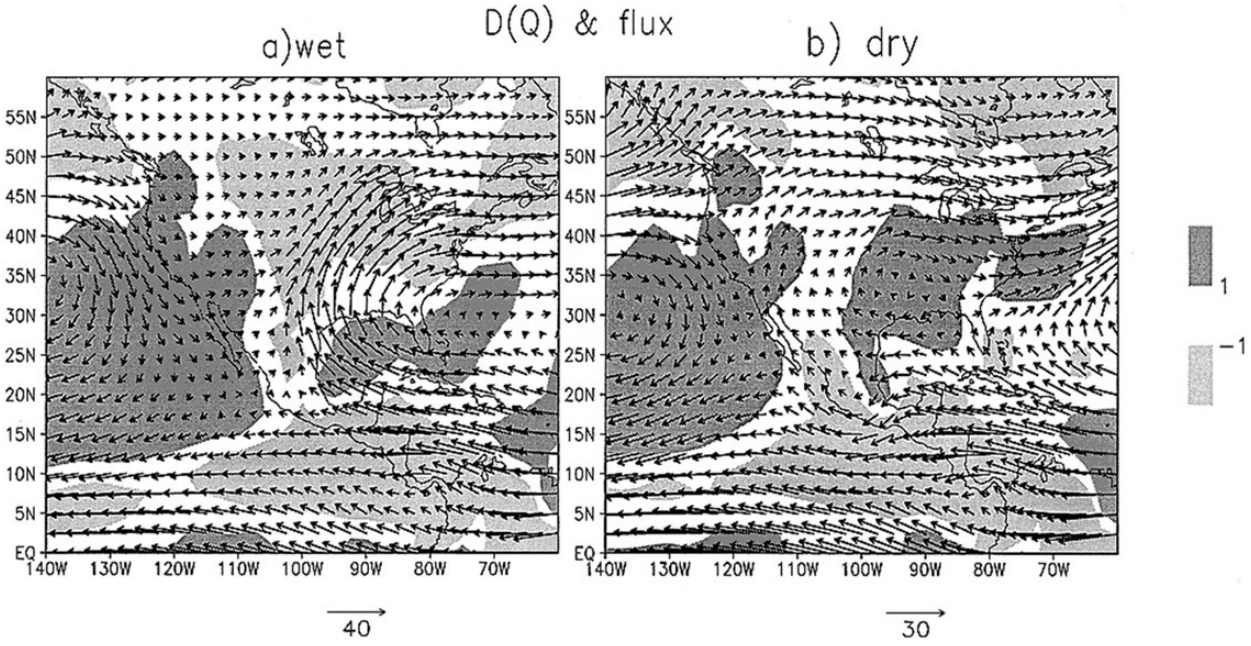

Figure 1.7: Composite of vertically integrated moisture flux (vectors, 10 kg (m s)$^{-1}$) and flux divergence $D(Q)$ (shading, mm day^{-1}) for (a) flooding and (b) drought events. Adapted from Fig. 5 of Mo et al. (1997).

Pluvial years over the Great Plains have also been linked to a southward-shifted North Pacific jet stream, creating a pattern consistent with frequent synoptic wave passages (Flanagan et al., 2018). Thus, above-normal rainfall is likely linked to synoptic-scale processes leading to individual events, rather than longer-time-scale features. However, the seasonal mean composite anomalies still show signals that are physically consistent with the occurrence of heavy rainfall. Abel et al. (2022) found that the moisture pathways for most individual heavy rainfall events in the Northern Great Plains vicinity actually originate from land sources, not the Gulf of Mexico. This finding is most likely a result of residual soil moisture from Gulf of Mexico sourced events (i.e., moisture recycling). Thus, while individual events do not require a pattern of moisture transport directly from the Gulf of Mexico, above average moisture transport over the season overall does have a direct impact on seasonal precipitation anomalies.

1.4 Trends in EREs & Connections to Climate Change

Among all classes of extreme weather phenomena, changes in precipitation extremes have the most well-understood connection to global climate change with adequate supporting data and physical understanding of the causes (Kunkel et al., 2013a). Fowler et al. (2021) provided a thorough review of our current understanding of the impact of global anthropogenic climate change on extreme rainfall. The theoretical reasoning for an increase in extreme precipitation from a thermodynamical perspective is related to the positive relationship between temperature and the capacity of the air to hold water vapor (i.e., the Clausius-Clapeyron relationship) (Trenberth et al., 2003). In simple terms, warming temperatures increase the upper limit of atmospheric precipitable water content, leading to the potential for greater rainfall rates. For typical globally averaged atmospheric conditions, the best approximation for the rate of increase in atmospheric moisture is

~7% per °C of warming (Fowler et al., 2021). This scaling rate has been both modeled and observed with heavy rainfall extremes increasing at approximately that rate globally on daily time scales (e.g., Pall et al., 2007; Westra et al., 2013). Numerous studies have actually suggested that shorter-duration (sub-daily) rainfall extremes are increasing at a much higher rate (e.g., Berg et al., 2013; Guerreiro et al., 2018; Lenderink and Van Meijgaard, 2008, 2010; Lenderink et al., 2021; Panthou et al., 2014; Park and Min, 2017; Westra et al., 2014), likely attributable to convective cloud feedback mechanisms and an increase in the likelihood of convective versus stratiform precipitation in a warmer environment. However, the scaling relationship has been shown to be geographically dependent, being lower over drier land regions with limited moisture availability, mainly in the subtropics (e.g., O'Gorman and Muller, 2010), but higher in several climatologically wetter areas, especially in the mid and high latitudes (e.g., Sun et al., 2007; Trenberth, 2011).

Recent studies have begun utilizing convection-permitting regional climate models to simulate rainfall in a future climate under a worst-case scenario carbon emissions trajectory (i.e., the Intergovernmental Panel on Climate Change RCP 8.5 scenario). These convection-permitting models are likely better at representing characteristics of convection (e.g., the diurnal cycle) compared to traditional climate models with parameterized convection (Ban et al., 2014; Prein et al., 2015, 2020). Findings indicate increases in short duration heavy rainfall intensities by the end of the century (e.g., Ban et al., 2015; Dougherty and Rasmussen, 2020; Kendon et al., 2014, 2019; Lenderink et al., 2021; Prein et al., 2017b). Conversely, light to moderate rainfall is projected to *decrease* in frequency in a warmer climate (e.g., Dai et al., 2020; Hu et al., 2020; Rasmussen et al., 2020) with a general decrease in overall rainfall. A decrease in overall rainfall may be attributed to a warmer troposphere that corresponds with decreasing relative humidity and an increase in

atmospheric stability. These results imply that the future climate will include more severe droughts and flash floods, concurrently (Fowler et al., 2021).

Observational investigations of changes in extreme rainfall have most rigorously been conducted for the CONUS due to the relatively dense Cooperative Observer rain gauge networks, with records dating back to the turn of the twentieth century for many stations. Numerous studies have documented a general increase in the frequency and intensity of heavy precipitation events across most of the CONUS over multidecadal time scales (e.g., Armal et al., 2018; Easterling et al., 2017; Feng et al., 2016; Groisman et al., 2012; Harp and Horton, 2022; Janssen et al., 2014; Karl and Knight, 1998; Kunkel et al., 1999, 2012, 2013a; Li et al., 2022a; Risser et al., 2019). For example, Kunkel et al. (2013a) utilized a dense network of rain gauge observations over the CONUS to find increasing trends in daily extreme precipitation from ~76% of all stations from 1948 to 2010, with ~15% of them being statistically significant. Increases in the occurrence of 2-day precipitation amounts exceeding the 1-in-5-yr recurrence threshold from 1895–2010 were statistically significant over the Midwest, Southeast, and CONUS overall (Fig. 1.8). Unfortunately, results from different studies investigating trends in extreme precipitation events are difficult to compare due to differences in methodology and metrics used to define “extreme”, but most studies come to similar conclusions that there has been an overall increase in their frequency and intensity, though it varies by region.

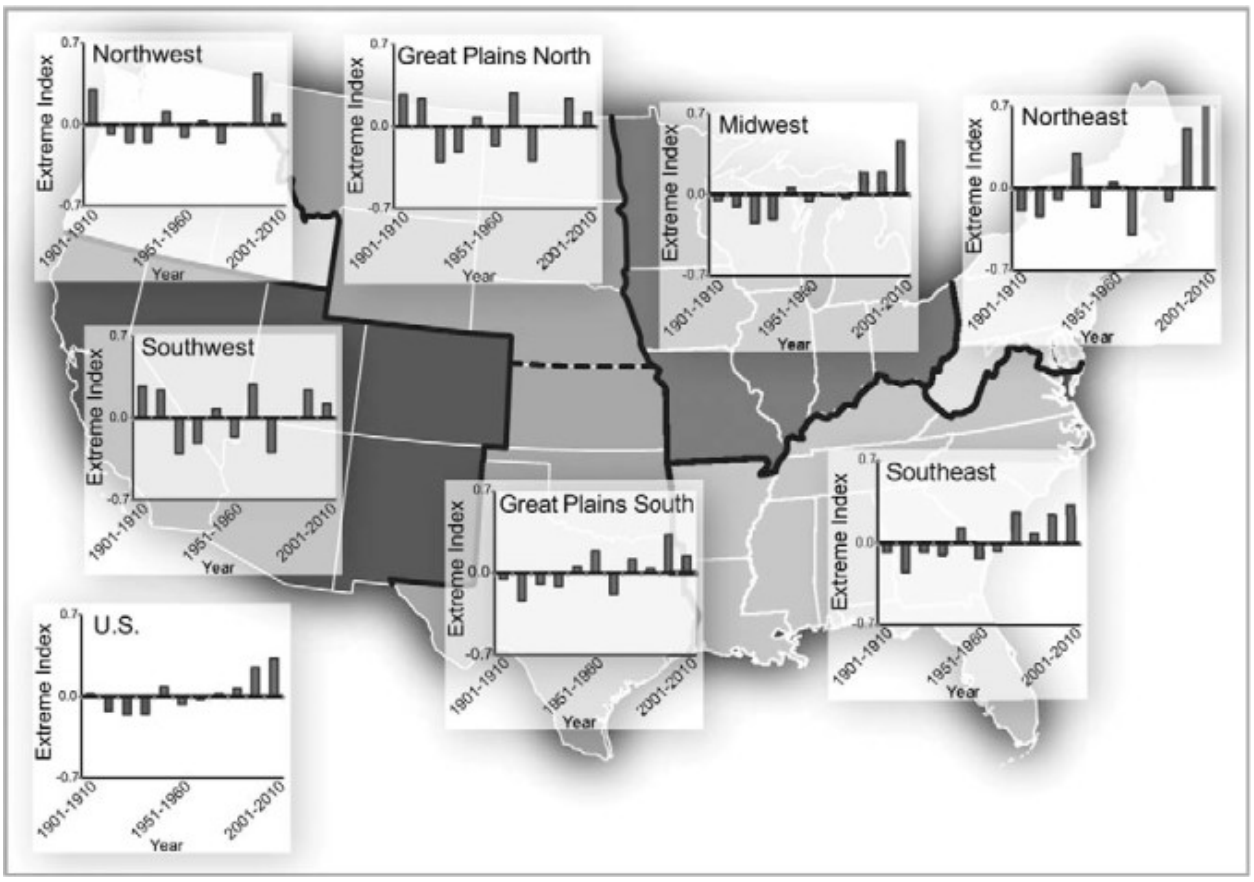

Figure 1.8: Time series of decadal values of a standardized index based on the number of 2-day precipitation totals exceeding a 1-in-5-yr recurrence threshold for seven regions and the CONUS overall. (Fig. 3 of Kunkel et al. (2013a))

Focusing on MCSs in the CONUS, Feng et al. (2016) utilized long-term (1979–2014) observations from satellite, radar, and rain gauges to show that changes in the characteristics of MCSs dominate the observed increase in April–June extreme rainfall across parts of the central CONUS. In general, results suggest that the frequency, intensity, and longevity of MCSs across the central CONUS are increasing, resulting in heavier rainfall totals. While total precipitation only showed an increase of ~3% per decade through the 35-yr period, precipitation from MCSs showed an increase of ~25% per decade, with non-MCS precipitation exhibiting a decrease. Hu et al. (2020) found similar results, with warm season (April–August) MCS rainfall from 1997–2018

increasing significantly, while non-MCS rainfall decreased, primarily due to an increase in frequency and duration of MCSs but a decrease in total rainfall area. In support of these observational findings, Prein et al. (2017a) utilized high-resolution regional climate simulations to find that MCSs may produce 15–40% higher maximum rainfall rates by the end of the century—related to an increase in warm cloud layer depth—along with an increase in MCS size and lifetime. The combined effect would result in an increase in total MCS rainfall volume by up to 80%. This thesis explores trends in MCS- and non-MCS-related EREs, but only during the summer months (June–August), when they are most common.

In addition to changing thermodynamic conditions in a warming climate, the change in MCS characteristics may be attributed to trends in large-scale flow patterns. For example, there is evidence of an increase in the strength of the LLJ (Feng et al., 2016; Fig. 1.9d) in association with an increase in the pressure gradient between the Rockies and the western Atlantic Ocean due to greater warming over land relative to the ocean (Feng et al., 2016; Fig. 1.9a).

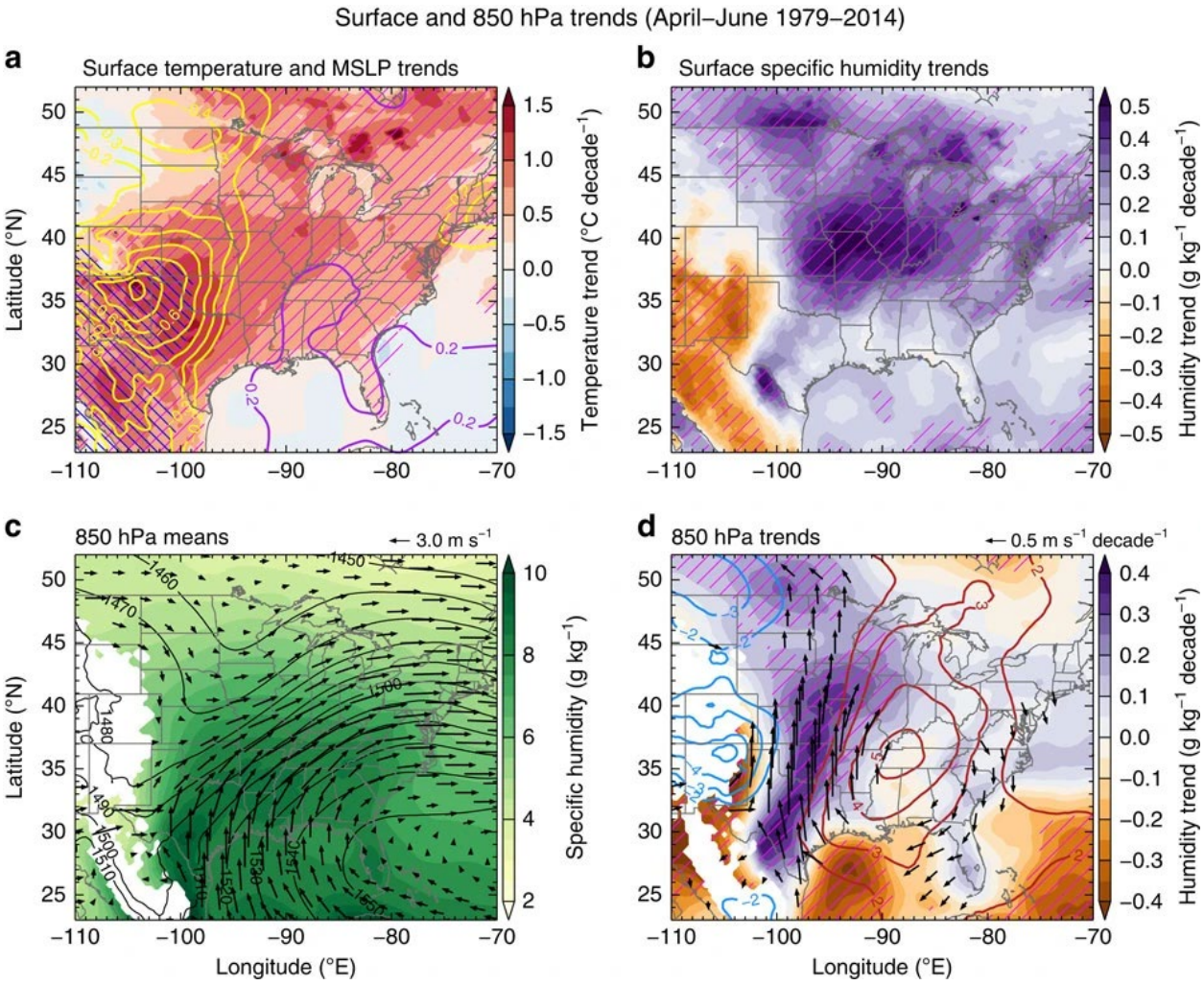

Figure 1.9: "(a) Surface temperature (shaded) and mean sea level pressure (MSLP) trends (MSLP contours in 0.1 hPa per decade intervals, purple/yellow contours denote positive/negative MSLP trends), (b) surface specific humidity trends (shaded), (c) 850 hPa mean specific humidity (shaded), geopotential height (contours, in 10 m intervals), and wind (arrows), and (d) 850 hPa trends in specific humidity (shaded), geopotential height (contours, in 1 m per decade intervals, red/blue contours denote positive/negative geopotential height trends), and wind (arrows, statistically significant at 95%). Grid points with a statistical significance exceeding the 95% confidence interval are marked by (a) pink hashes for temperature and blue hashes for MSLP, (b,d) purple hashes for specific humidity. Areas with mean surface pressure below 850 hPa are masked out in c and d." Figure and caption from Fig. 4 of Feng et al. (2016).

Despite the impact of global climate change on extreme precipitation events being relatively well understood, there are still major uncertainties in regional climate change due to the role of internal atmospheric variability (e.g., Deser et al., 2012). Additionally, trends in weather events such as EREs over relatively short time periods cannot be directly attributed to anthropogenic warming, as there are likely connections to other modes of climate variability, which limits the conclusions that can be made in observational studies with relatively short periods of record. While this thesis examines trends over a period of only 20 years, we also investigate the role of internal atmospheric variability (i.e., seasonal LSMPs and climate indices) in modulating interannual changes in EREs, which may provide additional insight into future trends.

1.5 Socioeconomic Impacts of Short-Duration EREs in the CONUS

Short-duration EREs from thunderstorms that result in flash flooding are more hazardous than longer-duration EREs, in part, because of their localized nature in both space and time making these events very difficult to forecast with precision (Terti et al., 2015). As a result of the sudden nature of short-duration EREs, the ability to provide advanced warning and subsequent emergency response is exacerbated. The sudden onset of flash flooding caused by short-duration EREs makes it more deadly than slow-rise flooding, and thus, flash flooding from thunderstorms results in the most flood-related fatalities in the United States (Ashley and Ashley, 2008). Flash flooding is particularly deadly at night due to the lack of visibility of floodwaters for motorists (Špitalar et al., 2014) and most flash flood fatalities are from vehicle-related drownings (Terti et al., 2015).

Flash flooding often causes significant damage to homes, infrastructure, and agriculture (e.g., Motha, 2011), and can even result in billion-dollar disasters. For example, the Missouri and Kentucky floods of late July 2022 caused $1.5 billion in damage and 42 deaths (NOAA National

Centers for Environmental Information, 2023). This event was caused by short duration EREs associated with MCSs, one training over the St. Louis, MO area and another over flood-prone areas of eastern KY (NOAA National Centers for Environmental Information, 2022), both peaking during the early morning hours. This type of destructive event demonstrates the importance of understanding and predicting short duration EREs, especially if they are expected to increase in frequency and intensity in our future climate.

As discussed in the previous section, the urgent key message from numerous recent studies is that more intense flash flood events are likely in a future climate. The increase in flood risks have been shown to be exacerbated by deteriorating stormwater infrastructure, ongoing urbanization in flood-prone areas, and lack of integration between land-use planning and flood risk management (Georgescu et al., 2021; Junqueira et al., 2021; Sohn et al., 2019; Swain et al., 2020). There is a projected increase in the likelihood of unprecedented short duration rainfall amounts in areas that are not currently accustomed to flash flooding, including populated cities (Dougherty and Rasmussen, 2020; Kunkel et al., 2013b; Li et al., 2022b; Neelin et al., 2017), potentially exacerbated by an increasing urban heat island effect (Fowler et al., 2021). These concerning facts should incentivize the implementation of climate change adaptation measures to current infrastructure (e.g., Coelho et al., 2022), as well as a transition away from fossil fuels to help mitigate the negative effects of anthropogenic climate change on extreme weather events overall.

1.6 Thesis Goals

The main objectives of this thesis include the following: (1) to develop a new climatology of EREs over the central and eastern CONUS; (2) to look for evidence of potential changes in their frequency or characteristics with respect to their location, intensity, size, duration, and diurnal

cycle; and (3) to find correlations with LSMPs that can help explain the interannual variability or trends in EREs. Our findings aim to motivate the need to improve numerical weather prediction and climate modeling of continental nocturnal convection, provide insight into what large-scale circulation patterns may drive changes in convective EREs, and aid in longer term forecasts that can help assess potential risk from convective EREs. Our investigation employs the national network of weather surveillance radars, which allows the production of an hourly, high resolution gridded precipitation dataset capable of capturing EREs at the convective scale. The dataset now spans over 20 years, and its high horizontal resolution (4 km) enables us to capture more detailed spatial and temporal characteristics of convective EREs than studies that used solely in-situ measurements.

The thesis is organized as follows: Chapter 2 describes the data and methodology, including the ERE identification algorithm, quality control, event type classification, and statistical methods. Results from the 20-yr climatology of the identified EREs are presented in chapter 3. Variability and apparent trends in the frequency and characteristics of EREs are presented and discussed in chapter 4. Correlations between EREs and seasonally-averaged meteorological fields are presented and discussed in chapter 5. Meteorological conditions associated with a selection of intense EREs with common characteristics are presented and discussed in chapter 6. Finally, chapter 7 will include a summary and discussion of the results and how they change the field, along with potential implications for society and future work.

Chapter 2

Data & Methods

This chapter highlights the methods and datasets employed in this thesis. The methods for constructing a comprehensive object-oriented database of EREs[1], quality control measures, classification procedures, and the datasets used will be discussed in section 2.1. The methods used for the analysis will be discussed in section 2.2.

2.1 Creating a Database of EREs

Previous studies investigating extreme precipitation have used various criteria to define an "extreme" event. Barlow et al. (2019) provides a thorough review of previous extreme precipitation studies highlighting the difficulty of comparing the results of these studies due to inconsistencies in methodology. In general, a typical definition of "extreme" consists of three distinct aspects (Barlow et al., 2019): (1) a metric (e.g., accumulation exceeding a fixed threshold or location-based percentile); (2) a timescale (e.g., short duration events employing 1-, 6-, or 24-hr accumulations or long duration events spanning 15–30 days); and (3) a spatial scale (e.g., station-based or grid-based). The metric and timescale chosen often depends on the type of weather systems that are of interest in a particular study (e.g., short-duration events caused by convection or long-duration events caused by synoptic scale systems), and the spatial scale depends on the dataset being used (i.e., gridded versus station-based).

[1] While there may be some events that include hail or wintery precipitation, the majority of the events are assumed to be caused by heavy rainfall, so all events are referred to as EREs for simplicity.

2.1.1 ERE Definition & Datasets Used

In this study, EREs were identified by comparing a high-resolution gridded precipitation dataset to the location-dependent 10-yr average recurrence interval (ARI) thresholds. Any grid point where the 12-hr accumulation exceeds the ARI threshold at that location is considered an instance of extreme precipitation. The ARI, also known as the return period, is a metric commonly used to express the probability of an extreme event occurring and can be interpreted as the average amount of time between repeated occurrences of a variable exceeding a threshold (Wilks, 2019). For the purposes of this study, an ARI is simply defined as $1/P$, where P is the annual probability of exceedance. For example, stating that "the ARI of 12-hr precipitation exceeding 100 mm is 10 years" at a grid point means that, within a given year, there is a 10% chance of precipitation accumulating at least 100 mm in 12 hours at that location. In other words, receiving 100 mm of precipitation in 12 hours would be a 1-in-10 year event. In this example we would call "100 mm" the "10-yr ARI threshold" at that grid point.

Referring to the three previously described aspects of the definition of a rainfall "extreme" from Barlow et al. (2019) study, the "metric" used in our definition is an accumulation exceeding the 10-yr ARI threshold obtained from the National Oceanic and Atmospheric Administration (NOAA) Atlas 14 precipitation frequency dataset (e.g., Perica et al., 2018) developed by the National Weather Service Hydrometeorological Design Studies Center (NWS/HDSC). The data file was obtained from the HDSC server at https://hdsc.nws.noaa.gov/pub/hdsc/data/tx/. NOAA Atlas 14 provides precipitation frequency estimates for a range of durations and ARIs with a grid resolution of 30 arc-seconds (~800 m). The estimates are derived via frequency analysis of partial duration time series obtained from historical station data, provided that the station has a record length of at least 30 years for daily stations and at least 20 years for those recording at sub-daily

durations with only a few exceptions (Perica et al., 2018). The uncertainty of the precipitation frequency estimates increases for larger ARIs, which is due to the limited observational records used to construct the dataset combined with the inherent non-stationarity of precipitation over time. An ARI of 10 years was chosen, as opposed to 50 and 100 years in similar studies (e.g., Stevenson and Schumacher, 2014), to account for the limited number of years observed in the study by increasing the event sample size. However, larger ARI thresholds (50- and 100-yr) were also examined and used to compare the results for higher-end EREs.

With a focus on short term (< 24 hour) convective rainfall events, the timescale chosen for this study was 12 hours, shorter than the lifetime of long-lived propagating MCSs (e.g., Yang et al., 2017), but reasonable for the maximum amount of time that a single MCS can precipitate over a single location. Unfortunately, this may not account for some EREs that result from multiple propagating MCSs training over the same area within a period that is longer than 12 hours, but for the purpose of examining the diurnal cycle of short-duration EREs, the timescale was not expanded. The 12-hr precipitation frequency estimates for a 10-, 50-, and 100-yr ARI over the CONUS from the NOAA Atlas 14 dataset is shown in Fig. 2.1. The values in Fig. 2.1a are the 10-yr ARI thresholds used for identifying EREs in this study.

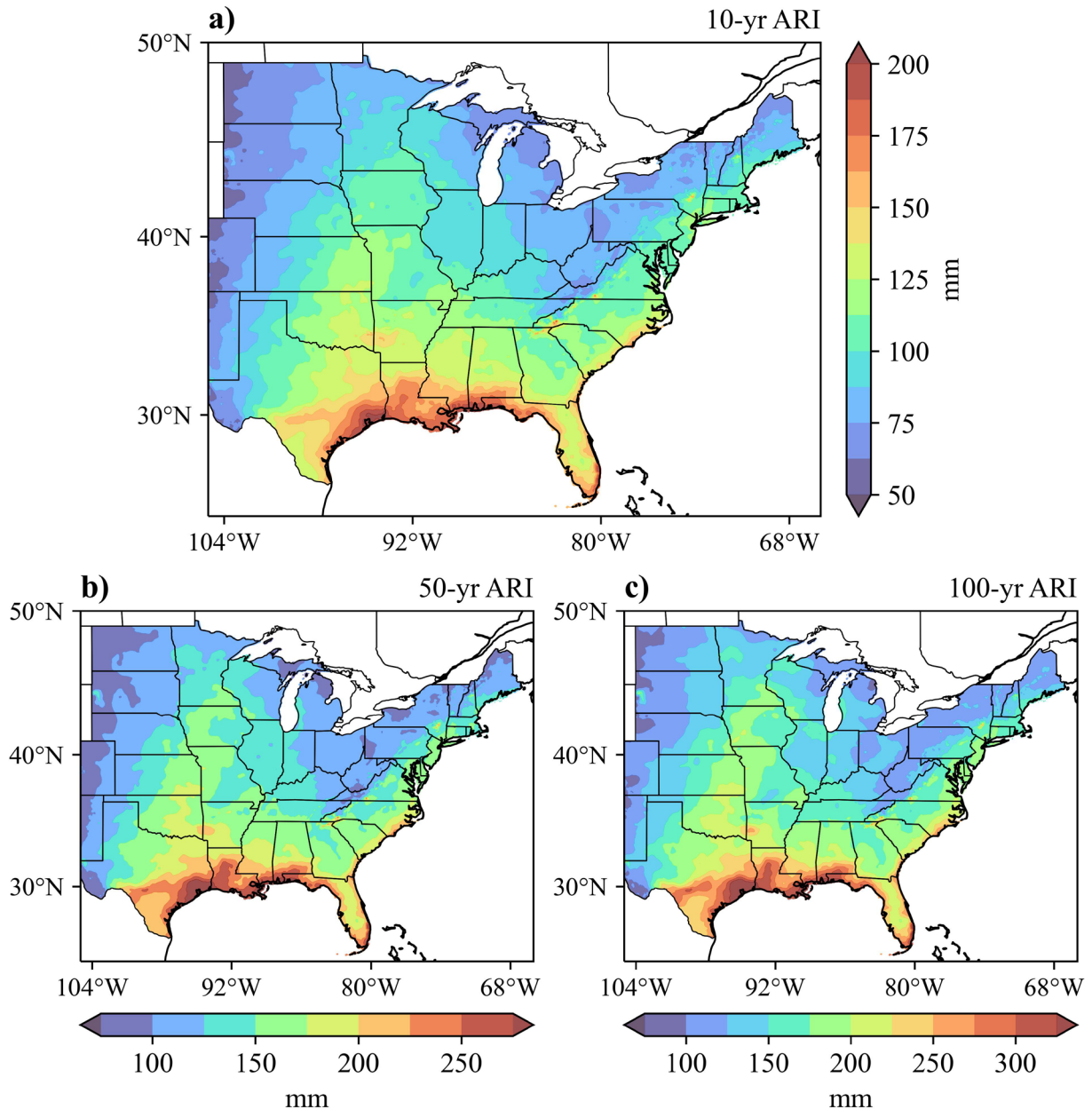

Figure 2.1: (a) 10-, (b) 50-, and (c) 100-yr ARI 12-hr precipitation frequency estimates from NOAA Atlas 14.

This study utilized the Stage IV (Fulton et al., 1998) quantitative precipitation estimates (QPEs) produced by the National Centers for Environmental Prediction Environmental Modeling Center (Lin and Mitchell, 2005). The Stage IV data were obtained from the National Center for

Atmospheric Research's Earth Observing Laboratory (Du, 2011). The dataset provides 1-, 6-, and 24-hr precipitation accumulations for the entire United States with 4-km horizontal grid spacing on a polar stereographic projection from January 2002 to present. Stage IV is based on radar-derived QPEs that are adjusted based on rain gauge observations (Hitchens et al., 2013). The radar data is sourced from the Next Generation Weather Radar (NEXRAD) network comprised of 142 operational Weather Surveillance Radar - 1988 Doppler (WSR-88D) radars within the CONUS. The Stage IV data are processed and undergo some degree of manual quality control (QC) by the NWS River Forecast Centers (RFCs). Radar locations and the borders between all River Forecast Center domains are presented in Fig. 2.2.

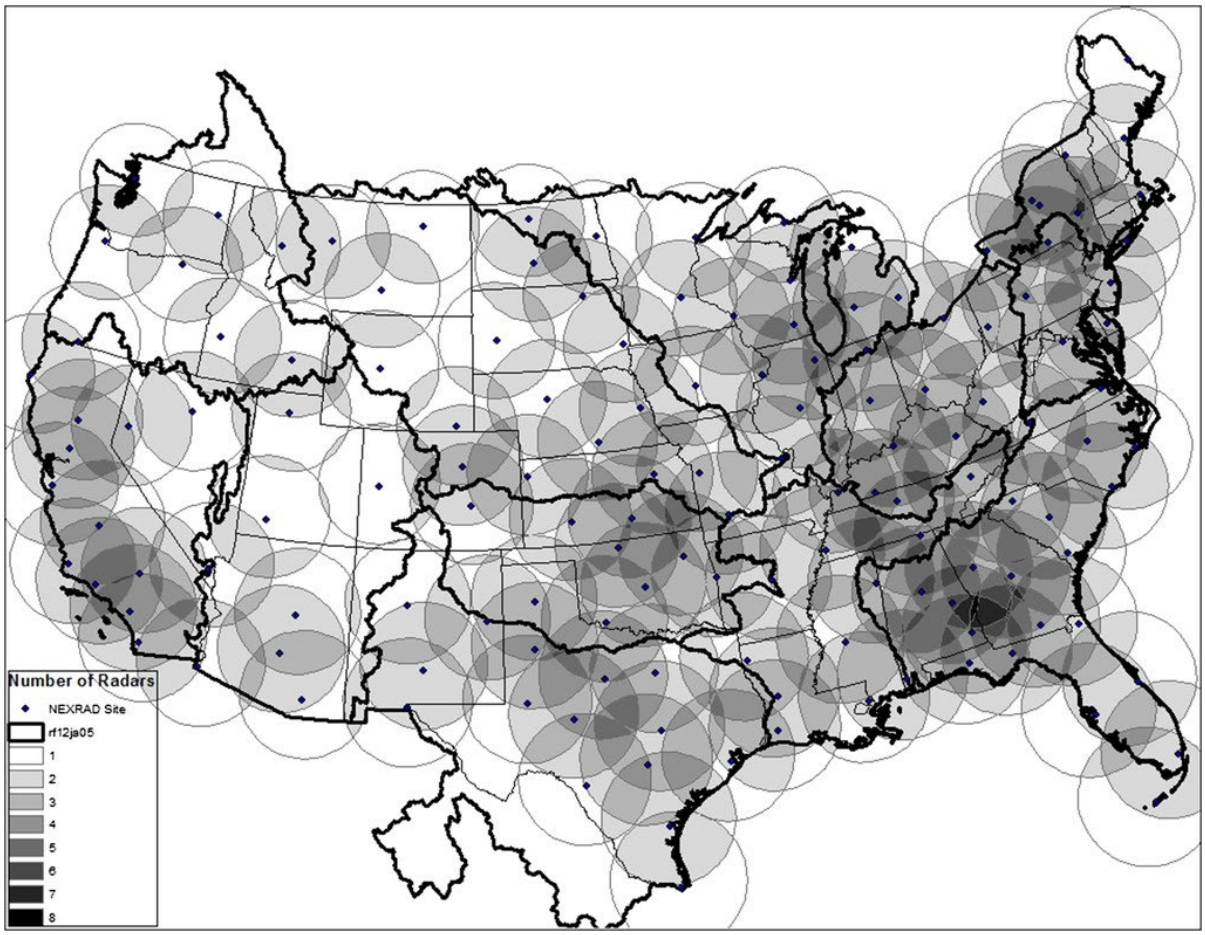

Figure 2.2: River Forecast Center domains and NEXRAD radar sites with range rings and overlap of other radars in the vicinity. (Fig. 1 of Nelson et al., 2016)

Given that the Stage IV precipitation dataset utilizes radar data, it has the distinct advantage of capturing extreme precipitation produced by deep convective cores, which are typically localized and sporadic in nature (e.g., Zhang et al., 2003). In contrast, studies that have just used in-situ measurements often miss EREs that occur between rain gauge sites (e.g., Risser et al., 2019) as these rain gauges are nonuniformly spaced and relatively sparse in some regions.

However, we acknowledge that there are also several caveats to using the Stage IV dataset for the purposes of this study that include but are not limited to the following, as described by Nelson et al. (2016): (1) Hourly QPEs suffer from lack of manual QC. For example, bad rain-gauge reports are often not filtered out (addressed in section 2.1.3); (2) Different River Forecast Centers may use different processing algorithms for generating QPEs, resulting in spatial discontinuities across River Forecast Center boundaries (Fig. 2.2); (3) Inherent biases exist in radar-based QPEs due to spatially varying radar coverage, range-dependent detection, anomalous propagation, beam blockage, bright band contamination, and representativeness bias due to the physical nature of rainfall (i.e., stratiform vs. convective) affecting reflectivity-to-rainfall relationships; (4) Temporal inhomogeneities may exist due to multiple changes in River Forecast Center processing methods, upgrades to the NEXRAD sites from 2011–2013, and the gradual incorporation of Multi-Radar Multi-Sensor (MRMS; Zhang et al., 2016) products starting in 2016.

Note that our methods of identifying EREs are similar to those used by Stevenson and Schumacher (2014). However, the differences between the two studies include that we analyzed 20 years of Stage IV data (as opposed to 10 years), employed a more recently updated ARI threshold dataset, and used a timescale of 12 hours (as opposed to 1, 6, and 24 hours). Our method accounts for events that straddle the 6- and 24-hr time bounds (i.e., the measurement-interval truncation problem; Barbero et al., 2017) by using iteratively summed 1-hr data files, ensuring that

certain events are not overlooked by the algorithm. Finally, we also utilize consistent QC and event type classification procedures to avoid potential human bias that can arise from manual methods.

2.1.2 Preliminary ERE Detection Algorithm

The full domain of investigation for this study is the CONUS east of 104°W (i.e., east of the Rockies), aligning with the western borders of North Dakota, South Dakota, and Nebraska. Starting at the beginning of the available Stage IV dataset (2002-01-01), 12-hr EREs were detected within the domain by summing hourly Stage IV gridded data files over the previous 12 hours, iteratively, and subtracting the 10-yr ARI threshold (Fig. 2.1a) at each grid point. Stage IV data were restricted to land only and the thresholds from the NOAA Atlas 14 dataset were resampled to match the 4-km Stage IV grid via linear interpolation. Any point where the difference between the 12-hr summed Stage IV precipitation and the 10-yr ARI threshold was greater than zero was considered an instance of extreme precipitation. Our approach then grouped all exceedance points within a radius of 250 km from the point of maximum exceedance (PME) into an event object. Any subsequent iteration within 12 hours of a detected event that had a PME within 250 km of a previous iteration would replace the previous event object if (1) the maximum exceedance value was greater or (2) if only the number of exceedance points was greater. If all attributes matched a previous event, only the accumulation period of the first instance was retained.

Each object identified as an ERE was assigned an identification number and several attributes were stored for each. Some of the key attributes include the following: (1) the maximum exceedance value above the 10-yr ARI threshold; (2) the 12-hr accumulation value associated with the PME; (3) the latitude and longitude of the PME; (4) the date and hour of the maximum hourly accumulation value recorded at the PME (i.e., the peak accumulation hour); (5) the first hour in

the 12-hr accumulation window over which at least 1 mm of precipitation fell at the PME (i.e., event onset) along with the end time of the accumulation window; (6) the number of exceedance points detected for the event. For each preliminary event, the 12-hr accumulation map array associated with the event, as well as the 1-hr accumulation map array during the peak accumulation hour, were exported for analysis, QC, and event type classification purposes.

Before analyzing each 12-hr accumulation map derived from the hourly Stage IV analyses, the data were cross-checked with an 18-hr accumulation map derived from the three 6-hr Stage IV analysis files containing the 12-hr period. Any 12-hr accumulation values that exceed the 18-hr accumulation from the 6-hr analyses were considered erroneous and were replaced with the latter at those grid points. This process takes advantage of the manual QC that the 6-hr analyses undergo by the River Forecast Centers that is often not performed on the hourly analyses. While this procedure may lead to overestimates of 12-hr precipitation wherever it was erroneous by replacing it with 18-hr precipitation, a significant number of events that appeared to be due to bad data or radar overestimates in the hourly analyses were eliminated. However, additional QC was still necessary, and the procedures used are discussed in section 2.1.3.

A maximum preliminary event radius of 250 km was chosen subjectively based on experimentation with typical simultaneous extreme-rain-producing MCS cases. One example of two simultaneous MCSs occurring just outside of their respective 250-km radii is represented in Fig. 2.3, with panels (a) and (b) presenting 12-hr accumulation maps associated with each respective event, with exceedance points highlighted in red and the 250-km range rings around the PME displayed. Both events had the same peak accumulation hour, and a radar mosaic showing both MCSs near that time is presented in panel (c).

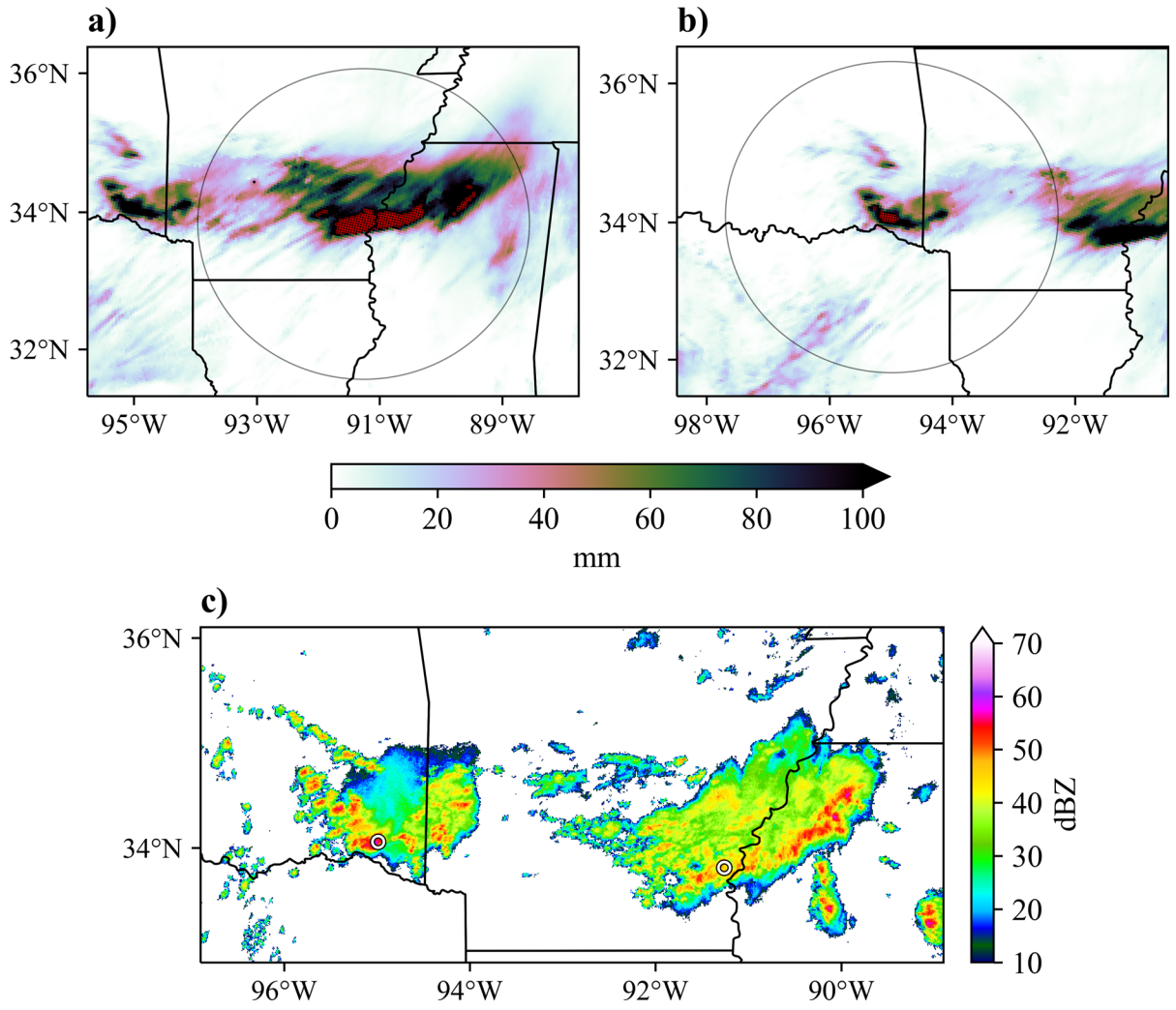

Figure 2.3: Total Stage IV 12-hr accumulation (mm) maps for (a) Event #08857 (2021-06-08 0600–1800 UTC) and (b) Event #08858 (2021-06-08 0300–1500 UTC) with a 250-km range ring around the PME and grid points exceeding the 10-yr ARI threshold outlined in red. (c) Multi-Radar Multi-Sensor composite reflectivity mosaic during the peak accumulation hour of both EREs (2021-06-08 1100 UTC) with the PME for both events denoted by small white circles.

There are several cases, however, where the exceedance points of a single event stretch farther than 250 km from the PME, or where exceedance points for one event overlap with another within the 12-hr time constraint. In these cases, the preliminary algorithm identified multiple events. To account for this issue, a post-processing algorithm was performed after implementing the QC

procedures described in section 2.1.3. Any events within 12 hours of each other that included any exceedance points that overlap the 250-km radius of another "event" were combined into a single event with updated attributes. If the 12-hr accumulation periods of the combined events are different, the accumulation maps are combined by only including the maximum 12-hr accumulation values. Fig. 2.4a is an example of a combined 12-hr accumulation map with exceedance points that extend outside the 250-km radius from the PME. This event was a case where a large, long-duration MCS produced its maximum extreme rainfall at a point relatively early in its lifecycle (Fig. 2.4b) before continuing to produce extreme rainfall greater than 250 km downstream (Fig. 2.4c).

All events in 2002 were ultimately removed from the analysis due to a large number of which, relative to subsequent years, that appeared to be triggered by artificially high QPEs that were unfiltered by the QC procedures described in 2.1.3. Being the first year in the dataset, it is assumed that the data may be less reliable as River Forecast Centers may not have established their processing and QC techniques yet.

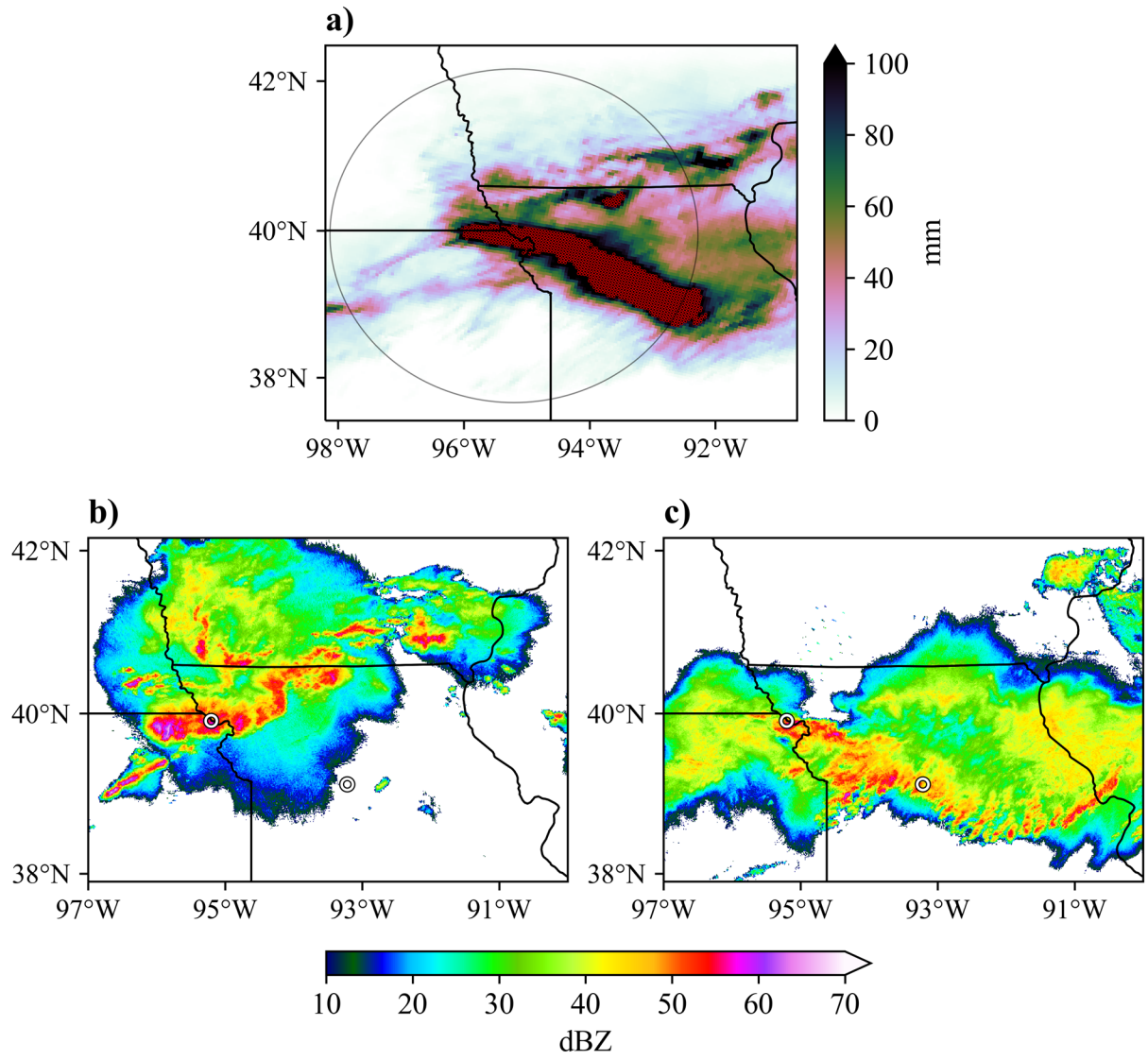

Figure 2.4: (a) Total Stage IV 12-hr accumulation (mm) map for Event #08899 from two merged 12-hr periods (2021-06-25 0000–1200 UTC and 2021-06-25 0200–1400 UTC) with a 250-km range ring around the PME and grid points exceeding the 10-yr ARI threshold outlined in red. (b) Multi-Radar Multi-Sensor composite reflectivity mosaic during the peak accumulation hour (2021-06-25 0130 UTC) and (c) during the peak accumulation hour of the secondary event (2021-06-25 1000 UTC) with the PME for both uncombined events denoted by small white circles.

The preliminary ERE detection algorithm identified a total of 10,856 event objects between 2003 and 2022, which was reduced to 9095 after QC and combining overlapping events. A map showing the number of events at all Stage IV grid points within the domain is displayed in Fig.

2.5. This map was obtained by summing binary map arrays of exceedance points for all QC-passed events in the 20-yr period. The results show significant spatial variability as some locations have apparently experienced up to 12 events, while large areas (e.g., coastal Massachusetts) apparently had none. This result is likely attributable to the spatial variations in EREs that are likely to occur over a relatively short period of study, and perhaps due to errors in the NOAA Atlas 14 thresholds and/or Stage IV QPEs. Ideally, given the ARI of 10 years used as a threshold and an observation period of 20 years, the average number of events over the entire domain would be 2, yet the average based on this analysis was ~1.3. The lack of events relative to the expected amount may be partly due to decadal changes in rainfall. However, this difference also implies that the Stage IV dataset may underestimate extreme rainfall amounts over several areas and caution should be used when comparing these amounts to the ARI thresholds from the NOAA Atlas 14 dataset. Indeed, Nelson et al. (2016), among other studies, have determined that Stage IV often underestimates heavy precipitation. Contrarily, Kim et al. (2022) suggests that the NOAA Atlas 14 precipitation frequency estimates are also underestimations and diverge from recent observations due to the inherent nonstationarity of precipitation over time. Thus, the underestimation of extreme precipitation in the Stage IV dataset may be significant over several areas, so it is likely that numerous lower-end EREs were missed by the detection algorithm. Conversely, several spurious events were detected that resulted from erroneously *high* Stage IV QPEs. The methods used for QC are described in the next section.

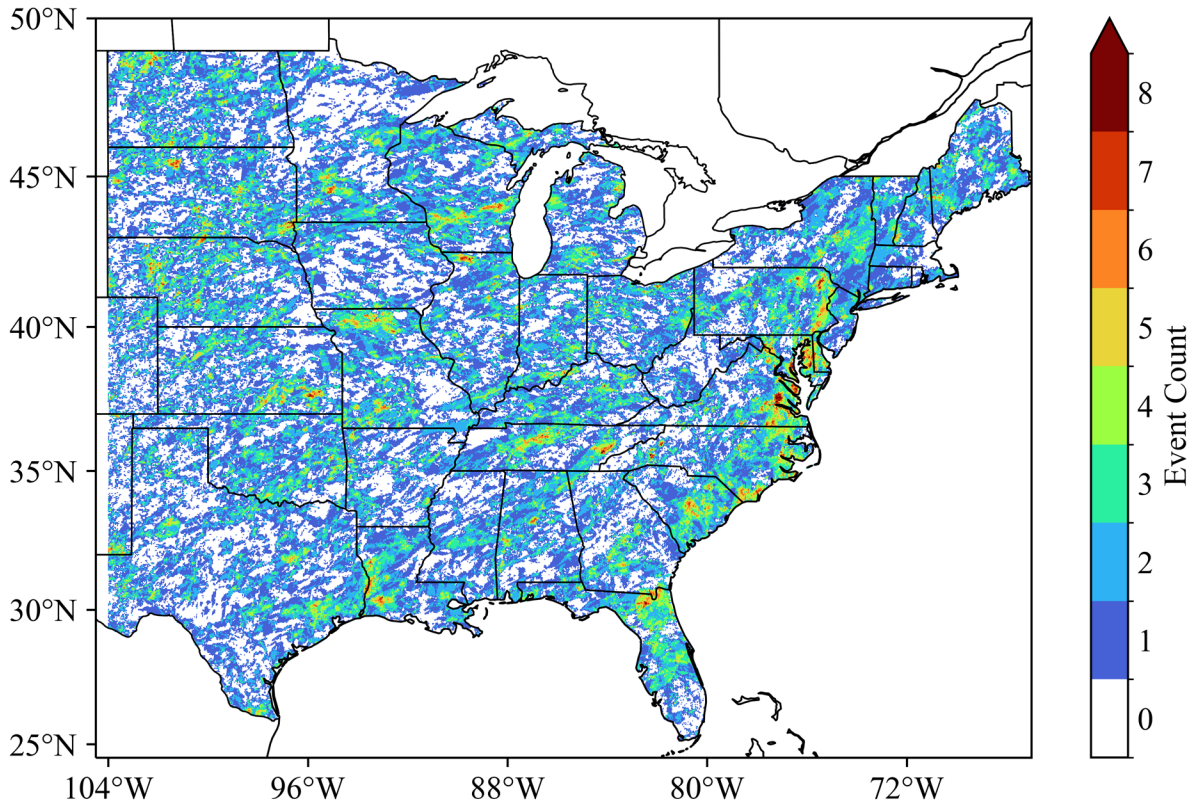

Figure 2.5: Map of total (QC-passed) 10-yr event counts at all Stage IV grid points over the full domain from 2003–2022.

2.1.3 Quality Control

As mentioned previously, the Stage IV data, particularly the hourly analyses, have significant problems with QC (e.g., Nelson et al., 2016). Poor data quality can result from random radar errors and bad rain gauge reports, which triggered the detection of numerous spurious events in the preliminary algorithm described in the previous section. Manual QC was considered, but in several cases, the decision on which events were erroneous would be rather subjective and could be inconsistent throughout the dataset, leading to the potential for unintentional human bias that can impact trend analyses. Instead, automated QC procedures were developed to filter out as many

spurious events as possible while minimizing the amount of potentially legitimate events that are falsely flagged as spurious events.

Defining the conditions in which an event is flagged as "bad" required a general idea of what the erroneous QPEs look like. The 12-hr accumulation maps for four spurious events are displayed in Fig. 2.6. Example accumulation maps for QC-flagged events due to bad rain gauge reports are shown in panels (a) and (b), which can have circular or "bull's-eye" patterns on the maps. Panel (c) shows another type of erroneous data with random isolated grid points having very high QPEs compared to their surroundings, and there is also a visible "hot and cold" bias along a River Forecast Center boundary (Fig. 2.2) in upstate New York, exemplifying the difference in River Forecast Center processing of Stage IV data. In panel (d), the patch of noisy data surrounded by lighter precipitation may be indicative of anomalous propagation embedded within a large stratiform precipitation field.

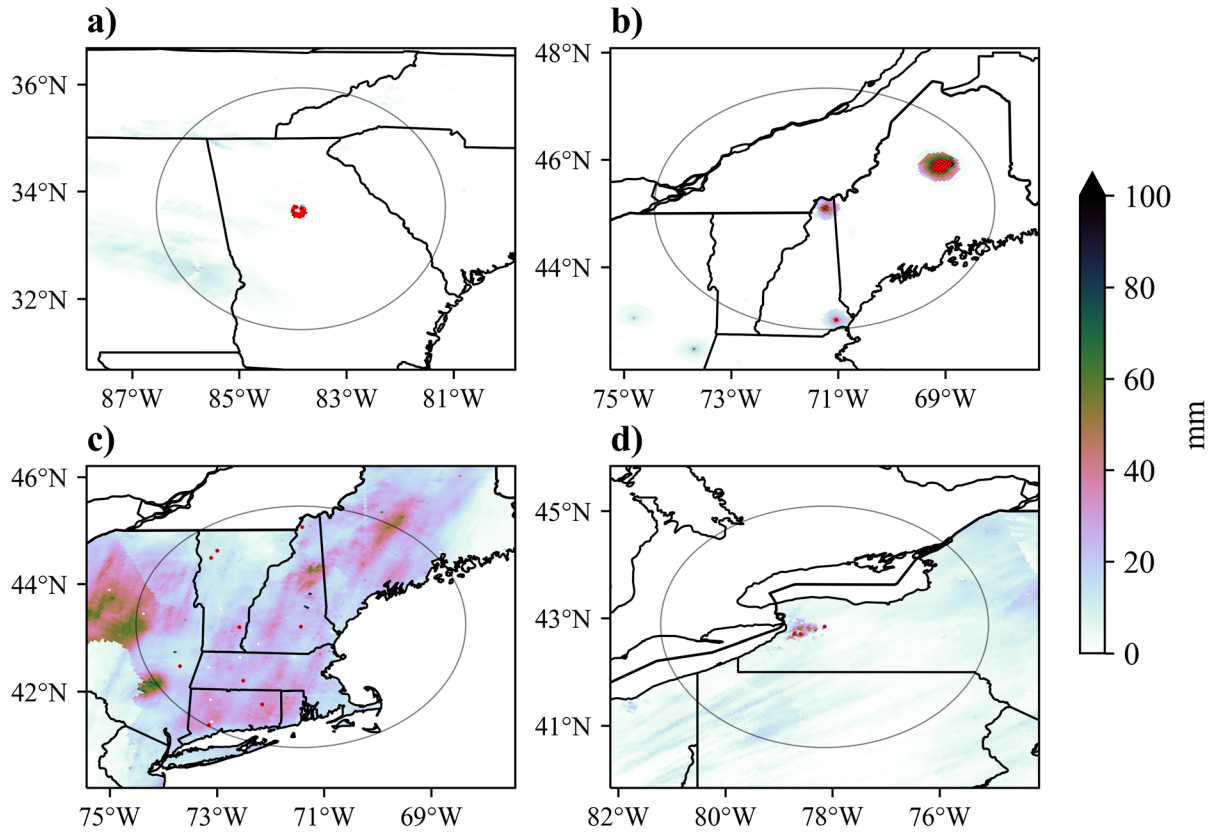

Figure 2.6: Example Stage IV 12-hr accumulation (mm) maps for QC-flagged events with 250-km range rings around each (spurious) event's PME and grid points exceeding the 10-yr ARI threshold highlighted in red. Accumulation maps are valid for the 12-hr periods ending (a) 2006-05-14 0100 UTC, (b) 2007-01-17 1100 UTC, (c) 2006-11-17 1200 UTC, and (d) 2004-12-08 0600 UTC.

The most common characteristic of the accumulation maps associated with spurious events was that the PME had a very high value relative to the surrounding grid points (i.e., noisiness in the data). To quantify this property, the average accumulation over all Stage IV pixels adjacent to the PME (a total of 8 grid points) was compared to the accumulation value at the PME. A fraction of the surrounding average accumulation to the PME accumulation (or "PME noise parameter" for short) had to be chosen as a threshold to delineate between spurious and legitimate events. To determine the best fraction to use as a threshold, the effectiveness of the condition was tested

against human QC for a random sample of 1000 events. The manual QC was performed by visually inspecting the 12-hr accumulation maps for each event and flagging any event objects clearly associated with erroneous data (e.g., Fig. 2.6). For events that were uncertain, they would only be flagged if the accumulation map was unsupported by radar observations, examined from a radar composite archive (available online at http://www2.mmm.ucar.edu/imagearchive/). QC thresholds were chosen at the value where a parameter maximizes the agreement with manual QC. For example, the value of the PME noise parameter at which the agreement between the manual and automated QC flags was maximized is 0.32 with an agreement at ~97.8% (Fig. 2.7). Thus, one of the four conditions used in the automated QC process is that the PME noise parameter must be at least 0.32 to pass.

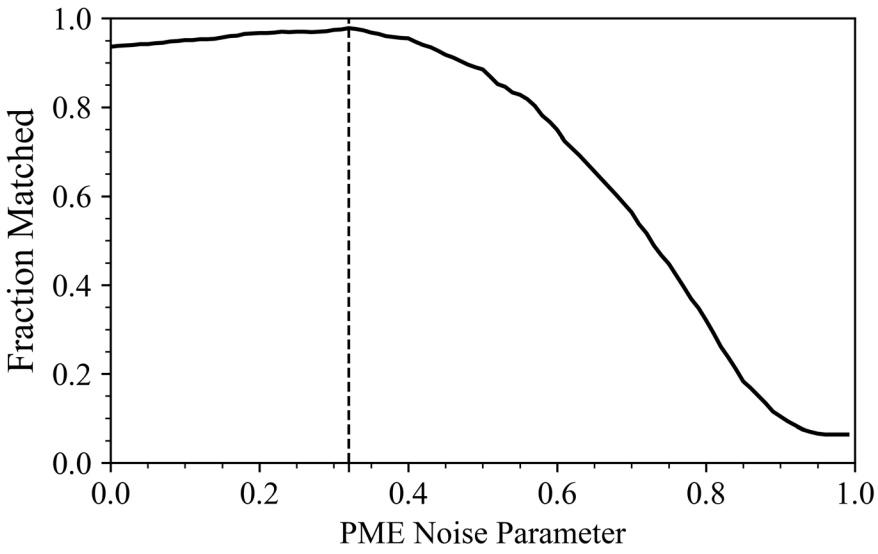

Figure 2.7: Fraction of the total events in the random test sample where the automated QC flags match the manual QC flags vs. the PME noise parameter (QC condition #1). The vertical dashed line represents the optimal parameter value for the condition (0.32).

Based on testing against the manual QC of 1000 randomly selected events, any event meeting at least one of the following conditions was flagged as "bad", in order from most to least effective (note that condition #1 was described previously): (1) The average 12-hr accumulation at all Stage IV grid points adjacent to the PME was < 32% of the maximum exceedance; (2) The minimum 12-hr accumulation value among all valid grid points adjacent to the PME was < 0.005 mm; (3) The fraction of the number of exceedance points divided by the maximum exceedance value (mm) was < 0.04; (4) The maximum 1-hr accumulation at the PME was > 254 mm. (Note: Condition #4 was obtained to be near the minimum value at which no manually passed events were eliminated instead of the value of maximum total agreement.) The combination of all four conditions led to the best total agreement with the human QC, with ~89.1% of QC flagged events in agreement and ~98.7% of QC passed events in agreement, leading to a total agreement of ~98.1%.

While these automated QC methods were unable to capture all types of erroneous events and sometimes mistook legitimate events for "bad" events, this problem only impacted about 1.9% of the test dataset. The main purpose was to eliminate as many spurious events as possible while maintaining a consistent QC procedure throughout the dataset. Out of the 10,856 total preliminary event objects (2003–2022), 543 (~5.0%) were automatically flagged as spurious and were filtered out of the dataset for all subsequent analyses.

The highest concentrations of QC-flagged events were found over the interior East Coast, especially over the Appalachians (Fig. 2.8), which is where radar data tended to be noisier due to orographic influences, such as the presence of ground clutter and beam blockage, and bad rain gauge reports were more prevalent. Throughout the sample period (2003–2022), there was a significant decreasing trend in the annual number of QC-flagged events (Fig. 2.9) due to improvements in data quality and QC methods over time.

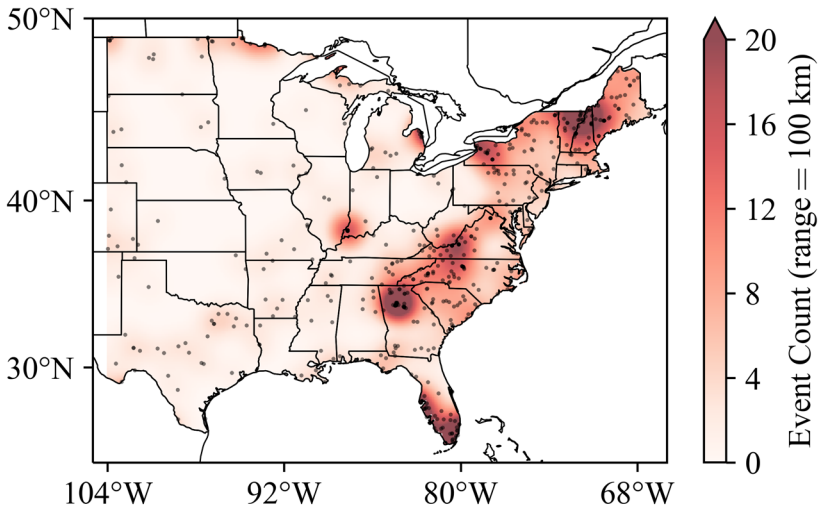

Figure 2.8: All 2003-2022 QC-flagged event PME locations (translucent black dots) with Gaussian smoothed (σ = 0.5°) neighborhood event count (range = 100 km) (color fill), scaled up at the domain edges based on the inverse fraction of valid domain area within the radius.

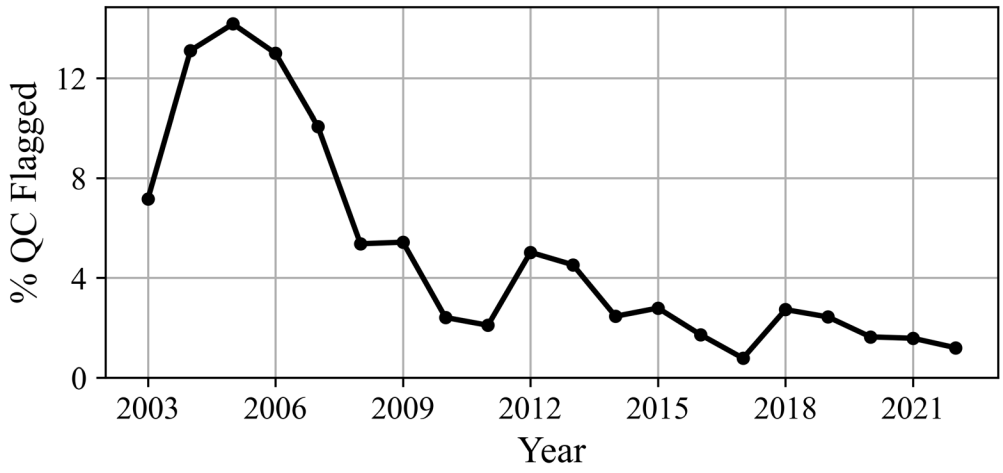

Figure 2.9: 2003–2022 time series of the fraction of total annual preliminary events that failed automatic QC.

2.1.4 Event Type Classification

EREs arise from a variety of rain-producing weather systems, but this study is focused specifically on summertime convection. Therefore, events associated with tropical cyclones and those

produced primarily by stratiform precipitation were identified and filtered out of the analysis. Among the different types of extreme-rain-producing convection, the localized variety, including air mass thunderstorms and supercells, have far different environmental properties than the nonlocalized variety and often have lesser impacts on society due to their sparse nature. Thus, methods were also developed to filter out events that were only associated with localized convection. Subclassifications were also created for events associated with MCSs and nocturnal convection.

2.1.4.1 Tropical Cyclones

All events where the center of a tropical cyclone (including tropical depressions and post-tropical cyclones) was present within 3 degrees of latitude or longitude of the PME and within 24 hours of the peak accumulation hour were classified as a TC-related event. The tropical cyclone track data that were utilized for this classification were obtained from the International Best Track Archive for Climate Stewardship (IBTrACS) dataset (Knapp et al., 2010, 2018).

2.1.4.2 Stratiform Precipitation

Stratiform precipitation is typically characterized by steady light to moderate accumulation rates over a large area that are persistent for several hours, often associated with synoptic scale weather systems (i.e., extratropical cyclones) and MCSs. While stratiform precipitation is typically lighter in nature, moderate steady rainfall over the same area can still lead to extreme precipitation over a 12-hr period, especially where heavier bands of precipitation become quasi-stationary. Stage IV accumulation patterns for events associated with primarily stratiform precipitation typically have a smoother appearance compared to convective events and their associated precipitation features

are typically larger in areal extent. A precipitation feature, adapted from the methods of Feng et al. (2016), can be defined as a contiguous area of 1-hr accumulation exceeding a threshold. Precipitation features were identified by grouping all adjacent grid points connecting to the respective event's PME that exceeded the specified threshold. An example 1-hr accumulation map during the peak accumulation hour of a typical ERE classified as "primarily-stratiform-related" and its associated 12-hr accumulation map is presented in Fig. 2.10. The 1-hr accumulation map reveals a very large 0.1 mm hr^{-1} precipitation feature with relatively light precipitation rates and the associated 12-hr accumulation map has a "smooth" appearance relative to typical convective ERE accumulation maps (e.g., Fig. 2.3a).

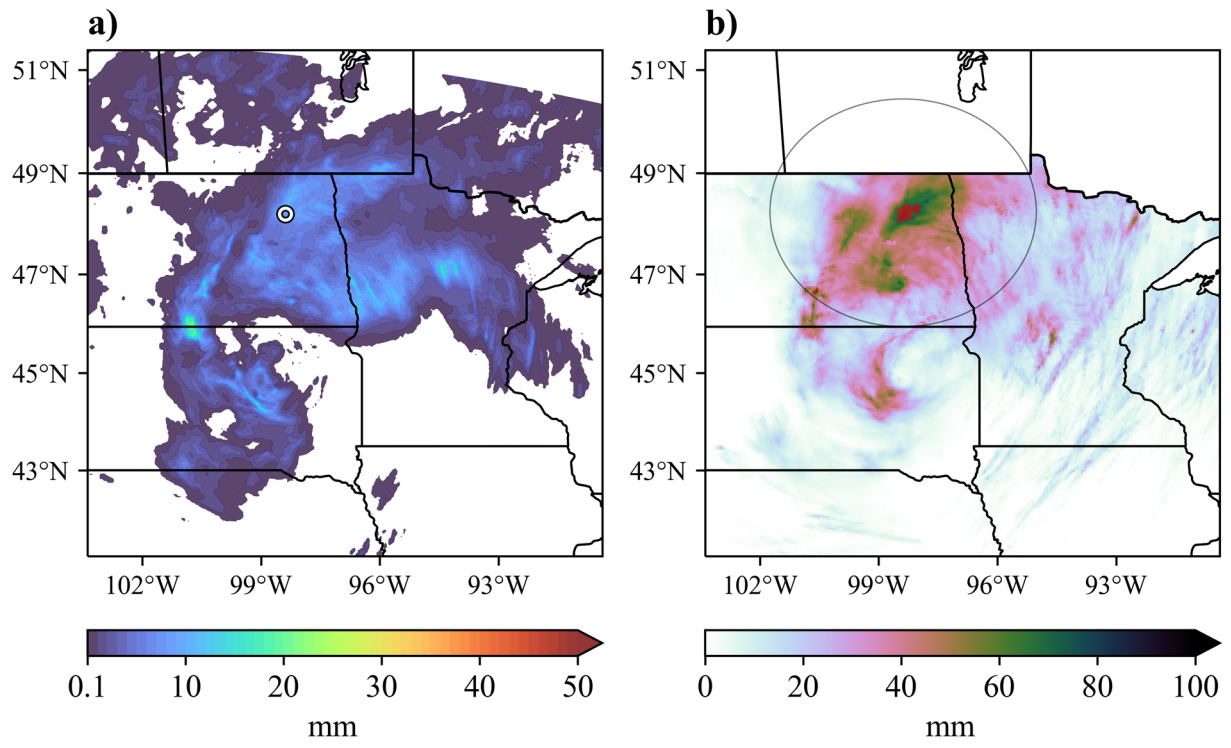

Figure 2.10: From an example ERE classified as primarily stratiform-related (Event #05925), (a) Stage IV 1-hr accumulation (mm) map during the peak accumulation hour (2015-05-17 1500–1600 UTC) with the PME indicated by a small white circle, and (b) Stage IV 12-hr accumulation (mm; ending 2015-05-18 0100 UTC) map with a 250-km range ring around the PME and grid points exceeding the 10-yr ARI threshold highlighted in red.

Similar to the methods that were used for QC described earlier, an automated process was developed to consistently identify events associated with primarily stratiform precipitation[2] throughout the dataset. Again, a sample of 1000 events was visually inspected for characteristics of stratiform precipitation and verified against radar data. These classifications were more challenging and more subjective than the manual QC, but it was still worthwhile to find optimal parameters for a consistent definition of primarily-stratiform-related events. An event meeting at least one of the following conditions, provided it was not already classified as TC-related, was classified as an event associated with primarily stratiform precipitation: (1) The maximum hourly accumulation at the PME through the 12-hr accumulation period was < 25 mm and the area of the 0.1 mm hr^{-1} precipitation feature during the peak accumulation hour was ≥ 40,000 km^2; (2) >99% of the 0.1 mm hr^{-1} precipitation feature during the peak accumulation hour had values of < 10 mm hr^{-1}.

These conditions were developed to maximize the agreement between human-identified primarily-stratiform-related events, while keeping any convective events falsely classified as primarily-stratiform-related to a minimum. As a result, the conditions only identified about 47.1% of the human-identified primarily-stratiform-related events, but also only falsely identified about 0.9%. Therefore, several primarily-stratiform-related events could remain within the filtered dataset, but only a few legitimate convective events were filtered out.

[2] Events classified as "primarily-stratiform-related" are not associated with stratiform precipitation from MCSs, but rather, large stratiform precipitation features associated with extratropical cyclones. However, extreme rainfall may still be associated with embedded convective elements within the stratiform precipitation shield.

2.1.4.3 Localized Convection

Several methods were tested on the same random sample as used for stratiform classification to identify events associated with localized convection, which appear on radar and accumulation maps as relatively small areas of heavy precipitation surrounded by an absence of any notable precipitation (e.g., Fig. 2.11a–b), or can have a very "splotchy" appearance (e.g., Fig. 2.11c–d). The storms being classified as "localized" can include quasi-stationary ordinary cell convection (e.g., air mass convection), slow-moving or training supercells, or back-building clusters that do not have a large areal extent at any point in their lifecycle. Fig. 2.11a–b shows an example of the 1- and 12-hr accumulation maps associated with a training supercell case, having a narrow streak appearance, and Fig. 2.11c–d shows the same for a quasi-stationary ordinary cell case, having a splotchy appearance.

A consistent and objective way to define an event associated with localized convection utilized the length threshold for an MCS, defined by Feng et al. (2016) as a minimum major axis length of the 1 mm hr^{-1} precipitation feature being 200 km. See Fig. 2.12 for a demonstration of how the major axis lengths were obtained. An ERE was classified as being caused by only localized convection if the approximate major axis length of the 1 mm hr^{-1} precipitation feature containing the PME was < 200 km throughout the accumulation period, provided it was not a TC- or primarily-stratiform-related event. Fig. 2.12a would be a case where the convection was localized, with a maximum precipitation feature length of ~75 km. If that precipitation feature length did not exceed 200 km throughout the event's accumulation period, then it was classified as a an ERE associated with localized convection.

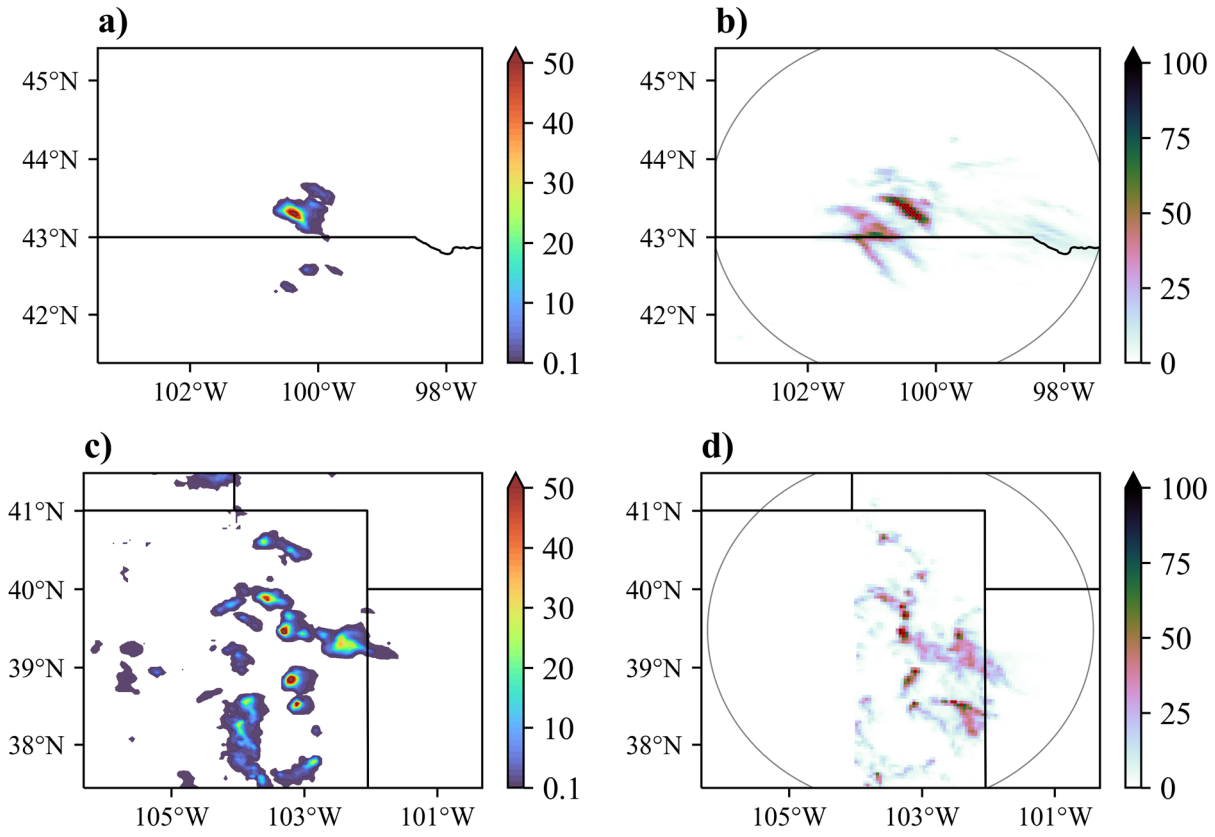

Figure 2.11: (a) Stage IV 1-hr accumulation (mm) during the peak accumulation hour and (b) Stage IV 12-hr accumulation (mm) for a training supercell case (Event #09525; peak 2022-08-05 0300; end 2022-08-05 0500) with a 250-km range ring around the PME and grid points exceeding the 10-yr ARI threshold highlighted in red. (c) and (d) as in (a) and (b) but for a quasi-stationary ordinary cell convection case (Event #9004; peak 2021-07-17 0000; end 2021-07-17 0400).

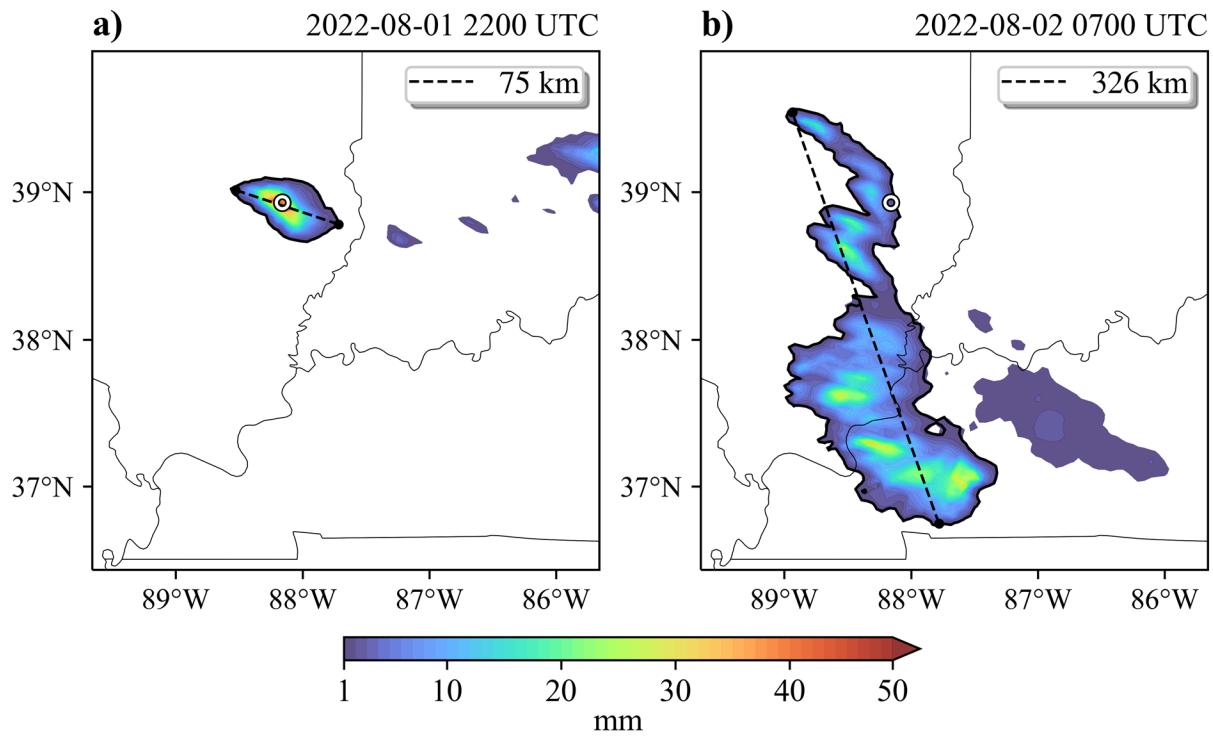

Figure 2.12: Stage IV 1-hr accumulation (color fill; mm) maps of the precipitation features associated with an event that evolved from (a) localized to (b) non-localized (Event #09514; peak 2022-08-01 2200 UTC; end 2022-08-02 0800 UTC). The small white circle is located at the PME and the 1 mm hr^{-1} precipitation feature associated with the event is outlined in black. The end points of the approximate major axis of the precipitation feature (black dots) are connected by a dashed black line, which is ~75 km long in (a) and ~326 km long in (b). The time stamps on the top right are at the end of the 1-hr accumulation periods.

2.1.4.4 MCSs

For an ERE to be classified as MCS-related, the major axis length of the 1 mm hr^{-1} precipitation feature containing the PME exceeded 200 km for at least four consecutive hours during the accumulation period, provided it was not a TC- or primarily-stratiform-related event. In other words, the precipitation feature associated with the ERE was nonlocalized (according to the previous section) for at least four consecutive hours. This definition was adapted from Feng et al. (2016). However, our definition may be stricter as our method does not track the precipitation

feature as it approaches or moves away from the PME. Thus, the number of MCS-related EREs in our results may be conservative. In addition, since this method only utilizes the characteristics of the precipitation feature, but not the surrounding environment, several of the events classified under the MCS category may be associated with large synoptic scale systems that contained widespread convection (e.g., quasi-stationary frontal squall lines or coastal lows). No methods were developed to separate EREs related to MCSs and EREs related to large-scale synoptic systems. As such, a substantial portion of the events that were classified as "MCS-related" through the entire seasonal cycle may be incorrectly identified. During JJA, however, EREs caused by large-scale weather systems are much less common due to weaker synoptic scale forcing mechanisms, so including synoptic scale systems should not significantly affect the results when considering only JJA events.

An example of an MCS-related event is shown in Fig. 2.12. Though the convection in that case began as localized, the associated precipitation feature attained a maximum major axis length of >200 km for 4 consecutive hours through the accumulation period, making it an MCS-related event.

2.1.4.5 Nocturnal Rainfall

An ERE was classified as nocturnal (i.e., being associated with rainfall occurring at night) if at least one of the following conditions was true: (1) The peak accumulation hour at the PME occurred between sunset and sunrise at that location. (The hours in which sunset or sunrise occurred do not count.); (2) At least half of the hours during the accumulation period at the PME occurred between sunset and sunrise at that location. For example, an event with the first hour of accumulation exceeding 1 mm hr^{-1} at the PME being 0500 UTC, the end of the accumulation

period being 1400 UTC (total accumulation period of 9 hours), and local sunrise at 1045 UTC would be considered nocturnal because the number of hours before sunrise would be counted as 5 hours (0500–1000 UTC), which is greater than half of the 9-hr accumulation period.

This approach may be somewhat conservative as events with a relatively modest nocturnal component to the accumulated rainfall, or where the associated precipitation feature propagates away from the PME into the nighttime hours, may not be classified as nocturnal. However, it is still important to differentiate between "nocturnal" and "diurnal" EREs in order to examine the diurnal cycle.

2.2 Statistical Methods

This section will briefly introduce our methods for detecting trends in EREs (chapter 4) and performing composite and correlation analysis with meteorological fields (chapter 5) along with their corresponding tests for statistical significance. Further details regarding the methods used to generate specific figures are stated in their respective results sections and/or figure captions.

2.2.1 Trend Analysis

Various subsets of the database of EREs described in section 2.1 (e.g., JJA MCS-related EREs) were used to construct time series of event counts per year through the sample period (2003–2022). These time series were investigated for possible trends using the Mann–Kendall nonparametric trend test, which tests against the null hypothesis that no trend is present in the time series (Wilks, 2019). The Mann–Kendall trend test is commonly used for detecting statistically significant monotonic increasing or decreasing trends in time series data and has often been applied to extreme precipitation (e.g., Kunkel et al., 2013a; Li et al., 2022a; Rahmani et al., 2016; Westra et al., 2013).

Unlike testing for significance in the slope of an ordinary linear regression, the Mann–Kendall trend test is a robust statistical method of identifying trends that may not be linear. The Mann–Kendall trend test is related to *Kendall's* τ (τ_K), which is an alternative to the conventional Pearson correlation coefficient that is robust and resistant to outliers (Wilks, 2019). Like the Spearman rank correlation coefficient, Kendall's τ is another type of rank-based correlation coefficient, which serves as a measure of the association between a variable and time, ranging from −1 to 1. In addition to the Mann–Kendall trend test for significance, Kendall's τ will be presented as a metric for the confidence in any positive or negative trend, consistent with (Kunkel et al., 2013a) and their presentation of trends in extreme precipitation. Instead of using the slope of an ordinary linear regression, the magnitude of a monotonic trend relating to the Mann–Kendall test can be represented using the *Theil–Sen slope* (β_{TS}) of the time series (Wilks, 2019). The Theil–Sen slope is calculated by computing the median of all pairwise combinations of points in the time series, yielding a robust estimate of the slope of a linear regression that is resistant to outliers. Kendall's τ, Theil–Sen slope, and the Mann–Kendall trend test *p*-values (p_{MK}) for a given time series were all calculated using the "pyMannKendall" Python package (Hussain and Mahmud, 2019). For individual tests, the trend was considered statistically significant when p_{MK} was less than α at the specified confidence level (e.g., $\alpha = 0.05$ for the 95% confidence level). However, if trends were calculated on a spatial grid, a correction was applied to the *p*-value significance threshold that addresses the false discovery rate for multiple hypothesis tests (described in section 2.2.3).

While event counts are a discrete quantity, it is unnecessary to use Poisson regression since our intention was not to model event counts but to simply detect trends in the data. Thus, linear or Theil–Sen slopes may be expressed as a continuous quantity in some analyses for the purpose of comparing trends in relatively small sample sizes.

2.2.2 Composite & Correlation Analysis

Composite and correlation analysis was used to identify potential relationships between seasonal LSMPs and JJA EREs associated with non-localized convection. Meteorological fields from the European Centre for Medium-Range Weather Forecasts Reanalysis v5 (ERA5; Hersbach et al., 2020) were utilized for the analysis, with monthly averaged data on single levels and pressure levels obtained from the Copernicus Climate Change Service Climate Data Store (Hersbach et al., 2023a,b). Some of the atmospheric variables that were analyzed include total column water vapor, 850-hPa wind, and 500-hPa geopotential height. Each relevant meteorological field was averaged over JJA, as well as over winter (December–February) and spring (March–May), for each year (2003–2022) to generate a time series at each grid point for each respective season.

Composite analysis was conducted by averaging relevant scalar meteorological fields during the appropriate season over the years with JJAs considered to be anomalously "active" and "inactive" regarding extreme rainfall (specified in section 5.1). The composite difference ("active" years minus "inactive" years) was then calculated and tested for statistical significance at each grid point using the Monte Carlo bootstrapping method (n = 5000), followed by a correction of the significance threshold (section 2.2.3). In each Monte Carlo simulation, a random selection of "active" and "inactive" years without replacement was used to recalculate the composite difference. The percentile of the true composite difference among the 5000 simulations was then converted to the p-value for a two-tailed test at each grid point. For vector fields (e.g., 850-hPa wind), the magnitude of the composite vector difference was tested for statistical significance using the same methods, but with a right-tailed test.

Prior to correlation analysis, both the ERE time series and the ERA5 time series at each grid point were detrended to avoid inflating the correlation coefficients due to common underlying

trends. The Pearson correlation coefficient between the appropriate ERE time series and the seasonally-averaged ERA5 field time series at each grid point was then calculated. Statistical significance of the correlation coefficients was also determined using Monte Carlo simulations (n = 5000), again followed by the significance level correction (section 2.2.3). In each Monte Carlo simulation, a new 20-yr time series of the respective ERA5 field was constructed at each grid point by taking a random sample of 20 years with replacement, and the correlation coefficient with the ERE time series was recalculated. The percentile of the true correlation coefficient among the 5000 simulated values was converted to the p-value for a two-tailed test at each grid point. For vector fields, the vector sum of the correlation coefficients calculated from the zonal and meridional components represents the direction in which the maximum positive correlation is found with the respective field. As with the composite vector difference, the magnitude of the maximum correlation vector was also tested for statistical significance using the Monte Carlo method with a right-tailed test.

Further details regarding specific analyses (e.g., time series used, levels of statistical significance) will be described in chapter 5 and within the respective figure captions.

2.2.3 Addressing Field Significance

When performing multiple hypothesis tests on a geographical array of data that are not spatially independent, a problem arises known as "field significance" (Livezey and Chen, 1983). In atmospheric sciences, field significance is a common issue, where false rejections of the null hypothesis tend to group together on a spatial grid, leading scientists to overinterpret the results as physically meaningful (Wilks, 2016). Most studies in atmospheric sciences neglect the issue of field significance, and instead simply stipple significance on a map where the p-values from the

local tests are smaller than the chosen α (e.g., $\alpha = 0.05$ for the 95% confidence level). According to Wilks (2016), a principled and straightforward solution to account for errors related to multiple hypothesis testing and field significance is to control the false discovery rate (FDR). Conceptually, the FDR is the expected fraction of rejections of the null hypothesis (i.e., "discoveries") among the local tests that are incorrect.

FDR correction of the significance tests can be achieved using the Benjamini/Hochberg procedure (Benjamini and Hochberg, 1995). This procedure involves ranking the *p*-values of the local tests and identifying the value of p_{FDR}, which is defined as the maximum ranked *p*-value ($p_{(i)}$) that is no greater than $(i/N)\alpha_{FDR}$, where i is the rank of the *p*-value, N is the number of tests, and α_{FDR} is the chosen control level for the FDR (Wilks, 2016). All tests where the *p*-value is no greater than p_{FDR} may be considered statistically significant for the chosen α_{FDR}.

The FDR approach using $\alpha_{FDR} = \alpha_{global}$ is rather conservative when the underlying data are spatially correlated. According to Wilks (2016), choosing $\alpha_{FDR} = 2\alpha_{global}$ yields approximately correct results given the typical spatial autocorrelation of meteorological fields (specifically 500-hPa heights). An example of the ranked *p*-values from correlation significance testing in chapter 5 is presented in Fig. 2.13. Note that the threshold for statistical significance using the FDR approach was drastically reduced, leaving ~7.2% being statistically significant ($p \leq p_{FDR}$ where $p_{FDR} \sim 0.0072$), as opposed to ~30.1% being statistically significant using the "naive stippling approach" ($p < \alpha_{global}$ where $\alpha_{global} = 0.05$).

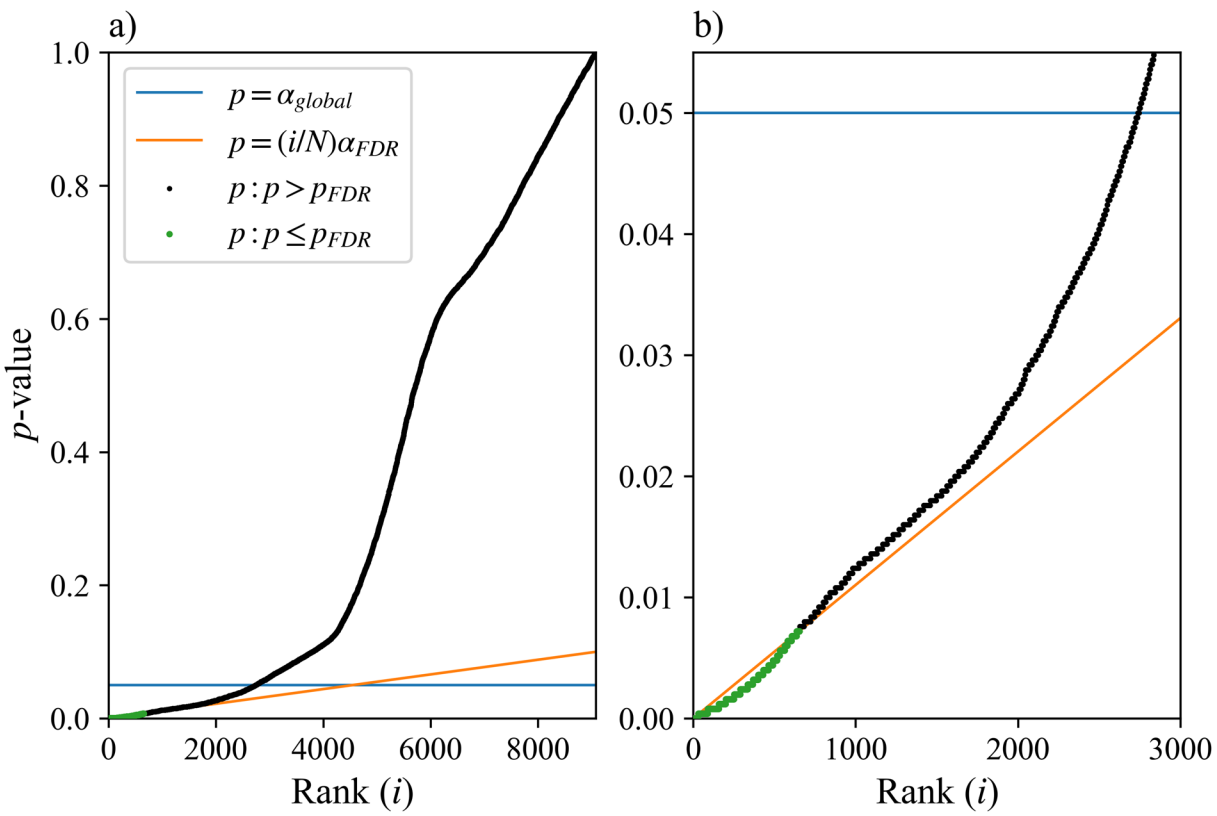

Figure 2.13: A collection of 9075 ranked *p*-values from the Monte Carlo testing of correlation coefficients between an ERE time series and ERA5 JJA-averaged 500-hPa geopotential heights on a geographic grid (results in section 5.2.5). (a) All *p*-values plotted as a function of their rank that were statistically significant (green) and not statistically significant (black) using the FDR approach with α_{FDR} = 0.1, yielding $p_{FDR} \sim 0.0072$. The blue line represents the global 95% confidence threshold ($\alpha_{global} = 0.05$) and the orange line represents the curve used to determine p_{FDR} (the maximum ranked *p*-value that is no higher than the orange curve). (b) As in (a) but zoomed in to the top 3000 ranked *p*-values for a more refined view.

We acknowledge that multiplying α by a factor of two may be too lenient for fields with less spatial autocorrelation. Nevertheless, the amount of significance was still drastically reduced for all analyses when compared to using the "naive stippling approach", thus accounting for a substantial amount of potentially overstated significance in the trends, composite differences, and correlations on spatial grids. Much of the significance at the 95% confidence level was eliminated when applying FDR correction, so significance at the 90% confidence level was also stippled in

the results. Another word of caution is that significance after FDR correction is sensitive to the distribution of the *p*-values, which may be sensitive to the geographical region being tested. The geographic footprint used for testing was kept consistent where appropriate and the bounds of the respective footprints are specified in the figure captions for the sake of reproducibility.

Chapter 3

20-Year Climatology of Short-Duration EREs

Previous studies have explored the climatology of extreme precipitation across the CONUS (chapter 1.1), including the seasonality of daily extreme rainfall and the diurnal cycle of hourly extreme rainfall. This chapter presents a 20-yr climatology of EREs based on the event object database described in section 2.1, including a breakdown of event types, intensities, and locations in section 3.1, seasonality in section 3.2, and the diurnal cycle of JJA EREs associated with nonlocalized convection in section 3.3. The key findings in relation to past studies will be briefly discussed in section 3.4.

3.1 Event Type Climatology

The algorithm described in section 2.1 identified a total of 9095 12-hr EREs exceeding the 10-yr ARI threshold from 2003–2022. A breakdown of the types of EREs based on the classification methods described in section 2.1.4 are presented in the first row of data in Table 3.1. TC- and stratiform-related[3] events accounted for the least number of events (4.0% and 5.0%, respectively), while MCS-related[4] events made up the largest portion of the dataset (43.5%). Filtering tropical cyclone, stratiform, and localized convection events out of the dataset left 6696 events, which is approximately 73.6% of the total. EREs associated with nonlocalized convection will be

[3] Events caused primarily by stratiform precipitation will simply be referred to as "stratiform-related" in this chapter (see section 2.1.4.2).

[4] Events referred to as "MCS-related" may include events associated with convection embedded within large synoptic scale features, especially outside of JJA (see section 2.1.4.4).

subsequently referred to as *filtered EREs*. For comparison purposes, the filtered EREs can be separated into MCS and non-MCS subclasses.

ARI (yr)	Total Count	% TC	% Stratiform	% Localized	% Non-MCS[5]	% MCS
10	9095	4.0	5.0	17.3	30.1	43.5
50	2714	6.7	1.8	11.3	25.7	54.4
100	1574	8.3	1.4	9.4	23.2	57.8
500	367	10.6	0.5	7.6	18.8	62.4
1000	198	13.1	0.5	7.1	19.7	59.6

Table 3.1: 2003–2022 total ERE counts exceeding each ARI threshold and percentages of each event classification that make up the total count.

Counts and proportions of the short-duration EREs that exceeded higher ARI thresholds (i.e., 50-, 100-, 500-, and 1000-yr events) with respect to event type are presented in Tables 3.1 and 3.2. Referring to Table 3.2, stratiform events were the least likely to exceed higher thresholds. Although TC-related EREs were the least common, they were also the most likely event class to exceed higher ARI thresholds, with about half of them exceeding the 50-yr ARI threshold and about 7% of them being 1000-yr events (Table 3.2). Previous studies agree that tropical cyclones often produce the most widespread and destructive EREs (e.g., Ashley and Ashley, 2008; Schumacher and Johnson, 2006). MCS-related events were the second most likely to be intense with ~37% exceeding the 50-yr ARI threshold and ~3% exceeding the 1000-yr ARI threshold (Table 3.2). Since MCSs were the most common event class, Table 3.1 emphasizes the importance of studying extreme-rain-producing MCSs, since a majority of all higher-end events (50-yr ARI or greater) resulted from MCSs (e.g., about 60% of 1000-yr events). This result supports previous

[5] Referring to *filtered* EREs that were not classified as MCS-related.

findings that the majority of 24-hr EREs with a 50-yr ARI are associated with MCSs (Schumacher and Johnson, 2006; Stevenson and Schumacher, 2014).

Class	10-yr count	% 50-yr	% 100-yr	% 500-yr	% 1000-yr
TC	365	50.1	35.6	10.7	7.1
Stratiform	457	10.7	4.8	0.4	0.2
Localized	1577	19.5	9.4	1.8	0.9
Non-MCS	2740	25.5	13.3	2.5	1.4
MCS	3956	37.3	23.0	5.8	3.0
All	9095	29.8	17.3	4.0	2.2

Table 3.2: 2003–2022 total ERE counts by classification with percentages of which exceeding the 50-, 100-, 500-, and 1000-yr ARI thresholds.

As expected, TC-related EREs were most common over the southeastern CONUS (Fig. 3.1a), where tropical cyclones often make landfall and bring devastating freshwater flooding to inland areas. EREs related to stratiform precipitation were most common over the Northeast, Midwest, and Northern Great Plains (Fig. 3.1b), likely from precipitation associated with extratropical cyclones over areas with relatively lower thresholds. EREs resulting from localized convection were most common over the Southern and Central High Plains (Fig. 3.1c), where isolated slow-moving afternoon convection often occurred during the summer over areas with generally lower ARI thresholds (Fig. 2.1a). Other hot spots for EREs associated with localized convection include the Southern Appalachians, where orographic influences likely play a role in producing more isolated intense rainfall (e.g., Smith et al., 2011), and South Florida, where afternoon air mass thunderstorms are common during the warm season, often associated with sea breeze circulations. MCS related events were more evenly distributed throughout the domain, with the most notable

relative maxima around portions of the Gulf Coast and over eastern portions of the Central Great Plains (Fig. 3.1d).

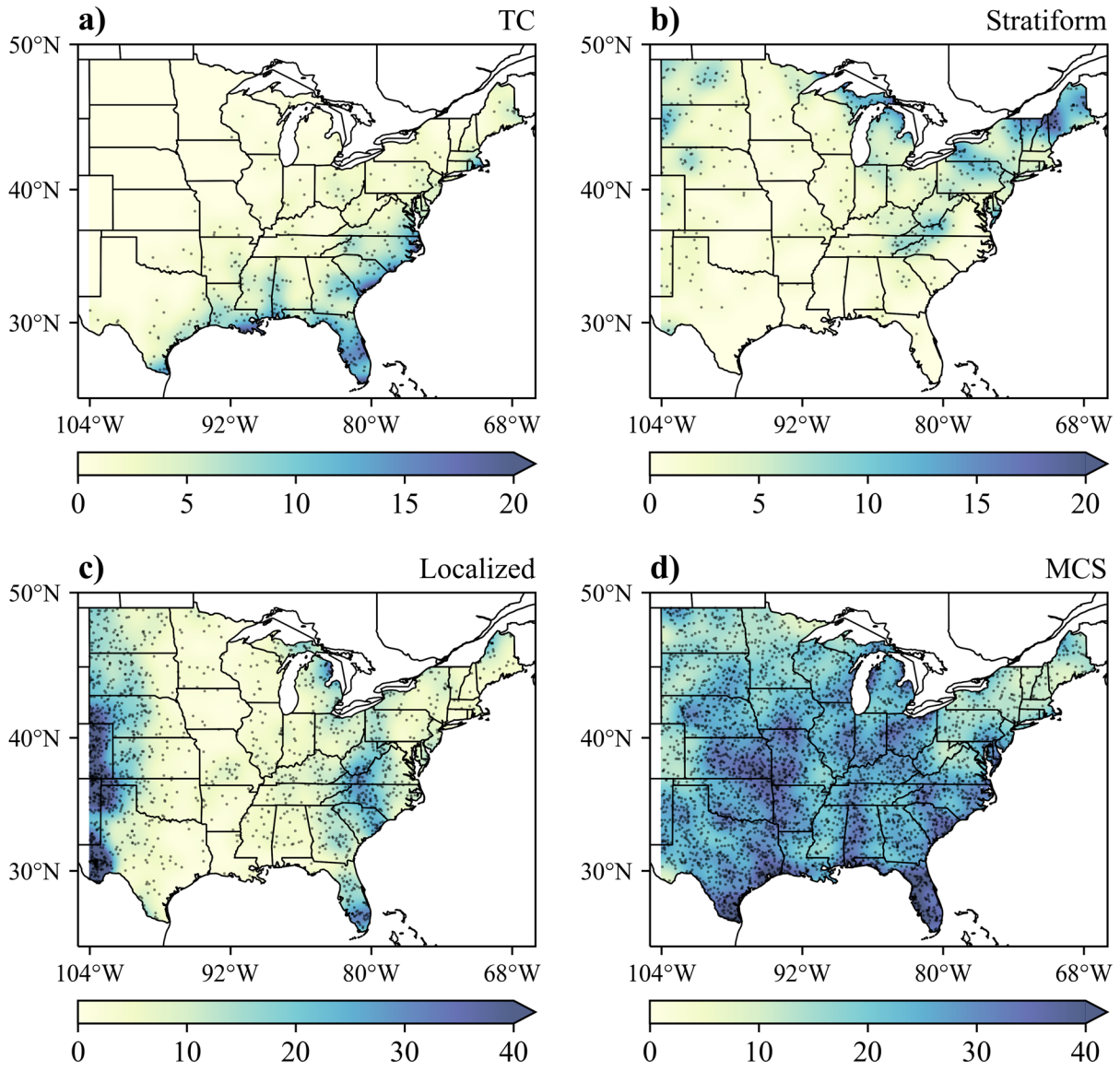

Figure 3.1: All 2003–2022 ERE points of maximum exceedance (translucent black dots) associated with (a) tropical cyclones, (b) primarily stratiform precipitation, (c) only localized convection, and (d) MCSs, with Gaussian smoothed ($\sigma = 0.5°$) neighborhood event counts (radius = 100 km) (color fill), scaled up at the domain edges based on the inverse fraction of valid domain area within the radius.

3.2 Seasonal Climatology

Consistent with previous studies, a JJA peak is evident for all classes of convective EREs (i.e., localized and filtered; Fig. 3.2). In contrast, TC-related EREs exhibit a peak in September and stratiform-related EREs have peaks in both May and September with a relative minimum during the summer. The peak in the overall frequency of EREs during JJA is expected due to the climatological maximum in convective activity over the central and eastern CONUS as discussed in section 1.1. Among filtered EREs, MCS event counts show a broader peak over the warm season than non-MCS events, with MCS events being much more common outside of JJA than non-MCS events. This variation in seasonality is likely due to stronger synoptic scale forcing mechanisms from the jet stream driving larger convective systems during the cool season. Since this study is motivated by convective EREs, the analysis focuses only on JJA, when about 60.1% of the total filtered EREs occurred, leaving a sample of 4024 events for the analysis. All JJA filtered ERE locations are plotted over the 10-yr ARI thresholds in Fig. 3.3.

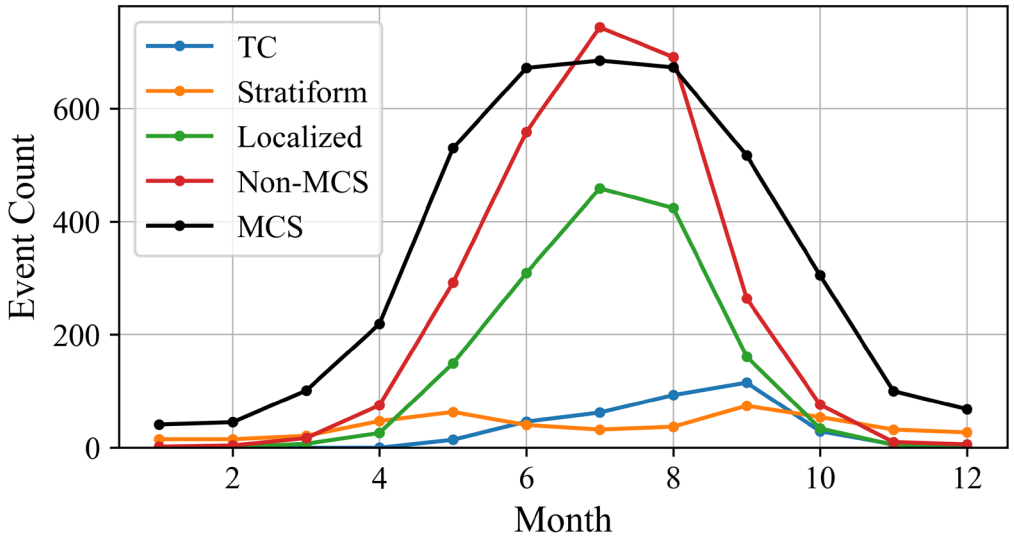

Figure 3.2: 2003–2022 event counts per month for events associated with tropical cyclones (blue), primarily stratiform precipitation (orange), only localized convection (green), and for filtered EREs that were *not* classified as MCS-related (red) and *were* classified as MCS-related (black).

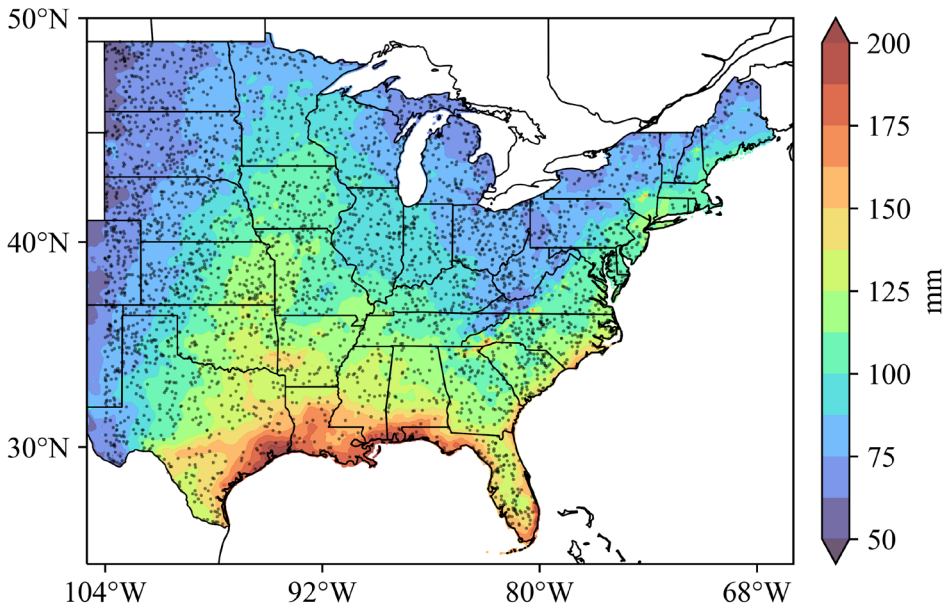

Figure 3.3: 10-yr ARI 12-hr precipitation frequency estimates from NOAA Atlas 14 (color fill; mm) and the locations of all 2003–2022 JJA filtered EREs (4024 events) at their respective points of maximum exceedance (translucent black dots).

The least number of events (~2.5%) occurred during the winter months (December–February), with most of the filtered EREs confined to the central Gulf Coast states (Fig. 3.4a). In the spring (March–May), ~18.4% of the filtered EREs occurred, with activity expanding north and west, especially into the Southern and Central Great Plains (Fig. 3.4b). During JJA, the EREs are most frequent and are focused farther north (Fig. 3.4c). The highest JJA event densities occur over the Central and Northern Great Plains, Mid-Mississippi Valley, Ohio Valley, and the Carolinas, with relatively lower event counts over the northern Gulf Coast states, where the ARI thresholds are the highest (Fig. 3.3). During the fall (SON), event counts are similar to springtime (~19.0%), with events more evenly distributed throughout the domain than any other season (Fig. 3.4d).

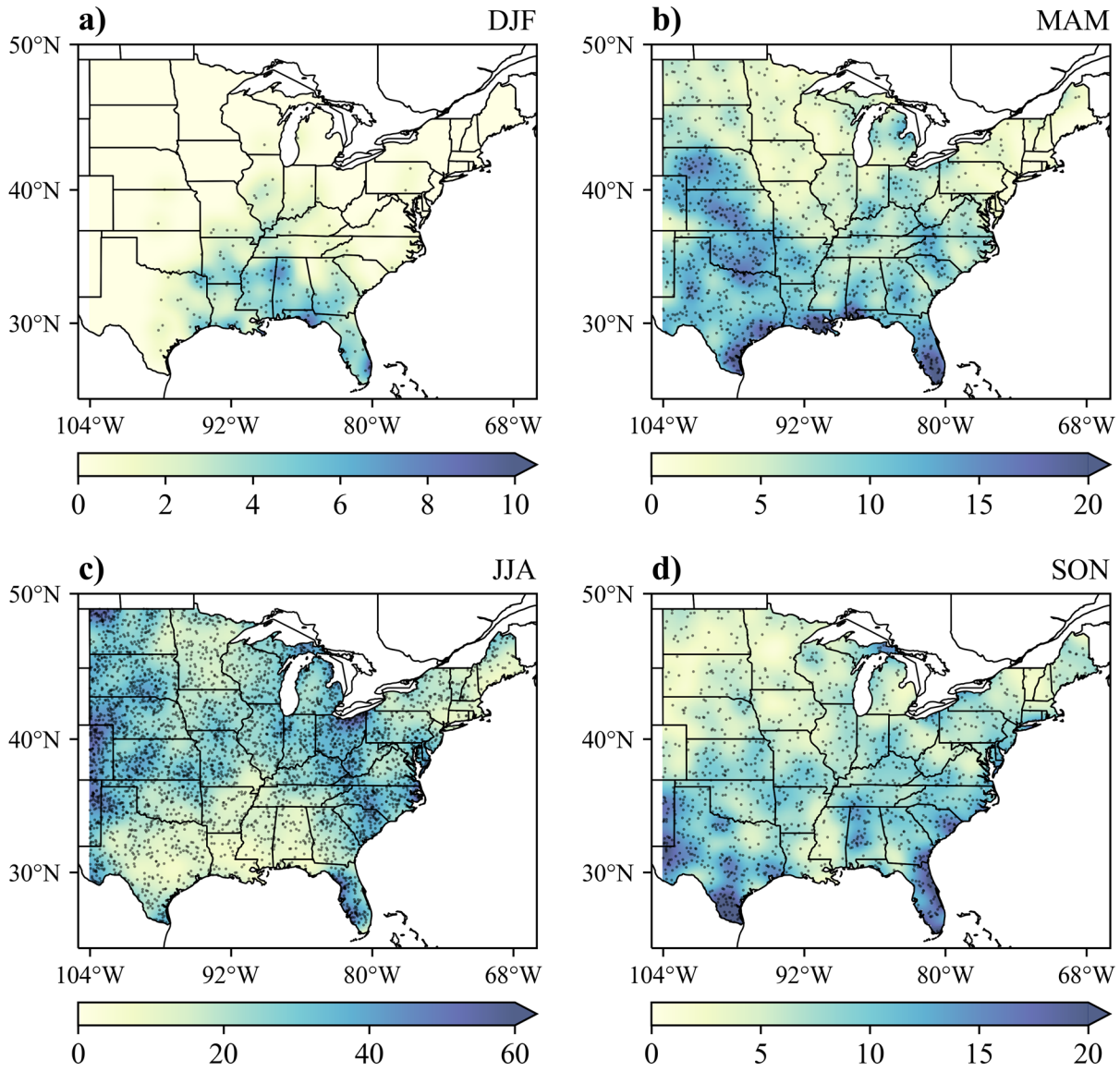

Figure 3.4: As in Fig. 3.1, but for 2003–2022 filtered EREs occurring during (a) December–February (DJF), (b) March–May (MAM), (c) June–August (JJA), and (d) September–November (SON).

While a 10-yr ERE can only be expected once every 10 years at a single location, the events are remarkably common during the summer when considering the entire central and eastern CONUS. In fact, an average of approximately 79 out of the 92 days in JJA (~86%) contained at

least one 10-yr ERE somewhere in the domain according to our 20-yr database, even with the Stage IV data likely underestimating precipitation over many areas (section 2.1.2).

Instead of characterizing each event as one point on a map, it can be more informative to plot all exceedance points for each event. Summing all accumulated precipitation above the 10-yr ARI threshold from all filtered EREs in the respective subset (e.g., Fig. 3.5) reveals several characteristics of the EREs, with the larger and more intense events being more distinguishable (black streaks where exceedance ≥100 mm above the 10-yr ARI threshold in Fig. 3.5). Despite high event densities over the Carolinas and Florida during the summer (Fig. 3.4c), Fig. 3.5c reveals that most of those events had very few exceedance points or occurred over localized areas, making those events nearly indiscernible. Widespread and intense EREs were most numerous during JJA along an axis from Texas to the Ohio Valley and Midwest and commonly had a northwest–southeast (NW–SE) orientation (Fig. 3.5c), unlike other seasons, where the exceedance swaths typically had more of a southwest–northeast orientation (Fig. 3.5a–b, d). This orientation is likely associated with the differences in large-scale flow patterns and perhaps the structure of convective systems during the summer. The environments associated with these NW–SE oriented EREs are examined in chapter 6 through case study composite analyses.

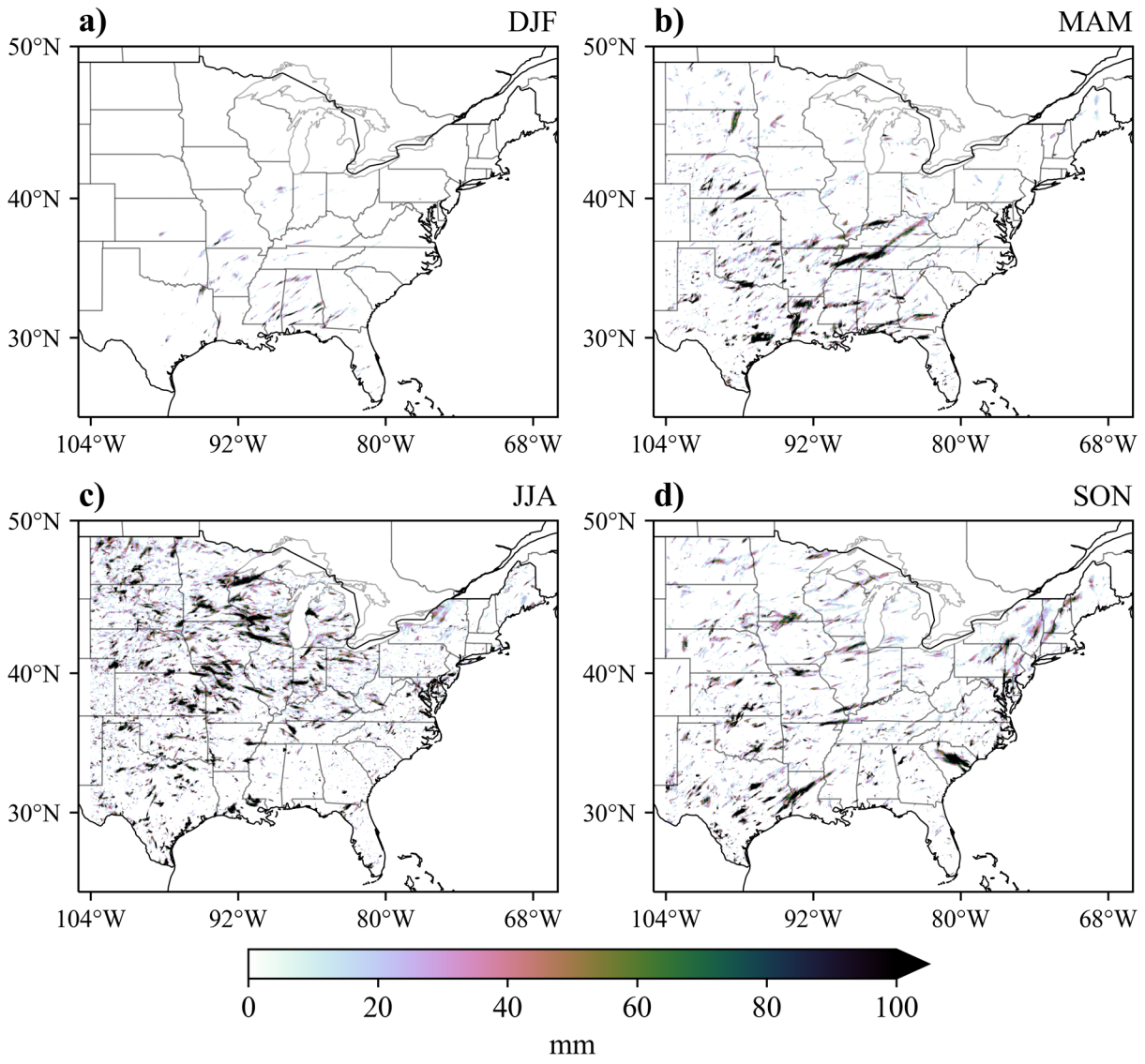

Figure 3.5: Total precipitation exceeding the 10-yr ARI threshold (mm) from all 2003–2022 filtered EREs during (a) December–February (DJF), (b) March–May (MAM), (c) June–August (JJA), and (d) September–November (SON).

JJA MCS-related EREs were most common over portions of the central CONUS (Fig. 3.6a), with the majority of JJA filtered EREs resulting from MCSs over that region (Fig. 3.6b). The area where MCS-related EREs were most common is similar to previous climatology studies on MCSs (e.g., Haberlie and Ashley, 2019; Fig. 1.1b), with a maximum in MCS precipitation occurring

between Oklahoma and Iowa. However, according to Fig. 3.6b, MCS-related JJA EREs account for over 80% of the filtered JJA EREs in some areas (e.g., northern Missouri), while total MCS rainfall contributes comparatively less (about 60%) of the overall May–August precipitation over those same areas according to Haberlie and Ashley (2019) (Fig. 1.1e). For analysis purposes, a subdomain over the central CONUS was selected to encompass the most climatologically active areas for MCS-related EREs (100–82°W, 34–46°N; Fig. 3.6). The sample size of JJA filtered EREs within the subdomain is 1656 events, with approximately 59% of them being classified as MCS-related. One other observation of note is the relative lack of MCS-related EREs over the High Plains, which is related to the relatively small-scale nature of convection commonly observed over that region.

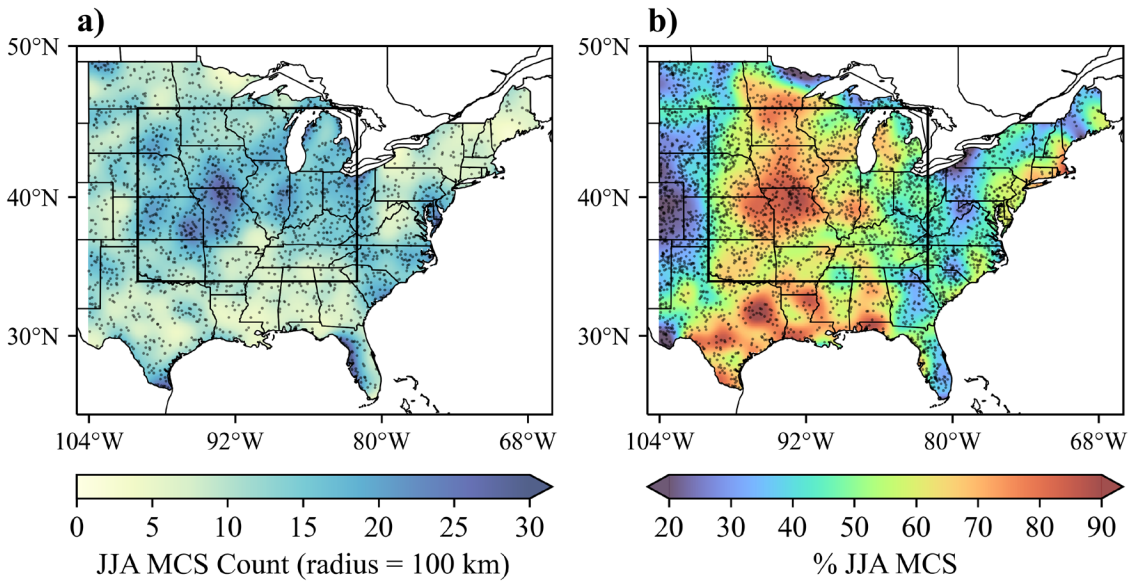

Figure 3.6: (a) All JJA MCS-related ERE points of maximum exceedance (translucent black dots) with Gaussian smoothed (σ = 0.5°) neighborhood (radius = 100 km) event count (color fill), scaled up at the domain edges based on the inverse fraction of valid domain area within the radius. (b) All JJA filtered ERE points of maximum exceedance (translucent black dots) with Gaussian smoothed (σ = 0.5°) neighborhood (radius = 100 km) event count proportion of the total filtered JJA EREs that were classified as MCS-related (color fill; %). The black box is the central CONUS domain (100–82°W, 34–46°N).

3.3 JJA Diurnal Cycle

Past studies that examined the diurnal cycle of extreme rainfall have only considered 1-hr extremes (e.g., Hitchens et al., 2013; Schumacher and Johnson, 2006; Stevenson and Schumacher, 2014), which can occur even with short-lived intense convection that does not produce substantial precipitation accumulations over large areas or last for several hours. This section will present the findings of the diurnal variations in EREs occurring over 12-hr timescales, focusing on the JJA filtered EREs.

When examining the full sample of 4024 JJA filtered EREs, the climatological minimum in ERE peak intensity times was generally during the late morning and early afternoon (1500–1800 UTC). The climatological maximum was between 2200 and 0100 UTC (Fig. 3.7a), which is during the early evening hours until around sunset throughout the domain during the summer. The peak end time of the 12-hr accumulation periods associated with the JJA filtered EREs was well into the night (0700–1000 UTC). The peak time of event onset was only about 1 hour before the peak in maximum intensity (2100–0000 UTC). This timing suggests that the heaviest precipitation often occurs relatively early in an event's lifetime, with a gradual trailing-off of precipitation intensities over time. Given this result, it is important to consider the entire period of an event to determine if there was a sufficient nocturnal component before or after the peak accumulation hour for the event to be classified as nocturnal. Therefore, if at least half of the accumulation period was at night, the event was classified as nocturnal, even if the peak accumulation hour was during daylight hours (section 2.1.4.5).

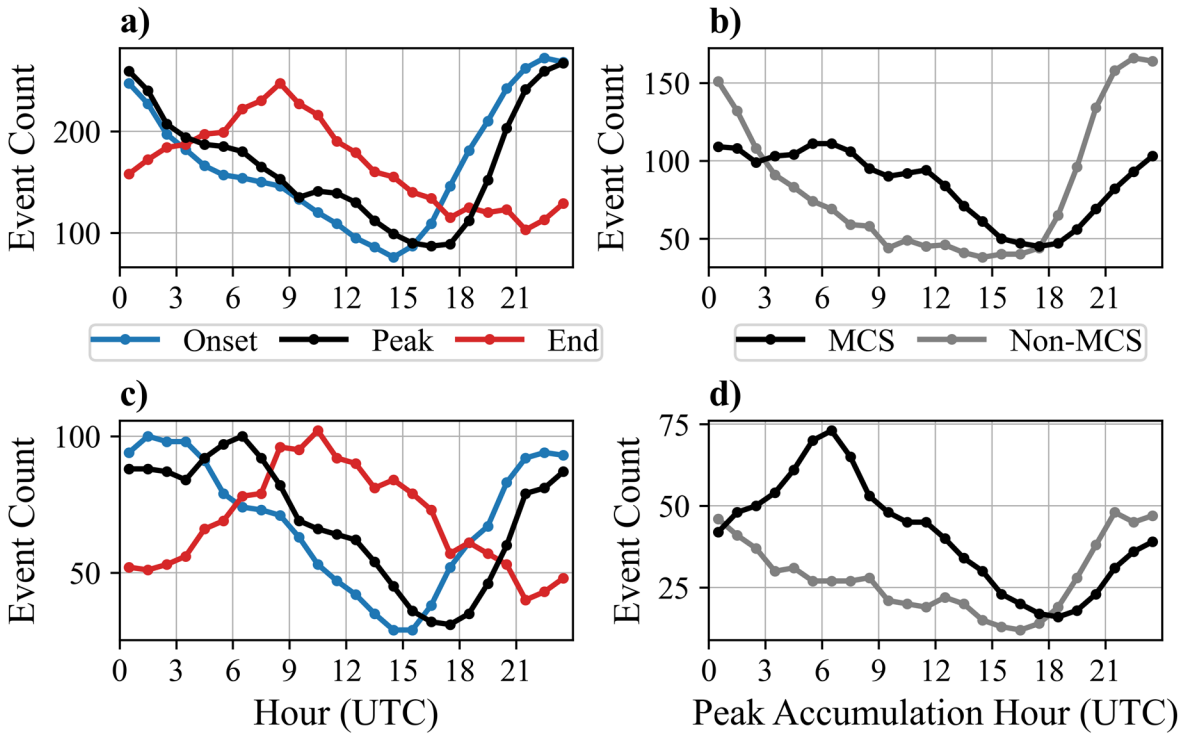

Figure 3.7: 3-hr running mean ERE count (2003–2022) for (a,b) JJA filtered EREs within the full domain and (c,d) JJA filtered EREs within the central CONUS subdomain. Blue, black, and red lines in (a) and (c) represent the onset hour (first hour with accumulation ≥1 mm), peak accumulation hour, and end of the accumulation period at the points of maximum exceedance, respectively. Black and grey lines in (b) and (d) represent MCS- and non-MCS-related JJA filtered EREs, respectively.

The 2200–0100 UTC peak in event times found in Fig. 3.7a is inconsistent with the peak in 1-hr EREs found by Stevenson and Schumacher (2014) which was approximately 0400–0600 UTC (Fig. 1.3). However, for MCS-related events only, the climatological peak is broader and includes hours well into the night (Fig. 3.7b) with the actual peak in MCS event intensities between 0400 and 0700 UTC. Thus, MCS-related EREs during JJA tend to peak later at night. The fraction of JJA filtered EREs that are MCS-related shows a clear maximum during the late night and morning hours (Fig. 3.8) with greater than 60% being classified as MCS-related between 0600 and 1500 UTC (0100–1100 local time).

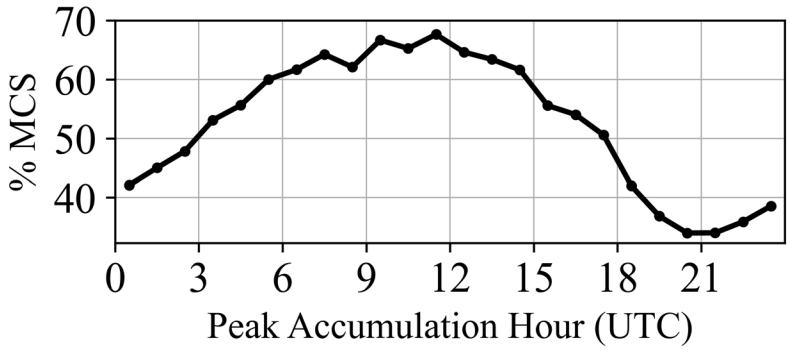

Figure 3.8: Percentage of the 3-hr running mean JJA filtered ERE counts that are classified as MCS-related, derived from Fig. 3.7b.

Isolating the central CONUS subdomain reveals a true nocturnal maximum in ERE frequency, with a clear peak between 0400 and 0700 UTC (Fig. 3.7c), which is significantly amplified when considering only MCS events (Fig. 3.7d). This timing aligns with numerous past studies (e.g., Easterling and Robinson, 1985; Wallace, 1975), confirming that the nocturnal maximum in warm season precipitation over that region is consistent with the timing of the nocturnal maximum in short-duration EREs.

Plotting the JJA filtered EREs that were classified as nocturnal in terms of event points (Fig. 3.9a–b) and exceedance values (Fig. 3.10a) reveals that nocturnal events dominated over the central CONUS region, especially over northwestern Missouri and vicinity, where around 90% of the filtered JJA EREs were nocturnal. Nocturnal JJA MCS-related EREs were more confined to the central CONUS subdomain with a maximum over the same region, where over 70% of JJA filtered EREs were nocturnal MCS-related (Fig. 3.9c–d). This result is consistent with Haberlie and Ashley (2019) (Fig. 1.2a), and the same area also saw the most precipitation during the Plains Elevated Convection at Night field campaign in 2015 (Geerts et al., 2017; Weckwerth and Romatschke, 2019).

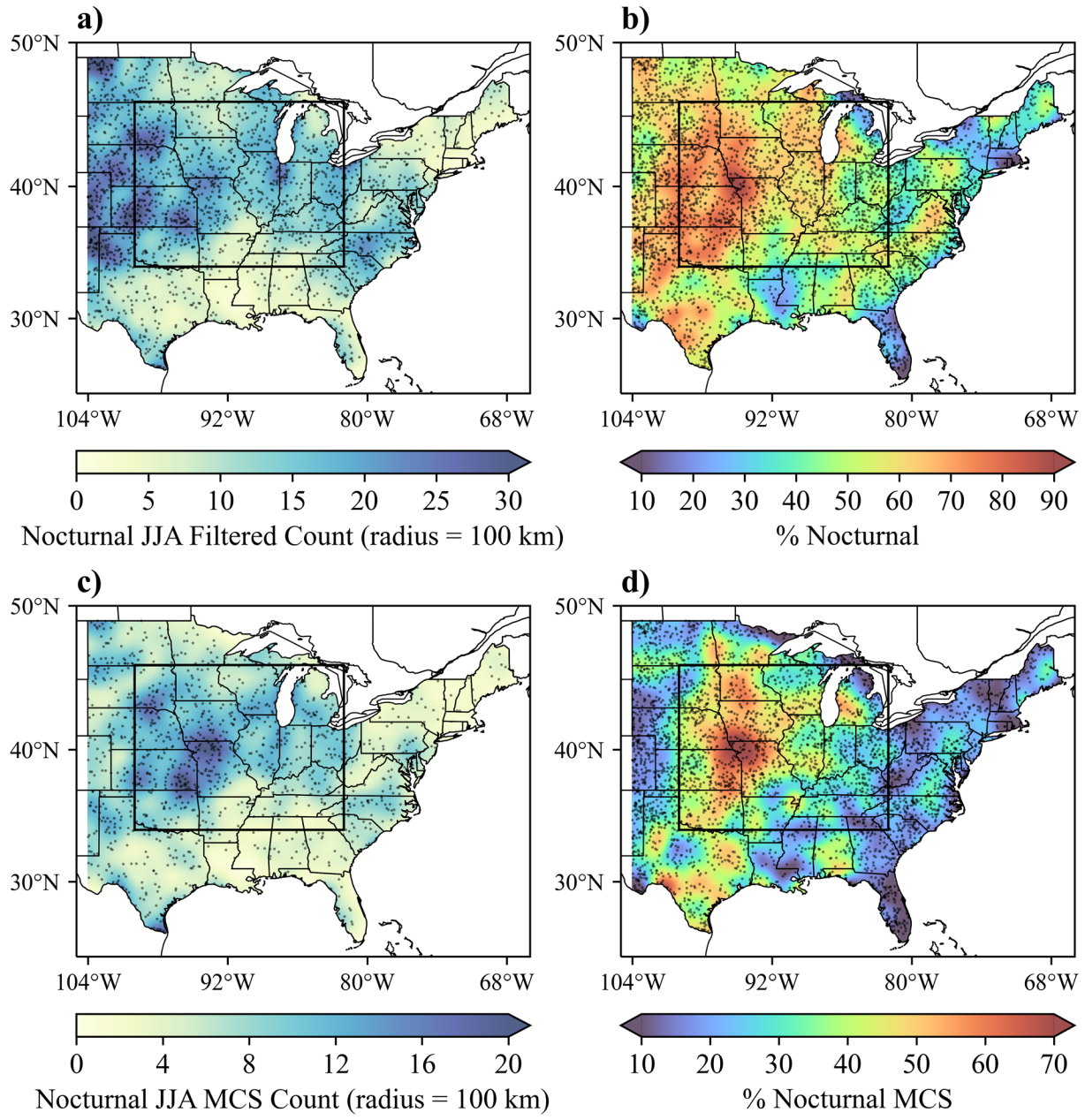

Figure 3.9: As in Fig. 3.6, but for (a,b) nocturnal JJA filtered EREs and (c,d) nocturnal JJA MCS-related EREs.

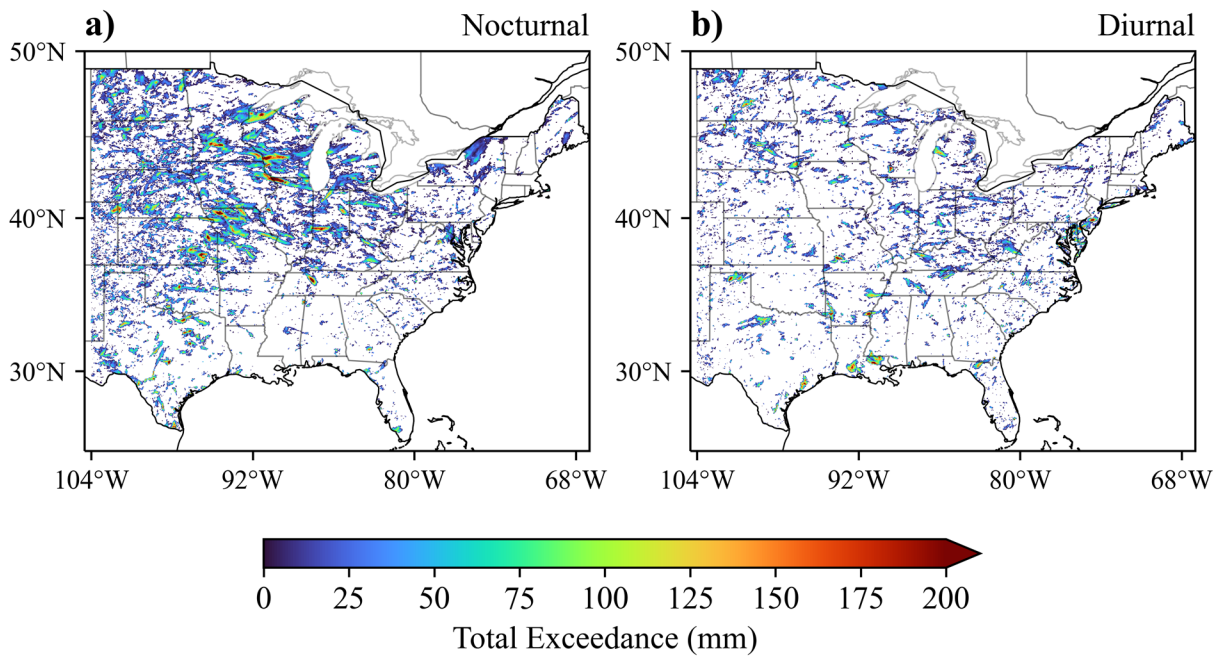

Figure 3.10: Map of total precipitation exceeding the 10-yr ARI threshold from all JJA filtered EREs classified as (a) nocturnal and (b) diurnal from 2003–2022.

Over the full domain, a little over half (~54%) of the filtered JJA EREs were classified as nocturnal, and ~60% within the central CONUS subdomain. However, event counts alone do not account for the relative magnitude nor spatial extent of the associated extreme rainfall, as it is evident that the nocturnal events (Fig. 3.10a) were often larger and more intense than diurnal events (Fig. 3.10b), especially over the central CONUS. In fact, nocturnal filtered EREs contributed to ~69% of the total extreme precipitation exceeding the 10-yr ARI threshold over the full domain, and ~78% over the central CONUS subdomain.

Regarding the areal coverage of extreme rainfall, the larger EREs (i.e., having more exceedance points) were often nocturnal events, with, for example, approximately 77% of events having at least 300 exceedance points (extreme rainfall covering ≥4,800 km^2) being classified as nocturnal (Table 3.3). Overall, the median number of exceedance points among the nocturnal JJA

filtered EREs is 12 (192 km^2), while for diurnal events it is only 5 (80 km^2). In other words, on average, nocturnal EREs were over double the size of diurnal EREs, which is an indication of more MCS versus non-MCS events. Referring to Table 3.4, events related to nocturnal MCSs were also the most likely to exceed higher ARI thresholds when compared to all JJA filtered EREs, with about 4% of nocturnal MCSs exceeding the 1000-yr ARI threshold, as opposed to 2.5% of all JJA filtered EREs. These findings serve as additional evidence that nocturnal MCSs are the most prevalent producers of extreme rainfall in the central and eastern CONUS during JJA.

Exceedance Point Count	JJA Filtered ERE Count	% Nocturnal
[1, 5)	1515	42.6
[5, 25)	1399	55.3
[25, 100)	772	63.9
[100, 300)	263	72.6
≥300	75	77.3
All Filtered	4024	53.7

Table 3.3: 2003–2022 total JJA filtered ERE counts and percentages of which that were classified as nocturnal within different exceedance point count (i.e., size) range bins, listed in interval notation up to 300.

JJA Event Type	10-yr count	% 50-yr	% 100-yr	% 500-yr	% 1000-yr
All Filtered	4024	33.0	19.4	4.5	2.5
MCS	2030	40.5	25.5	6.7	3.6
Nocturnal	2162	37.9	22.8	5.9	3.1
Nocturnal MCS	1206	44.2	28.6	8.0	4.0

Table 3.4: 2003–2022 total JJA filtered ERE counts by type with percentages that exceed 50-, 100-, 500-, and 1000-yr ARI thresholds.

3.4 Discussion

This chapter presented a 20-yr survey of EREs, having double the period of record used in the Stevenson and Schumacher (2014) study. Despite using different methods of classifying EREs, the result that MCSs produced the largest proportion of EREs and the majority of EREs exceeding 50-yr ARIs (Table 3.1) is consistent with previous studies (e.g., Schumacher and Johnson, 2006; Stevenson and Schumacher, 2014). Also consistent with previous studies, convective EREs showed a strong annual peak in JJA (Fig. 3.2) and JJA EREs associated with MCSs were found to peak in intensity most often during the nighttime hours (Fig. 3.7). We also found EREs associated with nonlocalized convection to be focused more over the north-central CONUS during the summer than other seasons, where the thresholds for defining extremes are generally lower (Figs. 3.3 and 3.4).

As has been suggested in prior studies (e.g., Maddox et al., 1979; Stevenson and Schumacher, 2014), our results provide new visual and quantitative evidence that nocturnal MCSs are the most prolific producers of extreme rainfall during the summer. For example, among all JJA filtered EREs, those that were classified as nocturnal contributed to nearly 70% of the total extreme rainfall volume over the domain, and produced extreme rainfall, on average, over double the geographical area of the diurnal events (Fig. 3.10). Nocturnal JJA MCS-related EREs were most common over eastern portions of the Central Great Plains, focused on eastern Kansas and northwestern Missouri (Fig. 3.9c–d) which is in line with previous observational studies (e.g., Haberlie and Ashley, 2019; Weckwerth and Romatschke, 2019). Prior research has established that a major short-coming of weather and climate models is the accurate representation of elevated nocturnal convection and propagating nocturnal MCSs that occur over land masses (e.g., Bechtold et al., 2014, 2020; Becker et al., 2021; Geerts et al., 2017; Tang et al., 2021). Thus, our results further motivate the need to

improve the depiction of nocturnal convection over continental locations in weather and climate models.

This need is furthered by the localized and complex nature of the extreme rainfall associated with convection revealed in the maps of exceedance above the chosen 10-yr ARI threshold (e.g., Figs. 3.5 and 3.10). Even the most intense swaths of extreme rainfall only had widths ranging from 20–40 km. The fine detail of the extreme rainfall captured in the Stage IV analyses demonstrates the importance of using high resolution gridded rainfall data for observational studies of EREs. The relatively small scale over which most of the EREs occur also raises a challenge for predicting the location and timing of EREs from convection. This challenge applies to forecasters as well as weather and climate models. Models with lower spatial resolutions, especially those that utilize convective parameterization schemes, are unable to resolve these convective EREs. Thus, the high resolution convection allowing models, which have greater skill in representing the diurnal cycle of rainfall (e.g., Ban et al., 2014), are necessary for the accurate representation of extreme-rain-producing convection (e.g., Fritsch and Carbone, 2004).

The climatology presented in this chapter provides critical insights into the nature and behavior of EREs, with a focus on those that are the most destructive and can have major impacts on society. While this chapter examines the nature of events over the entire 20-yr period, the next chapter will explore any observed changes in the EREs throughout the period.

Chapter 4

Interannual Variability & Trends

Extensive research has been conducted on the changes in rainfall associated with global climate change (section 1.4) with numerous studies documenting or predicting an increase in extreme events. While the period of record used in our study spans only 20 years, how the frequency and intensity of EREs changed from year to year and if there were any statistically significant trends in their frequency or characteristics through the period are questions of scientific and practical importance to society and the environment. From the database of EREs described in section 2.1, the time series of the total number of events per year that satisfied specific conditions (e.g., classification, season, time of day, and region) were obtained. The time series data provide information on the interannual variability and potential trends in the EREs through the 20-yr period (2003–2022). However, in addition to a relatively short sample period, the caveats regarding the Stage IV dataset (discussed at the end of section 2.1.1) suggest that the results in this chapter should be interpreted with some caution.

Annual event counts for separate classifications of EREs over the full domain will be presented in section 4.1. Seasonal trends in EREs are examined in section 4.2. The JJA filtered ERE time series, including counts of higher-end EREs and time series of different metrics of the EREs are presented in section 4.3. Changes in JJA filtered EREs are examined with respect to (1) the diurnal cycle in section 4.4, (2) storm size and duration in section 4.5, and (3) geographical subregion within the domain in section 4.6. The key findings will be discussed in relation to previous literature in section 4.7, along with a brief discussion of the caveats that may impact the interpretation of the results.

4.1 Annual Time Series for All ERE Types

The time series of overall annual ERE counts (Fig. 4.1a) exhibits no statistically significant trend ($\tau_K \sim 0.18$; $p_{MK} > 0.05$) due to a lack of consistent trends among different temporal subdivisions of the time series. This result of no significant overall trend is inconsistent with previous studies examining long-term trends in EREs over the CONUS. For example, 2-day precipitation exceeding the 99th percentile using rain gauge measurements from 1957–2010 exhibited a significant increasing trend over the CONUS as a whole ($\tau_K \sim 0.34$; $p_{MK} < 0.01$) (Kunkel et al., 2013a). However, comparison of these previous results with our results should be interpreted with caution due to the different datasets, methods of defining EREs, and periods of record. Nevertheless, our approach of dividing the database of EREs into subsets and examining their trends through the period of study can provide new insights into what specific types of EREs may be changing given the increase found in some studies.

Dividing the annual ERE count time series into their four main classes (defined in section 2.1.4) revealed varying results. TC-related EREs had no trend through the period (Fig. 4.1b) and exhibited the greatest amount of variability compared to other types with the number of events ranging from 0 in 2009 to 42 events in 2020. The coefficient of variation (*CV*), calculated as the ratio between the standard deviation and the mean of the time series, was used as a relative measure of overall variability in each time series. The TC-related ERE count timeseries has an exceptionally high *CV* of ~67.3% indicating a large degree of interannual variability.

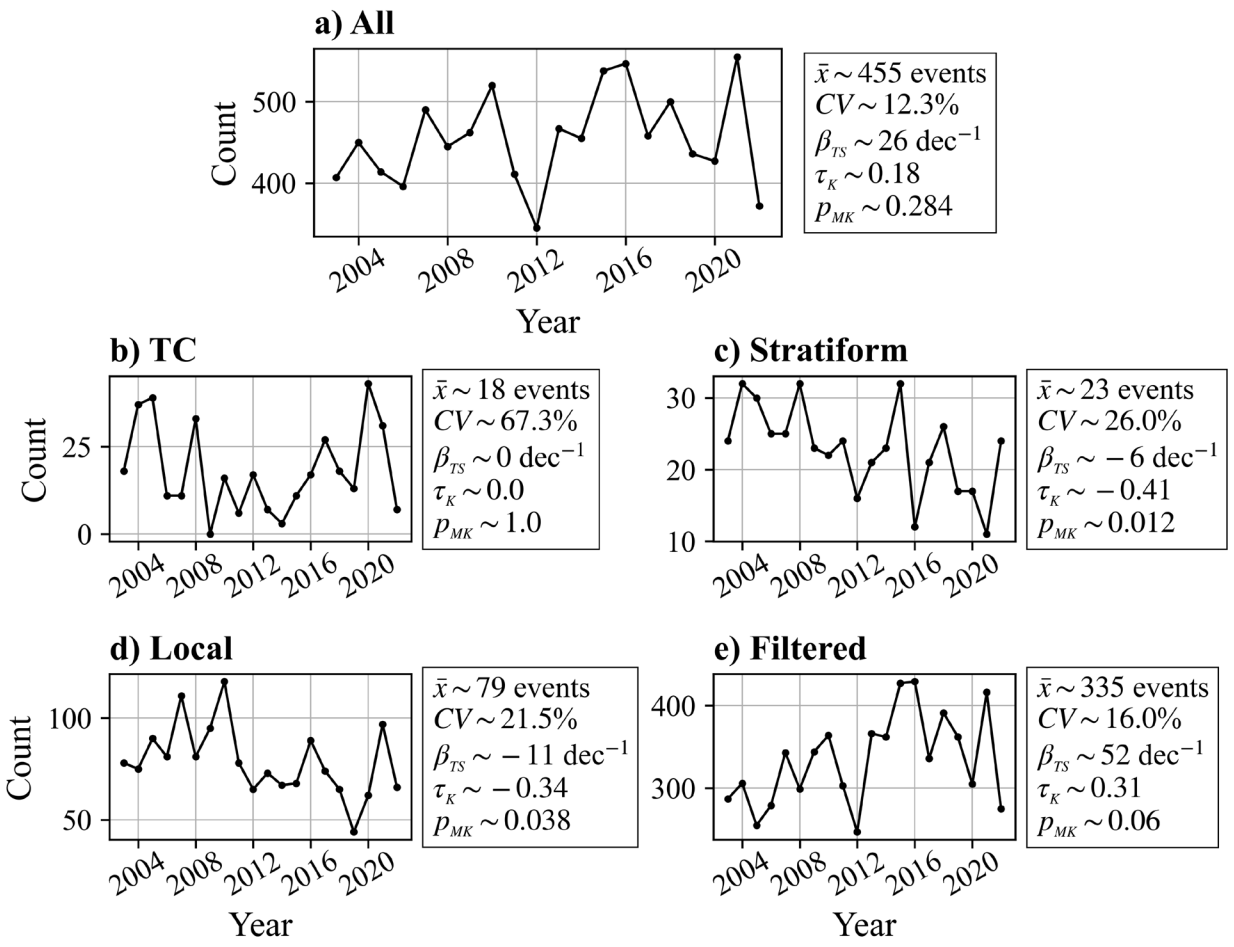

Figure 4.1: Annual ERE count time series for (a) all QC-passed events, (b) TC-related events, (c) primarily-stratiform-related events, (d) localized convection events, and (e) filtered events. Statistics, including sample mean ($\bar{x}$), coefficient of variation (CV), Theil–Sen slope (β_{TS}; events decade^{-1}), Kendall's τ (τ_K), and the p-value from Mann–Kendall trend tests (p_{MK}) are listed to the right of each time series. The average percent increase according to the β_{TS} of each time series is (a) 5.7, (b) 0, (c) –20.4, (d) –13.9, and (e) 15.5% decade^{-1}.

EREs from primarily stratiform precipitation (Fig. 4.1c) and from localized convection (Fig. 4.1d) both exhibited statistically significant *decreasing* trends at the 95% confidence level ($p_{MK} < 0.05$). While the annual average number of localized convection EREs is over three times greater than the primarily-stratiform-related EREs, the trend in the latter ($\tau_K \sim -0.41$) is slightly more confident than the former ($\tau_K \sim -0.34$), despite slightly more variability. The relative magnitude of

the trends can also be expressed by the average percent increase according to the Theil–Sen's slopes ($\beta_{TS} / \bar{x} \times 100\%$). The primarily-stratiform-related events had a greater relative decrease than the localized convection events (–20.4 vs. –13.9% decade^{-1}, respectively)

The last subset is the filtered EREs (Fig. 4.1e), which is left with a substantial increasing trend ($\beta_{TS} \sim 52$ events decade^{-1}). Compared to the time series of total unfiltered EREs with an average percent increase of 5.7% decade^{-1}, the filtered ERE time series has a relatively larger increase of 15.5% decade^{-1}. Although these trends are not significant at the 95% confidence level, the results suggest that any significant increasing trends in EREs would likely be related to the filtered EREs (i.e., EREs from non-localized convection), which will be the focus for the remainder of this thesis.

4.2 Seasonal Trends in EREs

Climatologically, EREs show a strong seasonal cycle (section 3.2), with the peak in event counts occurring during JJA (5526 total events and 4024 filtered events; Fig. 4.2a). When performing a Mann–Kendall trend test on each 3-month running count time series (2003–2022), statistically significant ($p_{MK} < 0.05$) trends become evident during specific times of the year. Positive trends are maximized during the summer months according to the Theil–Sen's slope values displayed in Fig. 4.2b and Kendall's τ coefficients in Fig. 4.2c, with the peak values appearing in JJA. The positive trends among the filtered EREs during much of the warm season (May–July through August–October) are statistically significant, as shown by *p*-values of less than 0.05 displayed in Fig. 4.2d. Unfiltered EREs, on the other hand, had lower trends than filtered EREs over all months, as explained by the decreasing trends in primarily stratiform-related and localized convection EREs (section 4.1). Thus, the *p*-values associated with positive trends are much larger for unfiltered EREs, indicating a lack of statistical significance.

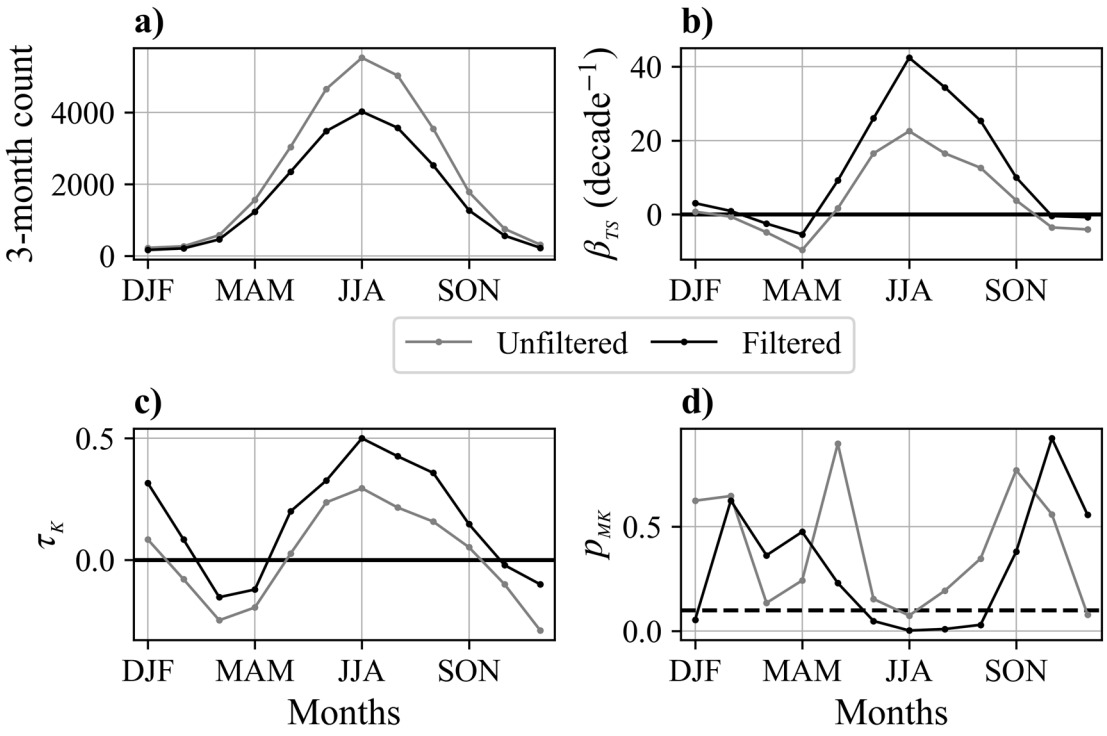

Figure 4.2: Centered at each month of the year, (a) the total 3-month running 20-yr (2003–2022) ERE count, and for the 20-yr time series of each 3-month running sum: (b) Theil–Sen slope (events decade^{-1}), (c) Kendall's τ, and (d) Mann–Kendall trend test p-values. Values are shown for all unfiltered 10-yr EREs (grey) and filtered EREs (black). The black horizontal line in (b) and (c) at zero is to help distinguish between positive and negative values. The dashed black line in (d) represents $p_{MK} = 0.05$, with any values below the line indicating statistical significance at the 95% confidence level. Months are abbreviated by their first letters (e.g., DJF represents December–February).

Contrary to previous studies (e.g., Feng et al., 2016), our results show a lack of any increasing trend in EREs during the spring months, with March–May events actually showing a slight *decreasing* trend for both filtered and unfiltered EREs (Fig. 4.2b–c). However, this decreasing trend is not statistically significant (Fig. 4.2d). Feng et al. (2016) used April–June, which did have an increasing trend in filtered EREs according to our dataset, but again, the trend was not statistically significant. However, it is difficult to compare results among different observational studies due to the differences in data, methodology, and period of record.

The significant increasing trend found particularly among the JJA filtered EREs is intriguing and could have important implications for society. Therefore, the remainder of the thesis will focus exclusively on the JJA filtered EREs.

4.3 JJA Filtered ERE Timeseries

The time series of the annual JJA filtered ERE count (Fig. 4.3a) reveals substantial variability in the number of events with a minimum of 127 events in 2012 and a maximum of 268 events in 2016 (more than double). With minimal investigation, the low event count anomaly in 2012 was likely associated with widespread extreme drought conditions over the Great Plains (NOAA National Centers for Environmental Information, 2013). As expected from the previous section, the JJA filtered ERE count time series exhibits a statistically significant increasing trend through the period ($p_{MK} < 0.05$). The trend is also significant at the 99% confidence level ($p_{MK} < 0.01$) with a Theil–Sen's slope of 42 events decade^{-1} and a relatively large Kendall's τ of ~0.5.

EREs can also be expressed using different metrics besides event counts. Total exceedance volume will be defined as the sum of all 12-hr accumulation exceedance above the 10-yr ARI threshold from all exceedance points in a group of events. This metric has the advantage of weighting the events by both size (i.e., area of exceedance) and intensity (i.e., magnitude of the exceedance). Thus, years with higher values of total exceedance volume may have included more widespread and destructive EREs, but not necessarily a higher number of events. On the other hand, very large and intense events may dominate the total exceedance volume, making the weaker and more localized extreme events negligible. Thus, it is important to examine both total exceedance volume as a measure of ERE severity and event count as a measure of ERE frequency,

although the time series of the two metrics are strongly correlated, with a correlation coefficient of approximately 0.8.

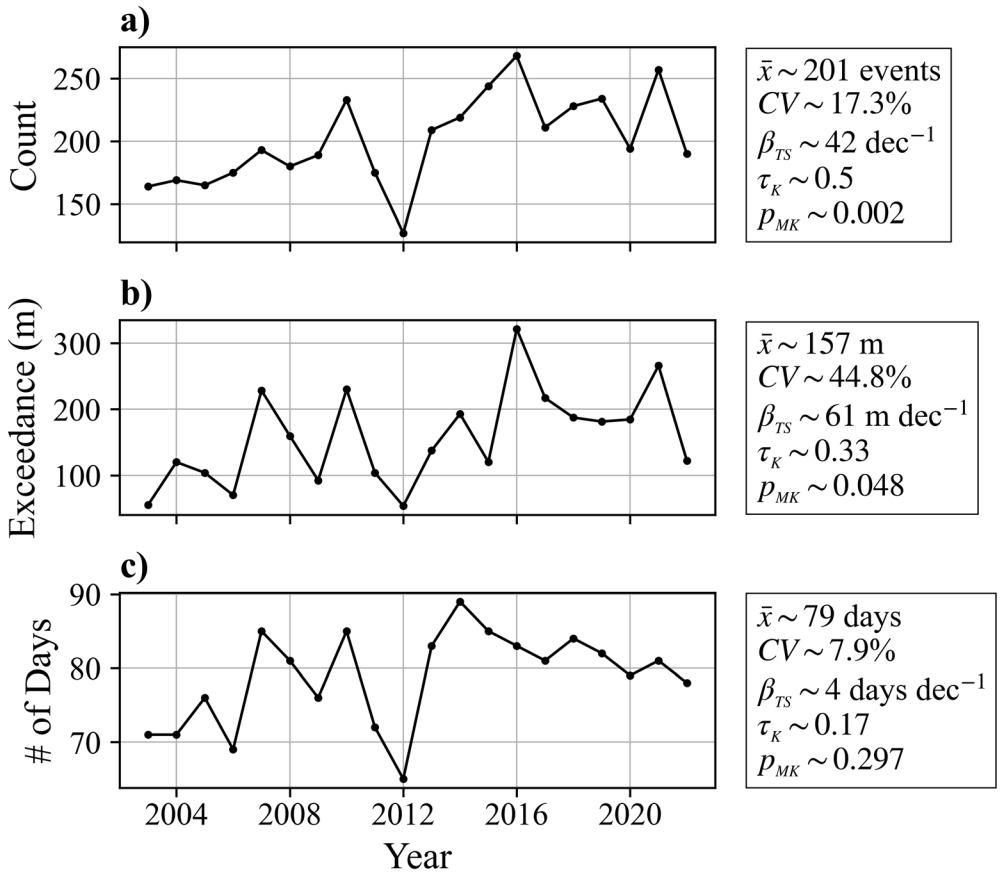

Figure 4.3: For JJA filtered EREs, 2003–2022 time series plots of (a) event count, (b) number of days with at least one event, and (c) total 10-yr ARI exceedance volume. As in Fig. 4.1, some relevant statistics are listed to the right of each time series. The average percent increase according to the β_{TS} of each time series is (a) 20.9, (b) 38.9, and (c) 5.1% decade^{-1}.

The annual time series of total exceedance volume from JJA filtered EREs (Fig. 4.3b) reveals a very large amount of variability throughout the period ($CV \sim 44.8\%$) compared to event counts ($CV \sim 17.3\%$). This variability is likely, in part, due to some years having a few highly anomalous events compared to others. The time series of total exceedance volume also has a statistically significant positive trend through the period ($p_{MK} < 0.05$), but the trend is much less confident than

that for event counts, with a Kendall's τ of ~0.33. However, the relative magnitude of the trend in total exceedance volume according to the Theil–Sen's slope (38.9% decade^{-1}) is substantially greater than that for event counts (20.9% decade^{-1}).

The total number of days that contained at least one event (at its peak accumulation hour) was also analyzed. As mentioned in section 3.2, the vast majority of days in JJA typically have at least one event within the domain. The time series of event days (Fig. 4.3c) exhibits much less overall variability than for other metrics of EREs ($CV \sim 7.9\%$) and does not include a significant increasing trend through the period ($p_{MK} > 0.05$). However, the number of event days is not as relevant to the potential societal impacts (i.e., flooding) as the other metrics (i.e., event counts or total exceedance volume) since multiple EREs can occur in a single day. Therefore, no further analysis of event day counts will be shown.

Analyzing the time series for events exceeding 50- and 100-yr ARI thresholds has the potential to reveal changes in "higher-end" EREs during the period when compared to the 10-yr EREs. Prior studies like Schumacher and Johnson (2006) and Stevenson and Schumacher (2014) also used 50- and 100-yr ARIs as extreme rainfall thresholds, not 10-yr ARI thresholds, so it is appropriate to consider these alternative thresholds for analysis. The time series of the number of JJA filtered EREs exceeding 50-yr ARI thresholds (Fig. 4.4a) and 100-yr ARI thresholds (Fig. 4.4b) are highly correlated to the 10-yr event count time series (Fig. 4.3a), with correlation coefficients of 0.92 and 0.90, respectively. However, as the sample size decreases for higher-end events, overall variability in the time series increases ($CV \sim 23.7\%$ and 28.6% for 50- and 100-yr events, respectively). As a result, the confidence in any increasing trend decreases for the higher-end events ($\tau_K \sim 0.38$ and 0.33 for 50- and 100-yr events, respectively), despite the positive trends still being statistically significant ($p_{MK} < 0.05$). However, the average percent increase is slightly higher for the higher end

events (20.9, 21.2, and 23.1% decade^{-1} for 10-, 50-, and 100-yr events, respectively), meaning that the higher end events increased slightly faster in a relative sense.

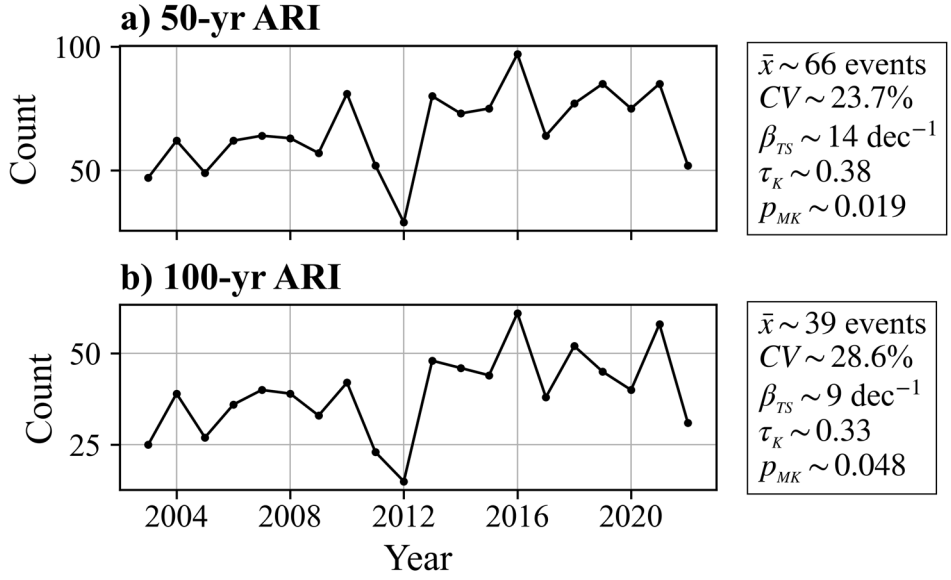

Figure 4.4: 2003–2022 event count time series plots for JJA filtered EREs exceeding (a) the 50-yr ARI threshold and (b) the 100-yr ARI threshold. As in Fig. 4.1, some relevant statistics are listed to the right of each time series. The average percent increase according to the β_{TS} of each time series is (a) 21.2 and (b) 23.1% decade^{-1}.

4.4 Changes in the JJA Diurnal Cycle

As presented in section 3.3, JJA filtered EREs undergo a strong diurnal cycle, with the peak in event maximum 1-hr rainfall occurring during the early evening hours (2100–0200 UTC; 1600–2200 local time) when considering the full domain (Fig. 3.7a). The 20-yr time series of JJA filtered EREs that were classified as diurnal (Fig. 4.5a) and those that were classified as nocturnal (Fig. 4.5b) based on the definition in section 2.1.4.5 both show a statistically significant increasing trend ($p_{MK} < 0.05$). The relative magnitude of the trend in the nocturnal events (17.6% decade^{-1}) was slightly higher than that of the diurnal events (15.1% decade^{-1}) and the confidence in both trends was nearly the same ($\tau_K \sim 0.40$ and 0.41 for nocturnal and diurnal, respectively). This difference is

likely due to the larger overall variability in the nocturnal ERE time series (CV ~ 21.6% for nocturnal vs. 16.8% for diurnal). Thus, we cannot confidently say that the nocturnal events increased faster than the diurnal events. The proportion of JJA filtered EREs that were nocturnal (Fig. 4.5c) exhibited no significant trend through the period, but a fair amount of variation. For example, it is noteworthy that ~ 60% of JJA filtered EREs were nocturnal in 2010, but only ~47% were nocturnal in 2021, while both years had relatively high event counts (Fig. 4.3a). This variable relationship between diurnal and nocturnal events was not further explored in this thesis but may be a subject for future work that can employ a longer sample period.

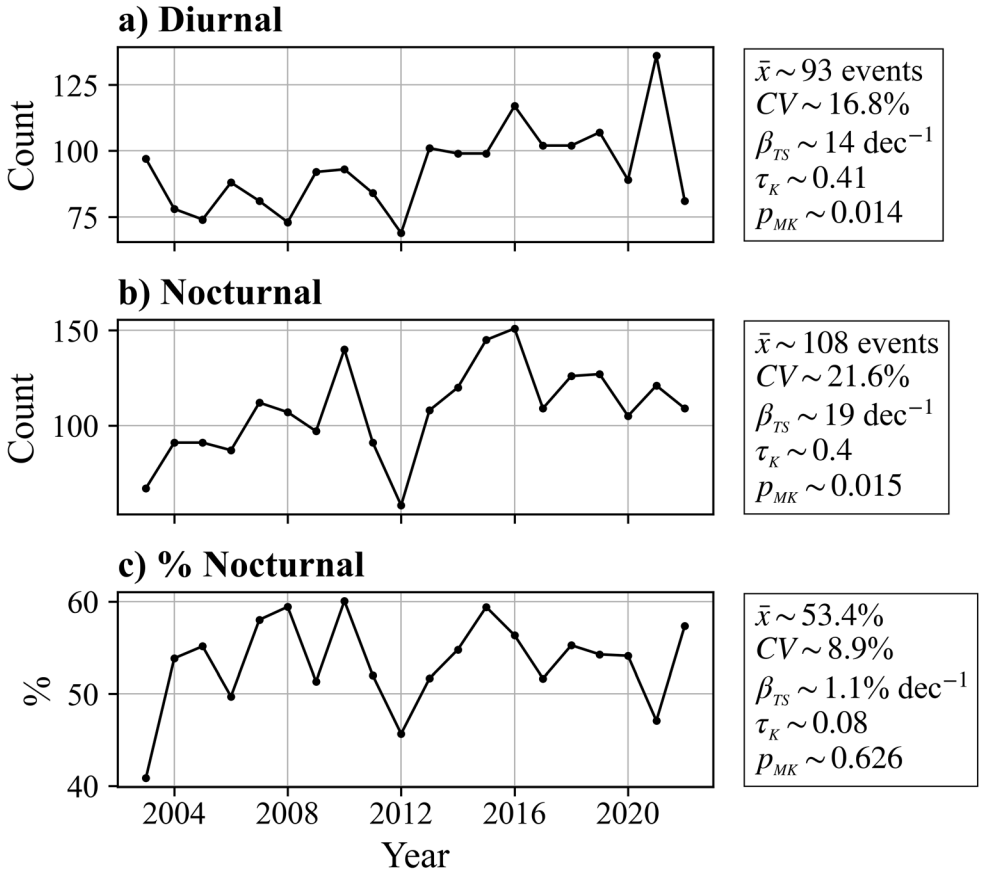

Figure 4.5: (a), (b) as in Fig. 4.4, but for JJA filtered EREs classified as (a) diurnal and (b) nocturnal. (c) The percentage of the total JJA filtered EREs per year that are classified as nocturnal. The average percent increase according to the β_{TS} of each time series is (a) 15.1, (b) 17.6, and (c) 2.1% decade^{-1}.

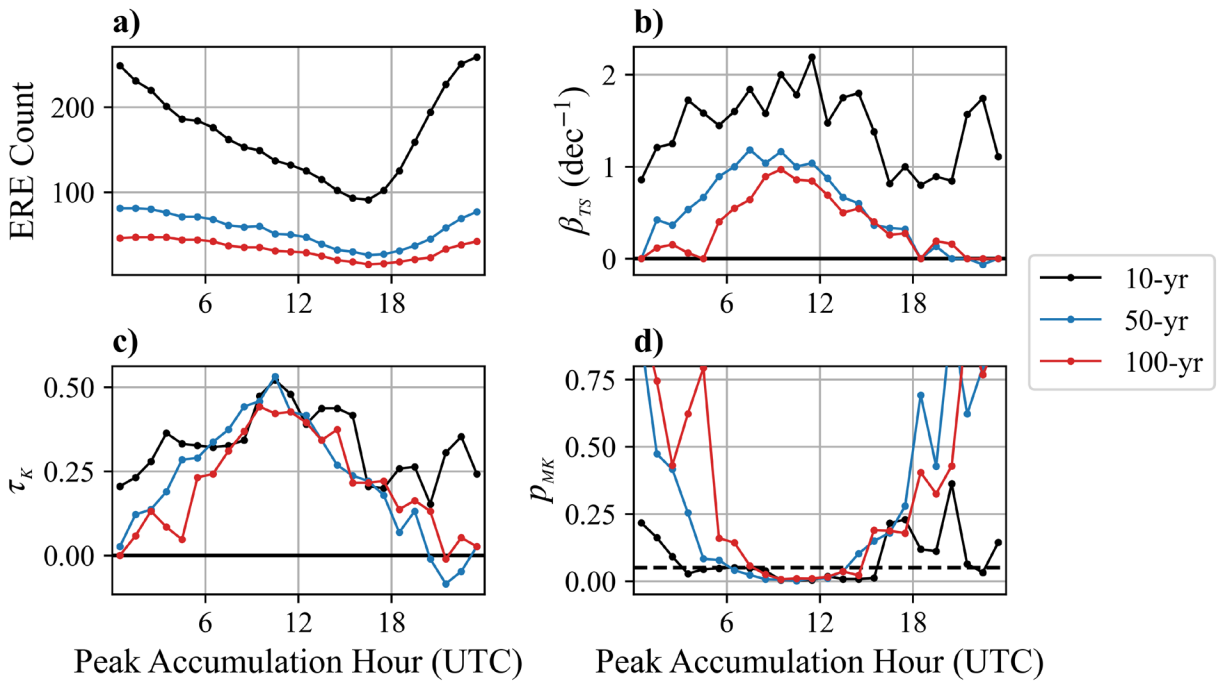

Figure 4.6: Centered at each hour of the day, (a) the total 5-hr running mean of 20-yr (2003–2022) ERE count, and for the 20-yr time series of each 5-hr running sum: (b) Theil–Sen slope (events decade^{-1}), (c) Kendall's τ, and (d) Mann–Kendall trend test p-values. Values are shown for all filtered JJA EREs (black), and those that exceeded the 50-yr (blue) and 100-yr (red) ARI thresholds. The black horizontal line in (b) and (c) at zero is to help distinguish between positive and negative values. The dashed black line in (d) represents $p_{MK} = 0.05$, with any values below the line indicating statistical significance at the 95% confidence level.

The same trend analysis was performed on the JJA filtered EREs that were classified as MCS-related and compared to those that were not (Fig. 4.7) and there is a striking difference between the two. Non-MCS-related JJA filtered EREs had no statistically significant trends throughout the diurnal cycle ($p > 0.05$), whereas MCS-related EREs exhibited an increasing trend that was statistically significant ($p < 0.05$) over nearly the entire diurnal cycle (Fig. 4.7d). This result may explain the previous finding that the increase in JJA filtered EREs was most prominent during the early morning hours. Visually, the graph showing the climatological diurnal cycle of percent contribution by MCS-related EREs (Fig. 3.8), closely resembles the trend statistics seen in Fig.

4.6b–d. As will be discussed in the next section, the finding that MCS-related EREs were the primary contributor to the increase through the diurnal cycle may imply that there was an increase in the size and/or duration of the convection associated with the EREs based on the Stage IV data.

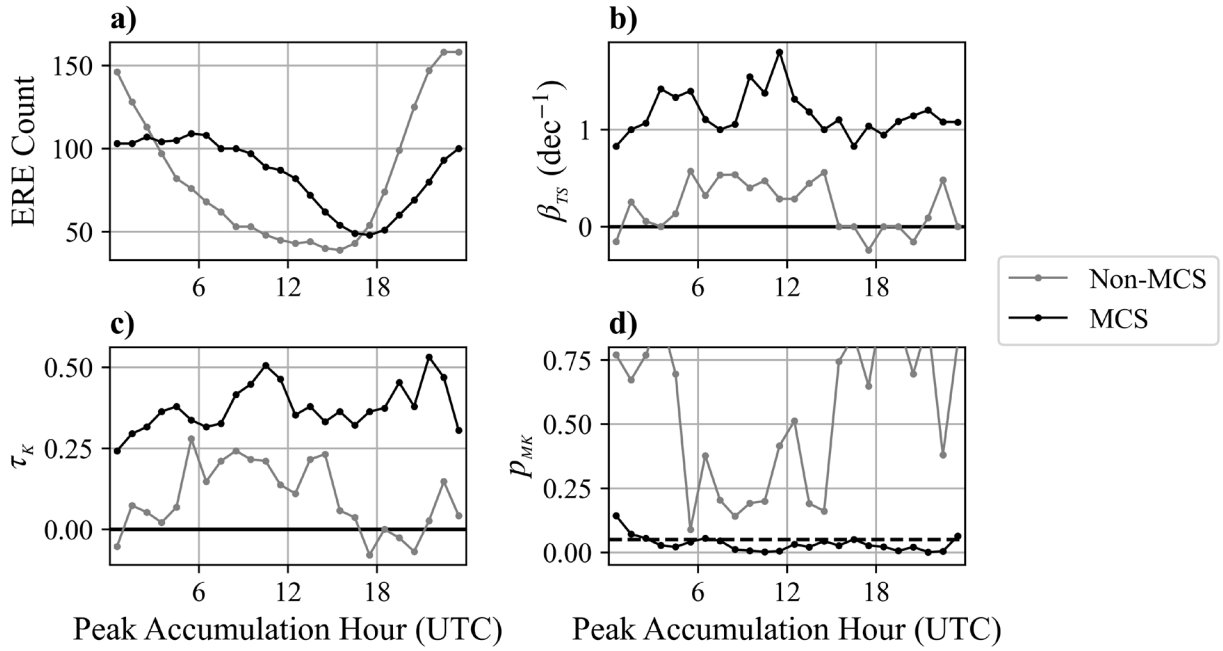

Figure 4.7: As in Fig. 4.6, but for JJA filtered non-MCS-related EREs (grey) and JJA MCS-related EREs (black).

4.5 Changes in Storm Size & Duration

Given the findings from the diurnal cycle trend analysis, there is a question on whether the positive trends found in the data were related to an increase in the size and duration of the storms associated with EREs. Since EREs were classified as MCS-related where the size and duration of the associated precipitation feature exceeded specific thresholds, comparison between the time series of event counts associated with MCS- and non-MCS-related JJA filtered EREs can provide some insight. As suspected, the increasing trend in the number of MCS-related JJA EREs was statistically significant ($p_{MK} < 0.05$, Fig. 4.8a), whereas for the non-MCS portion of JJA filtered

EREs, there was no statistically significant trend (Fig. 4.8b, $p_{MK} > 0.05$). In fact, the slope of an ordinary linear regression of the JJA MCS-related ERE time series is ~29 events decade^{-1}, but only ~6 events decade^{-1} for the JJA filtered non-MCS-related ERE time series. Quantitatively, this means that MCS-related events contributed to approximately 83% of the ordinary linear trend in JJA filtered EREs.

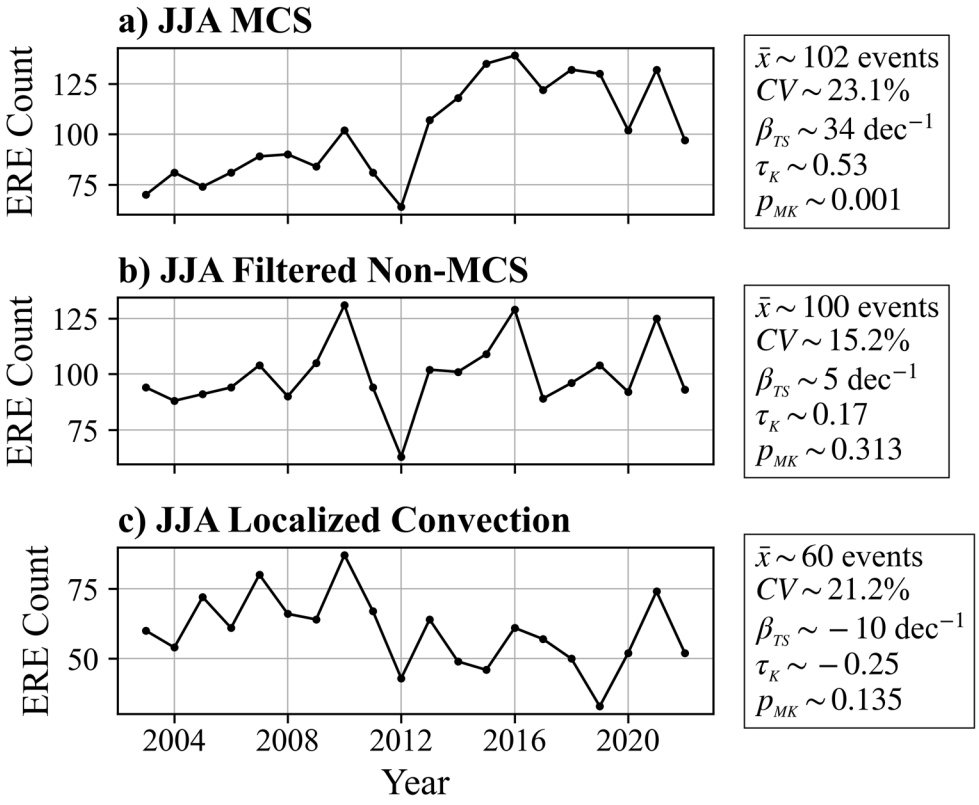

Figure 4.8: As in Fig. 4.4, but for (a) JJA MCS-related EREs, (b) JJA Filtered non-MCS-related EREs, and (c) JJA EREs from only localized convection. The average percent increase according to the β_{TS} of each time series is (a) 33.3, (b) 5.0, and (c) –16.7% decade^{-1}.

JJA EREs associated with localized convection exhibited a slight decreasing trend (Fig. 4.8c), but unlike the annual count time series for localized convection EREs, this trend was not statistically significant ($p > 0.05$). However, since localized convection related EREs are also

defined based on a precipitation feature size threshold (section 2.1.4.3), the result of a negative trend, in contrast to the filtered EREs, further suggests that the 20-yr trend in JJA convective EREs increases with respect to size of the associated storm.

A more direct approach in determining the dependence of storm size and duration on the trend is by performing the trend analysis on the time series of EREs falling within different range bins of relevant size and duration attributes. For example, the maximum major axis length of an event's associated 1 mm hr^{-1} precipitation feature was used as a measure of storm size, and the duration over which that value was at least 200 km throughout the event's lifetime was used as a measure of storm longevity. The histogram of convective (non-TC and non-stratiform) EREs with respect to storm size (Fig. 4.9a) reveals that the largest number of events have maximum precipitation feature lengths between 200 and 400 km. Performing the Mann–Kendall trend test on the time series of each group of events within 200-km maximum precipitation feature length range bins reveals a stronger trend for larger values. The maximum statistically significant ($p_{MK} < 0.05$) percent increase was evident for the filtered EREs with maximum precipitation feature lengths between 800 and 1000 km (~2.2% $decade^{-1}$), with the relative trend increasing with each 200-km range bin up to 1000 km (Fig. 4.9b). Beyond 1000 km, the trend was insignificant or nonexistent, likely due to both lower sample sizes and perhaps the different dynamics involved in driving very large rain systems (i.e., stronger synoptic scale forcing). Grouping the JJA convective EREs by the number of hours where the precipitation feature was at least 200 km (Fig. 4.9c) and performing the Mann–Kendall trend test on each resulting time series reveals a larger relative increasing trend for the events with longer-duration MCSs (Fig. 4.9d). However, the trends are not statistically significant for durations of 8 hours or longer, perhaps attributable to the smaller sample sizes. Nevertheless, the results serve as confirmation that the JJA filtered EREs that exhibited the greatest

increasing trends were characterized by larger and longer-duration precipitation features, but only to an extent, with EREs having the largest precipitation features showing no trend.

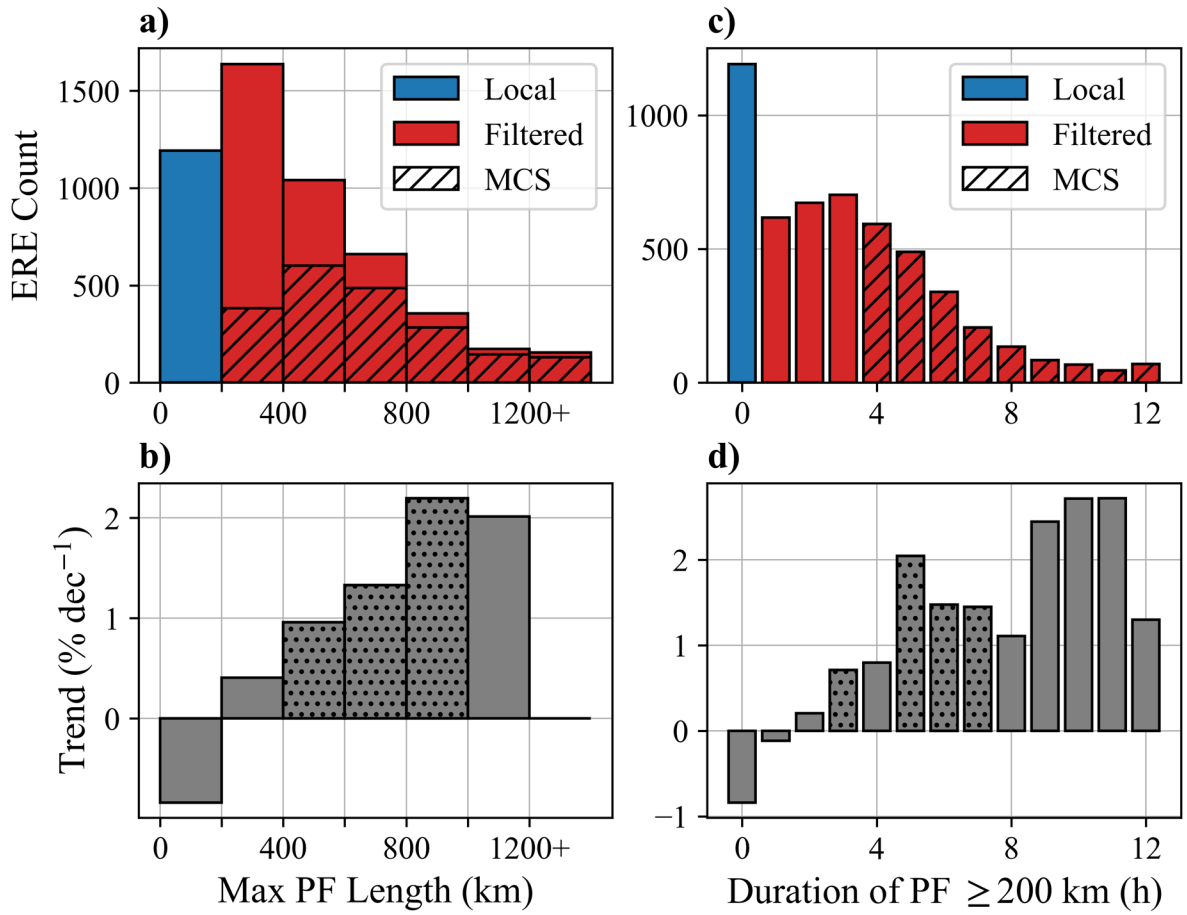

Figure 4.9: (a) 2003–2022 JJA convective (non-TC and non-stratiform) ERE count histogram with respect to the maximum major axis length of the associated 1 mm hr^{-1} precipitation feature (PF) through the accumulation period. The blue bar represents EREs associated with localized convection while the red bars represent the filtered EREs, where the portions that are classified as MCS-related are hashed. (b) Trends (% decade^{-1}) calculated from the Theil–Sen slope of the JJA ERE count time series for events within the respective bins from (a). Bars are stippled where the trend is statistically significant ($p_{MK} < 0.05$). The rightmost bar is for all events with max PF lengths exceeding 1200 km. (c,d) As in (a) and (b), but with respect to the maximum number of consecutive hours where the major axis length of the associated 1 mm hr^{-1} PF through the accumulation period was at least 200 km.

4.6 Regional Trends

Thus far, we have explored the trends observed in different types of EREs over the full central and eastern CONUS domain, but it is also informative to determine what specific regions within the domain experienced the greatest trends. Previous studies have often subdivided the domain into fixed subregions, such as Kunkel et al. (2013a), who defined regions like "Southeast" and "Midwest" using state borders. In contrast, our regional analysis does not invoke these regional differences, but considers event counts within a 500-km radius at each grid point on a map with 0.25° grid spacing. In this framework, evaluating the Theil–Sen's slope for the neighborhood event count time series at each grid point reveals the areas where the strongest trends in ERE frequency were observed in the dataset. Performing a Mann–Kendall trend test on each time series and subsequently correcting the significance tests using the FDR approach (section 2.2.3) reveals areas where the trend was statistically significant. As a result, the overall statistical significance in the trends was reduced compared to the individual trend tests. Considering the short sample period, trends will be considered statistically significant on spatial grids at the 90% confidence level (α_{FDR} = 0.2). Figs. 4.10–12 present maps of the Theil–Sen's slope with stippling of statistical significance (a) and maps of Kendall's τ (b) for several subsets of the JJA filtered ERE dataset. The 500-km radius where the maximum trend was observed is plotted on the maps, for reference, and the time series associated with the maximum trend is also presented in each figure (c).

The regional trend analysis for all JJA filtered EREs reveals a large area with statistically significant trends at the 90% confidence level (Fig. 4.10a). Trends of the largest magnitudes (β_{TS} > 10 events decade^{-1}) and strongest correlations (τ_K > 0.4; Fig. 4.10b) were found over portions of the Mid-Atlantic, Ohio Valley, and Midwest. Though not as large, statistically significant trends

were also found over the Upper Midwest and the Lower–Mid Mississippi Valley. A lack of statistically significant trends were found over the Northeast, Southeast, and Great Plains.

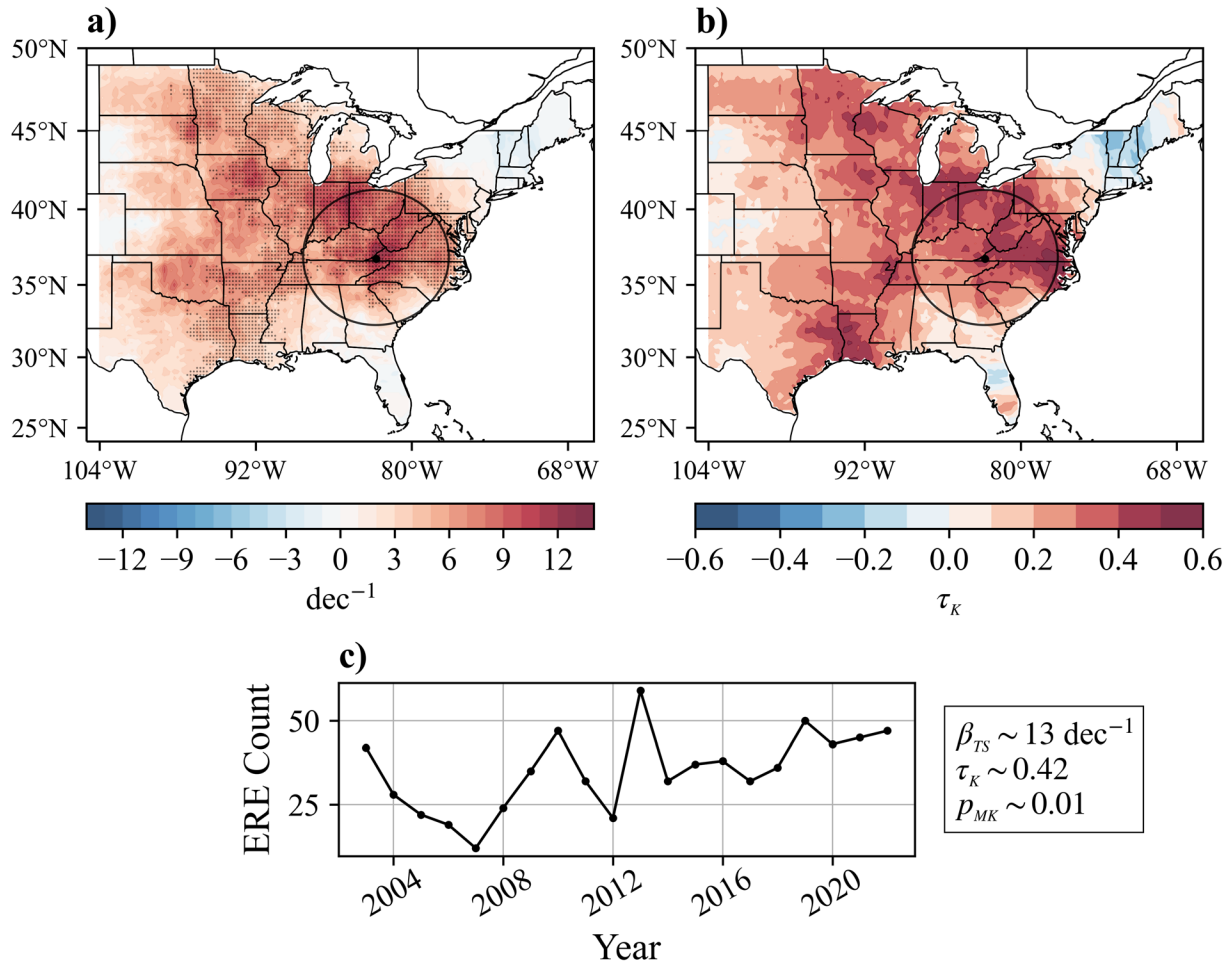

Figure 4.10: For JJA filtered EREs, (a) Theil–Sen slope (color fill; events decade^{-1}) and (b) Kendall's τ (color fill) applied to the 500-km neighborhood event count time series (2003–2022) at each point on a 0.25° grid over the full domain. The black circles indicate the 500-km radius where the trend is the largest, with the center point represented by a black dot. Stippling in (a) indicates where the trend is statistically significant (nonzero) at the 90% ($\alpha_{FDR} = 0.2$) confidence level. (c) 2003–2022 event count time series associated with the maximum trend with Mann–Kendall trend test statistics, including Theil–Sen slope (β_{TS}), Kendall's τ (τ_K), and p-values (p_{MK}) listed.

For JJA filtered EREs exceeding higher ARI thresholds, the regional trend analysis reveals that the increases were more confined to the central portion of the domain than the 10-yr JJA filtered EREs and did not include the Mid-Atlantic region. For example, the 50-yr JJA filtered EREs exhibited a maximum increasing trend centered over the Ohio Valley, with areas of significance over the Upper Midwest and extending southward into the Lower Mississippi Valley (not shown). The maximum increasing trend for 100-yr JJA filtered EREs was even farther west, centered over the Mid Mississippi Valley region (Fig. 4.11). The area where the increasing trends were most observed in higher-end EREs, compared to the 10-yr EREs, is likely explained by the climatology of MCS-related EREs, which account for the majority of all 50- and 100-yr EREs (Table 3.1). Supporting this idea, the areas with trends in 50- and 100-yr JJA filtered EREs over the central CONUS generally align with areas where the majority of JJA filtered EREs were MCS-related (Fig. 3.6b).

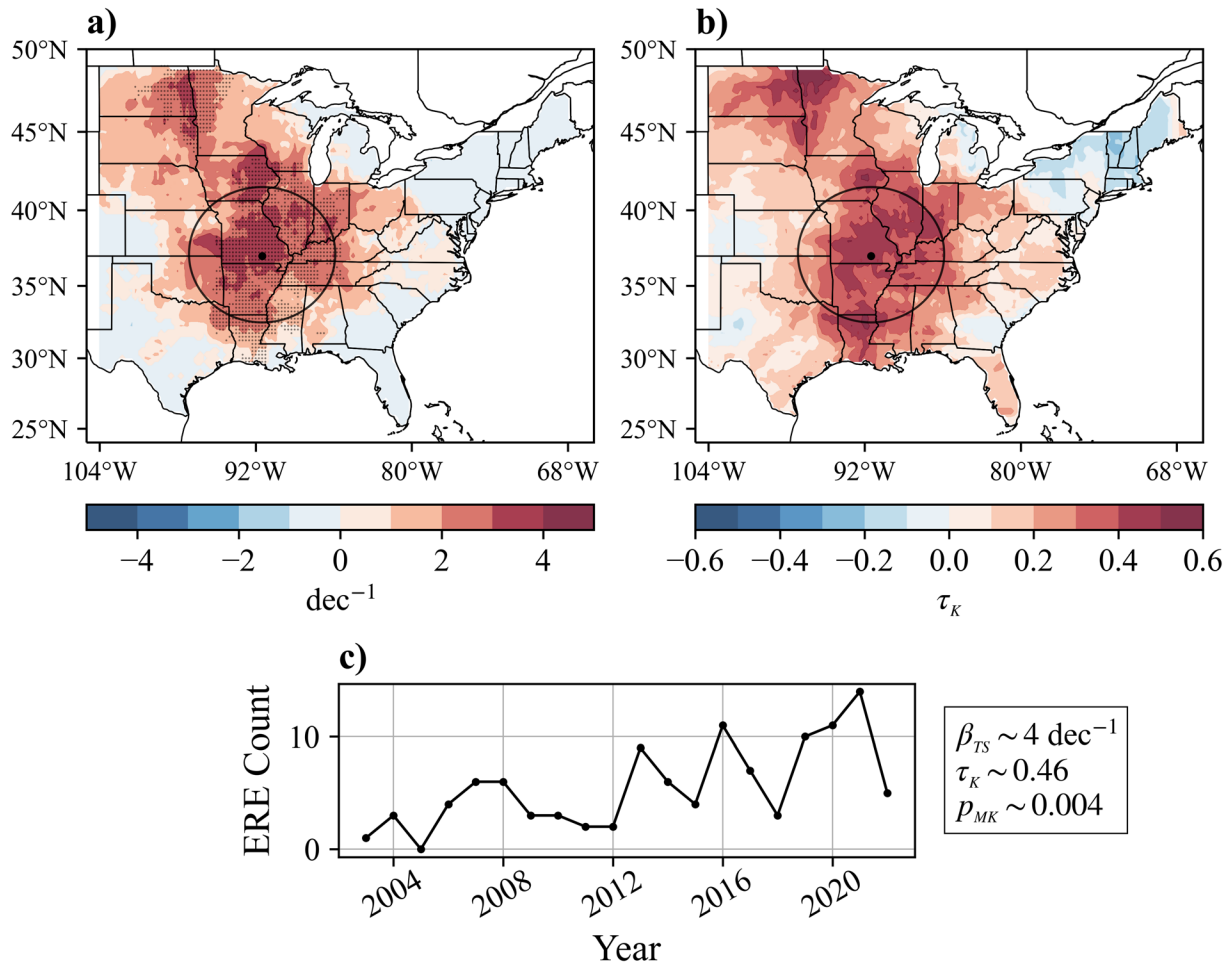

Figure 4.11: As in Fig. 4.10, but for JJA filtered EREs exceeding the 100-yr ARI threshold.

As anticipated due to the strong increasing trend in JJA MCS-related EREs, statistically significant increasing trends in those events at the 90% confidence level were widespread throughout the domain (Fig. 4.12). The maximum trend in JJA MCS-related EREs ($\beta_{TS} \sim 10$ events decade^{-1}) was centered over the Mid–Upper-Mississippi Valley region (Fig. 4.12a), but there were several other areas throughout the domain where Kendall's τ was greater than 0.4 (Fig. 4.12b). The only areas where no significant increasing trends were observed in JJA MCS-related EREs include the Northeast, Central High Plains, and Florida.

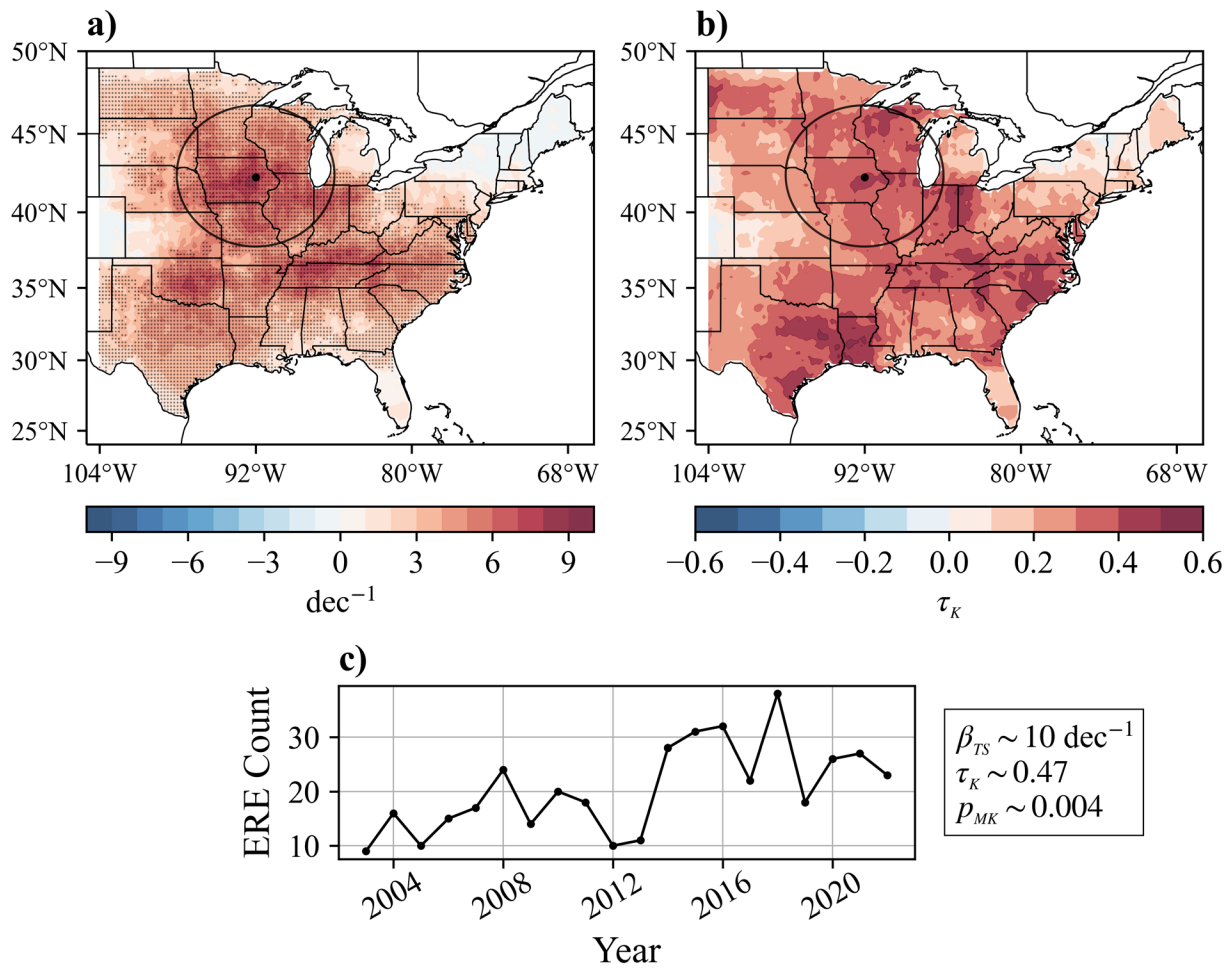

Figure 4.12: As in Fig. 4.10, but for JJA MCS-related EREs.

Significant regional trends in diurnal and nocturnal JJA filtered EREs were less apparent. Only isolated patches of statistically significant trends appeared in the diurnal events, namely areas centered around the Ohio Valley and the Ark-La-Tex region (not shown). Increasing trends in the nocturnal events were greatest over parts of the Midwest, Ohio Valley, and Mid-Atlantic (not shown). However, despite areas with Kendall's τ exceeding 0.4 over the Ohio Valley and Mid-Atlantic regions, the trends in nocturnal events were not statistically significant at the 90% confidence level anywhere after FDR correction.

4.7 Discussion

The results presented in this chapter offer a relatively unique perspective on the recent changes in short-duration EREs over the central and eastern CONUS. Unlike most previous studies on temporal variability and trends in EREs, this study utilized a database of event objects derived from a high resolution gridded precipitation product, namely Stage IV analyses. The hourly gridded data enables the examination of properties such as storm size, duration, and time of day, and no other observational studies have examined changes in all of those aspects of EREs. The Stage IV dataset has also never been used in any published studies for the purpose of detecting long-term trends, likely due to the relatively short period of record in the earliest days and possibly due to the potential caveats discussed earlier.

Besides the short sample period, there are several additional caveats in using the Stage IV analyses that should lead to extreme caution in the interpretation of the results. Most of these caveats, such as the spatial and temporal inhomogeneities in the Stage IV dataset, were previously discussed in section 2.1.1. However, the methods involved in our trend analysis are not quite different from those employed in some prior published studies, and actually have some relative benefits. For example, Feng et al. (2016) considered ordinary linear trends from 1997–2014, only an 18-yr period of record, and employed an hourly gridded precipitation dataset that also incorporates radar data and has a spatial resolution of 12 km, as opposed to 4 km.

Putting the caveats aside, one of our core findings was that the greatest increasing trend occurred in EREs associated with larger and longer duration MCSs, but not with localized convection (section 4.5). This finding also has implications on the diurnal cycle of EREs (section 4.4), since the relative proportion of MCS-related EREs peak during the late night and morning hours (Fig. 3.8). The finding that MCS-related EREs increased relative to EREs associated with

localized convection is consistent with previous observational studies (e.g., Feng et al., 2016; Hu et al., 2020) that found statistically significant increasing trends in MCS precipitation and frequency during the spring and summer from 1997–2014, but a negative trend in non-MCS precipitation. This finding also aligns with the projected increase in MCS precipitation volume according to regional convection permitting climate model projections in a warming climate (e.g., Prein et al., 2017a).

Some results from prior studies are somewhat contradictory to our findings. For example, Wasko et al. (2016) argued that the spatial extent of storms will decrease in a warming climate, but rainfall will be heavier and more concentrated within the convective cores. This concept appears to be supported by the decrease found in EREs resulting from widespread stratiform precipitation (Fig. 4.1c), but not supported by the increase in larger MCS-related EREs relative to EREs associated with localized convection. In addition, the regions found to have increasing trends (section 4.6) are not supported by future projections related to climate change. According to regional climate simulations by Prein et al. (2017b), a lack of significant increases in JJA extreme rainfall is present over the Midwest and Northern Plains, but significant increases are found elsewhere, including the Northeast. However, other past observational studies do show an increase over the Midwest (e.g., Kunkel et al., 2013a, Fig. 1.8). This increase may imply that the observed regional trends may not have a primary connection to anthropogenic warming but may be due to specific LSMPs that favor EREs over the Midwest (see chapters 5 and 6).

One potential discovery that has not been discussed in prior extreme rainfall literature is a potential eastward expansion of EREs from the Great Plains. Significant increasing trends in the JJA filtered EREs were only found to the east of the Great Plains (Fig. 4.10a), while JJA filtered EREs were just as common, climatologically, over the Great Plains (Fig. 3.4c). For higher-end

EREs (e.g., 100-yr ARI exceedance; Fig. 4.11), a signal for an increase in the number of events peaking later into the morning hours was evident (Fig. 4.6), and since the increase in these higher end events was found slightly to the east of where nocturnal MCSs were most common (Fig. 3.9), it is possible that higher-end EREs are peaking later at night farther to the east. Further research would be required to determine the reasons for this apparent eastward expansion. Also, note that the regional trend maps in their current state should be interpreted with caution, as the addition or removal of a single year from the beginning or end of the time series can lead to drastic changes in the results. These changes are likely due to the relatively small sample sizes of events within each 500-km radius. Thus, a longer sample period would be beneficial to solidify the regional trend results.

If our results are an indication of future trends as well, there could be significant negative impacts on society as an increased frequency of EREs means an increased likelihood of populations being impacted. However, it should be noted that the number of events and total exceedance volume is not always proportional to societal impacts, as even a relatively mediocre year in our timeseries, such as 2022 (Fig. 4.3), can have a few particularly destructive EREs that impact vulnerable or flood prone communities (section 1.5).

One red flag in our results is the discontinuity in the time series showing JJA MCS-related ERE counts (Fig. 4.8a) between the first ten years (2003–2012) and the second ten years (2013–2022). While the time series of JJA MCS-related EREs exhibited the most significant trend overall, there are no significant positive trends in the two subdivided time series. Kendall's τ for the first 10-yr period (2003–2012) was approximately 0.22, and approximately –0.13 for the second period (2013–2022). Thus, the 20-yr trend in JJA MCS-related EREs appeared not due to a consistent increase, but due to a step-function-like jump in event counts, with an average of 82 events per

year for 2002–2012 and 121 events per year for 2013–2022. Therefore, there is some reason to suspect that the increase was influenced by a systemic change in the dataset around 2013, which is when the upgrade of the NEXRAD network to dual-polarization technology was completed. However, it is unclear how the NEXRAD upgrade would only affect the detection of EREs associated with MCSs. Our discussions with the staff at the River Forecast Centers (section 2.1.1) indicated that changes in their techniques, including quality control procedures and use of dual-polarization technology, were not associated with a step function change around 2013. Thus, the trends observed in the data were likely not significantly influenced by the changes in the dataset, and instead may be attributed to natural variability, such as a shift in predominant weather patterns around the 2012–2014 timeframe, which will be explored in future work. Nonetheless, we stress the need for a more uniform high resolution long-term precipitation dataset to gain confidence in any observed trends, despite the agreement of the observed trends with past studies.

The significant interannual variability discovered suggests the potential value of seasonal and annual forecasts of rainfall extremes. The potential environmental factors driving this variability will be explored in the next chapter by examining the LSMPs associated with more active years. Any evidence of those patterns exhibiting an increase according to past studies could also help explain the increasing trends that were observed.

Chapter 5

Connections to Seasonal LSMPs

It has been well documented that EREs or periods of above average rainfall over the central and eastern CONUS are linked to specific LSMPs (section 1.3). Previous studies have examined LSMPs directly associated with the occurrence of EREs (e.g., Barlow et al., 2019), and seasonal (e.g., JJA-averaged) LSMPs associated with pluvial periods over specific regions (e.g., Abel et al., 2022; Flanagan et al., 2018). However, prior studies have not linked the occurrence of seasonal LSMPs to the occurrence of short-duration EREs, which is relevant in this study given the substantial interannual variability in extreme rainfall activity through the sample period (chapter 4). This chapter will present the results of both composite and correlation analyses between seasonally-averaged meteorological fields and a measure of JJA extreme rainfall activity (section 5.1). This approach can provide valuable insight into what predominant LSMPs may be associated with more frequent and severe EREs[6]. Many of the results are robust and appear to be physically consistent despite the relatively short sample period and potential issues with the ERE dataset (section 2.1). These caveats will be set aside when discussing the results in this chapter.

For contextual purposes, the ERE time series used for analysis as well as the difference in event locations between "active" and "inactive" summers will be presented in section 5.1. The results of correlation and composite analyses using various seasonally-averaged 2D meteorological fields from the ERA5 will be presented in section 5.2. Section 5.3 will discuss the major findings from the analysis and potential implications on trends and climate change.

[6] If unspecified, the terms "ERE" or "extreme rainfall" will refer specifically to the JJA filtered EREs for the remainder of this chapter.

5.1 ERE Index Time Series & Comparison of Anomalous Years

Composite and correlation analyses (section 2.2) were conducted on various meteorological fields using several variations of the JJA filtered ERE time series. Some of these variations include the time series of total event counts (Fig. 4.3a), total exceedance volume (Fig. 4.3b), and counts of events exceeding higher thresholds (e.g., 50- and 100-yr ARIs). The patterns that emerged in the correlation maps that were similar when using these different variations of the time series for analysis were considered robust in this thesis. Thus, any results that were vastly different when using different variations of the time series for analysis will not be presented.

Event counts will be considered a fair metric for overall ERE frequency, while total exceedance volume will be considered a fair metric of overall ERE intensity and spatial extent (section 4.3). The time series of these two metrics are highly correlated, but the composite and correlation analysis results using the two time series often exhibit notable differences in the areas of statistical significance. To avoid presenting the results of both analyses separately, the time series of overall ERE intensity and spatial extent were combined into a single index (Fig. 5.1). The time series of this combined index was constructed by standardizing the count and exceedance time series and taking the average value for each year. The Pearson correlation coefficient between the index time series and the time series of both event counts and exceedance volume is approximately 0.95, and thus, the index is a fair metric of both ERE frequency and severity.

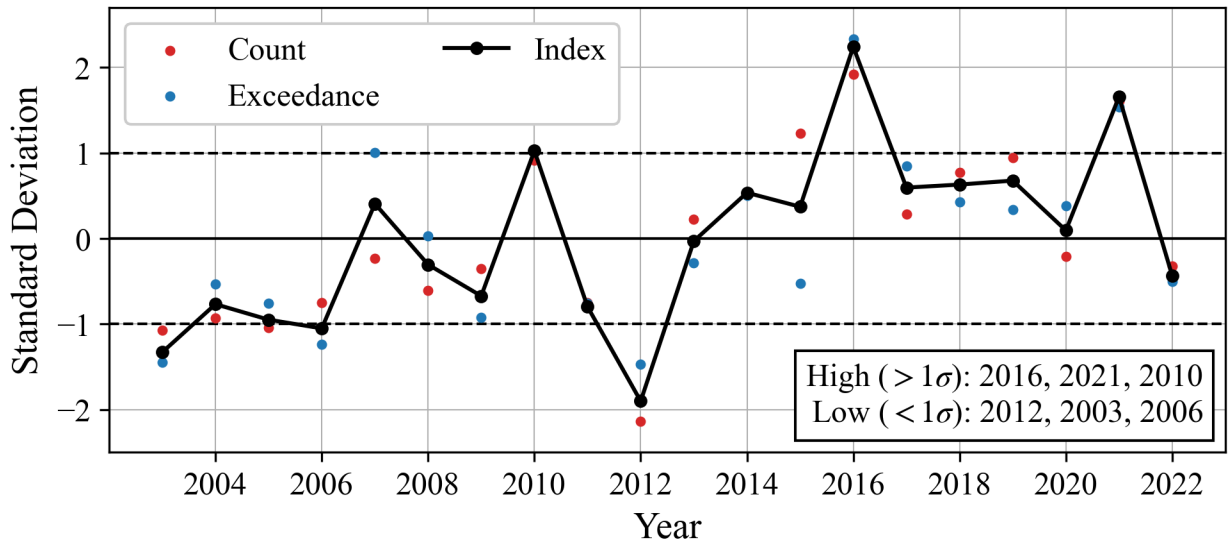

Figure 5.1: For JJA filtered EREs, 2003–2022 standardized time series plot of event count (red), total exceedance volume (blue), and the standardized average (black). The years where the index was at least one standard deviation from the mean (dashed lines) are listed on the bottom right in order of most to least anomalous.

For composite analysis, the difference was taken between the time-averaged meteorological fields during the years considered to be most active (i.e., "active years") and least active (i.e., "inactive years") based on the JJA filtered ERE index time series (Fig. 5.1). Years were considered anomalous if the index was at least one standard deviation from the 20-yr mean, leaving three active years (2016, 2021, 2010) and three inactive years (2012, 2003, 2006). When interpreting the composite analysis results, it is important to be aware of what regions were favored or not favored for JJA filtered EREs during active years compared to inactive years. The active years featured far more numerous events over the Great Plains, Midwest, and Ohio Valley regions (Fig. 5.2) with many more large and intense EREs during the active years (Fig. 5.3). However, there is very little difference or a slightly lower number of events during the active years over much of the Southeast, Mid-Atlantic coast, and Northeast (Fig. 5.2c). Thus, the LSMP differences observed

from the composite analysis are likely to favor EREs over the Great Plains, Midwest, and Ohio Valley, but not over the Southeast, Mid-Atlantic coast, and Northeast.

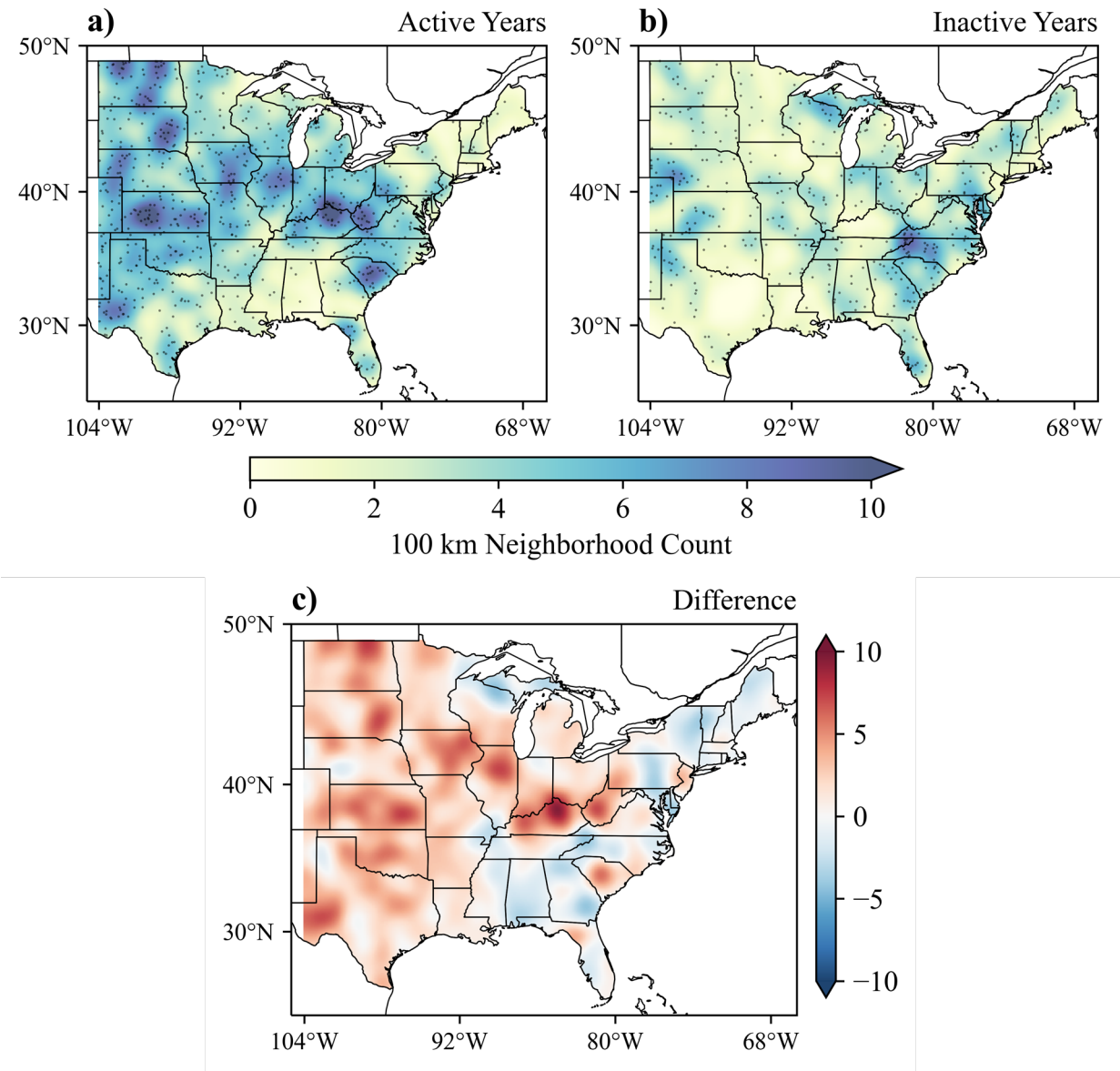

Figure 5.2: JJA filtered ERE points of maximum exceedance (translucent black dots) with Gaussian smoothed (σ = 0.5°) neighborhood event count (radius = 100 km) (color fill) during (a) all active ERE years (2016, 2021, 2010) and (b) all inactive years (2012, 2003, 2006). (c) The difference between the smoothed neighborhood event counts in (a) and (b) (active−inactive).

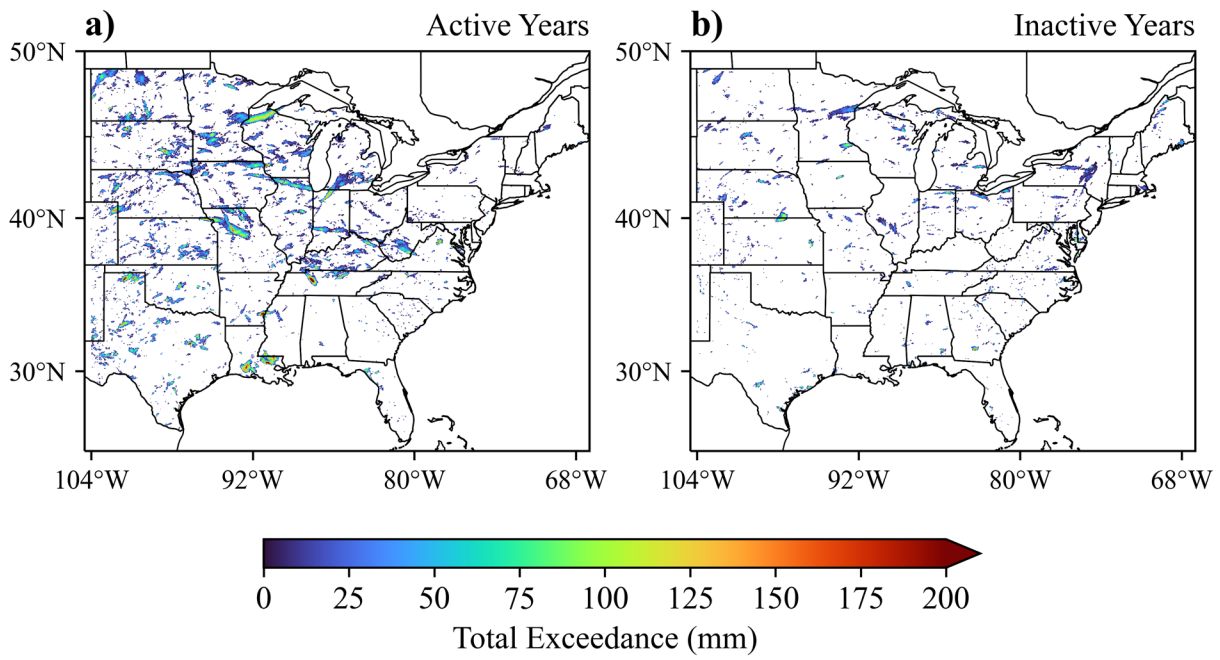

Figure 5.3: Total precipitation (mm) exceeding the 10-yr ARI threshold from all JJA filtered EREs during (a) all active years (2016, 2021, 2010) and (b) all inactive years (2012, 2003, 2006).

5.2 Composite & Correlation Analysis Results

In this section, results from the composite and correlation analysis between the JJA filtered ERE index time series (Fig. 5.1) and JJA-averaged ERA5 fields of various types will be explored, including single-level and surface fields, followed by moisture, wind, and geopotential height fields on multiple pressure levels. The purpose of this analysis is to identify LSMPs that distinguish between active and inactive summers. Relationships with parameters averaged over preceding spring and winter months will also be briefly discussed.

The results from the composite and correlation analysis with each ERA5 field will be presented in a four-panel plot. For context on the typical values of the respective field, and for side-by-side comparisons, panels (a) and (b) will show the composites for active and inactive years, respectively. Panel (c) will present the composite difference and panel (d) will present the

correlation coefficients obtained from the correlation analysis, with stippling of statistical significance at the 90% and 95% confidence levels after applying FDR correction (section 2.2).

5.2.1 Single-Level & Surface Fields

Composite analysis of the ERA5 JJA-averaged daily precipitation reveals that the active ERE years exhibited more precipitation over much of the central CONUS and slightly less precipitation over the East Coast states (Fig. 5.4a–c). Correlation analysis reveals the same general pattern (Fig. 5.4d), with positive correlations over the Great Plains and Midwest and slightly negative correlations over the Southeast states and New England. This depiction is fairly similar to the difference in the number of JJA filtered EREs between active and inactive years (Fig. 5.2), implying that summers with more EREs over a particular region are associated with more rainfall overall in that region. This result is expected, helping to validate our ERE database in comparison to the ERA5 dataset. However, only small areas of statistical significance were found, with the most notable area over the Midwest, centered on Wisconsin (Fig. 5.4c–d). This result implies that more rainfall over the northern tier of the domain likely coincides with more EREs overall, likely due to lower ARI thresholds with northward extent (e.g., Fig. 3.3).

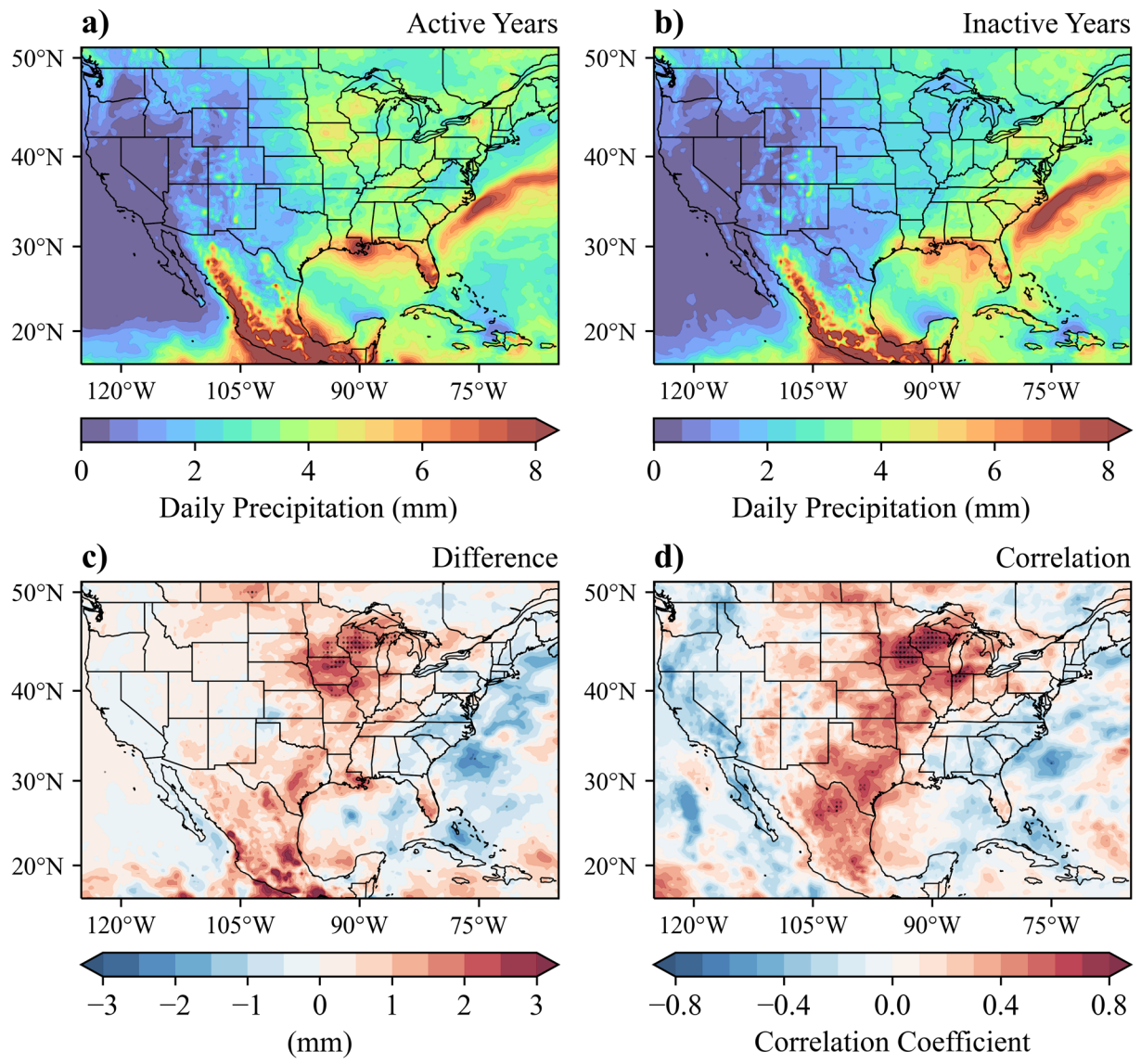

Figure 5.4: ERA5 JJA-averaged daily precipitation (shaded; mm) composite for (a) the active years (2016, 2021, 2010) and (b) the inactive years (2012, 2003, 2006). (c) Composite difference between (a) and (b) (active−inactive). From the 0.25° resolution ERA5 field linearly interpolated onto a 0.5° resolution grid (125–65°W, 15–52°N; N = 9075 tests), any stippling indicates where the composite difference is statistically significant (from two-tailed tests) at the 90% (translucent stippling; α_{FDR} = 0.2) and 95% (opaque stippling; α_{FDR} = 0.1) confidence levels based on Monte Carlo simulations (n = 5000 random selections of three active and inactive years without replacement). (d) Correlation coefficients of the detrended JJA filtered ERE index time series (2003–2022) with the detrended time series of ERA5 JJA-averaged daily precipitation at each grid point (shaded). As in (c), stippling indicates statistical significance (FDR-corrected) based on Monte Carlo simulations (n = 5000), but determined by resampling the ERA5 time series at all grid points with replacement and recalculating the correlation coefficients in each iteration.

Some basic surface parameters in the ERA5 that were analyzed include 10-m wind, mean sea level pressure, 2-m temperature, and 2-m dew point temperature. No consistent areas of statistically significant composite differences or correlations were found with the 10-m wind field (not shown) nor with the mean sea level pressure (not shown). The composite analysis of 2-m temperature reveals higher temperatures during the active years over large portions of the

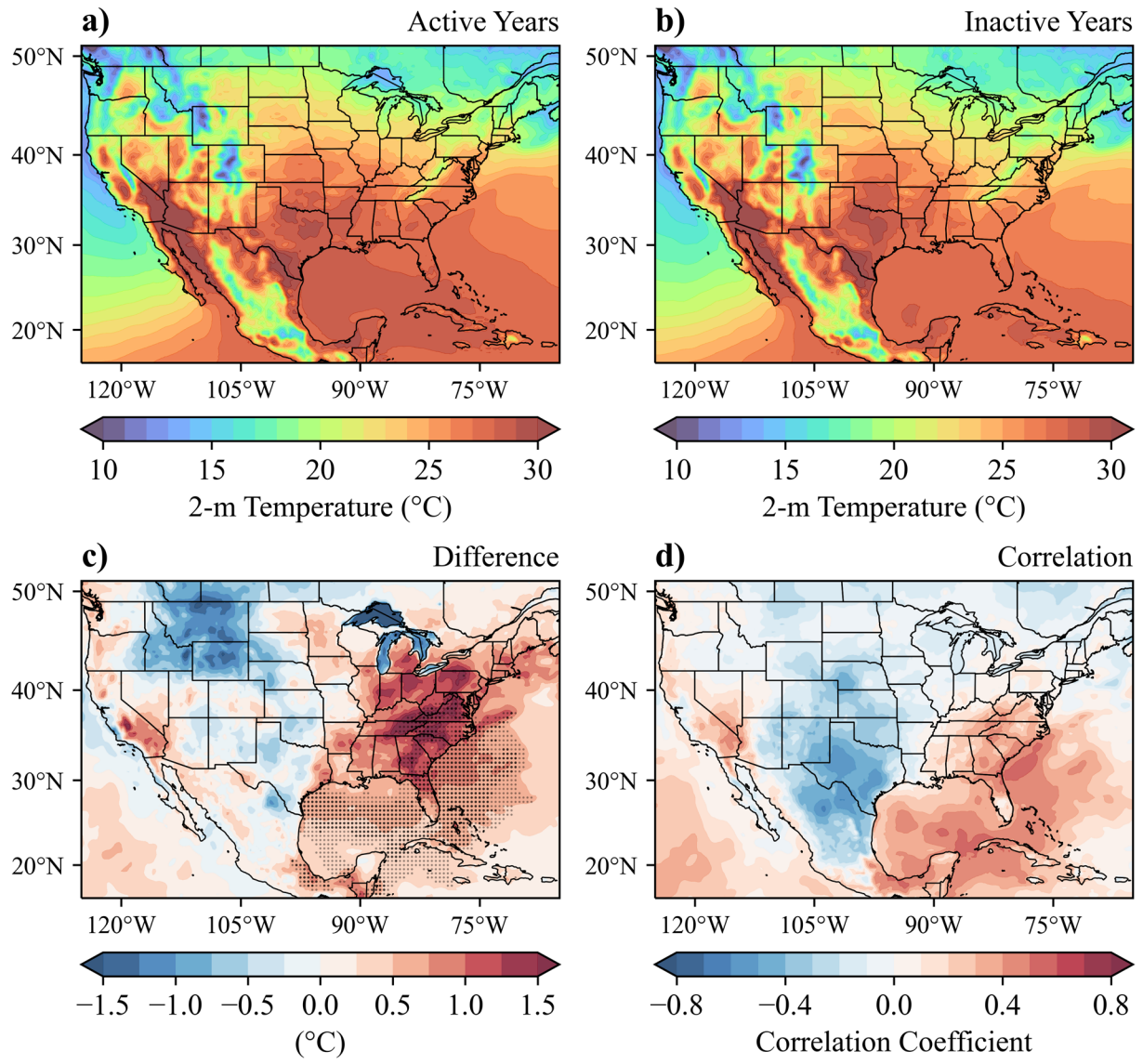

Figure 5.5: As in Fig. 5.4, but for ERA5 JJA-averaged 2-m temperature (°C).

southeastern CONUS, Gulf of Mexico, and adjacent southwestern Atlantic with statistical significance at the 95% confidence level (Fig. 5.5a–c). Weak to moderate positive correlations ($0.4 < r < 0.6$) with 2-m temperature were also found over those regions, with weak to moderate negative correlations over the Southern Great Plains vicinity, but the correlation coefficients were not statistically significant (Fig. 5.5d).

The surface field that yielded the most robust results was the 2-m dew point (Fig. 5.6), which

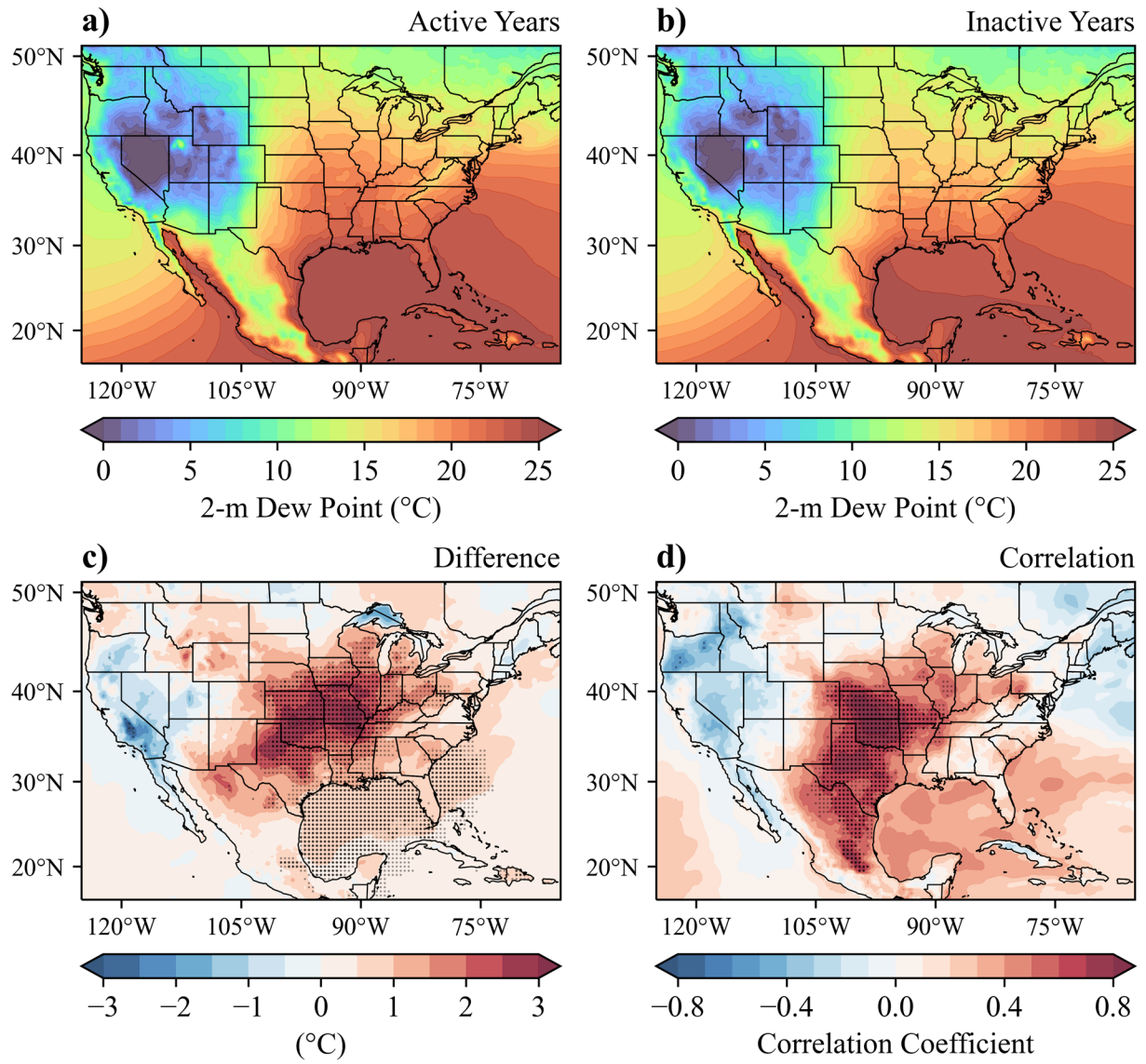

Figure 5.6: As in Fig. 5.4, but for ERA5 JJA-averaged 2-m dew point temperature (°C).

is a measure of moisture in the lowest levels of the atmosphere. Substantially higher dew points (>2°C) were found over the Southern–Central Great Plains and Mid-Mississippi Valley during the active years compared to the inactive years (Fig. 5.6a–c) and a strong correlation ($r > 0.7$) was found between the ERE index and 2-m dew point over the Southern–Central Great Plains (Fig. 5.6d). The positive composite differences and correlations were both statistically significant at the 95% confidence level over the Southern and Central Great Plains, indicating a robust positive relationship between JJA extreme rainfall activity and 2-m dew point over that region.

A potential relationship was also found between the EREs and convective available potential energy (CAPE)[7], which is a measure of instability in the atmosphere that can lead to thunderstorms and heavy rainfall given adequate lift and/or a lack of convective inhibition. The active years exhibited significantly higher ERA5 JJA-averaged CAPE than the inactive years, with a substantial difference of over 600 J kg^{-1} and statistical significance at the 90% confidence level over a portion of the Central Great Plains and Mid-Mississippi Valley (Fig. 5.7a–c). There was also a moderate correlation ($0.5 < r < 0.7$) over parts of the Central Great Plains, but there was no statistical significance in the correlation coefficients (Fig. 5.7d). Thus, the relationship with CAPE may not be considered robust. While surface-based CAPE is directly related to near-surface moisture, this finding reveals that high instability may not be as important for extreme rainfall as low-level moisture by itself. This finding may be surprising for those working in the area of severe convection taking place over midlatitude continental locations, but the result is consistent with the long known finding that low values of CAPE occur with tropical convection over oceanic locations (e.g., Xu and Emanuel, 1989).

[7] In ERA5, CAPE is calculated on the most unstable parcel originating below the 350 hPa level.

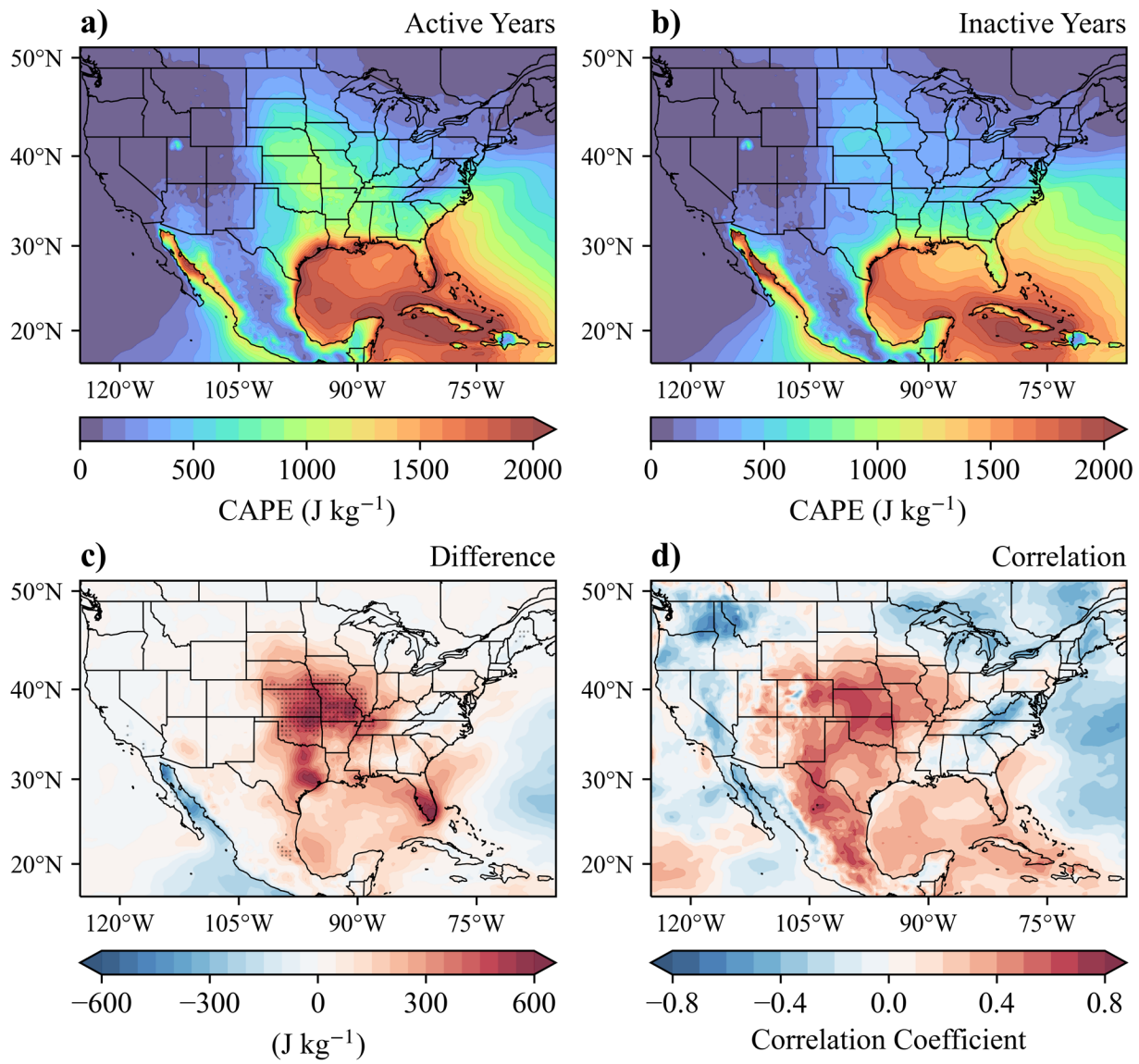

Figure 5.7: As in Fig. 5.4, but for ERA5 JJA-averaged convective available potential energy (J kg^{-1}).

5.2.2 Moisture

At the surface, the 2-m dew point had the strongest relationship with JJA filtered EREs (Fig. 5.6) compared to any other analyzed parameter. However, since extreme-rain-producing convection is often elevated rather than surface based, particularly for nocturnal convection over continental

locations, it is important to consider moisture above the surface, where stronger relationships may be found.

To examine moisture throughout the atmosphere, we utilized the ERA5 total column water vapor parameter, which is a measure of the total mass of water vapor from the surface to the top of the atmosphere (kg m^{-2}). Similar to 2-m dew point, composite and correlation analysis reveals a robust relationship between JJA filtered EREs and JJA-averaged total column water vapor from the Southern–Central Great Plains to the Ohio Valley (Fig. 5.8c–d), where statistically significant (95% confidence) positive differences and correlations were found. This result again stresses the relative importance of high water vapor contents for EREs.

Performing the composite and correlation analysis on specific humidity fields at various pressure levels can help identify the layers of the atmosphere where moisture had the most significant relationship with the EREs. The pressure levels analyzed for moisture include 925, 850, 700, and 500 hPa. The composite and correlation results for specific humidity at the 925- and 850-hPa levels were very similar, so only the results at 850-hPa are shown (Fig. 5.9). A very robust signal is evident in the 850-hPa moisture field with statistical significance in the composite difference over the majority of the domain, with the maximum composite difference found, again, over the Southern–Central Great Plains and Mid-Mississippi Valley (Fig. 5.9c). A strong correlation ($r > 0.7$) was found over a relatively widespread region encompassing most of the Southern and Central Great Plains with a maximum correlation coefficient of approximately 0.90 located in southern Kansas (Fig. 5.9d), thus explaining ~81% of the variance in the JJA filtered ERE time series. Statistically significant positive correlations at the 95% confidence level also extend south, into subtropical Mexico, and to the east into the Ohio Valley. Surprisingly, at 700 hPa and 500 hPa (not shown), no statistically significant results were found, though the

relationships were still positive over the majority of the domain. Thus, moisture in the low-levels (925–850 hPa) over the Southern and Central Great plains had the most significant relationship with the EREs.

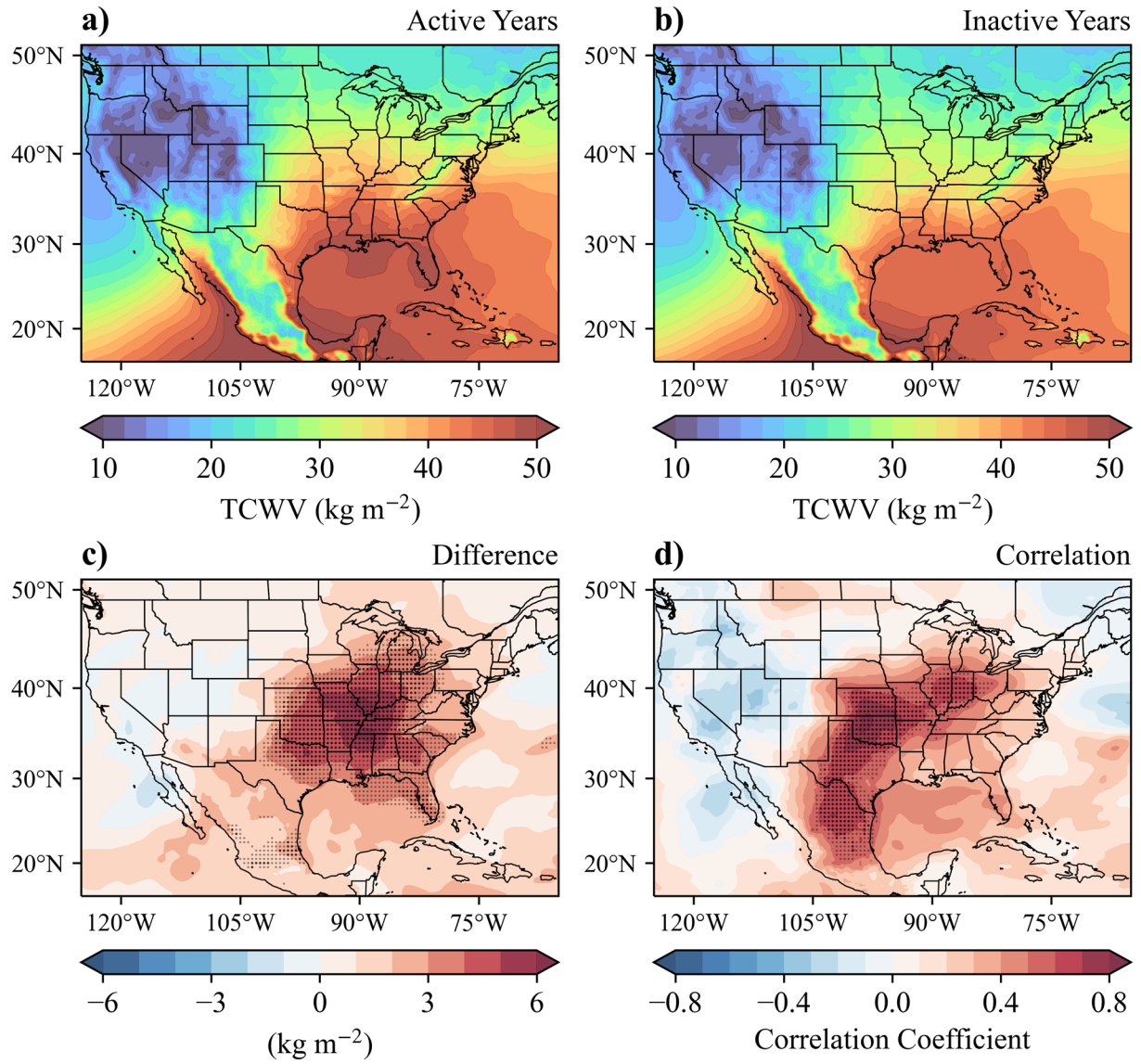

Figure 5.8: As in Fig. 5.4, but for ERA5 JJA-averaged total column water vapor (kg m^{-2}).

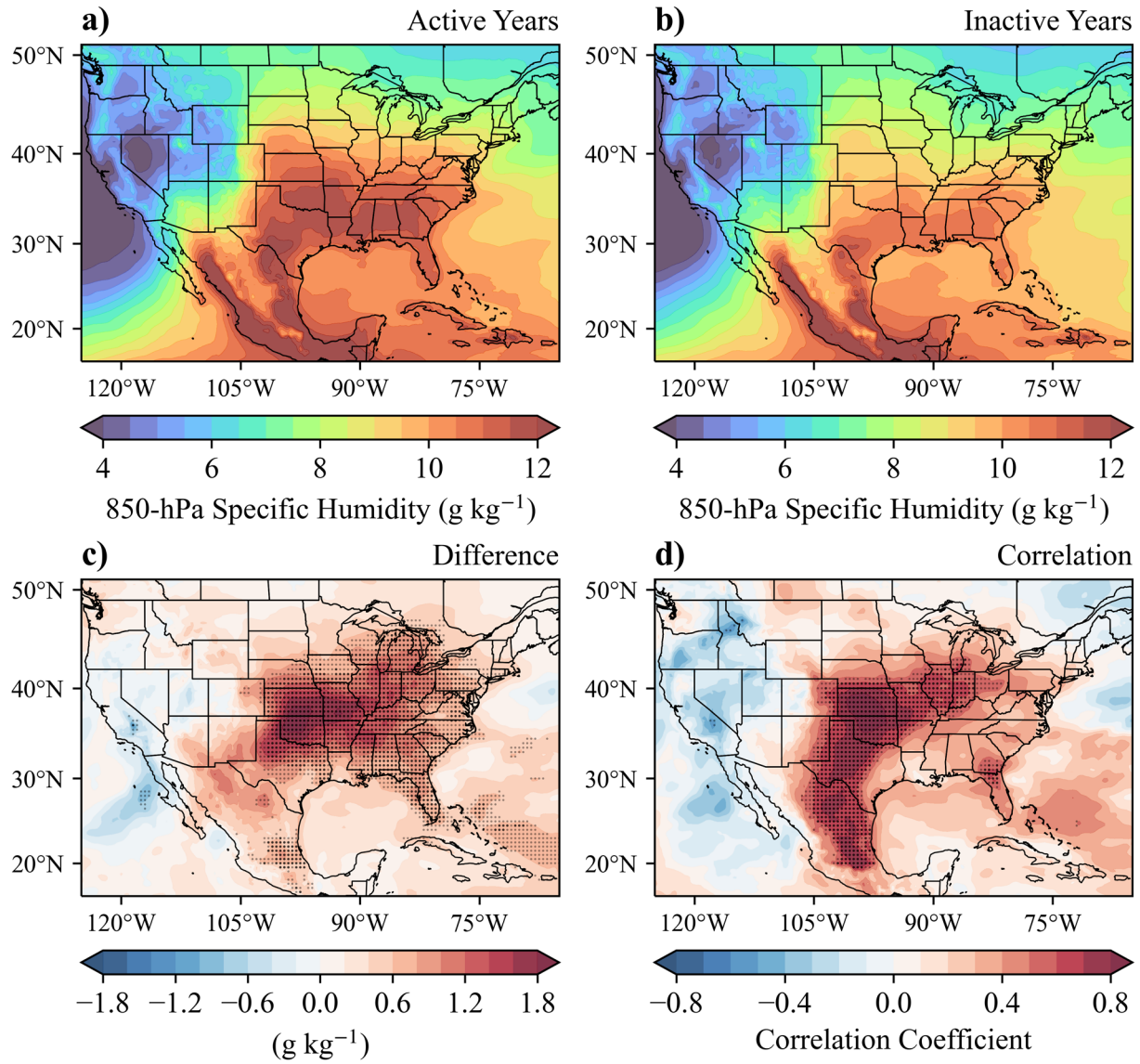

Figure 5.9: As in Fig. 5.4, but for ERA5 JJA-averaged 850-hPa specific humidity (g kg^{-1}).

5.2.3 Vertically Integrated Water Vapor Flux

Numerous studies have linked extreme rainfall to enhanced moisture transport (e.g., Mo et al., 1997), which can be quantified by the ERA5 vertically integrated water vapor flux (IVF) parameter, calculated as the total column water vapor (kg m^{-2}) multiplied by its vertically averaged horizontal advection (m s^{-1}). While the difference in JJA-averaged IVF between active and inactive years based on a side-by-side comparison may appear subtle (Fig. 5.10a–b), the magnitude of the composite difference is statistically significant at the 95% confidence level over a wide swath, stretching from the Western Gulf Coast to the Great Lakes region (Fig. 5.10c). A strong positive correlation ($r > 0.7$) exists over the same general region but is slightly more confined (Fig. 5.10d). The correlation with the meridional component of the IVF was statistically significant over that region, also at the 95% confidence level. Thus, there was a robust relationship between the JJA filtered EREs and northward moisture transport from the Gulf of Mexico to the Great Lakes. The vectors in both the composite difference and correlation maps indicate an anticyclonic flow pattern centered around the southeastern CONUS vicinity, suggesting that an anomalous anticyclone over that region may be responsible for anomalous poleward moisture transport around its western periphery.

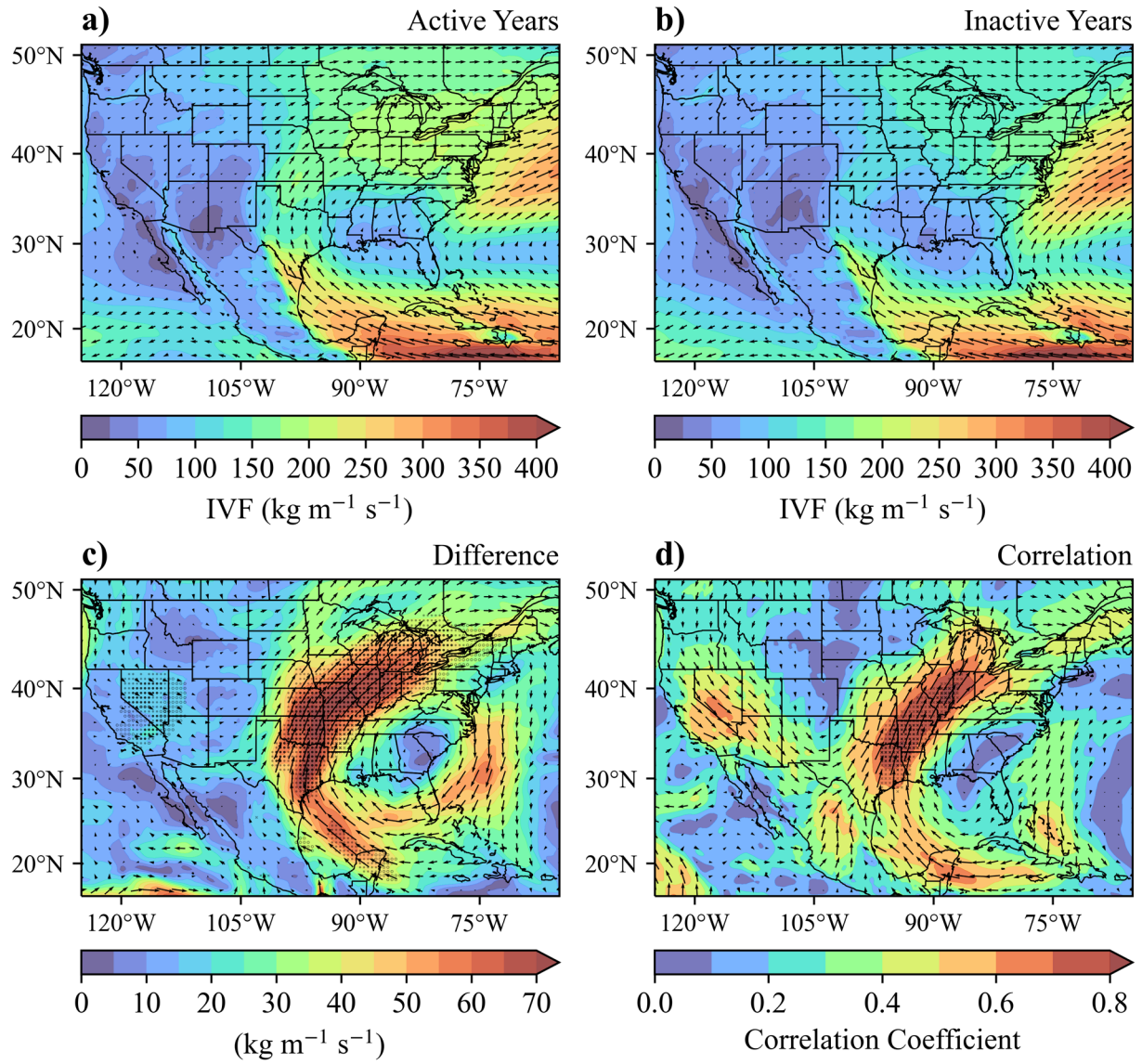

Figure 5.10: ERA5 JJA-averaged vertically integrated water vapor flux (kg m^{-1} s^{-1}) composite for (a) the active years (2016, 2021, 2010) and (b) the inactive years (2012, 2003, 2006). (c) Composite vector difference between (a) and (b) (active−inactive). (d) Correlation coefficients in the direction of their maximum positive value of the detrended JJA filtered ERE index time series (2003–2022) with the detrended time series of ERA5 JJA-averaged vertically integrated water vapor flux at each grid point. In (c) and (d), using the same significance testing methods as in Fig. 5.4c–d, but with right-tailed tests, any stippling with solid dots indicates where the magnitude of the composite difference in (c) or correlation coefficient in (d) is statistically significant at the 90% (translucent stippling; $\alpha_{FDR} = 0.2$) and 95% (opaque stippling; $\alpha_{FDR} = 0.1$) confidence levels. Any stippling with small open circles indicates statistical significance only in the zonal direction and any stippling with small ex symbols indicates statistical significance only in the meridional direction at the respective confidence levels using two-tailed tests.

5.2.4 Wind Fields

Since moisture transport is dependent on both low–mid-level moisture and flow patterns, it is important to perform the analysis on wind fields at different levels of the atmosphere. This can help identify layers where the flow patterns may have a significant relationship with EREs. In addition to 10-m winds, where no robust relationships were found (not shown), wind fields at 925, 850, 700, 500, 300, and 200 hPa were analyzed.

At 925 hPa (not shown), a flow pattern begins to emerge in the composite difference map that closely resembles the IVF pattern, but there is no statistical significance. At 850 hPa (Fig. 5.11), the same flow pattern becomes more apparent in both the composite difference and correlation maps. Correlation coefficients with southwesterly 850-hPa winds exceed 0.5 from eastern Texas to the Great Lakes (Fig. 5.11d), but there is still no statistical significance. Thus, unlike moisture content at 925 and 850 hPa, there were no robust relationships found between EREs and flow patterns at those levels.

At 700 hPa, the general flow patterns appear different than at 850 hPa, with much weaker southerly flow from the western Gulf of Mexico through the High Plains (Fig. 5.12a–b). However, a much stronger signal emerges in the relationship between EREs and 700-hPa wind compared to lower levels, especially from the correlation analysis. A strong correlation ($r > 0.7$) with southwesterly flow appears from the Texas Gulf Coast to the Midwest with statistical significance at the 95% confidence level with the northward component (Fig. 5.12d). This pattern is very similar to the correlation with IVF (Fig. 5.11d).

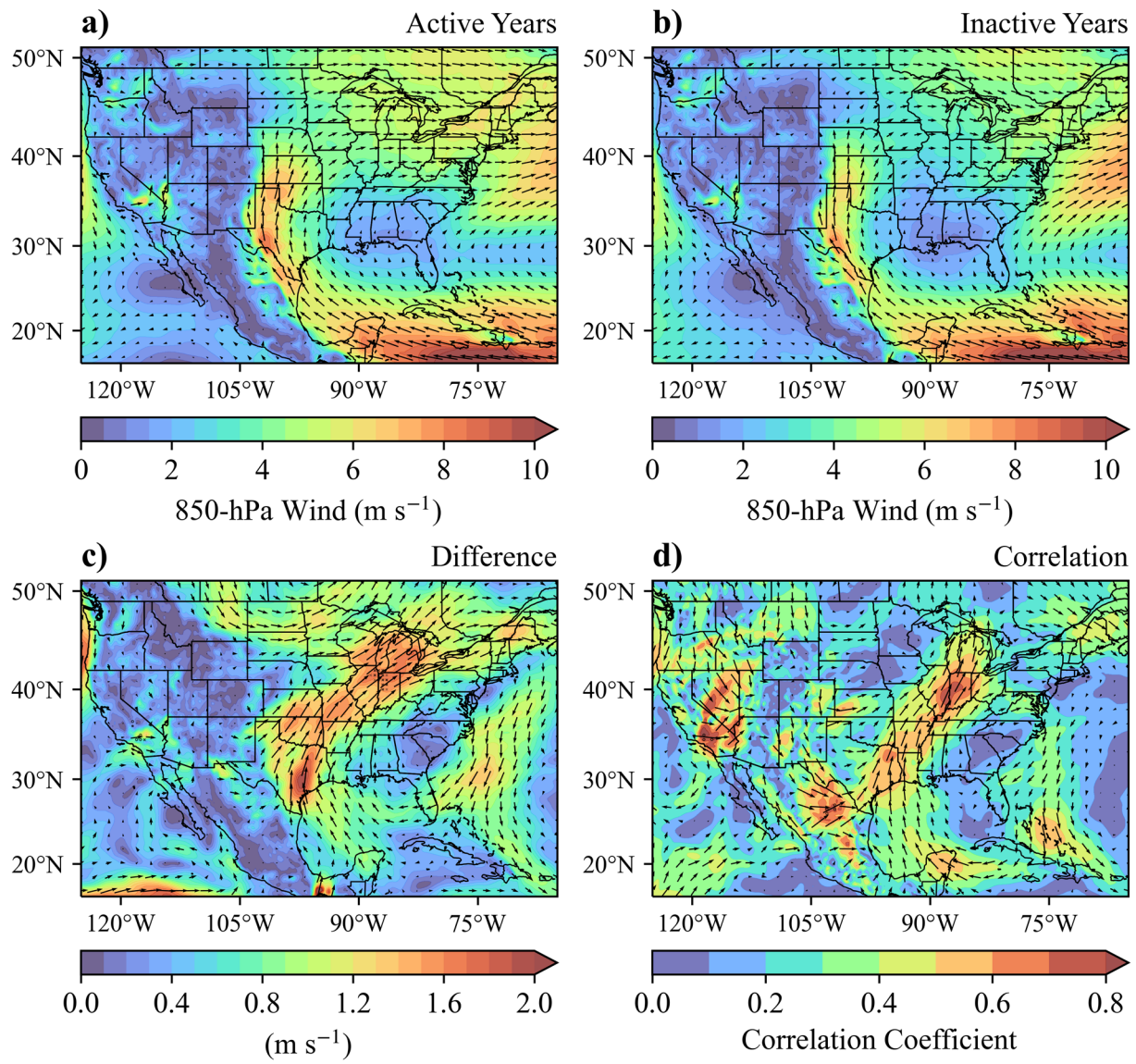

Figure 5.11: As in Fig. 5.10, but for 850-hPa wind (m s^{-1}).

At 500 hPa, the JJA-averaged flow pattern is also different from lower levels that were analyzed (Fig. 5.13a–b), with strong zonal flow dominating across the northern CONUS into Canada and very weak flow over the southern CONUS. One notable side-by-side difference between the active and inactive years is that the average 500-hPa flow over the northern CONUS and Canada during the active years is stronger and more zonal. This indicates that the active summers likely featured a stronger mid-level flow with less prominent ridging over the western

CONUS than during the inactive summers. In the composite difference map (Fig. 5.13c), the absence of ridging appears as a troughing pattern over the western CONUS, and the composite difference in the southerly flow was statistically significant at the 90% confidence level over the Missouri vicinity. A similar pattern appears in the correlation map, but with greater statistical significance (95% confidence) in the southerly component over a larger area (Fig. 5.13d). When

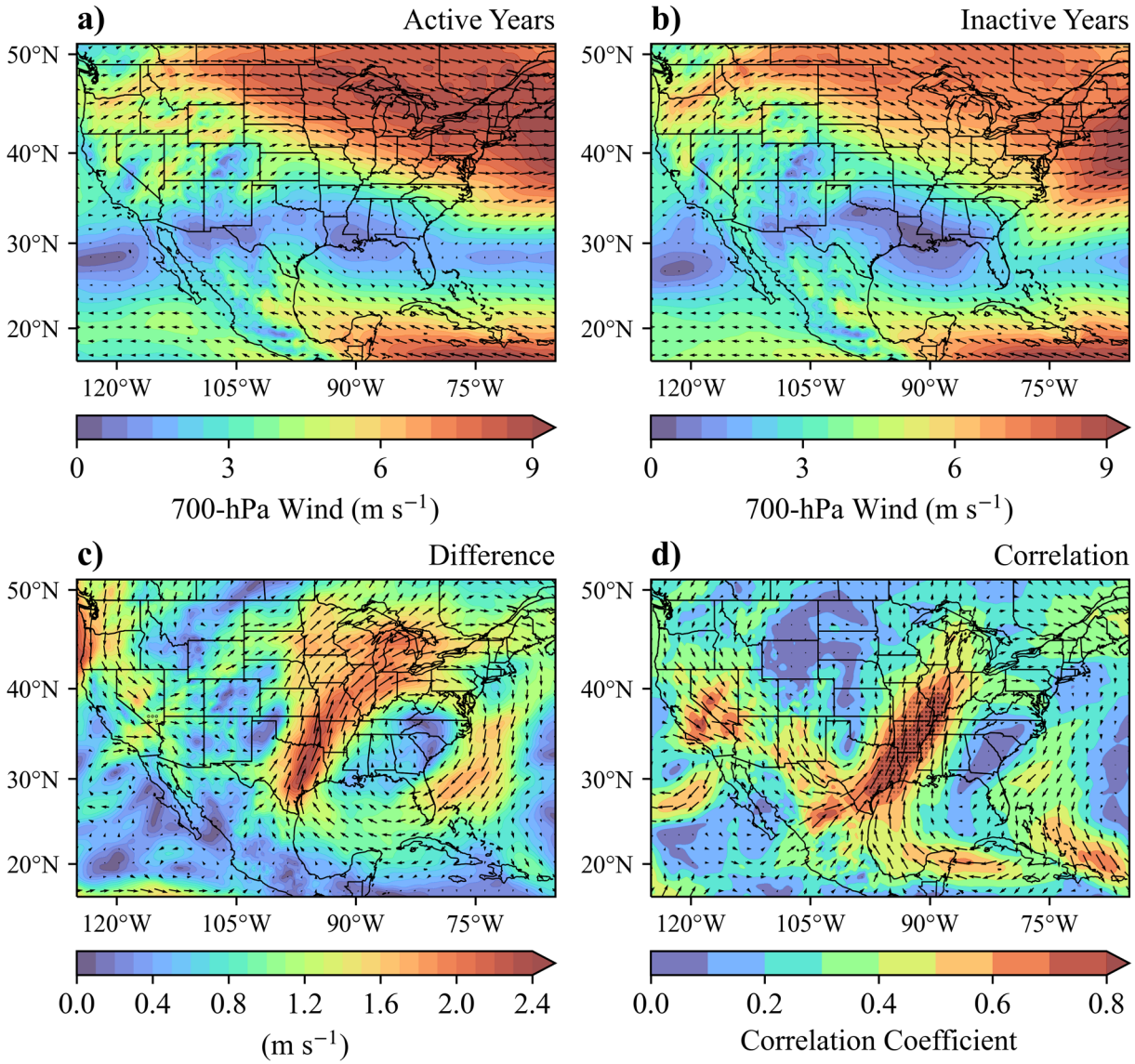

Figure 5.12: As in Fig. 5.10, but for 700-hPa wind (m s^{-1}).

comparing the 500-hPa flow composites for active and inactive years (Fig. 5.13a–b), the significant correlations and composite differences over the Lower–Mid Mississippi Valley region are indicative of less northerly 500-hPa flow over those regions. This significance is surprising given the relatively weak flow magnitudes over those regions.

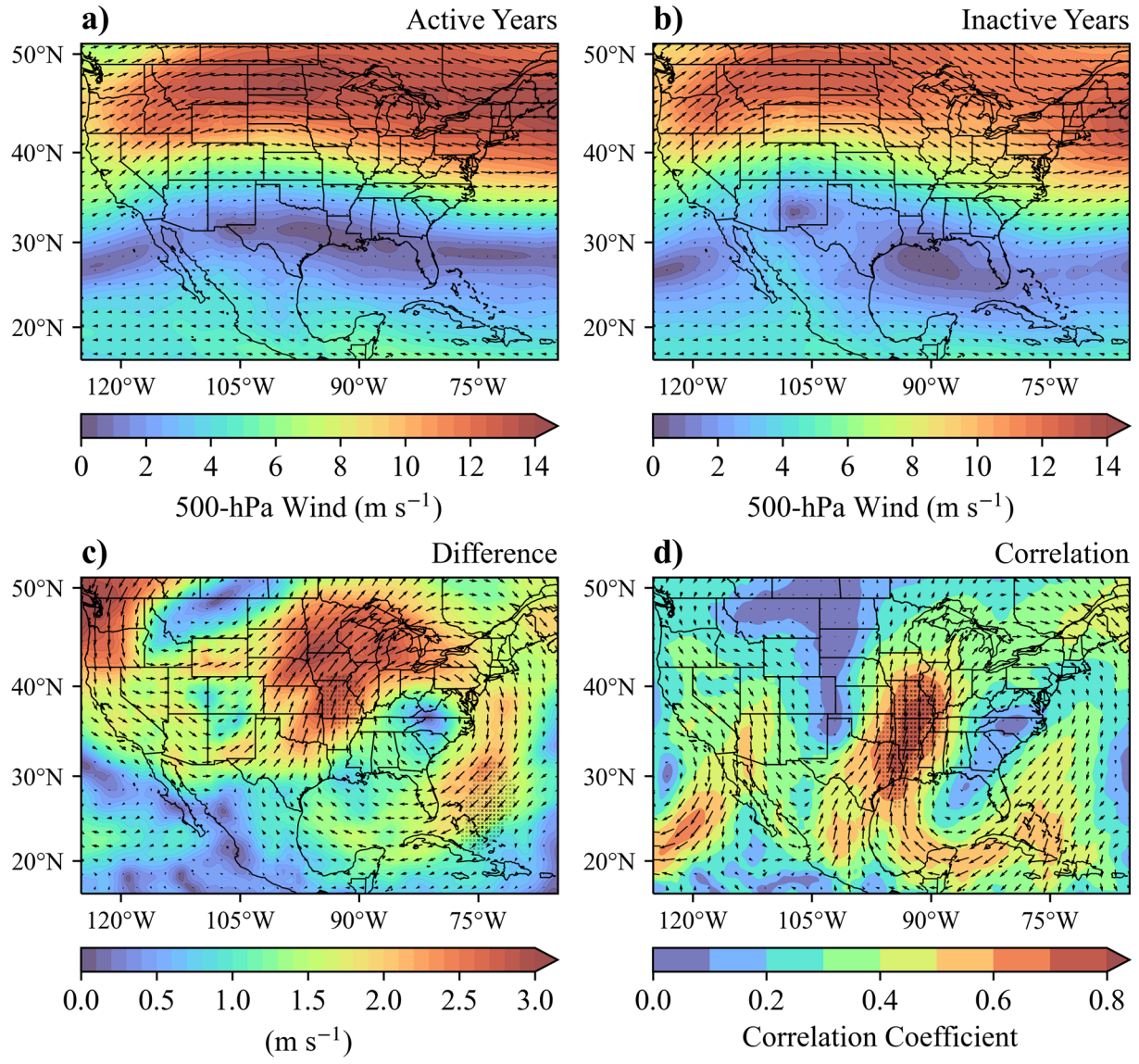

Figure 5.13: As in Fig. 5.10, but for 500-hPa wind (m s^{-1}).

At jet stream level (300–200 hPa), the flow patterns that emerge from the composite and correlation analysis results (not shown) appear very similar to those observed in the 500-hPa flow analysis. The strongest correlations ($r > 0.6$) were found with southwesterly upper-level winds over the Mid–Upper Mississippi Valley, but there was no statistical significance in the composite differences or correlation coefficients. The lack of evidence of a southward-shifted polar jet stream during active years does not support the findings of Flanagan et al. (2018).

5.2.5 Geopotential Height

Large scale flow patterns on isobaric surfaces aloft are driven by geopotential height gradients, with the flow being approximately geostrophic above the planetary boundary layer and its speed being dependent on the strength of the gradient. Performing composite and correlation analysis on JJA-averaged geopotential height fields can be useful in distinguishing any prominent patterns that are associated with more extreme rainfall. It is expected that the height patterns that are associated with more active years drive the flow patterns that contribute to enhanced moisture transport from the subtropics (Fig. 5.10). Geopotential height fields were analyzed at the 925-, 850-, 700-, 500-, and 250-hPa pressure levels.

The JJA mean geopotential height patterns at 925 hPa (not shown) and 850 hPa (Fig. 5.14a–b) are similar to the mean sea level pressure patterns (not shown), with the most notable feature being the semipermanent North Atlantic Subtropical High (NASH). During the active summers, the NASH extended farther to the west-northwest than during the inactive summers, with an area of higher 850-hPa heights evident over the southeastern CONUS and Southern Appalachians (Fig. 5.14c). Weak to moderate positive correlations ($0.4 < r < 0.6$) between the JJA filtered ERE index and 850-hPa heights were found over the same general region (Fig. 5.14d), but none were

statistically significant. Similar results were obtained from the mean sea level pressure and 925-hPa height fields (not shown), except that the positive correlations over the Southeast were slightly weaker. While these results were not statistically significant, higher heights over the Southeast relative to the Northern Plains is a signal for a stronger northwest–southeast height gradient during more active summers. This gradient would likely be associated with a stronger southwesterly flow

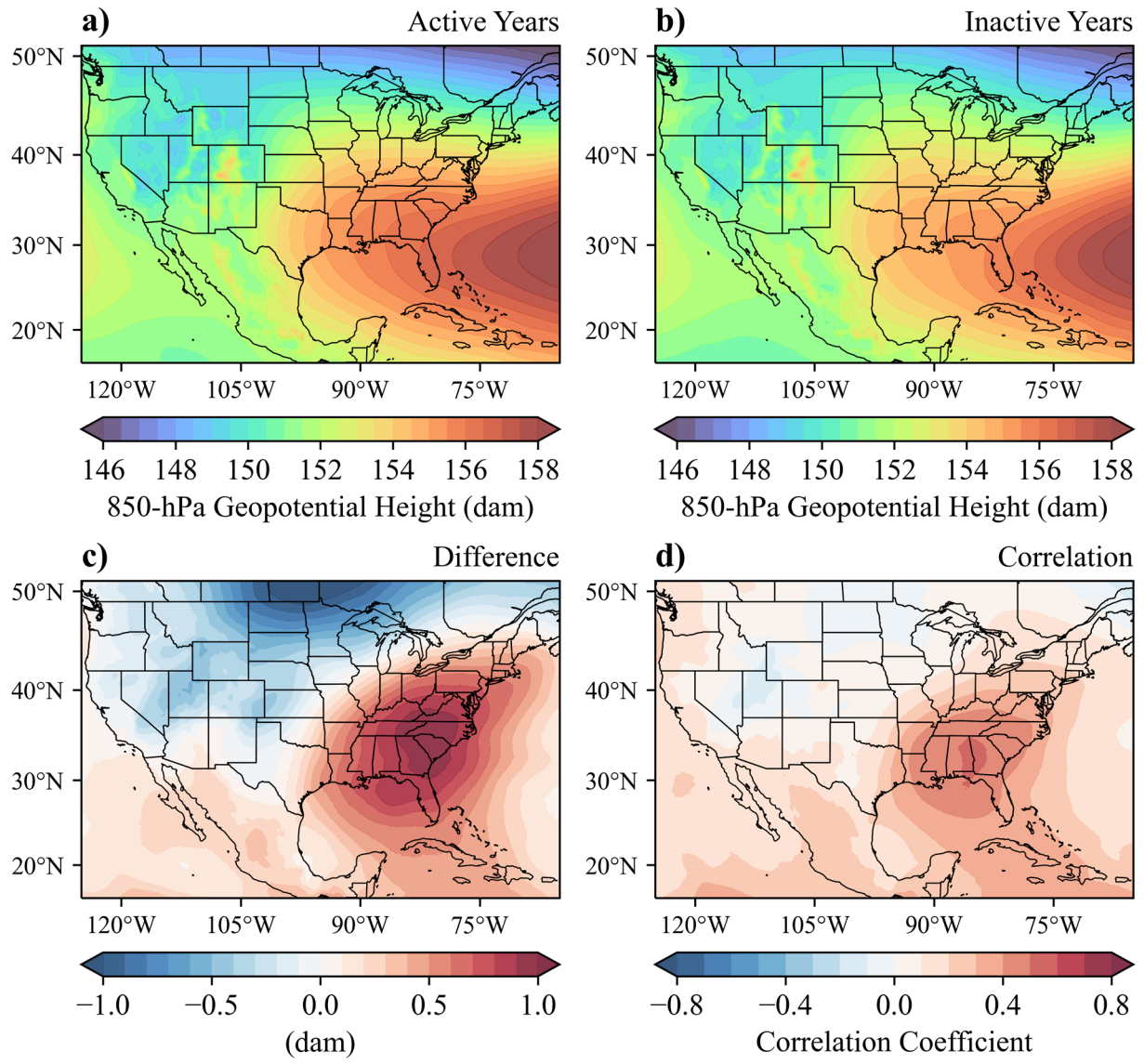

Figure 5.14: As in Fig. 5.4, but for ERA5 JJA-averaged 850-hPa geopotential height (dam).

from the Southern Great Plains to the Great Lakes (Fig. 5.11), which would enhance the moisture transport (Fig. 5.10) assuming that the moisture over the Southern Great Plains is relatively high, as was the case during more active summers (Fig. 5.9).

The analysis with 700-hPa geopotential heights (not shown) reveals a pattern that is similar to both the 850-hPa and 500-hPa results, but there is no statistical significance. In contrast to the 850-hPa geopotential height pattern, at 500 hPa, ridging is more evident over the southwestern CONUS (Fig. 5.15b), commonly referred to in the weather community as the "Sonoran Heat Ridge". The mid-level ridge associated with the NASH appears to be merged with the Sonoran Heat Ridge during the active years (Fig. 5.15a), but since the composites are seasonally-averaged, this may imply the presence of more prominent ridging over the eastern CONUS, which appears as a statistically significant (95% confidence) composite difference maximized over the Southern Appalachians (Fig. 5.15c). This height anomaly is often referred to in the weather community as the "Great Smokies Heat Ridge", likely associated with significantly higher 2-m temperatures over the eastern CONUS during the active years (Fig. 5.5). A moderate to strong correlation ($0.6 < r < 0.8$) between EREs and 500-hPa heights is evident over the Gulf of Mexico, which is also statistically significant at the 95% confidence level. This pattern appears to be a westward extension of mid-level ridging associated with the NASH. The enhanced 500-hPa height gradient that is created between the enhanced ridging over the southeastern CONUS relative to the Eastern Rockies could be responsible for stronger southerly 500-hPa flow that correlates with more active summers (Fig. 5.13d). The same would be true for the 700-hPa flow pattern (Fig. 5.12d).

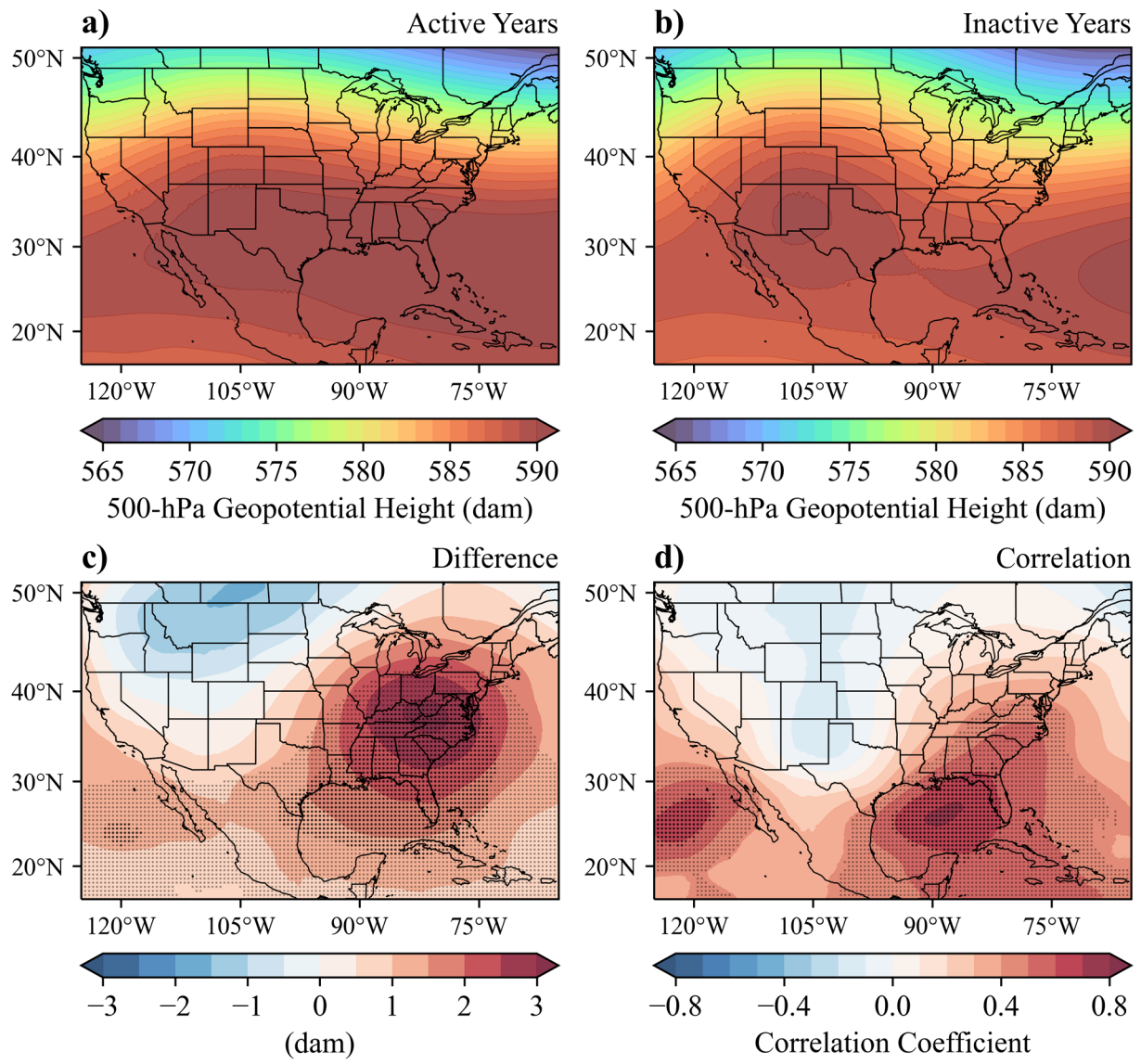

Figure 5.15: As in Fig. 5.4, but for ERA5 JJA-averaged 500-hPa geopotential height (dam).

From the JJA composites of 250-hPa heights, upper-level ridging is most evident over Mexico and the southwestern CONUS, but no longer associated with the NASH (Fig. 5.16a–b). The composite difference with 250-hPa heights reveals a similar result to the 500-hPa analysis, with the greatest statistically significant difference centered over the Ohio Valley. Statistical significance in the positive composite difference at the 95% confidence level was also found over

almost all of the tropics and subtropics within the analysis domain. The correlation analysis with 250-hPa heights, however, reveals lower confidence in the relationship, with statistical significance only at the 90% confidence level and slightly weaker correlations than at 500-hPa ($0.5 < r < 0.7$). This is still a robust signal that a significant relationship exists between the EREs and stronger upper-level ridging over the subtropics and southeastern CONUS.

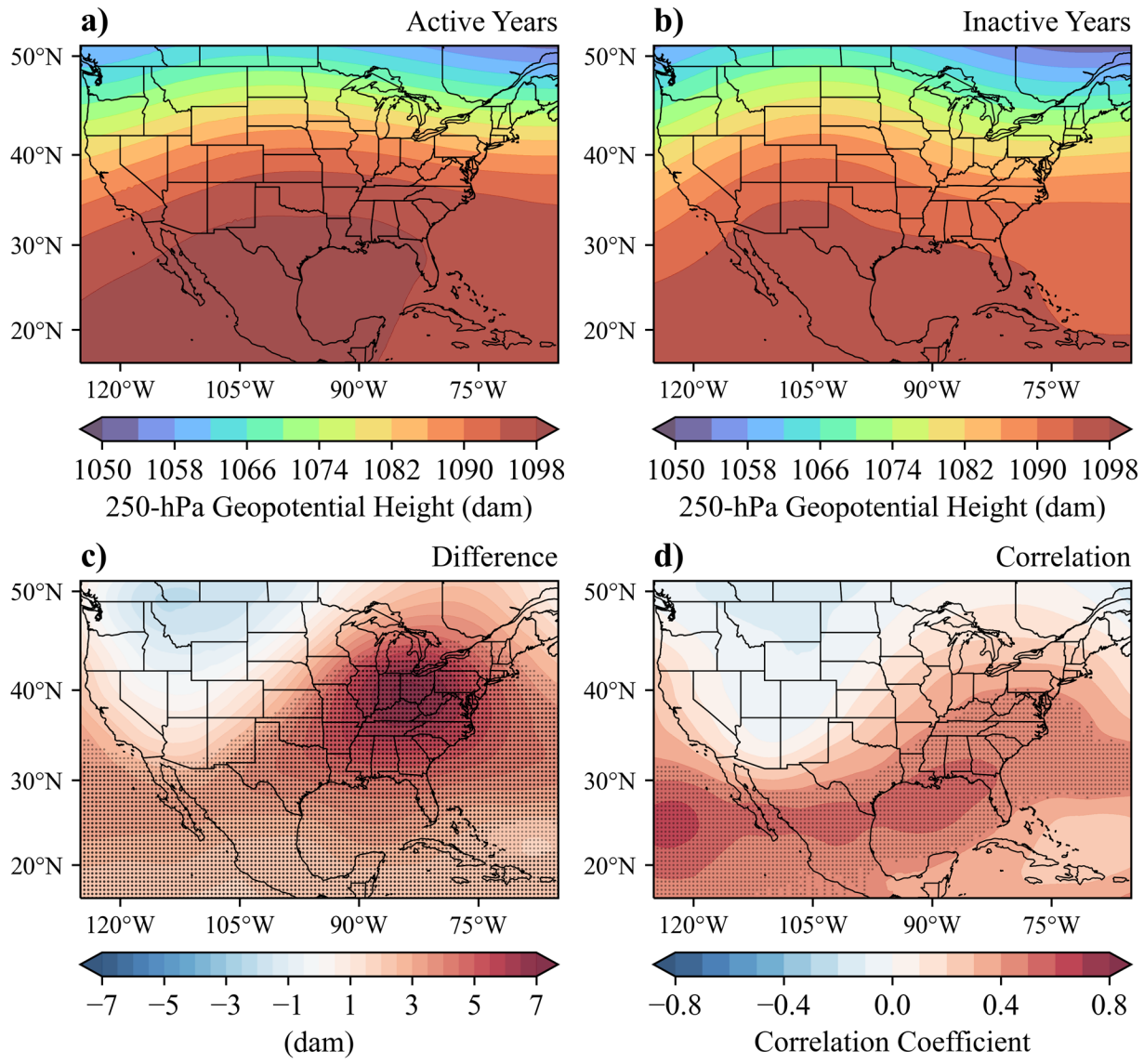

Figure 5.16: As in Fig. 5.4, but for ERA5 JJA-averaged 250-hPa geopotential height (dam).

5.2.6 Preceding Winter & Spring LSMPs

Composite and correlation analysis with the JJA filtered ERE index time series using ERA5 fields averaged over preceding seasons (i.e., winter and spring) can identify LSMPs that may share a lagged relationship with the summertime EREs. Awareness of these LSMPs can provide additional insight into why interannual variations in summertime EREs occur and can potentially aid in seasonal forecasts of summertime extreme rainfall activity over the domain. However, unlike correlations between JJA EREs and JJA-averaged fields, it is more difficult to infer any direct physical linkages between JJA EREs and LSMPs occurring during preceding months. Given the short sample period, correlations may appear by chance, and thus, caution should be applied when attempting to infer any cause-and-effect relationships.

During preceding spring months (March–May), the most robust correlations appeared with mid–upper-level wind and geopotential height fields, indicating a more prominent subtropical jet stream over Mexico and a weaker polar jet stream over the northern CONUS. For example, at 500-hPa, strong correlations ($r > 0.7$) with easterly winds over the northern CONUS suggest a weaker polar jet stream, and strong correlations with southwesterly winds over Mexico suggest a more prominent subtropical jet stream during more active years (Fig. 5.17a). This jet stream pattern corresponds to lower geopotential heights over the northern Mexico vicinity and higher heights over the tropics and southwestern Canada (Fig. 5.17b), statistically significant at the 90% confidence level. Very similar results appeared using composite analysis and when using upper level (i.e., 300-hPa) fields (not shown).

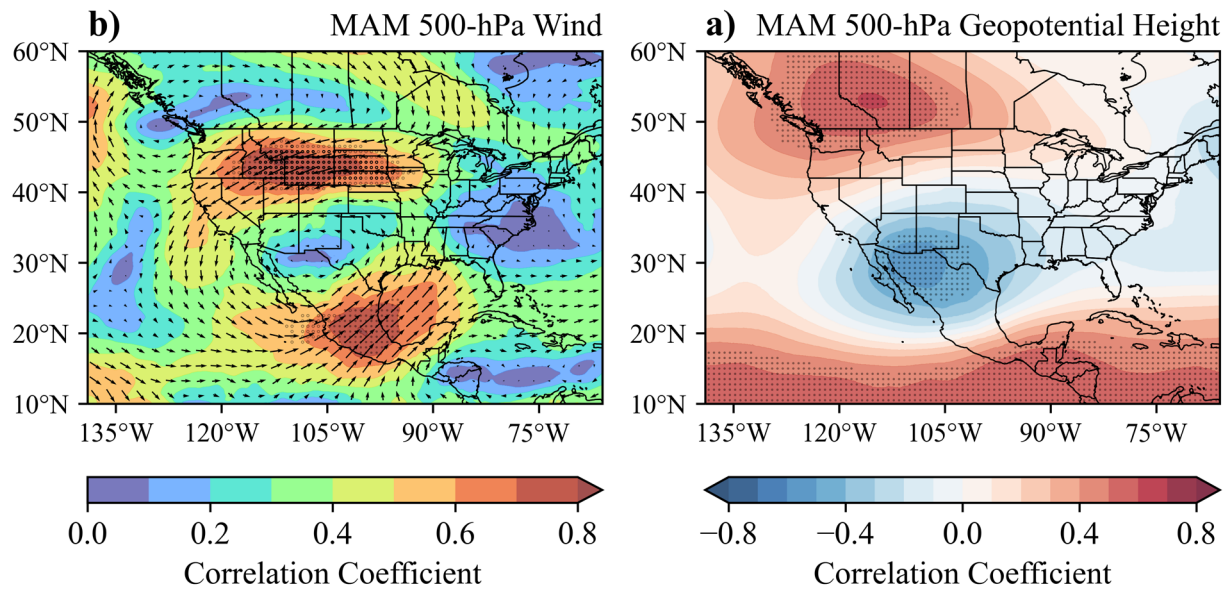

Figure 5.17: (a) As in Fig. 5.11d, but for March–May-averaged 500-hPa wind and (b) as in Fig. 5.4d, but for March–May-averaged 500-hPa geopotential height. ERA5 fields were linearly interpolated onto a 0.75° resolution grid (140–65°W, 9–60°N; $N = 6969$ tests) for the significance testing.

Correlation analyses between JJA EREs and March–May-averaged 2-m temperatures and precipitation (not shown) suggest that more active years may have exhibited cooler temperatures and more rainfall over the Southern Great Plains vicinity than the inactive years, but there was no consistent statistical significance. However, these correlations would be consistent with the enhanced subtropical jet stream and negative 500-hPa geopotential height correlations just to the west (Fig. 5.17). A reasonable hypothesis emerges from this finding: warmer temperatures and below average rainfall during the spring over the Southern Great Plains could create drought conditions that persist into the summer months and limit extreme rainfall activity. To explore the relationship between antecedent drought over the Southern Great Plains and JJA extreme rainfall activity, the Palmer Drought Severity Index (PDSI; Alley, 1984) averaged over the state of Texas was correlated with the timeseries of neighborhood event counts (radius = 500 km) at each point

on a 0.25° grid. PDSI time series data were obtained from the NOAA National Centers for Environmental Information Climate Division dataset (https://psl.noaa.gov/data/timeseries/; Vose et al., 2014). A positive PDSI is associated with moist conditions, whereas a negative PDSI is associated with drought conditions. Statistically significant positive correlations with March–May-averaged Texas PDSI can be found over the majority of the domain west of the Mississippi Valley (Fig. 5.18a). This finding suggests that summertime extreme rainfall activity may not only be linked to contemporaneous drought conditions (Fig. 5.18b), but also antecedent drought conditions over the Southern Great Plains, likely impacting ERE activity throughout the Great Plains. The

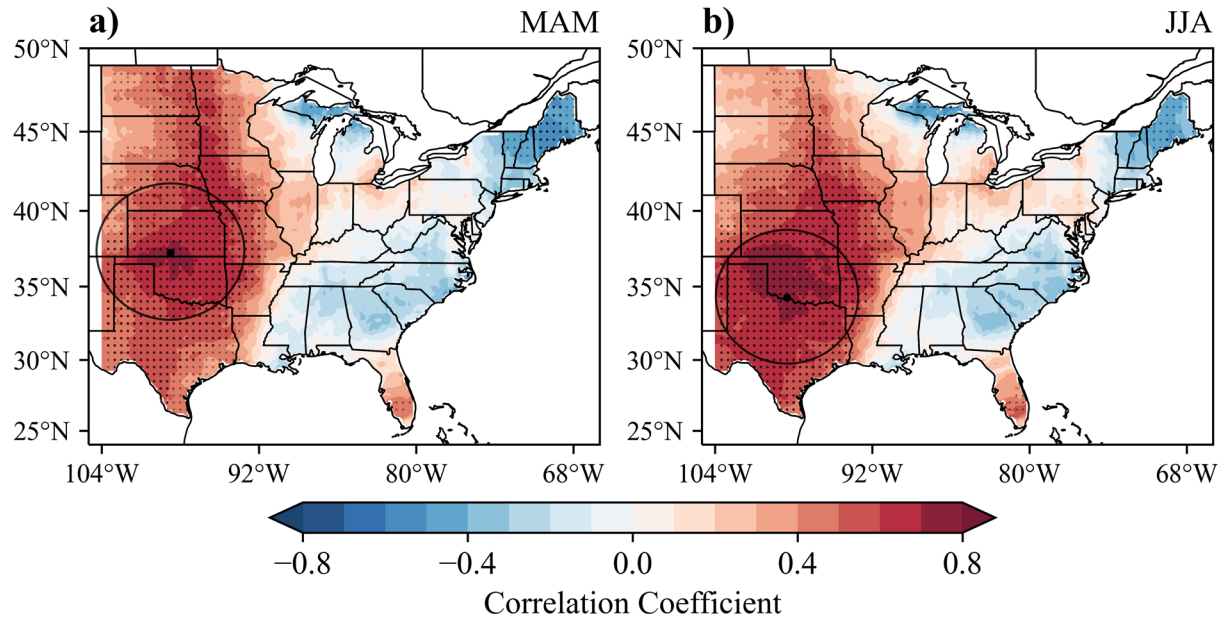

Figure 5.18: Maps of Pearson correlation coefficients between the JJA filtered ERE 500-km neighborhood count time series (2003–2022) at each point on a 0.25° grid over the full domain and the time series of (a) March–May-averaged and (b) JJA-averaged Palmer Drought Severity Index averaged over the state of Texas. Stippling indicates where the correlation coefficients are statistically significant using the FDR approach ($N = 7990$ tests) at the 90% (translucent stippling; $\alpha_{FDR} = 0.2$) and 95% (opaque stippling; $\alpha_{FDR} = 0.1$) confidence levels from Monte Carlo simulations ($n = 5000$ recalculations of the correlation coefficient at each grid point from random samples of the count time series with replacement). The black circles indicate the 500-km radius where the correlation is the strongest, with the center point represented by a black dot.

linkage to contemporaneous drought over the Southern Great Plains is expected due to the correlations found with JJA-averaged precipitation and low-level moisture over that region, which affects downstream moisture transport towards the north and northeast. However, drought over the Southern Great Plains has no significant correlation with EREs east of the Mississippi Valley, except over New England, where a reversed relationship was found. Similar results were found using wintertime (December–February) averaged Texas PDSI, but with weaker correlations and maximum statistical significance only at the 90% confidence level throughout most of the Great Plains.

Some of the strongest correlations with global circulation patterns were found when using December–February-averaged ERA5 fields, but it is difficult to infer any direct physical linkage to EREs during the following summer. These larger correlations are more likely a byproduct of stronger interannual variability of wintertime patterns compared to summertime patterns. During boreal winters, LSMPs over North America are often influenced by atmosphere–ocean coupling associated with the recurrent pattern of positive sea surface temperature anomalies over the central and eastern tropical Pacific known as El Niño, which varies naturally on interannual time scales. Any strong correlations with December–February-averaged fields reveal patterns that are often associated with El Niño conditions (e.g., Rasmusson and Wallace, 1983). Indeed, the correlation analysis with December–February-averaged global sea surface temperatures confirms the connection to El Niño, with moderate to strong correlations ($0.6 < r < 0.8$) evident over much of the central and eastern equatorial Pacific and widespread statistical significance at the 90% confidence level (Fig. 5.19). The pattern of sea surface temperature correlations also resembles a positive phase of the Pacific Decadal Oscillation (PDO), with a “blob” of negative correlations

over the north-central Pacific and an arc of positive correlations over the northeast Pacific (e.g., Mantua and Hare, 2002).

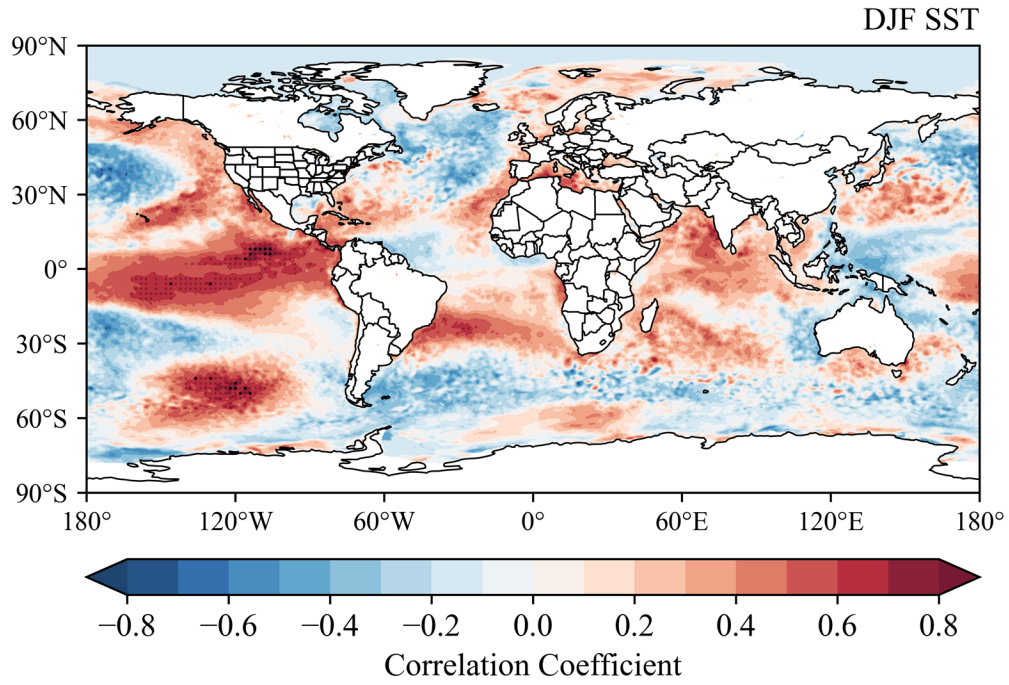

Figure 5.19: As in Fig. 5.4d, but for ERA5 December–February-averaged sea surface temperature, except that the 0.25° resolution ERA5 spatial fields were linearly interpolated onto a 2° resolution grid with all grid points over land areas excluded (179°W–179°E, 89°S–89°N; N = 10684 tests) for significance testing.

After removing any linear trends in the data, statistically significant correlations between JJA filtered EREs and several seasonally-averaged climate indices are evident (Table 5.1). Time series data for various climate indices were obtained from the NOAA Physical Sciences Laboratory website (https://psl.noaa.gov/gcos_wgsp/Timeseries/). For example, the December–February-averaged Niño 3.4 index (area averaged sea surface temperature from 5°S–5°N and 170–120°W) had a moderate positive correlation with JJA filtered EREs, with statistical significance at the 99% confidence level. However, there is no correlation with the JJA-averaged Niño 3.4 index and even

a slight reversal in the correlation coefficients relative to December–February and March–May, which would potentially indicate a neutral or cold phase of ENSO during more active summers. One may speculate that more EREs occurred during years transitioning from El Niño to neutral or even La Niña conditions. However, testing this hypothesis on all three active years gives inconsistent results. For example, while 2016 did feature a strong El Niño transitioning to a neutral phase, 2021 featured a La Niña transitioning to a neutral phase. Thus, using El Niño as a predictor of JJA filtered EREs may be ineffective, and a longer period of study should be used to assess seasonal predictability.

Index	***r* (DJF)**	***r* (MAM)**	***r* (JJA)**
PDSI_TX	0.56*	0.63**	0.67**
Niño 3.4	0.56**	0.50*	-0.16
PDO	0.47*	0.52*	0.42
GLBT	0.47*	0.48*	0.14

* Significant at the 95% confidence level.
** Significant at the 99% confidence level.

Table 5.1: Pearson correlation coefficients between the 2003–2022 detrended JJA filtered ERE index time series and the 2003–2022 detrended (1) Palmer Drought Severity Index averaged over the state of Texas (PDSI_TX), (2) Niño 3.4 sea surface temperature index (Niño 3.4), (3) Pacific Decadal Oscillation (PDO), and (4) global average temperature anomaly using stations and sea surface temperatures (GLBT), averaged over the preceding December–February (DJF), March–May (MAM), and corresponding June–August (JJA). Asterisks represent the level of statistical significance, determined using Monte Carlo testing (n = 5000 recalculations of the correlation coefficient on random samples of the climate index time series with replacement).

5.3 Discussion

In this chapter, we have identified several large-scale meteorological features that likely play a role in the occurrence of summertime EREs over the central and eastern CONUS, especially over the Great Plains, Midwest, and Ohio Valley (Fig. 5.2c). Based on prior studies, a key ingredient

for the occurrence of heavy rainfall over the central CONUS is northward moisture transport from the Gulf of Mexico (e.g., Mo et al., 1997; Fig. 1.7). The robust correlation between the ERE index time series and JJA-averaged northward IVF from the Texas Gulf Coast to the Great Lakes (Fig. 5.10) is validated due to consistency with these prior studies, despite differences in the definitions of extreme rainfall. This pattern of moisture transport originating from the Western Caribbean is highly reminiscent of the "Mayan Express" (Dirmeyer and Kinter, 2009), found during periods of excessive rainfall during the summer over the central CONUS (section 1.3).

Significant correlations with the ERE index were found with low-level (surface–850-hPa) moisture parameters over the Southern and Central Great Plains (Figs. 5.6 and 5.9), with a lack of statistical significance with moisture at 700 hPa and above. However, the southerly flow correlation associated with enhanced moisture transport was only found to be statistically significant at 700 and 500 hPa (Figs. 5.12 and 5.13). The mismatch in the pressure levels that yield statistical significance in the moisture and wind fields may be a biproduct of greater interannual variability at those levels. For example, low-level moisture may be more variable from year to year than moisture at higher levels, and vice versa for flow, which is dampened by friction in the low levels. Thus, moisture transport is likely maximized near the top of the boundary layer, where the LLJ typically resides (near 850 hPa). While the flow correlation at 850 hPa was not statistically significant (Fig. 5.11), it did have the same pattern as the correlation with IVF. In that case, our results are validated by previous findings that moisture transport around 850 hPa is the most relevant for EREs due to the role of the LLJ in producing widespread elevated convection (e.g., Schumacher and Johnson, 2009; Trier and Parsons, 1993). However, the location of the enhanced IVF and 850–500-hPa flow correlations was generally from the Texas Gulf Coast to the Great Lakes, which is east of where the Great Plains nocturnal LLJ typically resides (e.g., Shapiro et al.,

2016). Thus, we cannot connect the occurrence of a more prominent Great Plains LLJ to EREs during the summer, unlike Feng et al. (2016), who focused on the spring months. We note, however, that a linkage between the nocturnal LLJ over the Great Plains and the synoptic flow is an area of future exploration (see chapter 6).

A pattern of enhanced northward low-level moisture transport from the Gulf Coast to the Midwest would likely result from a stronger west–east pressure gradient in the low levels. Though we did not find statistical significance, there is still a suggestion that the flow pattern is related to a western extension of the NASH, which extends from the surface to 850 hPa based on our composites. This expansion of the NASH is most evident in the composite difference of 850-hPa heights (Fig. 5.14a–c). Zorzetto and Li (2021) studied the impacts of the NASH western ridge position on daily JJA precipitation over the CONUS, applied to historical rainfall records from 1948–2019. It was found that the westward extent of the NASH at 850 hPa significantly modulates the frequency of JJA extreme rainfall, especially over the Southeast and Upper Midwest, where a farther west NASH ridge would reduce and increase extreme rainfall, respectively. Our results generally agree that a westward extension of the NASH corresponds to more EREs, but we do not find statistical significance in the pattern, possibly due to our inclusion of EREs over the full domain instead of only the Midwest. Further analysis would be needed to verify the importance of the NASH western ridge position since the impact on extreme rainfall is regionally dependent.

Statistical significance in the ERE relationship with geopotential height fields was only found in the mid–upper-levels. Based on the composite analysis with 500- and 250-hPa heights, we find significantly higher heights over the eastern CONUS, potentially indicating the presence of the Great Smokies Heat Ridge during the active summers (Figs. 5.15a–c and 5.16a–c). Correlation coefficients, however, are maximized with 500-hPa heights over the Gulf of Mexico (Fig. 5.15d),

suggesting that the western extension of mid-level ridging associated with the NASH is important. The association of mid–upper-level ridging over the eastern CONUS and Gulf of Mexico with EREs is likely a new finding that deserves attention in future studies.

While we did not examine changes in LSMPs through the 20-yr period to help explain the increasing trend found in the JJA filtered EREs (chapter 4), there have been other studies that have previously documented these changes. For example, Feng et al. (2016) examined trends in the environments associated with MCSs during April–June from 1979–2014 and found that the strength of the meteorological patterns leading to heavier rainfall increased. For example, their study identified a significant increasing trend in surface moisture over the Central Plains and Mid-Mississippi Valley region (Fig. 1.9b), which is the same general area as the significance in the 2-m dewpoint composite difference in our study (Fig. 5.6c). According to Lenderink et al. (2017), large-scale moisture convergence appears to accelerate with surface dewpoint, and the strength of the moisture convergence has been directly linked to the size of extreme-rain-producing convection (e.g., Loriaux et al., 2017). Thus, an increasing trend in low-level moisture and associated convergence through the period may help to explain the apparent increase in extreme-rain-producing storm size (chapter 4). At 850-hPa, the trend in specific humidity was found by the Feng et al. (2016) study to be maximized over the Southern and Central Great Plains (Fig. 1.9d), closely aligned with the strong positive correlations we found with JJA filtered EREs (Fig. 5.9d). Their study also documented an increasing trend in southerly 850-hPa winds over the Great Plains in association with the LLJ, linked to increasing heights over the southeastern CONUS and decreasing heights over the Southern Rockies (Fig. 1.9d). Li et al. (2011) also documented a westward shift in the NASH western ridge position from 1948–2007 and the trend is expected to continue due to anthropogenic climate change based on numerical model simulations. If these

patterns are indeed increasing, there may be a valid physical explanation for the trends discussed in chapter 4 as well as reason to believe that the trends may continue.

Regarding LSMPs that were found during preceding winter and spring months, one physically plausible connection may be the effect of antecedent drought conditions over Texas during the spring on summertime extreme rainfall activity throughout the Great Plains (Fig. 5.18a). Drought conditions over the Southern Great Plains during the spring may persist into the summer months due to land-atmosphere feedbacks related to soil moisture (e.g., Miralles et al., 2019). There is also some suggestion that JJA filtered EREs may be connected to patterns related to El Niño, which would be supported by previous studies finding that above average summertime precipitation is favored over the Central and Northern Great Plains during El Niño years, with below average precipitation over the eastern CONUS (Wang et al., 1999). Armal et al. (2018) also found connections between summertime precipitation and El Niño, as well as the Pacific Decadal Oscillation and global temperatures, but the effects were regionally dependent. We also found correlations with those indices (Table 5.1), but there was no statistical significance, regionally. Again, however, further research is needed to assess the predictability of summertime EREs using climate indices.

Chapter 6

Intense NW–SE Oriented ERE Environmental Conditions

Several intense NW–SE oriented swaths of extreme rainfall were evident over a large portion of the central CONUS during JJA (Figs. 3.5c and 3.10a), often associated with the most intense EREs. These EREs are associated with southeastward-training convection from MCSs, which appears to be almost an exclusively summertime occurrence, whereas other seasons typically include more EREs associated with northeastward-training convection (Fig. 3.5). Previous studies have not explicitly recognized southeastward-training MCSs as leading culprits for the most widespread and intense EREs during the summer. Thus, it can be useful to distinguish the environmental conditions and LSMPs associated with the occurrence of these events to aid in short-term forecasting.

Unlike the previous chapter, which focused on seasonally-averaged environmental conditions, this chapter focuses on environmental conditions that are directly associated with a specific type of ERE. Meteorological field composites from five selected cases of intense NW–SE oriented EREs were examined. Details on the specific selected cases will be provided in section 6.1, and specific environmental conditions observed relating to mid–upper-level, low-level, moisture, and surface parameters will be presented in sections 6.2–6.5. The key findings and potential implications will be discussed in section 6.6.

6.1 Case Selection

Five cases of EREs producing NW–SE oriented extreme rainfall swaths were objectively selected from the 20-yr ERE database (Table 6.1). An event qualified as NW–SE oriented if the forward

azimuth of the 12-hr exceedance swath was at least 110° (east of north) with a major axis length of at least 100 km. Among the NW–SE oriented EREs with a major axis length of at least 200 km, the cases were ranked by total exceedance volume (i.e., sum of exceedance above the 10-yr ARI threshold from all points of exceedance in the event), and the top five exceedance events were selected for analysis. Total exceedance volume was used as a measure of an ERE's spatial coverage and intensity, so the top-ranked events would be most likely to appear as dark streaks in Fig. 3.5. Table 6.1 displays the event information, and each event was assigned a case number based on its total exceedance volume rank. Of particular note is that, while the peak accumulation hours vary, all five events can be classified as nocturnal according to the definition given in section 2.1.4.5.

Case	ID	Date	Peak Hour (UTC)	End (UTC)	Lat (°N)	Lon (°W)
1	8899	2021-06-25	0100	1200	39.91	95.20
2	2601	2007-08-19	0200	0900	43.96	91.70
3	4418	2011-07-28	0000	1100	42.50	90.45
4	9499	2022-07-26	0700	1600	38.88	91.02
5	7154	2017-07-20	0700	1000	44.13	91.26

Table 6.1: Selected NW–SE oriented ERE case information, ranked in order by total exceedance volume. The ID is associated with the event number in the 20-yr dataset, where more attributes associated with the events can be obtained. The date and peak accumulation hour at the PME, along with the end time of the 12-hr accumulation period are given. The latitude and longitude of the PME of each event is also given.

Based on archived radar data, all five cases were associated with MCSs of the training line/adjoining stratiform archetype (Schumacher and Johnson, 2005; Fig. 1.4a). Most of these MCSs bare a resemblance to the plan view schematic in Fig. 1.5 (Corfidi, 2003), with a leading progressive line followed by a training line of deep convection oriented from west-northwest to

east-southeast. For example, radar reflectivity images of the MCS in Case 1 are shown in Fig. 2.4 in the discussion of the methods that were utilized in this investigation.

All five cases occurred over the same general region of the central CONUS with three events taking place in or near southwestern Wisconsin and the other two cases in the Missouri vicinity (Fig. 6.1). The relatively narrow swaths of extreme rainfall accumulations (roughly 20–40 km in width) associated with these NW–SE oriented EREs present a challenge for forecasters and numerical models. To investigate the environments associated with these five events, meteorological fields from the ERA5 (Hersbach et al., 2023c,d) were analyzed at the start of each event's peak accumulation hour, centered at the location of each event's PME. For display purposes the ERA5 grids were then shifted to the average of the cases' PME locations

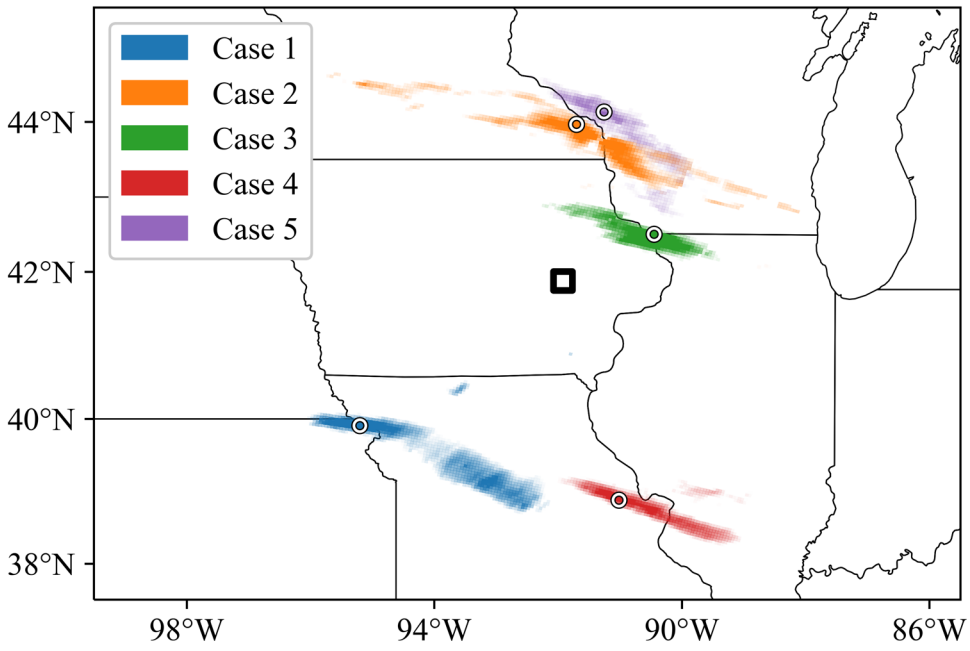

Figure 6.1: Exceedance swaths associated with each of the five selected NW–SE oriented ERE cases, color coded by case, and alpha-scaled by exceedance amount (0–100 mm). Opaque shading indicates exceedance values of 100 mm or greater. The white circles are the PME locations associated with each individual event and the black box is the average PME location.

(approximately 41.88°N, 91.92°W; black box in Fig. 6.1) and averaged together. This composite analysis method is similar to those utilized by Schumacher and Johnson (2005) and Stevenson and Schumacher (2014).

6.2 Mid–Upper Levels

Composite analysis of 500- and 200-hPa geopotential heights (Figs. 6.2a and 6.3a, respectively) reveals that the intense NW–SE oriented EREs occur beneath a positive mid–upper tropospheric height anomaly (based on the deviation from the JJA 2003–2022 ERA5 climatology), or along the northern edge of a strong mid–upper tropospheric ridge. The anomalies indicate that the ridge over the southern CONUS is stronger and expanded farther north than average for JJA. This ridging pattern indicates a clear difference between these summertime ERE cases and cooler season EREs, when mid–upper-level synoptic scale forcing for ascent is typically associated with troughing. Any subtle shortwave troughs that may be present are not evident in the composite height contours.

The NW–SE oriented EREs occurred within a zone of 15–20 m s^{-1} (30–40 knot) west-northwesterly 500-hPa flow along the northern edge of the ridge (Fig. 6.2b). This enhanced flow is associated with 15–20 m s^{-1} (30–40 knots) of mid-level (925–500-hPa) shear, oriented from northwest to southeast around the event locations (not shown), nearly parallel to the orientation of the ERE swaths. Based on previous literature (e.g., Schumacher and Johnson (2005); Fig. 1.4a), cell motion for training line/adjoining stratiform MCSs is generally aligned with the mid-level (925–500-hPa) shear vector, thus explaining the NW–SE orientation of the accumulation swaths.

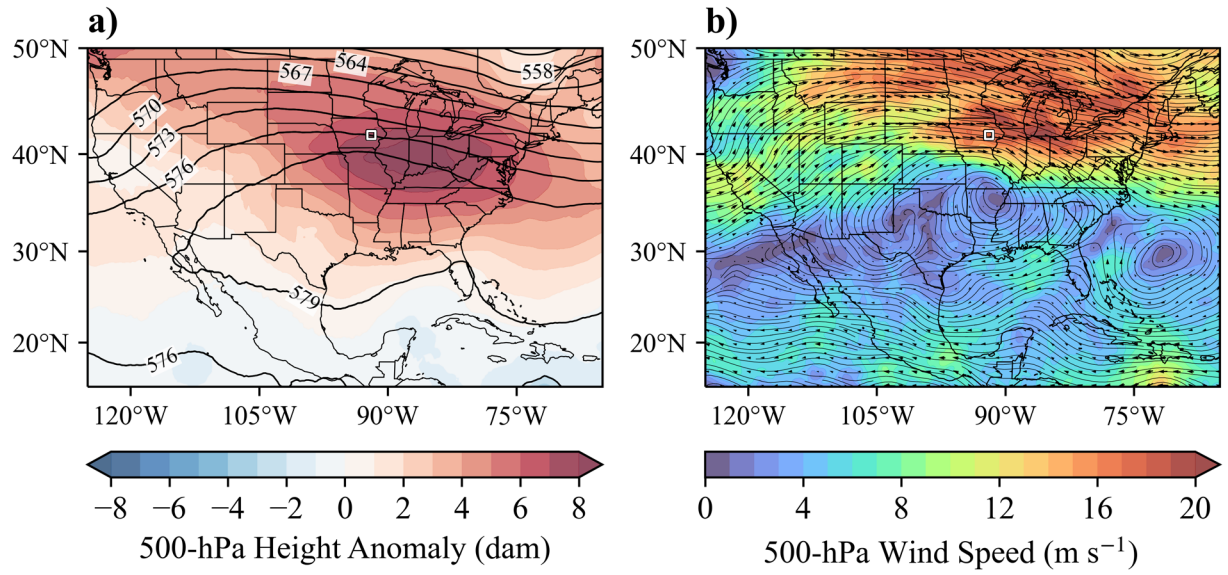

Figure 6.2: NW–SE case composite of ERA5 (a) 500-hPa geopotential height (contours; dam) and 500-hPa geopotential height anomaly based on the ERA5 2003–2022 JJA-mean climatology (color fill; dam), and (b) 500-hPa wind (vectors/streamlines) and wind speed (color fill; m s^{-1}). The white box in each map represents the average PME location.

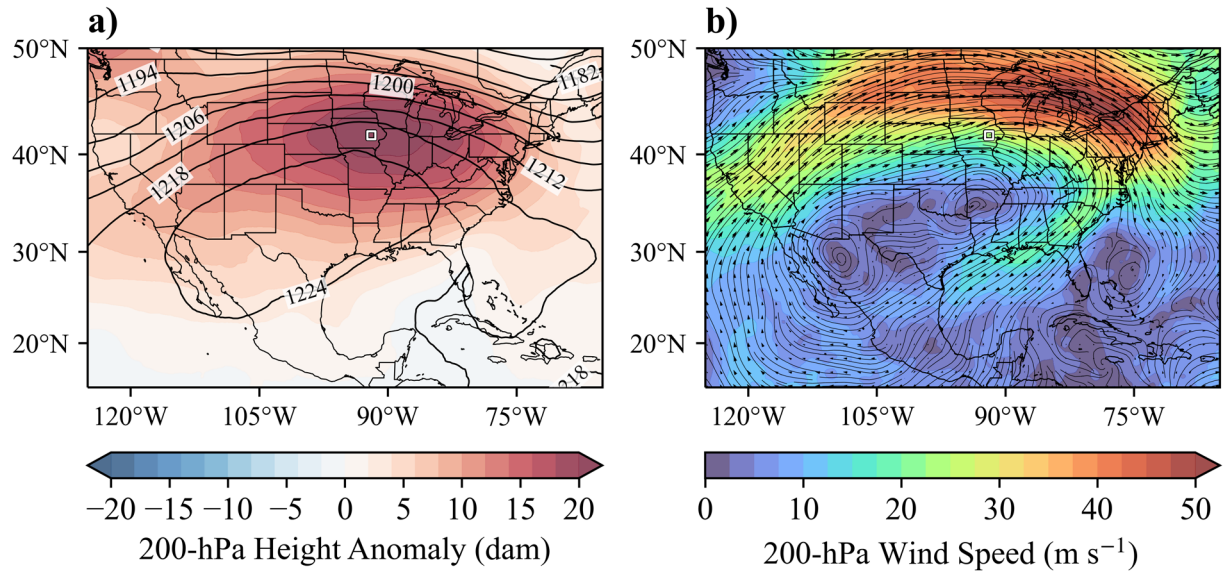

Figure 6.3: As in Fig. 6.2, but at 200-hPa.

At jet stream level (200 hPa), composite analysis suggests that the events occurred along the southern periphery of a strong jet streak, with 45–55 m s^{-1} (90–110 knot) flow curving anticyclonically around the northern edge of the ridge (Fig. 6.3b). Another key observation is the clearly discernable 200-hPa difluence evident near the event location, which would be consistent with ascent over that region according to the conservation of mass.

6.3 850 hPa & the LLJ

In the low levels (850 hPa), positive height anomalies are evident to the east of the EREs, appearing as a northwestward expansion of the NASH into the northeastern CONUS (Fig. 6.4a). To the west of the EREs, slightly *negative* 850-hPa height anomalies are evident, resulting in an enhanced NW–SE height gradient in the vicinity of the EREs. This height gradient results in a strengthened southwesterly 850-hPa flow of 15–20 m s^{-1} (30–40 knots) just south of the event location (Fig. 6.4b).

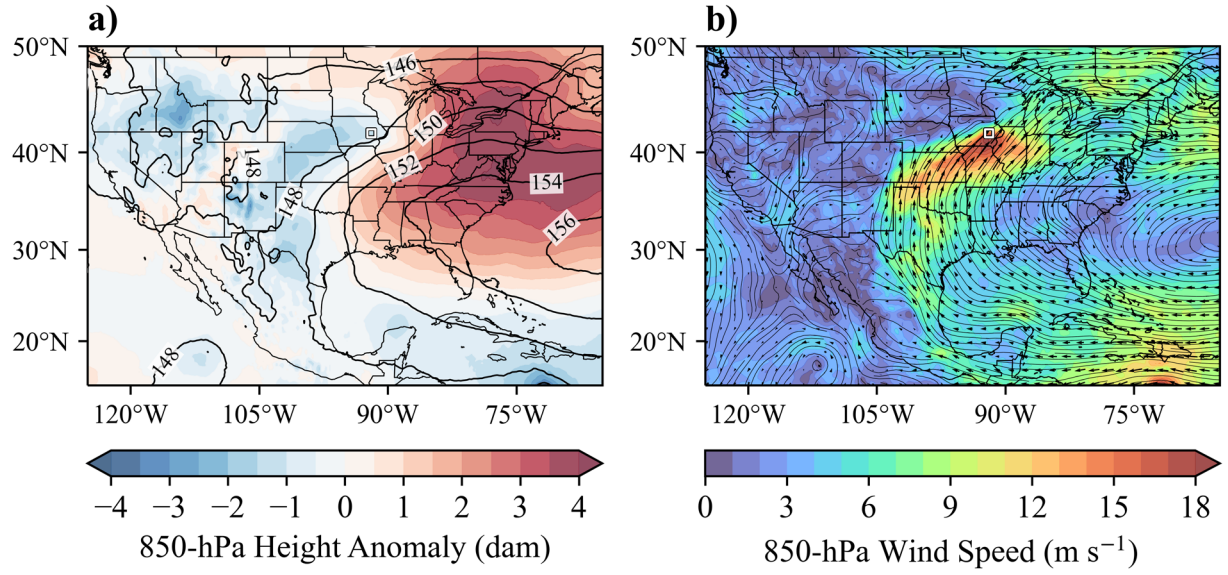

Figure 6.4: As in Fig. 6.2, but at 850-hPa.

The strong flow at 850 hPa is consistent with the presence of an LLJ (although the altitude of the LLJ wind maximum varies). It has long been known that the LLJ is responsible for advecting high θ_e air over a sloping frontal surface and/or creating strong moisture convergence at its terminus, which often results in elevated nocturnal convective initiation, upscale growth, and maintenance (e.g., Maddox, 1983; Maddox et al., 1979; Pitchford and London, 1962; Trier and Parsons, 1993). The composite of 850-hPa wind and specific humidity indicates that the events were centered at the northern terminus of a southwesterly LLJ (Fig. 6.4b), co-located with enhanced moisture (Fig. 6.5), and thus, strong moisture convergence. The strongest moisture flux convergence is only slightly offset to the north of the PME (black contour in Fig. 6.5), but likely co-located with the associated MCS.

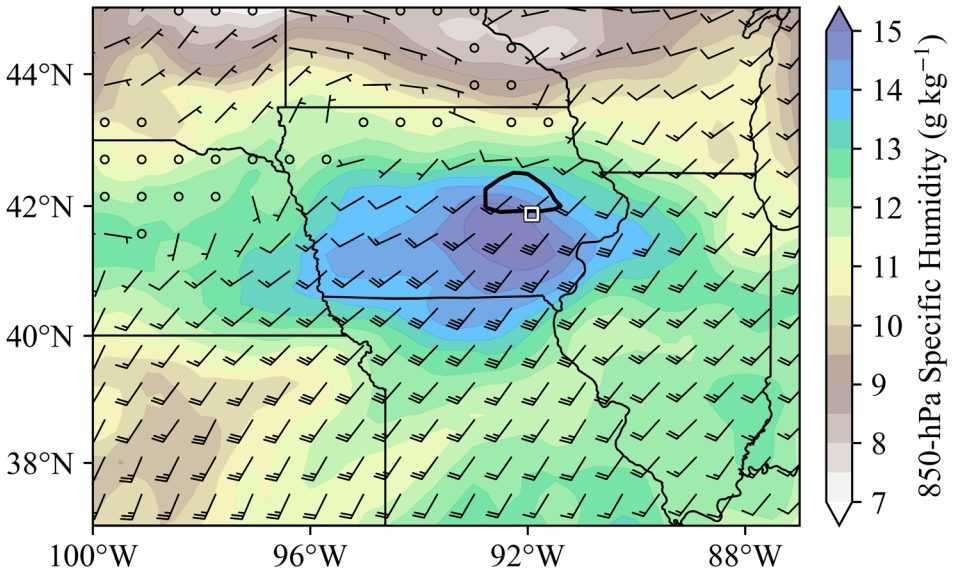

Figure 6.5: NW–SE case composite of ERA5 850-hPa specific humidity (color fill; g kg^{-1}) and 850-hPa wind (barbs; knots) with a thick black contour where the 850-hPa moisture flux convergence is 8 s^{-1}. The white box represents the average PME location.

Time series plots of maximum 850-hPa wind speed (Fig. 6.6) for each event indicate a maximum LLJ magnitude ranging from 23 to 37 m s^{-1} (46–74 knots), all peaking between 0200 and 0700 local time. The mean time series indicates a clear peak occurring between midnight and 0600 local time, consistent with a nocturnal formation of the LLJ (e.g., Shapiro et al., 2016). The most pronounced nocturnal enhancement of the LLJ occurred with the two southernmost cases (Cases 1 and 4), but the enhancement was smaller in the other cases. On average, the EREs began before the LLJ increased and ended after the LLJ reached its peak intensity. The peak rainfall intensity occurred several hours before the peak LLJ intensity, suggesting that any nocturnal intensification of the LLJ likely contributed more to the maintenance than to the initiation of the convection.

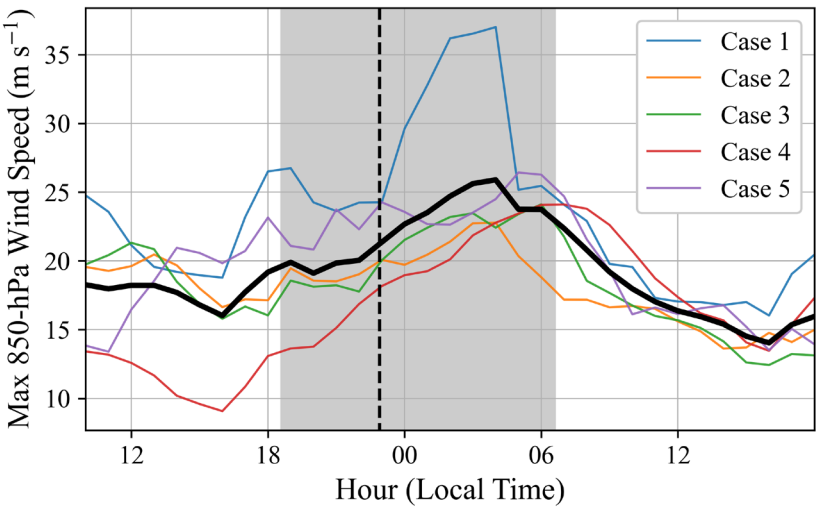

Figure 6.6: Time series of maximum 850-hPa wind speed within 5° of latitude and longitude from the PME for each NW–SE case, with the mean of all events displayed by the thick black line. The dashed black line represents the average peak accumulation hour of the events (~2300 local time). The shaded interval represents the time between the average start time (~1830 local time) and average end time (~0630 local time) of the events. Information on the timing of each individual event can be found in Table 6.1.

6.4 Total Column Moisture

The composite of total column water vapor indicates a very moist environment near the event locations with values of 50–60 kg m^{-2}, which is over 30 kg m^{-2} above normal for JJA based on the 2003–2022 ERA5 climatology (Fig. 6.7a). The relatively localized water vapor anomaly in the vicinity of the events may be attributed to the convergence and deepening of moisture near the northern terminus region of the LLJ. The composite of IVF indicates relatively strong southwesterly moisture transport surrounding the event location with subtle confluence also evident. On the large-scale, the moisture transport toward the event locations can be traced back to the subtropics around the western periphery of the NASH, but also from the Southern High Plains and Rockies. The moisture upstream from the event locations was near normal but did exhibit positive anomalies of 5–10 kg m^{-2} over many areas, especially over the Central Rockies.

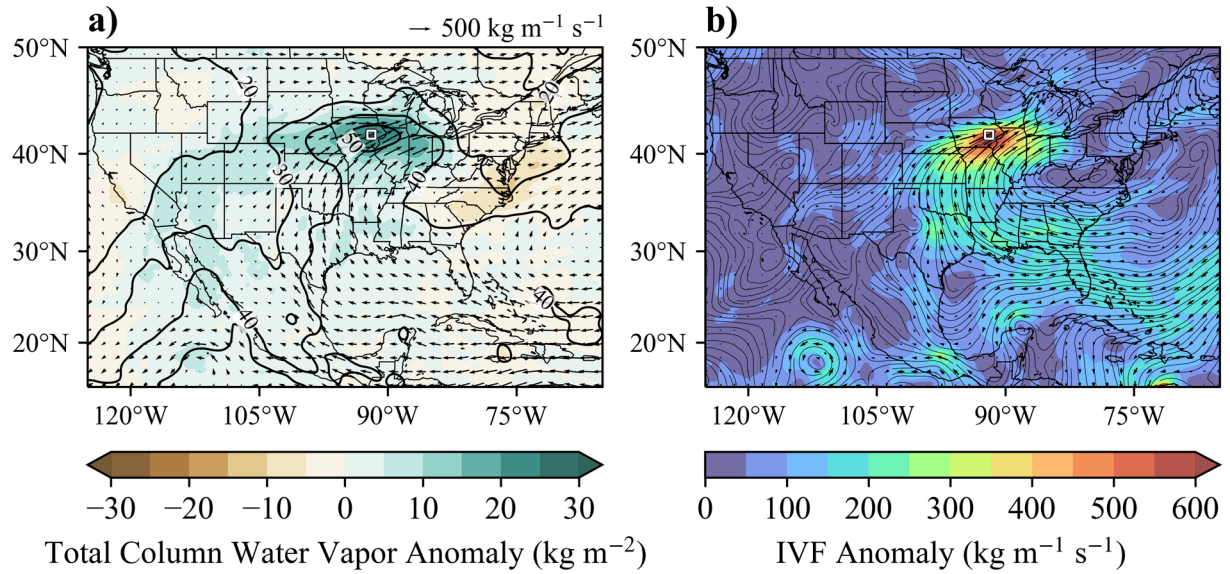

Figure 6.7: NW–SE case composite of ERA5 (a) total column water vapor (color fill; kg m^{-2}) and vertically integrated water vapor flux (IVF) (vectors/streamlines; kg m^{-1} s^{-1}) and (b) IVF vector anomaly (vectors/streamlines; kg m^{-1} s^{-1}) and its magnitude (color fill; kg m^{-1} s^{-1}) based on the ERA5 2003–2022 JJA-mean climatology. The white box represents the average PME location.

Moisture originating from land sources would be consistent with the findings of Abel et al. (2022), suggesting that the process of moisture recycling is important for extreme rainfall over the northern CONUS.

The composite anomaly of IVF (Fig. 6.7b) indicates the anomalous northwestern extension of the NASH circulation centered over the Mid-Atlantic region, manifesting as an inverted ridge type feature in Fig. 6.7a. The magnitude of the IVF anomaly near the event location is also quite high, tracing back to the subtropical Atlantic. Thus, both moisture recycling from land sources and moisture transport from the Gulf of Mexico and subtropical Atlantic likely played a role in the IVF anomaly. The enhanced southwesterly IVF is likely associated with the enhanced southwesterly winds at 850-hPa given the similar location of the anomaly to the enhanced flow in Fig. 6.4b.

6.5 Surface

Near the surface (Fig. 6.8), composite analysis reveals a strong temperature gradient to the south of the event location in the vicinity of a surface trough and wind shift, indicating a synoptic scale frontal zone. The composite indicates that the events occur on the cool side (~100–200 km to the north) of a roughly west-northwest to east-southeast oriented front, indicating that the convection is elevated above the frontal layer as opposed to surface-based. In all five cases, the front was indicated as stationary according to archived surface analyses, but the orientation of the boundary and distance between the ERE and the boundary varied somewhat among the different cases. The surface pattern also includes an elongated surface low centered to the west-southwest of the events, creating a modest pressure gradient to the south of the associated frontal boundary.

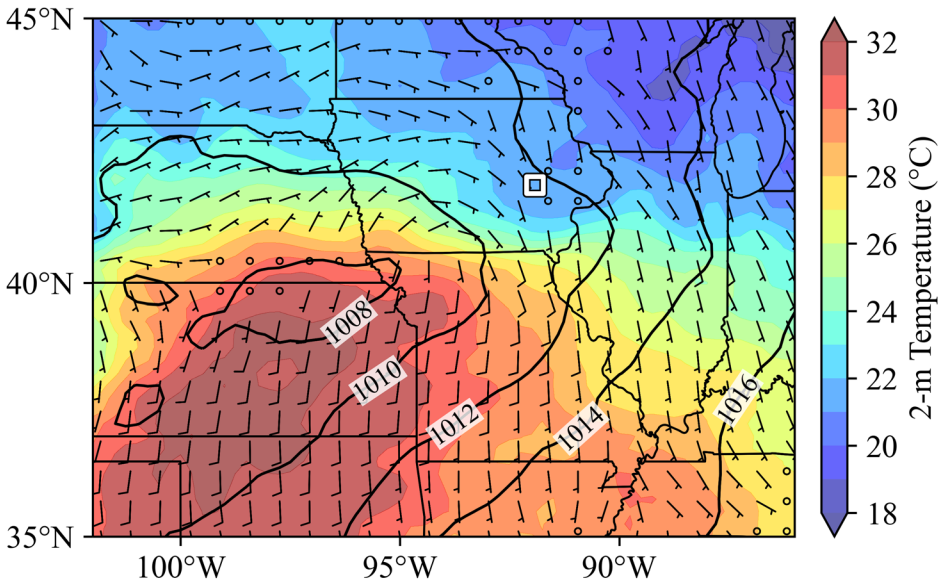

Figure 6.8: NW–SE case composite of ERA5 2-m temperature (color fill; °C), mean sea level pressure (contours; hPa), and 10-m wind barbs (knots). The white box represents the average PME location.

The presence of a surface front near these five EREs suggests the importance of the synoptic scale features in causing EREs. However, the presence of a stationary frontal boundary rather than a cold or warm front associated with a propagating extratropical cyclone during the cool season suggests that the summertime synoptic scale pattern associated with EREs is relatively unique.

6.6 Discussion

From composite analysis of the top 5 most intense NW–SE oriented EREs (all classified as nocturnal), we found a mesoscale and synoptic scale environment that aligns with previous studies of heavy-rain-producing warm season elevated MCSs (e.g., Moore et al., 2003). These environmental properties include anomalous deep layer moisture and strong moisture transport (Fig. 6.7a) and convergence in association with the LLJ (Figs. 6.4b and 6.5). The MCS position 100–200 km north of a surface boundary (Fig. 6.8), and beneath upper level divergence to the

south of a jet max (Fig. 6.3b), also matches Moore et al. (2003). The main difference in our results is that the events occurred just to the east of the mid-level ridge axis instead of to the west (Fig. 6.2a), leading to a northerly component in the mid-level flow and a resulting mid-level shear vector out of the northwest. Since the direction of the mid-level (925–500 hPa) shear vector dictates cell motion in training line/adjoining stratiform MCSs (Schumacher and Johnson, 2005; Fig. 1.4), this pattern explains the NW–SE orientation of the selected EREs. Another difference was a lack of evidence of an associated mid-level shortwave trough. However, it is possible that any subtle shortwave features evident in individual cases were cancelled out in the composite mean.

We also found an anomalous northwestward extension of the climatological North Atlantic anticyclonic circulation (i.e., the NASH) into the Mid-Atlantic region (Fig. 6.4a). In Fig. 6.7, this pattern appears to be associated with enhanced moisture transport from the subtropical Atlantic to the Gulf of Mexico, and northward into the central CONUS beneath the mid–upper tropospheric ridge. These results are highly reminiscent of the seasonal composite analysis of 850-hPa geopotential heights and IVF (Figs. 5.14 and 5.10, respectively), indicating the westward extension of the NASH. The anomalous mid–upper tropospheric ridging evident in Figs. 6.2a and 6.3a is also supported by the JJA composite analysis in the previous chapter (Figs. 5.15 and 5.16), where statistically significant results were found. For example, when comparing Figs. 5.15c and 6.2a, the 500 hPa ridge that was relatively absent during the inactive years (Fig. 5.15b) was indeed present during the EREs examined in this chapter.

Another factor likely influencing the development and maintenance of the nocturnal quasi-stationary MCSs producing the NW–SE oriented EREs is the apparent nocturnal enhancement of the LLJ. While the nocturnal LLJ is well-understood over the Great Plains in association with the sloping terrain (e.g., Shapiro et al., 2016), a relatively unexplored topic is the presence of LLJs

during the summer near stationary frontal systems to the east of the Great Plains, where the EREs occurred. The maximum 850-hPa wind speeds associated with the LLJs ranged from 23 to 37 m s^{-1} (46–74 knots), stronger than typical nocturnal LLJs found over the Great Plains, which normally have maximum speeds ranging from 12 to 25 m s^{-1} (25–50 knots) (Whiteman et al., 1997). These wind speeds are more in line with cyclone induced LLJs, which typically have speeds of 20 to 35 m s^{-1} (40–70 knots) (Lackmann, 2002), and a weak surface cyclone was observed in the case composite of mean sea level pressure (Fig. 6.8). Thus, the dynamics of this LLJ are likely related to the enhanced pressure gradient in association with the synoptic scale disturbance (e.g., Browning and Pardoe, 1973; Lackmann, 2002). LLJs have also been shown to be coupled with upper level tropospheric jet streaks (e.g., Uccellini and Johnson, 1979).

The LLJ near the stationary front in these cases did intensify during the night. Hence, it may be speculated that the observed nocturnal intensification of the LLJ may be due to similar mechanisms that drive the Great Plains nocturnal LLJ, namely, the Blackadar mechanism. At sunset, the effects of friction from boundary layer turbulent mixing are rapidly reduced, creating conditions favorable for inertial oscillations that can strengthen the low level flow to highly supergeostrophic levels (Blackadar, 1957; Shapiro and Fedorovich, 2010). These boundary layer processes are most often observed over the Great Plains and can occur in the absence of a synoptic scale disturbance due to differential heating of the gently sloping terrain (Holton, 1967; Shapiro et al., 2016). It is likely that similar dynamics may be at play in LLJs east of the Great Plains due to the reduction of surface stress and the shutdown of dry convective turbulence in the boundary layer at sunset (e.g., Laing and Fritsch, 2000). Studies on synoptically induced LLJs over land masses do not discuss the potential for a nocturnal enhancement of the flow outside of the Great Plains, so this topic may be an area for future investigation.

The findings in this chapter should provide valuable insight into the key ingredients involved in the production of some of the most prolific extreme-rain-producing MCSs during the summer. Recognizing these ingredients can aid in short term forecasting, which is of critical societal importance for these potentially destructive events. The narrow swaths of extreme rainfall accumulations in the cases discussed in this chapter suggest that short term forecasting of these events is a challenge. These extreme rainfall swaths are difficult to accurately represent in numerical weather prediction models with inadequate spatial resolutions, as simulations can generally accurately represent features greater than approximately 7 times their grid spacing (McTaggart-Cowan et al., 2020). For example, an extreme rainfall swath with a maximum width of 21 km may only be accurately represented by models with grid spacing of 3 km or less.

Chapter 7

Summary, Conclusions, & Future Work

Short-duration EREs pose substantial risks to society due to their low predictability and potential to result in deadly flash flooding (e.g., Ashley and Ashley, 2008). With growing evidence that the frequency and intensity of these events are increasing over many areas due to climate change (e.g., Fowler et al., 2021), including the CONUS (e.g., Kunkel et al., 2013a), it is imperative that we understand any long-term changes in the structure, diurnal cycle, duration, and location of extreme-rain-producing convection. It is also important to identify the environmental conditions and LSMPs that may explain the wide range of interannual variability in the occurrence of these EREs to potentially aid in forecasting, as these LSMPs generally have medium range predictability (Barlow et al., 2019). This study developed a detailed database of 12-hr duration EREs that exceeded the 10-yr ARI thresholds (according to the NOAA Atlas 14 dataset) over the central and eastern CONUS using the high-resolution gridded Stage IV precipitation analyses over a 20-yr period (2003–2022). The Stage IV dataset has the distinct advantage of capturing relatively localized extreme rainfall produced by convection using radar estimates, unlike the sole use of relatively sparse and non-uniform rain gauge measurements.

The few previous studies that utilized the Stage IV dataset (e.g., Stevenson and Schumacher, 2014) only examined extremes on time scales of 1, 6, 24 hours, or longer for their climatological statistics and associated environmental characteristics over a maximum period of 10 years. Our study avoids the measurement-interval truncation problem associated with these previous studies by utilizing iteratively summed 1-hr data to capture extremes that may straddle the 6- and 24-hr time bounds. The accumulation interval of 12 hours was chosen for the purpose of targeting EREs

produced by nonlocalized convection, including MCSs, and the use of hourly data enables the investigation of the timing and diurnal cycle of those EREs. In addition, no prior studies have been able to utilize the Stage IV dataset for investigating both interannual and multidecadal changes in ERE frequency or characteristics, as this study accomplishes, but with acknowledgement of the potential caveats.

7.1 Findings of the 20-yr ERE Climatology

The results of our 20-yr climatology of EREs generally align with previous studies (e.g., Dougherty and Rasmussen, 2019; Hitchens et al., 2013; Maddox et al., 1979; Schumacher and Johnson, 2006; Stevenson and Schumacher, 2014). For example, our results verify that the largest portion of short-duration EREs occur during JJA and are associated with MCSs. The diurnal cycle of these MCS-related EREs peaked during the nighttime hours over the central CONUS. The areas where the largest proportions of nocturnal EREs occurred were found to align with the long-known nocturnal maximum in warm season precipitation (e.g., Easterling and Robinson, 1985; Wallace, 1975). An area that stood out to have the highest concentration of intense nocturnal EREs was centered over eastern portions of the Central Great Plains, consistent with the nocturnal MCS climatology by Haberlie and Ashley (2019). Our climatology also provides new quantitative evidence in terms of extreme rainfall volume and spatial extent that nocturnal convection produces the most significant extreme rainfall over the domain during the summer, supporting previous studies. Since the representation of elevated nocturnal convection over continents is a significant challenge for numerical weather models (e.g., Bechtold et al., 2014), these findings should further motivate the need for improvement in the representation of nocturnal convection.

The unique mapping of accumulations from EREs that exceeded the 10-yr ARI thresholds reveals that these extremes often occur over very localized areas or narrow swaths (e.g., 20–40 km in width), even when the extreme rainfall is embedded within much larger precipitation features. The small-scale nature of these extremes poses a major challenge for operational forecasting as McTaggart-Cowan et al. (2020) found that models cannot well represent features less than approximately 7 times the model grid spacing. Thus, several studies have found that numerical models have low skill in predicting the precise locations of the extremes (e.g., Nielsen and Schumacher, 2016). Also, models without adequate spatial resolution, particularly those with convective parameterization, are unable to resolve convective scale processes that produce extreme rainfall amounts (e.g., Fritsch and Carbone, 2004). The finding that extreme rainfall can be so intense over localized areas motivates the need to improve the short term prediction of convective EREs via the use of high-resolution convection-allowing models. The challenge of accurately representing the location of these relatively small-scale events also suggests the need to employ ensemble modeling systems on these scales.

7.2 Trends Discovered & the Caveats

Time series of counts and total exceedance volume from EREs under various subsets reveal substantial interannual variability and statistically significant trends through the 20-yr period. Unlike previous studies that suggest an increase in springtime EREs associated with MCSs (e.g., Feng et al., 2016) with less evidence of an increase during the summer (e.g., Prein et al., 2017b), our database only revealed a significant increase in ERE frequency occurring during the summer months. This increase was only found with EREs associated with nonlocalized convection (i.e., filtered EREs), but sorting these events by their associated storm size and duration reveals that the

increasing trend was dominated by the larger and longer duration systems, classified as MCSs. The relative trend and overall variability in the time series of total exceedance volume of these EREs was also substantially greater than that for counts, with an observed increase of nearly 40% decade^{-1}. This finding aligns with numerous studies on the impact of climate change on convective rainfall. Using regional convection-allowing climate models, these studies suggest that future convective storms will be larger and produce heavier rainfall volumes (e.g., Feng, 2017; Hu et al., 2020; Prein et al., 2017a; Schumacher and Rasmussen, 2020) due to increasing moisture and instability. However, non-MCS precipitation, as well as the overall convective population, is projected to decrease due to increasing convective inhibition in a warming troposphere (e.g., Rasmussen et al., 2020), implying an increase in the occurrence of both droughts and floods in a future climate (Fowler et al., 2021). The increase in MCS-related EREs also has clear implications on a changing diurnal cycle of EREs as they tend to peak late at night and last into the morning hours, again motivating the need for improvement in the representation of elevated nocturnal convection. This thesis also discovered that the greatest increases in JJA filtered EREs were focused on the Mississippi and Ohio Valley regions, to the east of the Great Plains, where the EREs were found to be just as climatologically active. This regional contrast in trends suggests a possible eastward expansion of EREs from the Great Plains. The eastward expansion has not been previously proposed or discovered, suggesting that future research is needed to verify that this expansion is occurring and explain why these changes may be taking place.

However, these results relating to trends should be interpreted with caution due to the combination of the relatively short 20-yr period of record and the limitations of the Stage IV dataset (e.g., Nelson et al., 2016). Trends over such a short period cannot be directly attributed to anthropogenic climate change as rainfall patterns and amounts can undergo changes over decadal

timescales due to natural climate variability. Thus, any trends found in a study of only two decades may not necessarily be representative of long-term change and the contribution of climate change to any regional trends cannot be determined from our analysis. While it is worth noting that several of our results aligned with prior peer-reviewed studies of how EREs may be affected by climate change, we cannot conclude with certainty that the observed changes in our study were due to climate change.

The problem with using Stage IV analyses for detecting trends is that it is a relatively new and evolving dataset, meaning that the observed changes may have been affected by changes in the dataset itself. For example, a strong decreasing trend in the number of events per year that failed our QC indicates an increase in the quality of the data over time. Additionally, a few systemic changes took place during the period, including the 2011–2013 NEXRAD dual polarization upgrade and the gradual incorporation of Multi-Radar Multi-Sensor products into the Stage IV dataset. Upon discussions with representatives from multiple River Forecast Centers, the general consensus was that the NEXRAD upgrade should not have significantly affected quantitative precipitation estimates that would cause the jump in MCS-related EREs observed in the second half of the period. The incorporation of Multi-Radar Multi-Sensor products into the Stage IV data was not implemented by most River Forecast Centers until 2016 or later and the impact of the switch to Multi-Radar Multi-Sensor products on ERE detection is unknown. Discussion with the team creating the Multi-Radar Multi-Sensor products indicated that some dual-polarization variables were also not included in the calculation of radar-estimated quantitative precipitation estimates in their products until as late as 2020. However, the rain gauge technology used to correct radar-estimated precipitation and the River Forecast Centers' methods of performing that

correction did not change through the period, suggesting that there should not be a significant change in ERE detection.

7.3 Meteorological Conditions

Another aspect of this study was to perform composite and correlation analysis using various meteorological fields from the ERA5. The aim of this analysis was to identify LSMPs that distinguish between summers with greater versus less extreme rainfall activity associated with nonlocalized convection over the domain. Identifying the predominant LSMPs during active years may help to explain the wide range of interannual variability in these EREs and potentially aid in long-term or seasonal forecasting of potential impacts. To our knowledge, this statistical approach has not been previously conducted on seasonal time scales for the purposes of studying short-duration EREs. Composite analysis was also conducted on a sample of particularly intense nocturnal EREs occurring over the Mid–Upper Mississippi Valley region, associated with MCSs that had the common characteristic of training from northwest to southeast, a property that has not previously been explored. Similarities were found between the LSMPs associated with these events and the seasonal LSMPs found to distinguish more versus less active summers, which suggests a direct linkage of the seasonal LSMPs to the occurrence of intense EREs.

The most common environmental feature associated with EREs or extended periods of excessive rainfall that has been identified by nearly all previous studies is anomalous moisture transport and convergence (e.g., Holman and Vavrus, 2012; Mo et al., 1997). Our analysis revealed this stream of moisture transport during more active summers and during the ERE cases, originating from the Western Gulf of Mexico and stretching towards the Great Lakes region. This

pattern can be identified as the “Maya Express” (Dirmeyer and Kinter, 2009), which is known to favor enhanced rainfall over much of the central and northern CONUS.

While the seasonal LSMP composite and correlation analysis results regarding wind and geopotential height fields at and below 850 hPa lack statistical significance, there is a strong implication that the enhanced northward moisture transport may be driven by a westward expansion of the NASH. Dynamically, the increase in geopotential heights over the eastern CONUS relative to the Rockies would increase the pressure gradient in between, resulting in stronger southerly flow over that region, and stronger moisture transport from the subtropics as a result. Based on the case study composite of 850-hPa heights and wind, the enhanced pressure gradient in between is associated with an LLJ, which is a common ingredient for the initiation and maintenance of nocturnal MCSs (e.g., Trier and Parsons, 1993). Thus, the western extension of the NASH may also be associated with a stronger and/or more frequent LLJ over the central CONUS, which can directly result in more frequent and intense EREs. This westward expansion of the NASH has previously been linked to enhanced summertime rainfall over the Midwest (Zorzetto and Li, 2021). The NASH is also expected to expand westward overall in a future climate (Li et al., 2011), suggesting that the increasing trend in EREs over the central CONUS may continue as a result.

The most significant composite differences and correlations with geopotential heights appeared in the mid–upper levels, especially at 500 hPa. However, the NASH is less apparent in the mid-levels and does not extend into the upper levels. To our knowledge, this 500-hPa height pattern has not been identified as a significant LSMP associated with EREs, but it is plausible that the mid–upper level ridging is a result of the warmer temperatures that accompany the western extension of the NASH over the eastern CONUS, since heights are directly related to the mean

atmospheric virtual temperature via the hypsometric relationship. Further analysis would be required to determine if this is the case.

The strongest statistically significant correlations with JJA-averaged fields were found to be associated with low-level moisture over the Southern and Central Great Plains, particularly at the 925- and 850-hPa levels. With the southwesterly LLJ identified in the case study composite originating over the Southern Great Plains, it is reasonable to suspect that enhanced moisture over that region can lead to more extreme rainfall activity over both the Great Plains and Midwest. Enhanced moisture over the Southern and Central Great Plains has also been shown to be increasing in MCS environments, leading to increasing rainfall volumes from MCSs over the central CONUS, at least during the spring months (Feng et al., 2016). Greater low-level moisture would also lead to enhanced large-scale moisture convergence, according to Lenderink et al. (2017), which has a strong correlation with the spatial extent of EREs (Loriaux et al., 2017). Thus, the observed increase in storm size associated with JJA convective EREs may be attributed to increasing moisture convergence.

Correlations between the JJA filtered EREs and preceding winter and spring averaged meteorological fields revealed several statistically significant LSMPs. In theory, these results may be useful for seasonal prediction, but it is difficult to make physical connections between small-scale short-duration EREs to LSMPs occurring several months prior, especially with a 20-yr sample period. For example, there is a suggestion of a positive correlation with El Niño and the Pacific Decadal Oscillation along with their associated weather patterns during the preceding winter, but testing these indices as a predictor proves to be ineffective, despite some agreement with previous studies (e.g., Armal et al., 2018). However, one physically plausible predictor of summertime EREs that was found to have statistical significance would be antecedent drought

conditions over the Southern Great Plains, which can carry into the summer, leading to less EREs throughout the Great Plains, and vice versa. No reasonable predictors of JJA filtered EREs to the east of the Mississippi River were found, which may be a subject for future work.

The key ingredients identified from the case study of intense NW–SE oriented EREs were generally consistent with similar previous studies of extreme-rain-producing and/or nocturnal MCSs (e.g., Maddox et al., 1979; Moore et al., 2003; Schumacher and Johnson, 2005; Trier and Parsons, 1993), except for the lack of evidence of an associated mid-level shortwave trough. The EREs were found to occur near the northern edge of a strong mid–upper tropospheric ridge over the southern CONUS with a strong upper-level jet stream just to the north. The key environmental conditions involved in the production of these EREs include the following: (1) a strong southwesterly LLJ transporting moist air from the subtropics, and (2) a roughly east–west oriented quasi-stationary surface front, all in the presence of moderate to strong northwesterly mid-level shear, resulting in NW–SE training cell motions and sustained convection near the northern terminus of the LLJ, 100–300 km north of the front. These conditions typically peak at night, likely related to an enhancement of the LLJ.

The nocturnal intensification of the LLJ observed to the east of the Great Plains is not well understood. While the LLJ is likely associated with a synoptic scale system (e.g., Browning and Pardoe, 1973), the reasoning for an intensification after dark may be related to the shutdown of dry convective turbulence (Blackadar, 1957), but this mechanism is idealized in association with a strongly mixed boundary layer during the day, which was not always the case. Adding additional cases and examining them in greater detail can be useful for future work. However, idealized model simulations of the nocturnal enhancement of a synoptically induced LLJ east of the Great Plains would be needed to fully understand the dynamics involved.

7.4 Final Remarks

The uncertainties that arise in our results due to the limitations of the Stage IV dataset emphasize the need for a longer and more uniform gridded precipitation dataset. While the dataset can be improved if the River Forecast Centers utilize consistent processing and effective QC measures, a uniform dataset cannot be achieved due to the inherent limitations of our current radar technology for the purposes of estimating rainfall. However, given a longer period of record, repeating similar analyses as those employed in this study in the future can increase the confidence in any trends or significant LSMPs associated with summertime convective EREs.

Reference List

Abel, B. D., B. Rajagopalan, and A. J. Ray, 2022: Understanding the Dominant Moisture Sources and Pathways of Summer Precipitation in the Southeast Prairie Pothole Region. *Earth and Space Science*, **9 (3)**, https://doi.org/10.1029/2021EA001855.

Alley, W. M., 1984: The Palmer Drought Severity Index: limitations and assumptions. *Journal of Applied Meteorology and Climatology*, **23 (7)**, 1100–1109, https://doi.org/10.1175/1520-0450(1984)023<1100:TPDSIL>2.0.CO;2.

Armal, S., N. Devineni, and R. Khanbilvardi, 2018: Trends in extreme rainfall frequency in the contiguous United States: Attribution to climate change and climate variability modes. *Journal of Climate*, **31 (1)**, 369–385, https://doi.org/10.1175/JCLI-D-17-0106.1.

Ashley, S. T., and W. S. Ashley, 2008: Flood fatalities in the United States. *Journal of Applied Meteorology and Climatology*, **47 (3)**, 805–818, https://doi.org/10.1175/2007JAMC1611.1.

Ban, N., J. Schmidli, and C. Schär, 2014: Evaluation of the convection-resolving regional climate modeling approach in decade-long simulations. *Journal of Geophysical Research*, **119 (13)**, 7889–7907, https://doi.org/10.1002/2014JD021478.

——, ——, and ——, 2015: Heavy precipitation in a changing climate: Does short-term summer precipitation increase faster? *Geophysical Research Letters*, **42 (4)**, 1165–1172, https://doi.org/10.1002/2014GL062588.

Barbero, R., H. J. Fowler, G. Lenderink, and S. Blenkinsop, 2017: Is the intensification of precipitation extremes with global warming better detected at hourly than daily resolutions? *Geophysical Research Letters*, **44 (2)**, 974–983, https://doi.org/10.1002/2016GL071917.

Barlow, M., and Coauthors, 2019: North American extreme precipitation events and related large-scale meteorological patterns: a review of statistical methods, dynamics, modeling, and trends. *Climate Dynamics*, **53 (11)**, 6835–6875, https://doi.org/10.1007/s00382-019-04958-z.

Bartels, D. L., and R. A. Maddox, 1991: Midlevel cyclonic vortices generated by mesoscale convective systems. *Monthly Weather Review*, **119 (1)**, 104–118, https://doi.org/10.1175/1520-0493(1991)119<0104:MCVGBM>2.0.CO;2.

Bechtold, P., N. Semane, P. Lopez, J. P. Chaboureau, A. Beljaars, and N. Bormann, 2014: Representing equilibrium and nonequilibrium convection in large-scale models. *Journal of the Atmospheric Sciences*, **71 (2)**, 734–753, https://doi.org/10.1175/JAS-D-13-0163.1.

——, R. Forbes, I. Sandu, S. Lang, and M. Ahlgrimm, 2020: A major moist physics upgrade for the IFS. *ECMWF Newsletter*, **164**, 24–32.

Becker, T., P. Bechtold, and I. Sandu, 2021: Characteristics of convective precipitation over tropical Africa in storm-resolving global simulations. *Quarterly Journal of the Royal Meteorological Society*, **147 (741)**, 4388–4407, https://doi.org/10.1002/qj.4185.

Benjamini, Y., and Y. Hochberg, 1995: Controlling the False Discovery Rate: A Practical and Powerful Approach to Multiple Testing. *Journal of the Royal Statistical Society: Series B (Methodological)*, **57 (1)**, 289–300, https://doi.org/10.1111/j.2517-6161.1995.tb02031.x.

Berg, P., C. Moseley, and J. O. Haerter, 2013: Strong increase in convective precipitation in response to higher temperatures. *Nature Geoscience*, **6 (3)**, 181–185, https://doi.org/10.1038/ngeo1731.

Blackadar, A. K., 1957: Boundary Layer Wind Maxima and Their Significance for the Growth of Nocturnal Inversions. *Bulletin of the American Meteorological Society*, **38 (5)**, 283–290, https://doi.org/10.1175/1520-0477-38.5.283.

Brooks, H. E., and D. J. Stensrud, 2000: Climatology of heavy rain events in the United States from hourly precipitation observations. *Monthly Weather Review*, **128 (4)**, 1194–1201, https://doi.org/10.1175/1520-0493(2000)128<1194:COHREI>2.0.CO;2.

Browning, K. A., and C. W. Pardoe, 1973: Structure of low-level jet streams ahead of mid-latitude cold fronts. *Quarterly Journal of the Royal Meteorological Society*, **99 (422)**, 619–638, https://doi.org/10.1002/qj.49709942204.

Chappell, C. F., 1986: Quasi-Stationary Convective Events. *Mesoscale Meteorology and Forecasting*, American Meteorological Society, 289–310.

Coelho, G. de A., C. M. Ferreira, J. Johnston, J. L. Kinter, I. J. Dollan, and V. Maggioni, 2022: Potential Impacts of Future Extreme Precipitation Changes on Flood Engineering Design Across the Contiguous United States. *Water Resources Research*, **58 (4)**, https://doi.org/10.1029/2021WR031432.

Corfidi, S. F., 2003: Cold pools and MCS propagation: Forecasting the motion of downwind-developing MCSs. *Weather and Forecasting*, **18 (6)**, 997–1017, https://doi.org/10.1175/1520-0434(2003)018<0997:CPAMPF>2.0.CO;2.

Coumou, D., and S. Rahmstorf, 2012: A decade of weather extremes. *Nature Climate Change*, **2 (7)**, 491–496, https://doi.org/10.1038/nclimate1452.

Dai, A., R. M. Rasmussen, C. Liu, K. Ikeda, and A. F. Prein, 2020: A new mechanism for warm-season precipitation response to global warming based on convection-permitting simulations. *Climate Dynamics*, **55 (1–2)**, 343–368, https://doi.org/10.1007/s00382-017-3787-6.

Deser, C., A. Phillips, V. Bourdette, and H. Teng, 2012: Uncertainty in climate change projections: The role of internal variability. *Climate Dynamics*, **38 (3–4)**, 527–546, https://doi.org/10.1007/s00382-010-0977-x.

Dirmeyer, P. A., and J. L. Kinter, 2009: The "Maya Express": Floods in the U.S. Midwest. *Eos, Transactions AGU*, **90 (12)**, 101–102, https://doi.org/10.1029/2009EO120001.

Dougherty, E., and K. L. Rasmussen, 2019: Climatology of flood-producing storms and their associated rainfall characteristics in the United States. *Monthly Weather Review*, **147 (11)**, 3861–3877, https://doi.org/10.1175/MWR-D-19-0020.1.

——, and ——, 2020: Changes in future flash flood–producing storms in the United States. *Journal of Hydrometeorology*, **21 (10)**, 2221–2236, https://doi.org/10.1175/JHM-D-20-0014.1.

Du, J., 2011: NCEP/EMC 4KM Gridded Data (GRIB) Stage IV Data. Version 1.0. *UCAR/NCAR - Earth Observing Laboratory*, https://doi.org/10.5065/D6PG1QDD.

Easterling, D. R., and P. J. Robinson, 1985: The diurnal variation of thunderstorm activity in the United States. *Journal of Applied Meteorology and Climatology*, **24 (10)**, 1048–1058, https://doi.org/10.1175/1520-0450(1985)024<1048:TDVOTA>2.0.CO;2.

Easterling, D. R., J. L. Evans, P. Y. Groisman, T. R. Karl, K. E. Kunkel, and P. Ambenje, 2000: Observed variability and trends in extreme climate events: A brief review. *Bulletin of the American Meteorological Society*, **81 (3)**, 417–426, https://doi.org/10.1175/1520-0477(2000)081<0417:OVATIE>2.3.CO;2.

Easterling, D. R., and Coauthors, 2017: Precipitation Change in the United States. Climate Science Special Report: Fourth National Climate Assessment, Volume I. *U.S. Global Change Research Program*, 207–230, https://doi.org/10.7930/J0H993CC.

Feng, Z., 2017: Near doubling of storm rainfall. *Nature Climate Change*, **7 (12)**, 855–856, https://doi.org/10.1038/s41558-017-0017-5.

——, L. R. Leung, S. Hagos, R. A. Houze, C. D. Burleyson, and K. Balaguru, 2016: More frequent intense and long-lived storms dominate the springtime trend in central US rainfall. *Nature Communications*, **7 (1)**, 1–8, https://doi.org/10.1038/ncomms13429.

Fischer, E. M., and R. Knutti, 2016: Observed heavy precipitation increase confirms theory and early models. *Nature Climate Change*, **6 (11)**, 986–991, https://doi.org/10.1038/nclimate3110.

Flanagan, P. X., J. B. Basara, J. C. Furtado, and X. Xiao, 2018: Primary atmospheric drivers of pluvial years in the United States Great Plains. *Journal of Hydrometeorology*, **19 (4)**, 643–658, https://doi.org/10.1175/JHM-D-17-0148.1.

Fowler, H. J., and Coauthors, 2021: Anthropogenic intensification of short-duration rainfall extremes. *Nature Reviews Earth and Environment*, **2 (2)**, 107–122, https://doi.org/10.1038/s43017-020-00128-6.

Fritsch, J. M., and R. E. Carbone, 2004: Improving quantitative precipitation forecasts in the warm season: A USWRP research and development strategy. *Bulletin of the American Meteorological Society*, **85 (7)**, 955–966, https://doi.org/10.1175/BAMS-85-7-955.

Fritsch, J. M., R. J. Kane, and C. R. Chelius, 1986: The contribution of mesoscale convective weather systems to the warm-season precipitation in the United States. *Journal of Applied*

Meteorology and Climatology, **25 (10)**, 1333–1345, https://doi.org/10.1175/1520-0450(1986)025<1333:TCOMCW>2.0.CO;2.

Fulton, R. A., J. P. Breidenbach, D. J. Seo, D. A. Miller, and T. O'Bannon, 1998: The WSR-88D rainfall algorithm. *Weather and Forecasting*, **13 (2)**, 377–395, https://doi.org/10.1175/1520-0434(1998)013<0377:TWRA>2.0.CO;2.

Gao, Y., L. R. Leung, C. Zhao, and S. Hagos, 2017: Sensitivity of U.S. summer precipitation to model resolution and convective parameterizations across gray zone resolutions. *Journal of Geophysical Research*, **122 (5)**, 2714–2733, https://doi.org/10.1002/2016JD025896.

Geerts, B., and Coauthors, 2017: The 2015 plains elevated convection at night field project. *Bulletin of the American Meteorological Society*, **98 (4)**, 767–786, https://doi.org/10.1175/BAMS-D-15-00257.1.

Georgescu, M., A. M. Broadbent, M. Wang, E. S. Krayenhoff, and M. Moustaoui, 2021: Precipitation response to climate change and urban development over the continental United States. *Environmental Research Letters*, **16 (4)**, 044001, https://doi.org/10.1088/1748-9326/abd8ac.

Groisman, P. Y., R. W. Knight, and T. R. Karl, 2012: Changes in intense precipitation over the Central United States. *Journal of Hydrometeorology*, **13 (1)**, 47–66, https://doi.org/10.1175/JHM-D-11-039.1.

Guerreiro, S. B., H. J. Fowler, R. Barbero, S. Westra, G. Lenderink, S. Blenkinsop, E. Lewis, and X. F. Li, 2018: Detection of continental-scale intensification of hourly rainfall extremes. *Nature Climate Change*, **8 (9)**, 803–807, https://doi.org/10.1038/s41558-018-0245-3.

Haberlie, A. M., and W. S. Ashley, 2019: A radar-based climatology of mesoscale convective systems in the United States. *Journal of Climate*, **32 (5)**, 1591–1606, https://doi.org/10.1175/JCLI-D-18-0559.1.

Harp, R. D., and D. E. Horton, 2022: Observed Changes in Daily Precipitation Intensity in the United States. *Geophysical Research Letters*, **49 (19)**, https://doi.org/10.1029/2022GL099955.

Herman, G. R., and R. S. Schumacher, 2016: Extreme precipitation in models: An evaluation. *Weather and Forecasting*, **31 (6)**, 1853–1879, https://doi.org/10.1175/WAF-D-16-0093.1.

——, and ——, 2018: Money doesn't grow on trees, but forecasts do: Forecasting extreme precipitation with random forests. *Monthly Weather Review*, **146 (5)**, 1571–1600, https://doi.org/10.1175/MWR-D-17-0250.1.

Hersbach, H., and Coauthors, 2020: The ERA5 global reanalysis. *Quarterly Journal of the Royal Meteorological Society*, **146 (730)**, 1999–2049, https://doi.org/10.1002/qj.3803.

Hersbach, H., and Coauthors, 2023a: ERA5 monthly averaged data on single levels from 1940 to present. *Copernicus Climate Change Service (C3S) Climate Data Store (CDS)*, https://doi.org/10.24381/cds.f17050d7.

——, and Coauthors, 2023b: ERA5 monthly averaged data on pressure levels from 1940 to present. *Copernicus Climate Change Service (C3S) Climate Data Store (CDS)*, https://doi.org/10.24381/cds.6860a573.

——, and Coauthors, 2023c: ERA5 hourly data on single levels from 1940 to present. *Copernicus Climate Change Service (C3S) Climate Data Store (CDS)*, https://doi.org/10.24381/cds.adbb2d47.

——, and Coauthors, 2023d: ERA5 hourly data on pressure levels from 1940 to present. *Copernicus Climate Change Service (C3S) Climate Data Store (CDS)*, https://doi.org/10.24381/cds.bd0915c6.

Hitchcock, S. M., and R. S. Schumacher, 2020: Analysis of Back-building convection in simulations with a strong low-level stable layer. *Monthly Weather Review*, **148 (9)**, 3773–3797, https://doi.org/10.1175/MWR-D-19-0246.1.

Hitchens, N. M., M. E. Baldwin, and R. J. Trapp, 2012: An object-oriented characterization of extreme precipitation-producing convective systems in the midwestern United States. *Monthly Weather Review*, **140 (4)**, 1356–1366, https://doi.org/10.1175/MWR-D-11-00153.1.

——, H. E. Brooks, and R. S. Schumacher, 2013: Spatial and temporal characteristics of heavy hourly rainfall in the United states. *Monthly Weather Review*, **141 (12)**, 4564–4575, https://doi.org/10.1175/MWR-D-12-00297.1.

Holman, K. D., and S. J. Vavrus, 2012: Understanding simulated extreme precipitation events in Madison, Wisconsin, and the role of moisture flux convergence during the late twentieth and twenty-first centuries. *Journal of Hydrometeorology*, **13 (3)**, 877–894, https://doi.org/10.1175/JHM-D-11-052.1.

Holton, J. R., 1967: The diurnal boundary layer wind oscillation above sloping terrain. *Tellus*, **19 (2)**, 200–205, https://doi.org/10.3402/tellusa.v19i2.9766.

Houze, R. A., 2004: Mesoscale convective systems. *Reviews of Geophysics*, **42 (4)**, https://doi.org/10.1029/2004RG000150.

Hu, H., L. R. Leung, and Z. Feng, 2020: Observed Warm-Season Characteristics of MCS and Non-MCS Rainfall and Their Recent Changes in the Central United States. *Geophysical Research Letters*, **47 (6)**, https://doi.org/10.1029/2019GL086783.

Hussain, Md., and I. Mahmud, 2019: pyMannKendall: a python package for non parametric Mann Kendall family of trend tests. *Journal of Open Source Software*, **4 (39)**, 1556, https://doi.org/10.21105/joss.01556.

Janssen, E., D. J. Wuebbles, K. E. Kunkel, S. C. Olsen, and A. Goodman, 2014: Observational- and model-based trends and projections of extreme precipitation over the contiguous United States. *Earth's Future*, **2 (2)**, 99–113, https://doi.org/10.1002/2013ef000185.

Judt, F., 2018: Insights into atmospheric predictability through global convection-permitting model simulations. *Journal of the Atmospheric Sciences*, **75 (5)**, 1477–1497, https://doi.org/10.1175/JAS-D-17-0343.1.

——, 2020: Atmospheric predictability of the tropics, middle latitudes, and polar regions explored through global storm-resolving simulations. *Journal of the Atmospheric Sciences*, **77 (1)**, 257–276, https://doi.org/10.1175/JAS-D-19-0116.1.

Junqueira, J. R., S. Serrao-Neumann, and I. White, 2021: A systematic review of approaches for modelling current and future impacts of extreme rainfall events using green infrastructure. *Journal of Cleaner Production*, **290**, 125173, https://doi.org/10.1016/j.jclepro.2020.125173.

Karl, T. R., and R. W. Knight, 1998: Secular Trends of Precipitation Amount, Frequency, and Intensity in the United States. *Bulletin of the American Meteorological Society*, **79 (2)**, 231–242, https://doi.org/10.1175/1520-0477(1998)079<0231:STOPAF>2.0.CO;2.

Keene, K. M., and R. S. Schumacher, 2013: The bow and arrow mesoscale convective structure. *Monthly Weather Review*, **141 (5)**, 1648–1672, https://doi.org/10.1175/MWR-D-12-00172.1.

Kendon, E. J., N. M. Roberts, C. A. Senior, and M. J. Roberts, 2012: Realism of rainfall in a very high-resolution regional climate model. *Journal of Climate*, **25 (17)**, 5791–5806, https://doi.org/10.1175/JCLI-D-11-00562.1.

——, ——, H. J. Fowler, M. J. Roberts, S. C. Chan, and C. A. Senior, 2014: Heavier summer downpours with climate change revealed by weather forecast resolution model. *Nature Climate Change*, **4 (7)**, 570–576, https://doi.org/10.1038/nclimate2258.

——, R. A. Stratton, S. Tucker, J. H. Marsham, S. Berthou, D. P. Rowell, and C. A. Senior, 2019: Enhanced future changes in wet and dry extremes over Africa at convection-permitting scale. *Nature Communications*, **10 (1)**, 1794, https://doi.org/10.1038/s41467-019-09776-9.

Khajehei, S., A. Ahmadalipour, W. Shao, and H. Moradkhani, 2020: A Place-based Assessment of Flash Flood Hazard and Vulnerability in the Contiguous United States. *Scientific Reports*, **10 (1)**, 448, https://doi.org/10.1038/s41598-019-57349-z.

Kim, J., E. Shu, K. Lai, M. Amodeo, J. Porter, and E. Kearns, 2022: Assessment of the standard precipitation frequency estimates in the United States. *Journal of Hydrology: Regional Studies*, **44**, 101276, https://doi.org/10.1016/j.ejrh.2022.101276.

Knapp, A. K., and Coauthors, 2008: Consequences of more extreme precipitation regimes for terrestrial ecosystems. *BioScience*, **58 (9)**, 811–821, https://doi.org/10.1641/B580908.

Knapp, K. R., M. C. Kruk, D. H. Levinson, H. J. Diamond, and C. J. Neumann, 2010: The international best track archive for climate stewardship (IBTrACS). *Bulletin of the American Meteorological Society*, **91 (3)**, 363–376, https://doi.org/10.1175/2009BAMS2755.1.

Knapp, K. R., H. J. Diamond, J. P. Kossin, M. C. Kruk, and C. J. Schreck, 2018: International Best Track Archive for Climate Stewardship (IBTrACS) Project, Version 4. *NOAA National Centers for Environmental Information*, **27 (4)**.

Kunkel, K. E., K. Andsager, and D. R. Easterling, 1999: Long-term trends in extreme precipitation events over the conterminous United States and Canada. *Journal of Climate*, **12 (8)**, 2515–2527, https://doi.org/10.1175/1520-0442(1999)012<2515:lttiep>2.0.co;2.

——, D. R. Easterling, D. A. R. Kristovich, B. Gleason, L. Stoecker, and R. Smith, 2012: Meteorological causes of the secular variations in observed extreme precipitation events for the conterminous United States. *Journal of Hydrometeorology*, **13 (3)**, 1131–1141, https://doi.org/10.1175/JHM-D-11-0108.1.

——, and Coauthors, 2013a: Monitoring and understanding trends in extreme storms: State of knowledge. *Bulletin of the American Meteorological Society*, **94 (4)**, 499–514, https://doi.org/10.1175/BAMS-D-11-00262.1.

——, T. R. Karl, D. R. Easterling, K. Redmond, J. Young, X. Yin, and P. Hennon, 2013b: Probable maximum precipitation and climate change. *Geophysical Research Letters*, **40 (7)**, 1402–1408, https://doi.org/10.1002/grl.50334.

Lackmann, G. M., 2002: Cold-frontal potential vorticity maxima, the low-level jet, and moisture transport in extratropical cyclones. *Monthly Weather Review*, **130 (1)**, 59–74, https://doi.org/10.1175/1520-0493(2002)130<0059:CFPVMT>2.0.CO;2.

Laing, A. G., and J. M. Fritsch, 2000: The large-scale environments of the global populations of mesoscale convective complexes. *Monthly Weather Review*, **128 (8)**, 2756–2776, https://doi.org/10.1175/1520-0493(2000)128<2756:tlseot>2.0.co;2.

Lenderink, G., and E. Van Meijgaard, 2008: Increase in hourly precipitation extremes beyond expectations from temperature changes. *Nature Geoscience*, **1 (8)**, 511–514, https://doi.org/10.1038/ngeo262.

——, and ——, 2010: Linking increases in hourly precipitation extremes to atmospheric temperature and moisture changes. *Environmental Research Letters*, **5 (2)**, 025208, https://doi.org/10.1088/1748-9326/5/2/025208.

Lenderink, G., R. Barbero, J. M. Loriaux, and H. J. Fowler, 2017: Super-Clausius-Clapeyron scaling of extreme hourly convective precipitation and its relation to large-scale atmospheric conditions. *Journal of Climate*, **30 (15)**, 6037–6052, https://doi.org/10.1175/JCLI-D-16-0808.1.

Lenderink, G., H. De Vries, H. J. Fowler, R. Barbero, B. Van Ulft, and E. Van Meijgaard, 2021: Scaling and responses of extreme hourly precipitation in three climate experiments with a convection-permitting model. *Philosophical Transactions of the Royal Society A*, **379 (2195)**, 20190544, https://doi.org/10.1098/rsta.2019.0544.

Li, M., Q. Sun, M. A. Lovino, S. Ali, M. Islam, T. Li, C. Li, and Z. Jiang, 2022a: Non-uniform changes in different daily precipitation events in the contiguous United States. *Weather and Climate Extremes*, **35**, 100417, https://doi.org/10.1016/j.wace.2022.100417.

Li, W., L. Li, R. Fu, Y. Deng, and H. Wang, 2011: Changes to the North Atlantic subtropical high and its role in the intensification of summer rainfall variability in the southeastern United States. *Journal of Climate*, **24 (5)**, 1499–1506, https://doi.org/10.1175/2010JCLI3829.1.

Li, Z., S. Gao, M. Chen, J. J. Gourley, C. Liu, A. F. Prein, and Y. Hong, 2022b: The conterminous United States are projected to become more prone to flash floods in a high-end emissions scenario. *Communications Earth and Environment*, **3 (1)**, 86, https://doi.org/10.1038/s43247-022-00409-6.

Lin, Y., and K. E. Mitchell, 2005: The NCEP stage II/IV hourly precipitation analyses: Development and applications. *85th AMS Annual Meeting, American Meteorological Society - Combined Preprints*, San Diego, CA, URL https://ams.confex.com/ams/pdfpapers/83847.pdf.

Livezey, R. E., and W. Y. Chen, 1983: Statistical field significance and its determination by Monte Carlo techniques. *Monthly Weather Review*, **111 (1)**, 46–59, https://doi.org/10.1175/1520-0493(1983)111<0046:SFSAID>2.0.CO;2.

Loriaux, J. M., G. Lenderink, and A. Pier Siebesma, 2017: Large-scale controls on extreme precipitation. *Journal of Climate*, **30 (3)**, 955–968, https://doi.org/10.1175/JCLI-D-16-0381.1.

Maddox, R. A., 1983: Large-scale meteorological conditions associated with midlatitude, mesoscale convective complexes. *Monthly Weather Review*, **111 (7)**, 1475–1493, https://doi.org/10.1175/1520-0493(1983)111<1475:LSMCAW>2.0.CO;2.

——, C. F. Chappell, and L. R. Hoxit, 1979: Synoptic and meso-scale aspects of flash flood events. *Bulletin of the American Meteorological Society*, **60 (2)**, 115–123, https://doi.org/10.1175/1520-0477-60.2.115.

——, K. W. Howard, D. L. Bartels, and D. M. Rodgers, 1986: Mesoscale Convective Complexes in the Middle Latitudes. *Mesoscale Meteorology and Forecasting*, American Meteorological Society, 390–413.

McTaggart-Cowan, R., P. A. Vaillancourt, L. Separovic, S. Corvec, and A. Zadra, 2020: A convection parameterization for low-CAPE environments. *Monthly Weather Review*, **148 (12)**, 4917–4941, https://doi.org/10.1175/MWR-D-20-0020.1.

Min, S. K., X. Zhang, F. W. Zwiers, and G. C. Hegerl, 2011: Human contribution to more-intense precipitation extremes. *Nature*, **470 (7334)**, 378–381, https://doi.org/10.1038/nature09763.

Miralles, D. G., P. Gentine, S. I. Seneviratne, and A. J. Teuling, 2019: Land–atmospheric feedbacks during droughts and heatwaves: state of the science and current challenges.

Annals of the New York Academy of Sciences, **1436 (1)**, 19–35, https://doi.org/10.1111/nyas.13912.

Mo, K. C., J. N. Paegle, and R. W. Higgins, 1997: Atmospheric processes associated with summer floods and droughts in the central United States. *Journal of Climate*, **10 (12)**, 3028–3046, https://doi.org/10.1175/1520-0442(1997)010<3028:APAWSF>2.0.CO;2.

Moore, B. J., K. M. Mahoney, E. M. Sukovich, R. Cifelli, and T. M. Hamill, 2015: Climatology and environmental characteristics of extreme precipitation events in the southeastern United States. *Monthly Weather Review*, **143 (3)**, 718–741, https://doi.org/10.1175/MWR-D-14-00065.1.

Moore, J. T., F. H. Glass, C. E. Graves, S. M. Rochette, and M. J. Singer, 2003: The environment of warm-season elevated thunderstorms associated with heavy rainfall over the central United States. *Weather and Forecasting*, **18 (5)**, 861–878, https://doi.org/10.1175/1520-0434(2003)018<0861:TEOWET>2.0.CO;2.

Motha, R. P., 2011: The Impact of Extreme Weather Events on Agriculture in the United States. *Challenges and Opportunities in Agrometeorology*, 397–407.

Neelin, J. D., S. Sahany, S. N. Stechmann, and D. N. Bernstein, 2017: Global warming precipitation accumulation increases above the current-climate cutoff scale. *Proceedings of the National Academy of Sciences of the United States of America*, **114 (6)**, 1258–1263, https://doi.org/10.1073/pnas.1615333114.

Nelson, B. R., O. P. Prat, D. J. Seo, and E. Habib, 2016: Assessment and implications of NCEP stage IV quantitative precipitation estimates for product intercomparisons. *Weather and Forecasting*, **31 (2)**, 371–394, https://doi.org/10.1175/WAF-D-14-00112.1.

Nielsen, E. R., and R. S. Schumacher, 2016: Using convection-allowing ensembles to understand the predictability of an extreme rainfall event. *Monthly Weather Review*, **144 (10)**, 3651–3676, https://doi.org/10.1175/MWR-D-16-0083.1.

——, and ——, 2020: Observations of extreme short-term precipitation associated with supercells and mesovortices. *Monthly Weather Review*, **148 (1)**, 159–182, https://doi.org/10.1175/MWR-D-19-0146.1.

NOAA National Centers for Environmental Information, 2013: *Monthly Drought Report for Annual 2012*. URL https://www.ncei.noaa.gov/access/monitoring/monthly-report/drought/201213.

——, 2022: *Monthly National Climate Report for July 2022*. URL https://www.ncei.noaa.gov/access/monitoring/monthly-report/national/202207.

——, 2023: U.S. Billion-Dollar Weather and Climate Disasters. URL https://www.ncei.noaa.gov/access/billions/.

NWS/NOAA, 2021: Natural hazard statistics. URL https://www.weather.gov/hazstat/.

——, 2023: Glossary. URL http://www.weather.gov/glossary/.

O'Gorman, P. A., and C. J. Muller, 2010: How closely do changes in surface and column water vapor follow Clausius-Clapeyron scaling in climate change simulations? *Environmental Research Letters*, **5 (2)**, 025207, https://doi.org/10.1088/1748-9326/5/2/025207.

Pall, P., M. R. Allen, and D. A. Stone, 2007: Testing the Clausius-Clapeyron constraint on changes in extreme precipitation under CO2 warming. *Climate Dynamics*, **28 (4)**, 351–363, https://doi.org/10.1007/s00382-006-0180-2.

Panthou, G., A. Mailhot, E. Laurence, and G. Talbot, 2014: Relationship between surface temperature and extreme rainfalls: A multi-time-scale and event-based analysis. *Journal of Hydrometeorology*, **15 (5)**, 1999–2011, https://doi.org/10.1175/JHM-D-14-0020.1.

Park, I. H., and S. K. Min, 2017: Role of convective precipitation in the relationship between subdaily extreme precipitation and temperature. *Journal of Climate*, **30 (23)**, 9527–9537, https://doi.org/10.1175/JCLI-D-17-0075.1.

Perica, S., S. Pavlovic, M. St Laurent, C. Trypaluk, D. Unruh, and O. Wilhite, 2018: Precipitation-Frequency Atlas of the United States. Volume 11, Version 2.0. Texas. https://doi.org/10.25923/1ceg-5094.

Peters, J. M., and R. S. Schumacher, 2014: Objective categorization of heavy-rain-producing MCS synoptic types by rotated principal component analysis. *Monthly Weather Review*, **142 (5)**, 1716–1727, https://doi.org/10.1175/MWR-D-13-00295.1.

Pitchford, K. L., and J. London, 1962: The Low-Level Jet as Related to Nocturnal Thunderstorms over Midwest United States. *Journal of Applied Meteorology*, **1 (1)**, 43–47, https://doi.org/10.1175/1520-0450(1962)001<0043:tlljar>2.0.co;2.

Prein, A. F., and Coauthors, 2015: A review on regional convection-permitting climate modeling: Demonstrations, prospects, and challenges. *Reviews of Geophysics*, **53 (2)**, 323–361, https://doi.org/10.1002/2014RG000475.

——, C. Liu, K. Ikeda, S. B. Trier, R. M. Rasmussen, G. J. Holland, and M. P. Clark, 2017a: Increased rainfall volume from future convective storms in the US. *Nature Climate Change*, **7 (12)**, 880–884, https://doi.org/10.1038/s41558-017-0007-7.

——, R. M. Rasmussen, K. Ikeda, C. Liu, M. P. Clark, and G. J. Holland, 2017b: The future intensification of hourly precipitation extremes. *Nature Climate Change*, **7 (1)**, 48–52, https://doi.org/10.1038/nclimate3168.

——, C. Liu, K. Ikeda, R. Bullock, R. M. Rasmussen, G. J. Holland, and M. Clark, 2020: Simulating North American mesoscale convective systems with a convection-permitting climate model. *Climate Dynamics*, **55 (1–2)**, 95–110, https://doi.org/10.1007/s00382-017-3993-2.

Rahmani, V., S. L. Hutchinson, J. A. Harrington, and J. M. S. Hutchinson, 2016: Analysis of frequency and magnitude of extreme rainfall events with potential impacts on flooding: a

case study from the central United States. *International Journal of Climatology*, **36 (10)**, 3578–3587, https://doi.org/10.1002/joc.4577.

Rasmussen, K. L., A. F. Prein, R. M. Rasmussen, K. Ikeda, and C. Liu, 2020: Changes in the convective population and thermodynamic environments in convection-permitting regional climate simulations over the United States. *Climate Dynamics*, **55 (1–2)**, 383–408, https://doi.org/10.1007/s00382-017-4000-7.

Rentschler, J., and M. Salhab, 2020: *People in Harm's Way: Flood Exposure and Poverty in 189 Countries*. Policy Research Working Paper;No. 9447. © World Bank, Washington, DC. URL http://hdl.handle.net/10986/34655 License: CC BY 3.0 IGO.

Risser, M. D., C. J. Paciorek, T. A. O'Brien, M. F. Wehner, and W. D. Collins, 2019: Detected changes in precipitation extremes at their native scales derived from in situ measurements. *Journal of Climate*, **32 (23)**, 8087–8109, https://doi.org/10.1175/JCLI-D-19-0077.1.

Rotunno, R., J. B. Klemp, and M. L. Weisman, 1988: A theory for strong, long-lived squall lines. *Journal of the Atmospheric Sciences*, **45 (3)**, 463–485, https://doi.org/10.1175/1520-0469(1988)045<0463:ATFSLL>2.0.CO;2.

Schumacher, R. S., and R. H. Johnson, 2005: Organization and environmental properties of extreme-rain-producing mesoscale convective systems. *Monthly Weather Review*, **133 (4)**, 961–976, https://doi.org/10.1175/MWR2899.1.

——, and ——, 2006: Characteristics of U.S. extreme rain events during 1999-2003. *Weather and Forecasting*, **21 (1)**, 96–85, https://doi.org/10.1175/WAF900.1.

——, and ——, 2008: Mesoscale processes contributing to extreme rainfall in a midlatitude warm-season flash flood. *Monthly Weather Review*, **136 (10)**, 3964–3986, https://doi.org/10.1175/2008MWR2471.1.

——, and ——, 2009: Quasi-stationary, extreme-rain-producing convective systems associated with midlevel cyclonic circulations. *Weather and Forecasting*, **24 (2)**, 555–574, https://doi.org/10.1175/2008WAF2222173.1.

——, and K. L. Rasmussen, 2020: The formation, character and changing nature of mesoscale convective systems. *Nature Reviews Earth and Environment*, **1 (6)**, 300–314, https://doi.org/10.1038/s43017-020-0057-7.

——, A. J. Clark, M. Xue, and F. Kong, 2013: Factors influencing the development and maintenance of nocturnal heavy-rain-producing convective systems in a storm-scale ensemble. *Monthly Weather Review*, **141 (8)**, 2778–2801, https://doi.org/10.1175/MWR-D-12-00239.1.

Shapiro, A., and E. Fedorovich, 2010: Analytical description of a nocturnal low-level jet. *Quarterly Journal of the Royal Meteorological Society*, **136 (650)**, 1255–1262, https://doi.org/10.1002/qj.628.

——, ——, and S. Rahimi, 2016: A unified theory for the great plains nocturnal low-level jet. *Journal of the Atmospheric Sciences*, **73 (8)**, 3037–3057, https://doi.org/10.1175/JAS-D-15-0307.1.

Smith, J. A., M. L. Baeck, A. A. Ntelekos, G. Villarini, and M. Steiner, 2011: Extreme rainfall and flooding from orographic thunderstorms in the central Appalachians. *Water Resources Research*, **47 (4)**, https://doi.org/10.1029/2010WR010190.

Sohn, W., J. H. Kim, M. H. Li, and R. Brown, 2019: The influence of climate on the effectiveness of low impact development: A systematic review. *Journal of Environmental Management*, **236**, 365–379, https://doi.org/10.1016/j.jenvman.2018.11.041.

Špitalar, M., J. J. Gourley, C. Lutoff, P. E. Kirstetter, M. Brilly, and N. Carr, 2014: Analysis of flash flood parameters and human impacts in the US from 2006 to 2012. *Journal of Hydrology*, **519**, 863–870, https://doi.org/10.1016/j.jhydrol.2014.07.004.

Stevenson, S. N., and R. S. Schumacher, 2014: A -10-Year survey of extreme rainfall events in the central and eastern United States using gridded multisensor precipitation analyses. *Monthly Weather Review*, **142 (9)**, 3147–3162, https://doi.org/10.1175/MWR-D-13-00345.1.

Sun, Y., S. Solomon, A. Dai, and R. W. Portmann, 2007: How often will it rain? *Journal of Climate*, **20 (19)**, 4801–4818, https://doi.org/10.1175/JCLI4263.1.

Swain, D. L., O. E. J. Wing, P. D. Bates, J. M. Done, K. A. Johnson, and D. R. Cameron, 2020: Increased Flood Exposure Due to Climate Change and Population Growth in the United States. *Earth's Future*, **8 (11)**, e2020EF001778, https://doi.org/10.1029/2020EF001778.

Tang, S., P. Gleckler, S. Xie, J. Lee, M. S. Ahn, C. Covey, and C. Zhang, 2021: Evaluating the Diurnal and Semidiurnal Cycle of Precipitation in CMIP6 Models Using Satellite- and Ground-Based Observations. *Journal of Climate*, **34 (8)**, 3189–3210, https://doi.org/10.1175/JCLI-D-20-0639.1.

Terti, G., I. Ruin, S. Anquetin, and J. J. Gourley, 2015: Dynamic vulnerability factors for impact-based flash flood prediction. *Natural Hazards*, **79 (3)**, 1481–1497, https://doi.org/10.1007/s11069-015-1910-8.

Trenberth, K. E., 2011: Changes in precipitation with climate change. *Climate Research*, **47 (1–2)**, 123–138, https://doi.org/10.3354/cr00953.

——, A. Dai, R. M. Rasmussen, and D. B. Parsons, 2003: The changing character of precipitation. *Bulletin of the American Meteorological Society*, **84 (9)**, 1205–1218, https://doi.org/10.1175/BAMS-84-9-1205.

Trier, S. B., and D. B. Parsons, 1993: Evolution of environmental conditions preceding the development of a nocturnal mesoscale convective complex. *Monthly Weather Review*, **121 (4)**, 1078–1098, https://doi.org/10.1175/1520-0493(1993)121<1078:EOECPT>2.0.CO;2.

Trier, S. B., and C. A. Davis, 2002: Influence of balanced motions on heavy precipitation within a long-lived convectively generated vortex. *Monthly Weather Review*, **130 (4)**, 877–899, https://doi.org/10.1175/1520-0493(2002)130<0877:IOBMOH>2.0.CO;2.

Trier, S. B., C. A. Davis, and J. D. Tuttle, 2000: Long-lived mesoconvective vortices and their environment. Part I: Observations from the central United States during the 1998 warm season. *Monthly Weather Review*, **128 (10)**, 3376–3395, https://doi.org/10.1175/1520-0493(2000)128<3376:LLMVAT>2.0.CO;2.

Uccellini, L. W., and D. R. Johnson, 1979: The Coupling of Upper and Lower Tropospheric Jet Streaks and Implications for the Development of Severe Convective Storms. *Monthly Weather Review*, **107 (6)**, 682–703, https://doi.org/10.1175/1520-0493(1979)107<0682:tcoual>2.0.co;2.

Villarini, G., 2016: On the seasonality of flooding across the continental United States. *Advances in Water Resources*, **87**, 80–91, https://doi.org/10.1016/j.advwatres.2015.11.009.

——, R. Goska, J. A. Smith, and G. A. Vecchi, 2014: North atlantic tropical cyclones and U.S. flooding. *Bulletin of the American Meteorological Society*, **95 (9)**, 1381–1388, https://doi.org/10.1175/BAMS-D-13-00060.1.

Vose, R. S., and Coauthors, 2014: Improved historical temperature and precipitation time series for U.S. climate divisions. *Journal of Applied Meteorology and Climatology*, **53 (5)**, 1232–1251, https://doi.org/10.1175/JAMC-D-13-0248.1.

Wallace, J. M., 1975: Diurnal Variations in Precipitation and Thunderstorm Frequency over the Conterminous United States. *Monthly Weather Review*, **103 (5)**, 406–419, https://doi.org/10.1175/1520-0493(1975)103<0406:dvipat>2.0.co;2.

Wang, H., M. Ting, and M. Ji, 1999: Prediction of seasonal mean United States precipitation based on El Niño sea surface temperatures. *Geophysical Research Letters*, **26 (9)**, 1341–1344, https://doi.org/10.1029/1999GL900230.

Wasko, C., A. Sharma, and S. Westra, 2016: Reduced spatial extent of extreme storms at higher temperatures. *Geophysical Research Letters*, **43 (8)**, 4026–4032, https://doi.org/10.1002/2016GL068509.

Weckwerth, T. M., and U. Romatschke, 2019: Where, when, and why did it rain during PECAN? *Monthly Weather Review*, **147 (10)**, 3557–3573, https://doi.org/10.1175/MWR-D-18-0458.1.

Westra, S., L. V. Alexander, and F. W. Zwiers, 2013: Global increasing trends in annual maximum daily precipitation. *Journal of Climate*, **26 (11)**, 3904–3918, https://doi.org/10.1175/JCLI-D-12-00502.1.

Westra, S., and Coauthors, 2014: Future changes to the intensity and frequency of short-duration extreme rainfall. *Reviews of Geophysics*, **52 (3)**, 522–555, https://doi.org/10.1002/2014RG000464.

Whiteman, C. D., X. Bian, and S. Zhong, 1997: Low-level jet climatology from enhanced rawinsonde observations at a site in the southern Great Plains. *Journal of Applied Meteorology*, **36 (10)**, 1363–1376, https://doi.org/10.1175/1520-0450(1997)036<1363:LLJCFE>2.0.CO;2.

Wilks, D. S., 2016: "The stippling shows statistically significant grid points": How research results are routinely overstated and overinterpreted, and what to do about it. *Bulletin of the American Meteorological Society*, **97 (12)**, 2263–2273, https://doi.org/10.1175/BAMS-D-15-00267.1.

——, 2019: Statistical methods in the atmospheric sciences (4th ed.). *Elsevier*.

Winkler, J. A., B. R. Skeeter, and P. D. Yamamoto, 1988: Seasonal variations in the diurnal characteristics of heavy hourly precipitation across the United States. *Monthly Weather Review*, **116 (8)**, 1641–1658, https://doi.org/10.1175/1520-0493(1988)116<1641:SVITDC>2.0.CO;2.

Xu, K.-M., and K. A. Emanuel, 1989: Is the tropical atmosphere conditionally unstable? *Monthly Weather Review*, **117 (7)**, 1471–1479, https://doi.org/10.1175/1520-0493(1989)117<1471:ittacu>2.0.co;2.

Yang, Q., R. A. Houze, L. R. Leung, and Z. Feng, 2017: Environments of Long-Lived Mesoscale Convective Systems Over the Central United States in Convection Permitting Climate Simulations. *Journal of Geophysical Research: Atmospheres*, **122 (24)**, 13–288, https://doi.org/10.1002/2017JD027033.

Zhang, F., C. Snyder, and R. Rotunno, 2003: Effects of moist convection on mesoscale predictability. *Journal of the Atmospheric Sciences*, **60 (9)**, 1173–1185, https://doi.org/10.1175/1520-0469(2003)060<1173:EOMCOM>2.0.CO;2.

Zhang, J., and Coauthors, 2016: Multi-Radar Multi-Sensor (MRMS) quantitative precipitation estimation: Initial operating capabilities. *Bulletin of the American Meteorological Society*, **97 (4)**, 621–638, https://doi.org/10.1175/BAMS-D-14-00174.1.

Zhang, S., and Coauthors, 2023: Dynamics Governing a Simulated Bow-and-Arrow-Type Mesoscale Convective System. *Monthly Weather Review*, **151 (3)**, 603–623, https://doi.org/10.1175/MWR-D-22-0091.1.

Zorzetto, E., and L. Li, 2021: Impacts of the North Atlantic subtropical high on daily summer precipitation over the conterminous United States. *Journal of Hydrometeorology*, **22 (7)**, 1697–1712, https://doi.org/10.1175/JHM-D-20-0242.1.